Vascular imaging in brain metastasis

Manon Simard

Trinity College

Department of Oncology

A thesis submitted to the University of Oxford in partial fulfilment for the requirements of the degree of Doctor of Philosophy

Trinity Term 2019

ACKNOWLEDGEMENTS

First, and foremost, I need to give my thanks to Prof. Niki Sibson for allowing me to initially get a glimpse of Oxford and of the great research taking place in the group, when I first came for an internship, as part of my M.Sc. I must also express my gratitude to Niki and Prof. Michael Chappell for taking a chance on me, with a biochemistry and molecular biology background, to learn about MRI physics (only a bit!) and applications for my DPhil project. It has definitely been a learning experience, but I've truly enjoyed the process. Niki, I also need to acknowledge your support and guidance throughout this experience, they have been essential for me to get where I am now. Many thanks to the Cancer Imaging Centre of Oxford (CRUK/EPSRC), since without your funding, working on this project and living in Oxford would have been impossible.

I must also give a *giant* 'thank you' to James Larkin! James, for all those sessions in the tiny MRI control room, the early hours, late nights, non-stop questions (most of the first two years, right?), singing 'Let it go' during femoral cannulations and everything in between, thank you! You've taught me so much and I'll try my hardest not to forget most of it.

Dear Sibsons, past and present, thank you for all the wonderful memories and random conversations in the office or at lunch. You have been like a family to me these last years and I've enjoyed sharing them with you immensely. I must express a special shout-out to the lab pub-crew: James, Maria, Nili, Kevin, Kleo, Mario, Yasemin and Jess. Our Friday pub sessions were therapeutic and crucial to my mental health at times but also a lot of fun! They have truly been an integral part of my Oxford experience.

To Kleo and Kevin, thank you for being my 'first friends' in Oxford, remaining friends and for all the lovely moments we've shared together. To Manuel, thank you for your positive attitude and warmth and for the random ice cream treats when the British summer *finally* decided to show up! To Sarah, my wonderful Dutch friend, your brightness, both scientific and in attitude, as well as your amazing friendship are things that I have cherished deeply. I could never forget our cryostat *life* chats.

To my office buddy, DPhil companion and most importantly great friend Niloufar, you have embellished these past four years by always being there for me personally,

emotionally and sometimes scientifically too! We have been fast friends since the day we met in the green building and it has absolutely helped to have someone like you to go through the ups and downs of DPhil life. I couldn't have done it without you mon amie!

To my fellow DPhil Oncology friends, Jakob, Ellie, Tzveta, Angela and Giovanna, we've survived the last few months! Thank you for sharing your joys, frustrations and the library with me during this writing process. Many thanks as well to my Trinity College friends, Nicolaus, Marc-Antoine, Justine and Michael for being part of my life (since Fresher's week!) in Oxford.

J'aimerais également remercier mes parents Martine et Marc pour leur soutien incessant tout au long de ma vie et de m'encourager à poursuivre mes rêves, même si cela signifie de se retrouver dans un autre continent. À mes chers frères, merci de toujours être là pour moi, malgré la distance qui nous sépare. À ma belle-sœur (SIL) Christine, merci énormément pour toujours répondre à mes appels, de me comprendre si bien et de toujours me demander comment vont mes rats! Merci aussi pour me faire parler à mon cher Olivier quand j'ai besoin d'un peu plus de motivation. Au reste de ma famille, merci de comprendre pourquoi je suis au loin, même si cela signifie manquer certains événements importants.

À mes amies, Caro, Mel, Audrey, ainsi que plusieurs autres, merci pour votre amitié qui ne connait pas de distance et surtout à Caro qui est toujours là pour moi et qui se cherche toujours une raison pour qu'on puisse se voir plus souvent!

Más importante, muchas gracias a Egon. You have made all of this possible with your love and support. Thank you for making me come to Oxford in the first place and embarking on this unforgettable journey. Thank you for proof-reading this thesis, bringing me food and understanding the long working hours, either from experiments or in the past few weeks of writing I can't wait to see what will happen as we continue on this wonderful adventure!

ABSTRACT

Vascular imaging in brain metastasis

A thesis submitted to the University of Oxford in partial fulfillment for the requirements of the degree of Doctor of Philosophy

Trinity Term 2019

Manon Simard, Trinity College

Perfusion MRI is an important technique in the imaging of brain tumours, since tumour blood flow can differentiate between primary brain tumours and metastases and can also inform treatment planning and outcome. Currently, clinical perfusion MRI techniques are most commonly performed using gadolinium-based contrast agents, which carry a risk of toxicity from gadolinium deposition in tissues and from nephrogenic systemic fibrosis.

Arterial spin labelling (ASL) MRI is a contrast agent-free MRI technique to obtain measurements of blood flow in organs such as the brain but has, thus far, mainly been limited to preclinical and clinical research studies. Recommendations for the standardisation of this technique in the clinic have been proposed, to facilitate its incorporation into routine clinical practice. Such recommendations have yet to be proposed for the preclinical use of ASL MRI. The work presented here encompasses, firstly, an optimisation of the ASL MRI technique for use in rats through the use of a multiphase pseudo-continuous labelling approach (MP-pCASL MRI). This sequence and its output cerebral blood flow (CBF) measurements were validated with gold-standard autoradiography and, subsequently, applied to a rat breast cancer brain metastasis model. CBF was monitored during tumour progression and compared to clinically-relevant MRI techniques. MP-pCASL MRI CBF measurements demonstrated a decrease in metastasis blood flow over time, correlating with a decreased microvessel density and increased levels of hypoxia histologically.

Subsequently, vascular normalisation treatment, using either bevacizumab or cediranib, was performed in this rat model of brain metastasis and MP-pCASL MRI was assessed as a contrast-free detection technique for vascular normalisation. Although, vascular normalisation was not established upon bevacizumab treatment of brain metastases, cediranib treatment led to a decrease in the permeability factor, K^{trans}, from dynamic contrast-enhanced (DCE) MRI, the current detection method for this treatment. Furthermore, metastasis blood flow obtained with MP-pCASL MRI was maintained during cediranib treatment, compared to a significant decrease in brain metastasis blood flow in vehicle-treated rats. Thus, MP-pCASL MRI could be used as a novel detection method for the onset of vascular normalisation in brain metastases, particularly in circumstances where the injection of contrast-agents, required for DCE MRI, is contraindicated and/or in situations where multiple MRI sessions may be needed.

In conclusion, the proposed, rat-optimised, MP-pCASL MRI technique can provide accurate and reproducible CBF measurements in rats and successfully identify brain regions with dysregulated blood, such as brain metastases. Finally, MP-pCASL MRI can detect vascular normalisation in brain metastases. It is hoped that the findings presented in this thesis can lead to a standardisation of preclinical ASL MRI and to the incorporation of ASL MRI for the imaging of brain tumours and their response to vascular normalisation treatments in both preclinical and clinical settings.

RESEARCH CONTRIBUTIONS

Peer-reviewed journal articles

- Larkin, J. R., **Simard, M. A**.[1], Khrapitchev, A. A., Meakin, J. A., Okell, T. W., Craig, M., Ray, K. J., Jezzard, P., Chappell, M. A. and Sibson, N. R. (2018) 'Quantitative blood flow measurement in rat brain with multiphase arterial spin labelling magnetic resonance imaging', *Journal of Cerebral Blood Flow & Metabolism*, p. 0271678X1875621. doi: 10.1177/0271678X18756218.

- Buck, J., Larkin, J. R., **Simard, M. A**., Khrapitchev, A. A., Chappell, M. A. and Sibson, N. R. (2018) 'Sensitivity of multiphase pseudocontinuous arterial spin labelling (MP pCASL) magnetic resonance imaging for measuring brain and tumour blood flow in mice', *Contrast Media and Molecular Imaging*, 2018. doi: 10.1155/2018/4580919.

- Ray, K. J., **Simard, M. A.**, Larkin, J. R., Coates, J., Kinchesh, P., Smart, S. C., Higgins, G. S., Chappell, M. A. and Sibson, N. R. (2019) 'Tumor pH and protein concentration contribute to the signal of amide proton transfer magnetic resonance imaging', *Cancer Research*, 79(7), pp. 1343–1352.

- Msayib, Y., Craig, M., **Simard, M. A.,** Larkin, J. R., Shin, D. D., Liu, T. T., Sibson, N. R., Okell, T. W. and Chappell, M. A. (2019) 'Robust estimation of quantitative perfusion from multi-phase pseudo-continuous arterial spin labelling', *Magnetic Resonance in Medicine*, p. 308.

Patents

- Chappell, M. A., Craig, M., Larkin J. R. and **Simard, M.A.** Methods and Systems of Multiphase Arterial Spin Labelling. Filed date: 27/10/2017 (USPTO 62/577,994).

Conference proceedings

Oral presentations

- **Simard M. A**., Larkin, J. R., Chappell, M. A. and Sibson, N.R. (2018) 'Quantitative perfusion measurements in rat brain metastasis using arterial spin labelling MRI', *Annual Brain Metastasis Research and Emerging Therapy Conference*, Marseille, France.

[1] Co-first authors.

- **Simard M. A**., Larkin, J. R., Chappell, M. A. and Sibson, N.R. (2017) 'Quantitative blood flow measurement of pre-clinical brain metastasis with multiphase pseudo-continuous ASL MRI', *Cancer Imaging Conference,* London, UK.

- **Simard M. A**., Larkin, J. R., Ray, K. J., Khrapitchev, A. A., Meakin, J. A., Jezzard, P., Chappell, M. A. and Sibson, N.R. (2016) 'Arterial Spin Labelling MRI of cerebral tumours in rats', *British Neuro-Oncology Society Conference,* Leeds, UK.

Poster presentations

- **Simard M. A**., Larkin, J. R., Chappell, M. A., Khrapitchev, A. A. and Sibson, N.R. (2016) 'Optimisation of pre-clinical ASL MRI in rodents', *British Chapter of the ISMRM Post-Grad Symposium,* London, UK.

- **Simard M. A**., Larkin, J. R., Ray, K. J., Chappell, M. A. and Sibson, N.R. (2016) 'Applying quantitative multiphase pCASL to a pre-clinical brains metastasis model', *British Chapter of the ISMRM Annual Meeting,* Leeds, UK.

- **Simard M. A**., Larkin, J. R., Khrapitchev, A. A., Meakin, J. A., Okell, T. W., Jezzard, P., Chappell, M. A. and Sibson, N.R. (2017) 'Validation of quantitative preclinical pseudo-continuous ASL in rat brain', *ISMRM Annual Meeting,* Honolulu, USA.

- **Simard M. A**., Larkin, J. R., Khrapitchev, A. A., Ray, K. J., Chappell, M. A. and Sibson, N.R. (2017) 'Application of multiphase pseudo-continuous ASL for quantitative blood flow measurements in rat brain metastasis', *ISMRM Annual Meeting,* Honolulu, USA.

- **Simard M. A**., Larkin, J. R., Chappell, M. A. and Sibson, N.R. (2018) 'Multiphase pseudo-continuous arterial spin labelling MRI for quantitative cerebral blood flow measurements in a rat model of breast cancer brain metastasis', *International Biennial Metastatic Research Society Congress*, Princeton, USA.

- **Simard M. A**., Ray, K. J., Larkin, J. R., Chappell, M. A. and Sibson, N.R. (2018) 'Non-invasive characterisation of a rat model of brain metastasis using MP-pCASL and APT MRI', *British Chapter of the ISMRM Annual Meeting*, Oxford, UK.

- **Simard M. A**., Larkin, J. R., Ray, K. J., Smart, S. C., Allen, P. D., Chappell, M. A. and Sibson, N.R. (2019) 'Non-invasive detection of vascular normalisation in a rat brain metastasis model', *29th International Symposium on Cerebral Blood Flow, Metabolism and Function,* Yokohama.

- **Simard M. A**., Larkin, J. R., Ray, K. J., Smart, S. C., Allen, P. D., Chappell, M. A. and Sibson, N.R. (2019) 'Non-invasive detection of vascular normalisation in a rat brain metastasis model', *Brain Metastasis Research Symposium,* Vienna, Austria.

Co-author on conference proceedings

- Larkin, J. R., **Simard M. A**., Khrapitchev, A. A., Ray, K. J., Meakin, J. A., Kinchesh, P., Smart, S. C., Jezzard, P., Chappell, M. A. and Sibson, N.R. (2016)' Multiphase pCASL for imaging blood flow in rodent brains', *ISMRM Annual Meeting,* Singapore.

- Ray, K. J., **Simard M. A**., Larkin, J. R., Khrapitchev, A. A., Chappell, M. A. and Sibson, N.R. (2016) ' Exploring endogenous CEST MRI as a means of pH imaging of brain metastases', *Cancer Imaging Conference,* Manchester, UK.

- Buck, J., Larkin, J. R., Khrapitchev, A. A., **Simard M. A**., Ray, K. J., Westphal, R., Chappell, M. A. and Sibson, N.R. (2017) 'Adaptation of multiphase pseudo-continuous ASL to image cerebral blood flow in mice at 9.4T', *ISMRM Annual Meeting,* Honolulu, USA.

- Chappell, M. A., Craig, M., Larkin, J. R., **Simard M. A**., Sibson, N.R. and Okell, T. W. (2018) 'Robust estimation of quantitative perfusion from multi-phase pseudo-continuous arterial spin labelling', *ISMRM Annual Meeting,* Paris, France.

- Croal, P. L., Ray, K. J., Larkin, J. R., **Simard M. A**., Sutherland, B., Kennedy, J., Sibson, N.R. and Chappell, M. A. (2018) 'How valuable is T1 and T2 information for model-based analysis of CEST MRI in disease?', *ISMRM Annual Meeting,* Paris, France.

- Ray, K. J., **Simard M. A**., Larkin, J. R., Chappell, M. A. and Sibson, N.R. (2018) 'Separation of the contribution of protein concentration and pH to measured APT signal changes in a preclinical model of brain metastasis', *ISMRM Annual Meeting,* Paris, France.

- Peter, J., Ray, K. J., **Simard M. A**., Chappell, M. A. and Sibson, N.R. (2018) 'Selective acidification of tumour extracellular pH using glucose measured by Amine Proton Transfer MRI', *British Chapter of the ISMRM Annual Meeting*, Oxford, UK.

- Larkin, J. R., de Bernardi, **Simard M. A**., Ray, K. J. and Sibson, N.R. (2018) 'Vascular mapping by MRI and histology in a rat brain metastasis model with radiotherapy', *British Chapter of the ISMRM Annual Meeting*, Oxford, UK.

- Larkin, J. R., **Simard M. A**., de Bernardi, A., Perez-Balderas, F., Johanssen, V. A. and Sibson, N.R. (2019) 'Improved delineation of true metastasis volume with multimodal MRI in a rat model', *Brain Metastasis Research Symposium,* Vienna, Austria.

- Larkin, J. R., **Simard M. A**., de Bernardi, A., Perez-Balderas, F., Johanssen, V. A. and Sibson, N.R. (2019) 'Improved delineation of true metastasis volume with multimodal MRI in a rat model', *29th International Symposium on Cerebral Blood Flow, Metabolism and Function,* Yokohama.

CONTENTS

Acknowledgements i
Abstract iii
Research contributions iv
Contents vii
List of figures xi
List of tables xiv
Abbreviations xv

1. Introduction ..... - 1 -
1.1 Cancer and brain metastases ..... - 1 -
1.1.1 Cancer and tumour progression ..... - 1 -
1.1.2 Metastatic cascade ..... - 2 -
1.1.3 Brain metastases ..... - 4 -
1.2 Current clinical prognosis and treatment of patients with brain metastases - 7 -
1.2.1 Current clinical guidance for brain metastasis detection and treatment ..... - 7 -
1.3 Arterial spin labelling MRI ..... - 10 -
1.3.1 Labelling strategies in ASL MRI ..... - 12 -
1.3.2 Obstacles in the clinical implementation of ASL ..... - 13 -
1.4 Novel treatment strategies of brain metastases ..... - 14 -
1.5 Tumour angiogenesis and anti-angiogenic therapy ..... - 16 -
1.5.2 Anti-angiogenic treatment and vascular normalisation ..... - 20 -
1.6 Preclinical models of brain metastasis ..... - 24 -
1.6.1 Preclinical ASL MRI ..... - 26 -
1.7 Thesis aims ..... - 28 -

2. Methods and materials ..... - 29 -
2.1 Cell lines and *in vitro* cell culture ..... - 29 -
2.2 Animals ..... - 30 -
2.2.1 Preclinical intracerebral brain metastasis model ..... - 30 -
2.2.2 Perfusion-fixation ..... - 32 -
2.3 Magnetic resonance imaging ..... - 33 -
2.3.1 Multiphase pCASL MRI ..... - 34 -
2.3.2 Diffusion-weighted MRI ..... - 35 -
2.3.3 T_1-weighted imaging ..... - 36 -
2.3.4 T_2-weighted imaging ..... - 36 -
2.3.5 Dynamic contrast-enhanced MRI ..... - 37 -
2.3.6 Relaxometry ..... - 37 -
2.3.7 Chemical exchange saturation transfer MRI ..... - 38 -
2.3.8 Segmentation of regions of interest in the brain ..... - 39 -
2.4 Immunohistochemistry ..... - 40 -

2.4.1 Tissue sectioning ..... - 40 -
2.4.2 Antigen retrieval protocol ..... - 41 -
2.4.3 Standard immunohistochemistry protocol ..... - 41 -
2.4.4 IHC analysis ..... - 42 -

3. Optimisation of preclinical arterial spin labelling in rats ..... - 45 -
3.1 Introduction ..... - 45 -
3.1.1 Clinical recommendations for arterial spin labelling (ASL) ..... - 45 -
3.1.2 Preclinical ASL MRI ..... - 46 -
3.1.3 Multiphase pCASL MRI ..... - 47 -
3.1.4 Chapter aim and hypotheses ..... - 49 -
3.2 Methods ..... - 51 -
3.2.1 Animals ..... - 51 -
3.2.2 Power Doppler ultrasound ..... - 51 -
3.2.3 Bloch simulations ..... - 53 -
3.2.4 Magnetic resonance imaging ..... - 54 -
3.2.5 [^{14}C]-Iodoantipyrine autoradiography ..... - 61 -
3.3 Results ..... - 65 -
3.3.1 Considerations prior to starting pCASL MRI ..... - 65 -
3.3.2 MP-pCASL MRI optimisation ..... - 70 -
3.3.3 Post-processing of MP-pCASL MRI ..... - 78 -
3.3.4 Comparison of MP-pCASL MRI to other CBF measurement methods ..... - 85 -
3.4 Discussion ..... - 93 -
3.4.1 Parameter selection for MP-pCASL prior to MRI ..... - 93 -
3.4.2 MP-pCASL MRI optimisation ..... - 94 -
3.4.3 Impact of analysis on MP-pCASL MRI CBF measurements ..... - 97 -
3.4.4 Comparisons of CBF from MP-pCASL MRI with other CBF measurement methods ..... - 98 -
3.4.5 Optimised MP-pCASL MRI in naïve rats ..... - 100 -
3.5 Conclusion ..... - 103 -

4. Multiphase pCASL MRI in a rat model of breast cancer brain metastasis ..... - 105 -
4.1 Introduction ..... - 105 -
4.1.1 Clinical research applications of arterial spin labelling MRI ..... - 105 -
4.1.2 ASL in rodent brain metastasis ..... - 107 -
4.1.3 Chapter hypotheses and aims ..... - 108 -
4.2 Methods ..... - 110 -
4.2.1 Rat intracerebral brain metastasis model ..... - 110 -
4.2.2 Magnetic resonance imaging ..... - 111 -
4.2.3 Immunohistochemistry ..... - 113 -
4.3 Results ..... - 114 -
4.3.1 ENU brain metastasis progression imaged with clinically relevant MRI techniques ..... - 114 -
4.3.2 Effect of brain metastasis on brain tissue relaxation times ..... - 120 -
4.3.3 MP-pCASL MRI of ENU brain metastases ..... - 124 -
4.3.4 Histological findings during ENU brain metastasis growth ..... - 127 -
4.4 Discussion ..... - 131 -

4.4.1 Clinically relevant MRI methods for imaging brain metastases ..... - 131 -
4.4.2 Brain metastases affect brain tissue relaxation times ..... - 133 -
4.4.3 MP-pCASL MRI as a non-invasive method for perfusion measurement in brain metastases ..... - 134 -
4.4.4 Relating histological findings of ENU brain metastasis progression to MRI results ..... - 135 -
4.5 Conclusion ..... - 138 -

5. Vascular normalising effects of bevacizumab treatment in rat brain metastases ..... - 141 -
5.1 Introduction ..... - 141 -
5.1.1 Vascular normalisation ..... - 141 -
5.1.2 Bevacizumab ..... - 142 -
5.1.3 Current detection method of vascular normalisation in tumours ..... - 143 -
5.1.4 Chapter aims ..... - 145 -
5.2 Methods ..... - 147 -
5.2.1 Rat breast cancer brain metastasis model ..... - 147 -
5.2.2 Experimental plan ..... - 147 -
5.2.3 Bevacizumab ..... - 148 -
5.2.4 Magnetic resonance imaging ..... - 149 -
5.2.5 Immunohistochemistry ..... - 150 -
5.3 Results ..... - 152 -
5.3.1 Dynamic contrast-enhanced MRI for detection of vascular normalisation with bevacizumab ..... - 152 -
5.3.2 GBCA-free MRI of bevacizumab-treated rat brain metastases ..... - 154 -
5.3.3 Effects of bevacizumab treatment on brain vasculature histology and brain metastasis hypoxia levels ..... - 159 -
5.4 Discussion ..... - 165 -
5.4.1 Bevacizumab treatment of rat brain metastases did not result in a normalisation of the tumour vasculature ..... - 165 -
5.4.2 Shortcomings of bevacizumab treatment in rat brain metastases ..... - 166 -
5.5 Conclusion ..... - 169 -

6. Vascular normalisation in rat brain metastases using cediranib ..... - 171 -
6.1 Introduction ..... - 171 -
6.1.1 Chapter aims ..... - 173 -
6.2 Methods ..... - 175 -
6.2.1 Rat breast cancer brain metastasis model ..... - 175 -
6.2.2 MRI and treatment plan ..... - 175 -
6.2.3 Cediranib ..... - 177 -
6.2.4 Magnetic resonance imaging ..... - 178 -
6.2.5 High-performance liquid chromatography and mass spectrometry ..... - 178 -
6.2.6 Immunohistochemistry ..... - 180 -
6.3 Results ..... - 182 -
6.3.1 Cediranib treatment inhibits brain metastasis growth over time ..... - 182 -
6.3.2 Dynamic contrast-enhanced MRI for detection of vascular normalisation with cediranib ..... - 184 -

6.3.3 Changes detected by non-invasive MRI techniques during cediranib treatment of rat brain metastases ..... - 186 -
6.3.4 Cediranib concentration in brain metastases ..... - 193 -
6.3.5 Histological assessment of rat brain metastases after cediranib treatment ..... - 194 -
6.4 Discussion ..... - 201 -
6.4.1 Cediranib treatment of rat brain metastases yielded changes in MRI, supporting the vascular normalisation hypothesis ..... - 201 -
6.4.2 Cediranib was efficiently delivered to sites of brain metastases ..... - 204 -
6.4.3 Cediranib treatment of rat brain metastases could not be observed by histological analysis ..... - 205 -
6.5 Conclusion ..... - 208 -

7. Conclusions, critique and future work ..... - 209 -
7.1 Conclusions ..... - 209 -
7.2 Critique and future work ..... - 211 -
7.2.1 Additional improvements to MP-pCASL MRI ..... - 211 -
7.2.2 Consideration of brain metastasis heterogeneity in MRI analyses ..... - 212 -
7.2.3 Discrepancies between histological and MRI results ..... - 214 -
7.2.4 Clinical perspectives of MP-pCASL MRI and vascular normalisation of brain metastases ..... - 216 -
7.3 Concluding remarks ..... - 217 -

References ..... - 219 -

Appendix I: Peer-reviewed article ..... - 241 -

Appendix II: Detection of perfused vessels in rat brain metastases ..... - 255 -
Aim ..... - 255 -
Method ..... - 255 -
Result and discussion ..... - 256 -

List of figures

Figure 1.1: Hallmarks of cancer. ..... - 2 -
Figure 1.2: Metastatic cascade. ..... - 3 -
Figure 1.3: Relative incidence of primary tumours and brain metastases by tumour type. ..... - 5 -
Figure 1.4: Blood-brain barrier. ..... - 7 -
Figure 1.5: Arterial spin labelling acquisition and quantitation. ..... - 11 -
Figure 1.6: Tumour-associated vessels. ..... - 17 -
Figure 1.7: Vascular normalisation of tumour vessels. ..... - 23 -
Figure 1.8: Ectopic injections for brain metastasis models. ..... - 26 -
Figure 2.1 Segmentation of brain regions of interest on MRI. ..... - 40 -
Figure 2.2 Brain regions of interest in IHC. ..... - 43 -
Figure 3.1 Advantage of multiphase pCASL MRI over traditional label-control pCASL MRI. ..... - 48 -
Figure 3.2 Measuring carotid blood velocity in rats using Power Doppler ultrasound. ..... - 53 -
Figure 3.3 MP-pCASL MRI labelling plane locations. ..... - 55 -
Figure 3.4 MP-pCASL MRI sequence at varying label durations. ..... - 55 -
Figure 3.5 Schematic of background suppression in MP-pCASL MRI. ..... - 58 -
Figure 3.6 Pulse sequence of MP-pCASL MRI. ..... - 66 -
Figure 3.7 Carotid blood velocity in naïve rat strains. ..... - 67 -
Figure 3.8 Relaxometry of oxygenated rat blood at 37 ˚C at 9.4 T. ..... - 68 -
Figure 3.9 Inversion efficiency of multiphase pCASL MRI determined by Bloch simulations. ..... - 69 -
Figure 3.10 Selection of bandwidth and echo time at 9.4 T based on signal to noise ratio in EPI MRI. ..... - 70 -
Figure 3.11 Angled labelling plane in MP-pCASL MRI leads to improved inversion and robust CBF output. ..... - 72 -
Figure 3.12 Effect of location of angled labelling plane in MP-pCASL MRI on rat CBF. - 73 -
Figure 3.13 Effect of MP-pCASL MRI label duration on rat apparent CBF. ..... - 74 -
Figure 3.14 Imaging efficiency of MP-pCASL MRI according to label duration. ..... - 75 -
Figure 3.15 Labelled blood arrival time and selection of optimal post-label delay. ..... - 76 -
Figure 3.16 Background suppression in 2D MP-pCASL MRI. ..... - 78 -
Figure 3.17 Selection of α and β in modified Fermi function for MP-pCASL MRI analysis. ..... - 79 -
Figure 3.18 Supervoxel analysis improves CBF measurements. ..... - 81 -
Figure 3.19 Supervoxel parameter selection for MP-pCASL MRI analysis. ..... - 81 -
Figure 3.20 MP-pCASL MRI analysis pipeline. ..... - 83 -
Figure 3.21 Optimal phase offsets in each supervoxel ROI in rats. ..... - 84 -
Figure 3.22 CBF map comparison between of traditional label-control pCASL MRI and MP pCASL MRI. ..... - 86 -
Figure 3.23 Measured CBF and coefficient of variation comparison between traditional label-control pCASL MRI and MP-pCASL MRI. ..... - 87 -
Figure 3.24 CBF maps from gold-standard [14C]-iodoantipyrine autoradiography and MP pCASL MRI. ..... - 88 -

Figure 3.25 CBF quantitation of gold-standard [^{14}C]-iodoantipyrine autoradiography and MP-pCASL MRI. ..... - 89 -
Figure 3.26 CBF quantitation comparison of [^{14}C]-iodoantipyrine autoradiography and 1- and 2-compartment model analyses of MP-pCASL MRI data. ..... - 91 -
Figure 3.27 Example CBF maps and measurements from MP-pCASL MRI in rat brain. ..... - 92 -
Figure 4.1 Arterial spin labelling MRI publications over time. ..... - 106 -
Figure 4.2 Rat experimental plan imaging of brain metastasis progression. ..... - 111 -
Figure 4.3 Anatomical imaging of ENU brain metastasis progression in BDIX rats. ..... - 115 -
Figure 4.4 Apparent diffusion coefficient of ENU brain metastases during tumour progression in BDIX rats. ..... - 117 -
Figure 4.5 Relative cerebral blood volume of ENU brain metastases during tumour progression in BDIX rats. ..... - 119 -
Figure 4.6 T_1 relaxation time of ENU brain metastases during tumour progression in BDIX rats. ..... - 121 -
Figure 4.7 T_2 relaxation time of ENU brain metastases during tumour progression in BDIX rats. ..... - 123 -
Figure 4.8 Arrival time of MP pCASL MRI labelled blood in ENU brain metastases at three weeks post-injection. ..... - 124 -
Figure 4.9 Cerebral blood flow of ENU brain metastases during tumour progression in BDIX rats. ..... - 126 -
Figure 4.10 Vessel density in ENU brain metastases in BDIX rats over time. ..... - 128 -
Figure 4.11 Hypoxic fraction in ENU brain metastases in BDIX rats over time. ..... - 129 -
Figure 4.12 Angiogenesis in ENU brain metastases in BDIX rats over time. ..... - 130 -
Figure 5.1 Rat experimental plan for bevacizumab treatment and imaging in brain metastases. ..... - 148 -
Figure 5.2 Anatomical changes in brain metastases treated with bevacizumab. ..... - 153 -
Figure 5.3 Brain metastasis permeability following bevacizumab treatment. ..... - 154 -
Figure 5.4 Cerebral blood flow in bevacizumab-treated brain metastases over time ..... - 155 -
Figure 5.5 Variations in APTR* signal of brain metastases treatment with bevacizumab ..... - 156 -
Figure 5.6 Tissue water diffusion in bevacizumab-treated brain metastases. ..... - 157 -
Figure 5.7 T_1 relaxation measurements in bevacizumab-treated brain metastases. ..... - 158 -
Figure 5.8 Summary of MRI findings for bevacizumab treatment in rat brain metastases. ..... - 159 -
Figure 5.9 Microvessel density in brain metastases treated with bevacizumab. ..... - 160 -
Figure 5.10 Vascular maturation index following bevacizumab treatment in brain metastases. ..... - 162 -
Figure 5.11 Effect of bevacizumab treatment on the hypoxic fraction of rat brain metastases. ..... - 163 -
Figure 6.1 Rat experimental plan for cediranib treatment and imaging in brain metastases. ..... - 176 -
Figure 6.2 Anatomical changes in brain metastases treated with cediranib. ..... - 183 -
Figure 6.3 Brain metastasis permeability in cediranib-treated rats. ..... - 185 -
Figure 6.4 Effect of cediranib treatment on brain metastasis blood flow over time. - 187 -
Figure 6.5 Changes in APTR* in cediranib-treated brain metastases. ..... - 188 -

Figure 6.6 Apparent diffusion coefficients in cediranib-treated brain metastases. - 189 -
Figure 6.7 Effect of cediranib treatment on T_1 relaxation of brain metastases. - 190 -
Figure 6.8 Summary of MRI findings of cediranib treatment and withdrawal in rat brain metastases. - 192 -
Figure 6.9 Cediranib concentration in brain metastases and rat plasma following treatment. - 194 -
Figure 6.10 Microvessel density of brain metastases treated with cediranib. - 197 -
Figure 6.11 Pericyte positive staining in cediranib-treated brain metastases. - 198 -
Figure 6.12 Vascular maturation index following cediranib treatment in brain metastases. - 199 -
Figure 6.13 Effect of cediranib treatment on the hypoxic fraction of rat brain metastases. - 200 -
Figure II.1 Tomato lectin in brain metastases. - 256 -

List of tables

Table 3.1 Blood gas analysis results from i-STAT G3+ cartridge. ..... - 60 -
Table 3.2 Bloch simulation input parameters. ..... - 69 -
Table 3.3 CBF measurements from whole brain in label-control pCASL MRI and MP-pCASL MRI. ..... - 86 -
Table 3.4 CBF measurements from whole brain in [14C]-IAP AR and MP pCASL MRI. - 89 -
Table 3.5 Recommended clinical and preclinical ASL parameters. ..... - 102 -
Table 4.1 Immunohistochemistry antibodies and concentrations ..... - 113 -
Table 5.1 Location of MRI technique-specific methods and analysis protocols ..... - 149 -
Table 5.2 Immunohistochemistry antibodies and concentrations ..... - 150 -
Table 6.6.1 Number of brain metastasis-bearing rats in treatment groups at each time point. ..... - 176 -
Table 6.6.2 Location of MRI technique-specific methods and analysis protocols ..... - 178 -
Table 6.6.3 Immunohistochemistry antibodies and concentrations. ..... - 181 -

Abbreviations

[^{14}C]-IAP	Carbon-14 iodoantipyrine
˚	Degree
˚C	Degree centigrade
2D	Two dimension
3D	Three dimension
5-ALA	5-aminolevulinic acid
ADC	Apparent diffusion coefficient
Ang-2	Angiopoietin-2
ANOVA	Analysis of variance
APT	Amide protein transfer
APTR*	Amide protein transfer ratio
ASL	Arterial spin labelling
SMA	Alpha smooth muscle actin
BBB	Blood-brain barrier
BDIV	Berlin Druckrey IV
BDIX	Berlin Druckrey IX
bpm	Breaths per minute
CAM	Cellular adhesion molecule
CASL	Continuous arterial spin labelling
CBF	Cerebral blood flow
CBV	Cerebral blood volume
CEST	Chemical exchange saturation transfer
CSF	Cerebral spinal fluid
cm	Centimetre
CTLA-4	Cytotoxic T-lymphocyte-associated protein 4
CUP	Cancer of unknown primary
DAB	3,3’-diaminobenzidine tetrahydrochloride hydrate
DCE	Dynamic contrast-enhanced
DMEM	Dublecco's modified eagle medium
DMSO	Dimethyl sulfoxide
DSC	Dynamic susceptibility contrast
DTI	Diffusion tensor imaging
DWI	Diffusion weighted imaging
EGFR	Endothelial growth factor receptor
EMEA	European Medicals Association
ENU	*N*-ethyl-*N*-nitrosourea
EPC	Endothelial progenitor cells
EPI	Echo planar imaging
FA	Flip angle
FA	Fractional anisotropy

FBS	Foetal bovine serum
FDA	Food and Drug Administration
FGF	Fibroblast growth factor
FLAIR	Fluid-attenuated inversion recovery
FMO	Flavin-containing monooxygenase
FOV	Field of view
γ_0	Gyromagnetic ratio
g	Force per unit of mass due to gravity
g	Gram
G_{amp}	Gradient amplitude
GBCA	Gadolinium-based contrast agent
G_{max}	Maximal gradient
G_{pe}	Phase encoding gradient
G_{ro}	Readout gradient
GSC	Glioblastoma stem-like cells
G_{ss}	Slice selective gradient
h	Hour
H_2O	Water
H_2O_2	Hydrogen peroxide
HCl	Hydrochloric acid
HER2	Human epidermal growth factor receptor 2
HIF	Hypoxia-inducible factor
HPLC-MS	High-performance liquid chromatography mass-spectrometry
HRP	Horseradish peroxidase
HSC	Hematopoietic stem cell
Hz	Hertz
i.p.	Intraperitoneal
i.v.	Intravenous
IgG	Immunoglobulin G
IHC	Immunohistochemistry
IS	Internal standard
kDa	Kilodalton
kg	Kilogram
kHz	Kilohertz
K^{trans}	Transfer constant
kV	Kilovolt
L	Litre
µCi	Microcurie
µg	Microgram
µL	Microlitre
µm	Micrometre
µs	Microsecond
µT	Microtesla

M	Molar
M_0	Net magnetisation
mCi	Millicurie
mg	Milligram
MHz	Millihertz
min	Minute
mL	Millilitre
mm	Millimetre
mM	Millimolar
mmol	Millimole
mol	Mol
MP-pCASL	Multiphase pseudo-continuous arterial spin labelling
MPIO	Micron-sized particle of iron oxide
MRI	Magnetic resonance imaging
MRM	Multiple reaction monitoring
MRS	Magnetic resonance spectroscopy
ms	Millisecond
MSC	Mesenchymal stem cells
MDSC	Myeloid-derived suppressor cells
MT	Magnetisation transfer
mT	Millitesla
MTT	Mean transit time
N_2O	Nitrous oxide
NICE	National Institute on Health Care Excellence
NSCLC	Non-small cell lung cancer
O_2	Oxygen
OCT	Optimal cutting temperature
P-gp	P-glycoprotein
PASL	Pulsed arterial spin labelling
PBST	Phosphate-buffered saline with Tween-20
pCASL	Pseudo-continuous arterial spin labelling
PD1	Programmed cell death protein 1
PDGF	Platelet-derived growth factor
PHD	Prolyl-hydroxylase domain
PlGF	Placental growth factor
PLD	Post-label delay
PLP	Periodate-lysine-paraformaldehyde
ppm	Parts per million
qPCR	Quantitative polymerase chain reaction
rCBV	Relative cerebral blood volume
RF	Radiofrequency
RF_{amp}	Radiofrequency amplitude
ROI	Region

rpm	Rotations per minute
s	Seconds
SD	Sprague-Dawley
SNR	Signal-to-noise
SRS	Stereotactic radiosurgery
T	Tesla
TE	Echo time
TEeff	Effective echo time
Texp	Experimental time
TKI	Tyrosine kinase inhibitor
TNF	Tumour necrosis factor
TR	Repetition time
UGT	Uridine 5’-diphospho-glucuronosyltransferase
UK	United Kingdom
USA	United States of America
USPIO	Ultra-small super-paramagnetic iron oxide
V	Volt
v/v	Volume/volume
VEGF	Vascular endothelial growth factor
VEGFR	Vascular endothelial growth factor receptor
VMI	Vascular maturation index
w/v	Weight/volume
WBRT	Whole brain radiotherapy

CHAPTER 1

Introduction

1.1 Cancer and brain metastases

1.1.1 Cancer and tumour progression

Cancer is one of the leading causes of death in the world, second only to cardiovascular diseases, accounting for over 17 % of all deaths (Ritchie and Roser, 2019). Cancer, although seen from childhood onwards, is often thought of as a disease affecting the elderly population since it commonly arises through the accumulation of a series of mutations. These mutations lead to the aberrant expression of oncogenes and of tumour suppressor genes, thereby promoting an uncontrolled growth of cells. “The hallmarks of cancer”, first published in 2000, defined the characteristics of cancer cells that are shared between most solid tumours: a limitless replicative potential, a sustained angiogenesis, the evasion of apoptosis, a self-sufficiency in growth signals, insensitivity to anti-growth signals, and tissue invasion and metastasis (Hanahan and Weinberg, 2000). These

hallmarks were revised a decade later to incorporate an additional four characteristics, specific not only to the tumour cells but also to their microenvironment: genomic instability and mutation, tumour-promoting inflammation, avoidance of immune destruction, and a deregulation of cellular energetics (Figure 1.1; Hanahan and Weinberg, 2011).

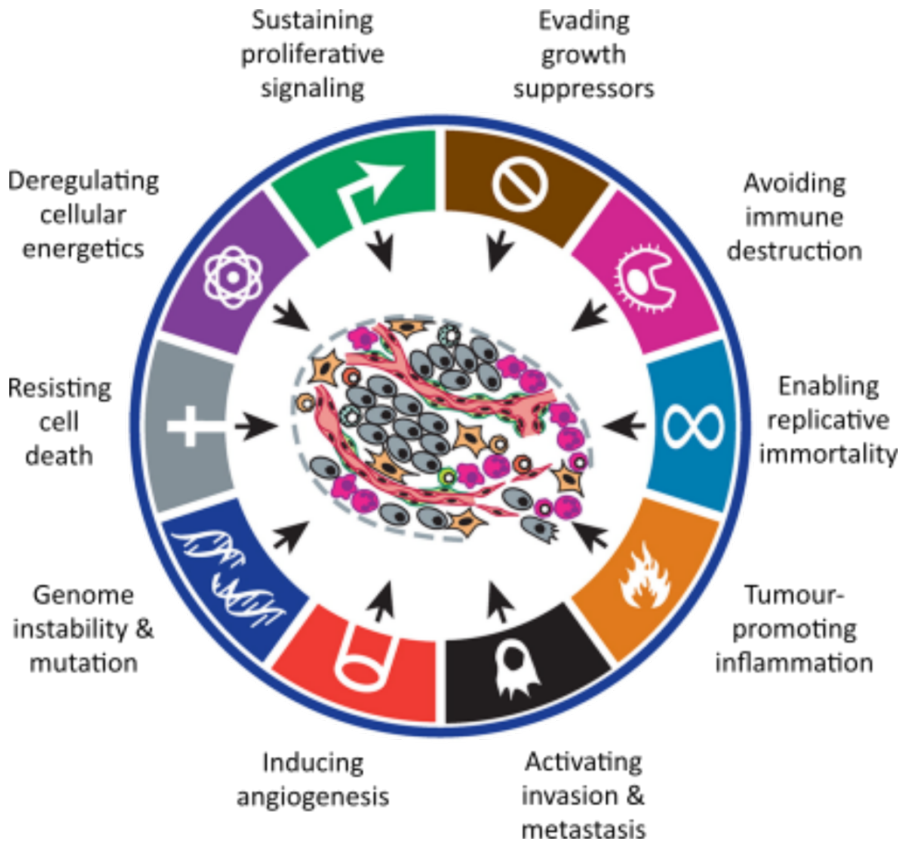

Figure 1.1: Hallmarks of cancer. Hallmarks of cancer modified with permission from Hanahan and Weinberg, 2011.

1.1.2 Metastatic cascade

As mentioned, the invasion and metastatic potential of tumour cells is one of the hallmarks of cancer. Metastases are estimated to account for up to 90 % of cancer-associated mortality (Gupta and Massagué, 2006). The metastatic cascade is a multi-step

process by which a cancer cell from the primary tumour migrates to a neighbouring or distant tissue, involving multiple other hallmarks of cancer during this process, to form secondary tumours or metastases (reviewed in detail in Steeg, 2006). Metastatic cells intravasate into proximal blood vessels, entering the systemic circulation, where they must evade immune detection, another hallmark of cancer cells. These tumour cells are then arrested at the site of a different, and possibly distant, organ and will extravasate into the surrounding tissue. Once in the new organ, metastatic cells initiate colonisation, sometimes following a period of dormancy, and establish a new solid tumour. An overview of this metastatic cascade is presented in Figure 1.2.

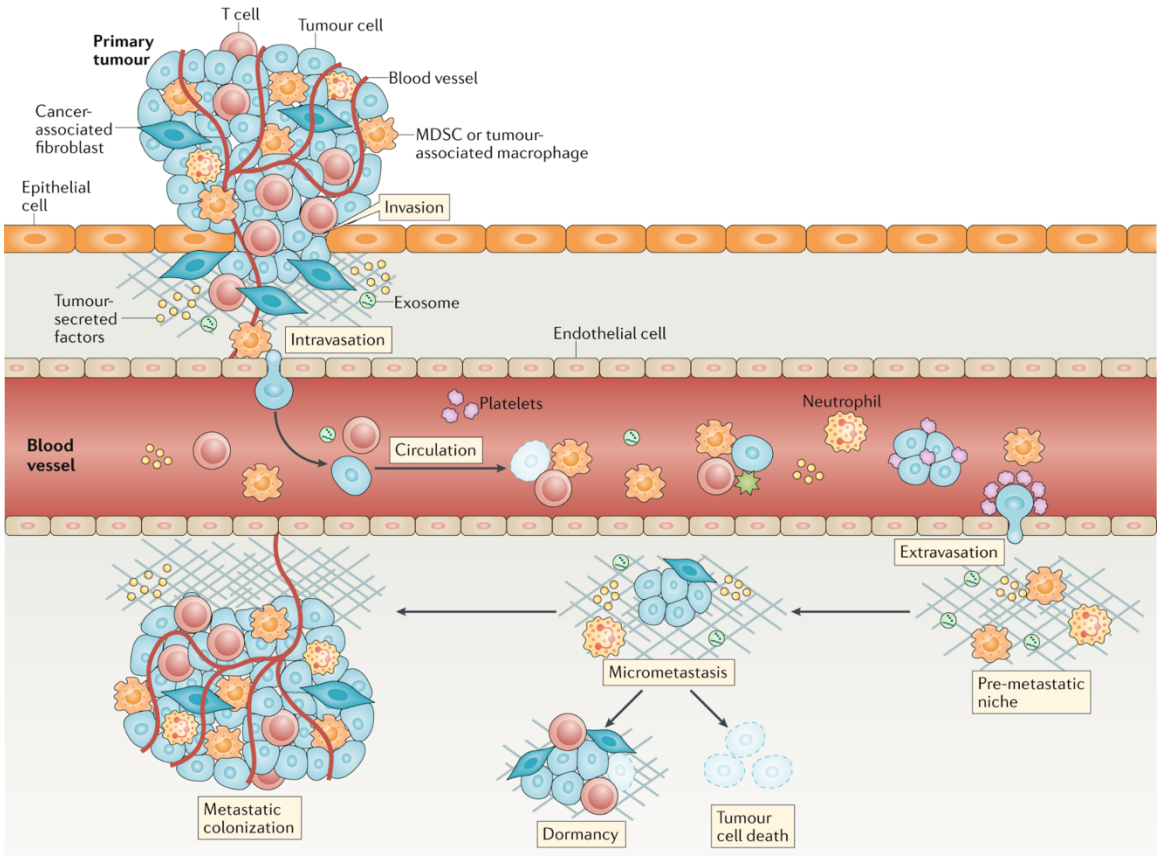

Figure 1.2: Metastatic cascade. The steps of the metastatic cascade from a single cell of the primary tumour to the establishment of a metastatic colony, as presented by Anderson *et al.*, 2019, with permission (MDSC: myeloid-derived suppressor cell).

Over time, different theories have been proposed to explain the mechanism of tumour cell metastasis. The first was proposed by Rudolf Virchow in 1858. He believed that cancers metastasised through a liquid, but was quickly disproved by Karl Tiersch who demonstrated that metastatic cancers originated from the spread of malignant cells in the body. At this point, it was believed that many cells were shed from the primary tumour and a few would be successful at colonising a randomly chosen new organ in the body. However, in 1889, Stephen Paget proposed the 'seed and soil' hypothesis, in which he stipulated that the target organ for metastases is not chosen at random, but is targeted specifically by tumour cells, the 'seeds', since the organ in question possesses a congenial 'soil' for their growth (Paget, 1889). Four decades later, James Ewing proposed the theory that circulatory patterns and mechanical forces between the sites of primary tumour and metastasis were responsible for the organ specificity of metastases (Ewing, 1928). However, seminal work performed by Isaiah Fidler and colleagues in the 1970s-80s proved that although tumour cells circulated through all organs of the body, metastases only formed in congenial organs, supporting the 'seed and soil' hypothesis (Fidler and Kripke, 1977; Hart and Fidler, 1980). The advent of these findings promoted research on the pre-metastatic niche, at both the site of the primary and secondary tumour, and on the organo-tropism of metastasising cells.

1.1.3 Brain metastases

Brain metastases occur in 20-40 % of all cancer patients and most commonly originate from lung cancer, breast cancer or melanoma primary tumours (Figure 1.3; Walker, Robins and Weinfeld, 1985; Schouten *et al.*, 2002; Barnholtz-Sloan *et al.*, 2004). Brain metastases are the most common type of intracranial neoplasm found in adults and the

incidence of brain metastases is on the rise (Gavrilovic and Posner, 2005; Smedby *et al.*, 2009). This increased incidence is, in part, owing to a higher prevalence of primary tumours giving rise to brain metastases and the metastasis of other tumour types to the brain (Tabouret *et al.*, 2012). Advances in primary tumour treatments are contributing to improved patient survival and to earlier detection of primary tumours through increased screening platforms and improvements in medical imaging (Morton, Ko and Silbergeld, 2018). These longer overall survival rates increase the probability of metastatic cell awakening from dormancy states, leading to detectable metastatic lesions in patients.

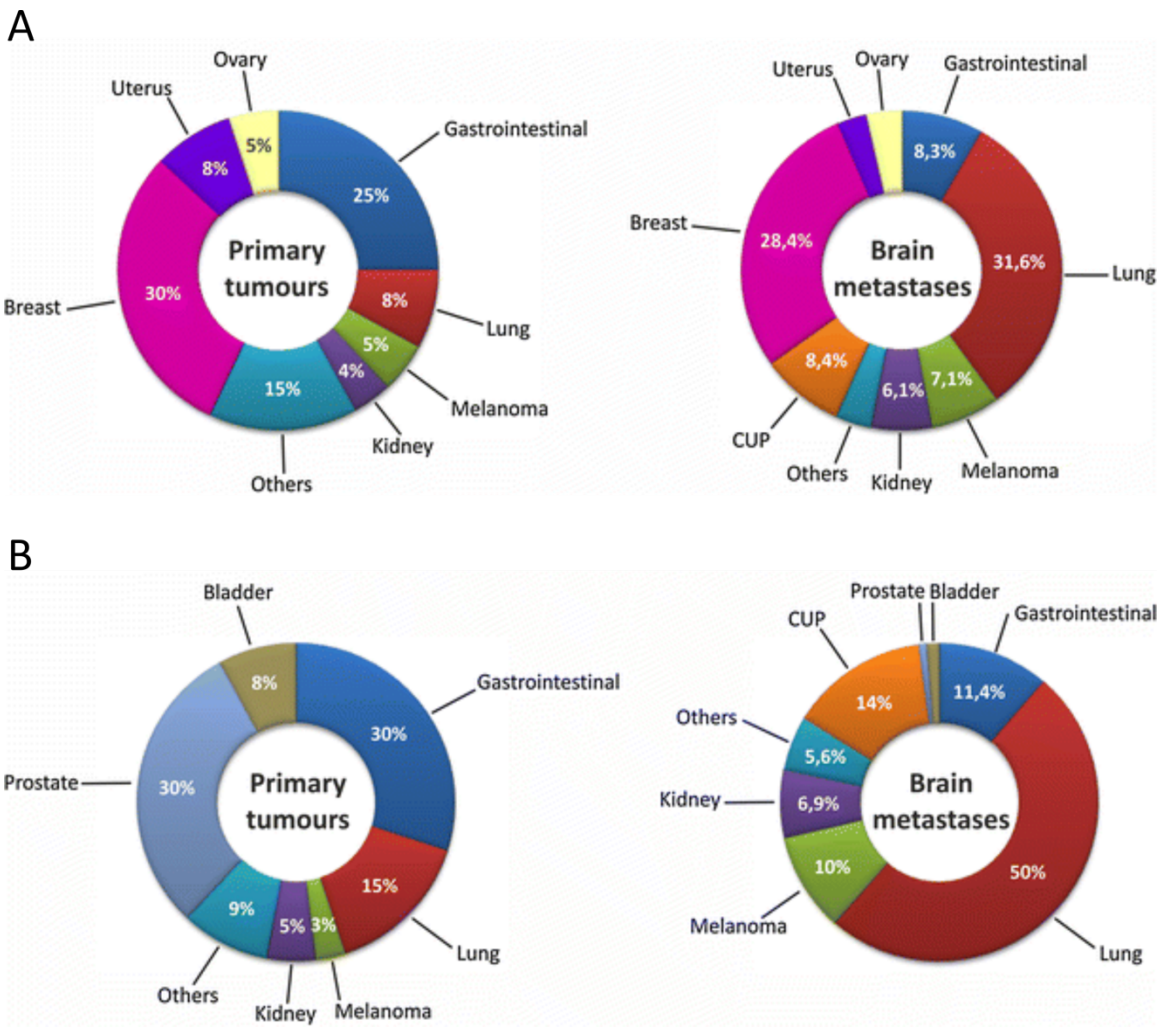

Figure 1.3: Relative incidence of primary tumours and brain metastases by tumour type. Demonstrated for women (**A**) and men (**B**) separately, modified with permission from Preusser *et al.*, 2012 (CUP: cancer of unknown primary).

Brain metastases are detected at late stages of the disease since their detection relies on blood-brain barrier (BBB) breakdown at tumour sites. The BBB is a neuro-protective semi-permeable membrane protecting the brain from neurotoxins and pathogens. It is composed of endothelial cells, linked by tight junctions, surrounded by pericytes and end feet of astrocytes and of neurons (schematic of the BBB in Figure 1.4). Although the BBB is neuro-protective, it also delays the detection of brain pathologies owing to the restrictive passage of diagnostic agents. The current clinical detection limit for brain metastases is typically when a tumour reaches a diameter of approximately 5-10 mm as seen by contrast-enhanced magnetic resonance imaging (MRI; Katakami *et al.*, 2011), additionally limited by the spatial resolution of MRI. At this point, treatment options are limited and patient prognosis is poor, typically with a median patient survival of 1 month without treatment and with only a short survival increase of 2-3 months with therapy (Pease, Edwards and Moss, 2005; Stelzer, 2013). Treatment of brain metastases is limited to surgical resection, stereotactic radiosurgery (SRS) and whole brain radiotherapy (WBRT) owing to the restricted passage of chemotherapeutic agents across the BBB.

This short survival time and increased incidence of brain metastases highlight the need for earlier detection, better imaging techniques and improved therapies.

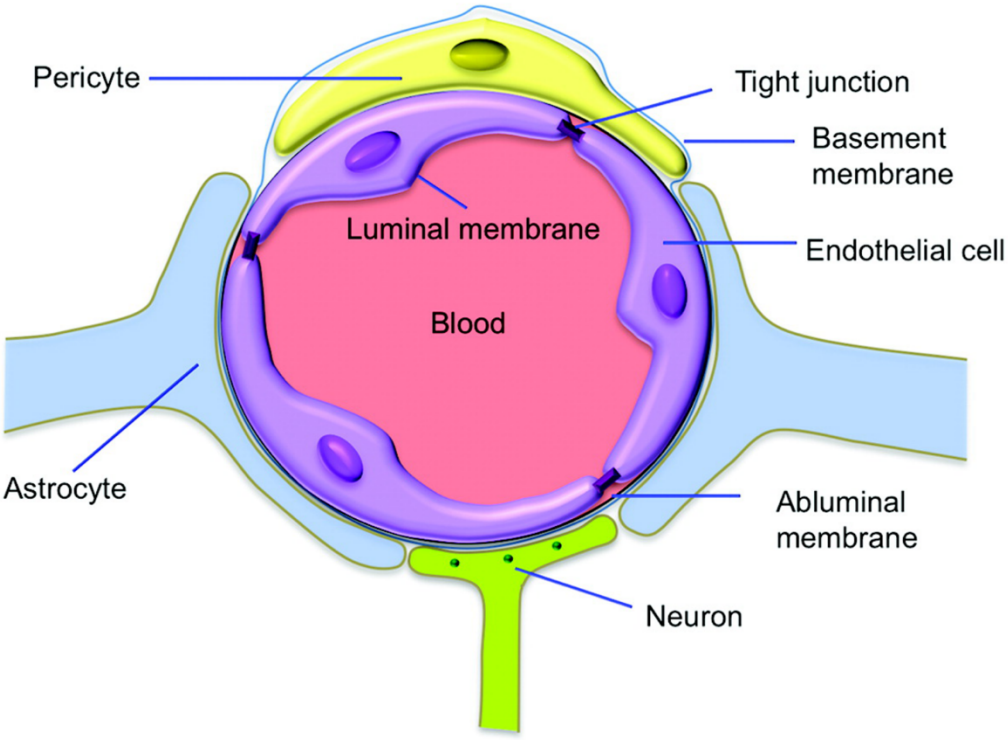

Figure 1.4: Blood-brain barrier. Schematic representing the difference cell types and their organisation in the blood-brain barrier, modified with permission from Liu, Perlin and Xue, 2012.

1.2 Current clinical prognosis and treatment of patients with brain metastases

1.2.1 Current clinical guidance for brain metastasis detection and treatment

In the UK, current NICE (National Institute on Health and Care Excellence) guidelines recommend standard structural MRI in the case of suspected brain metastases, which comprises T_2-weighted, T_1-weighted pre- and post-contrast volume, diffusion weighted imaging (DWI) and fluid-attenuated inversion recovery (FLAIR) imaging, unless MRI is contra-indicated (NICE guidance NG99). If brain metastases are detected, the patient will either undergo surgery or SRS in the case of a single brain metastasis or low tumour burden, or WBRT or no treatment in the case of multiple brain metastases (NG99). During

follow-up, standard structural MRI, as used for initial brain metastasis detection, is considered and advanced MRI techniques such as MR perfusion, diffusion tensor imaging (DTI) and MR spectroscopy (MRS) are performed in instances where results from standard structural imaging are unclear concerning treatment response and potential recurrence.

1.2.1.1 Standard structural clinical MRI

Structural or anatomical MRI such as T_2-weighted and T_1-weighted imaging allows the detection and localisation of brain tumours including brain metastases. Furthermore, in T_1-weighted imaging, the intravenous administration of a paramagnetic contrast agent, typically gadolinium-based, will result in its accumulation in brain metastasis lesions if BBB breakdown is present and will significantly reduce the T_1 relaxation time of tumour regions. The accumulation of gadolinium in brain voxels leads to hyperintense regions that facilitate tumour visualisation and provide an estimate of the size of the metastasis.

DWI is also performed as an indirect measure of tissue cellularity in brain tumours (Chen *et al.*, 2013). The apparent diffusion coefficient (ADC) obtained from DWI represents the movement of water protons in the tissue and is measured in mm^2/s. In the context of brain tumours where cells grow rapidly and in close proximity, with a complex tumour microenvironment, the diffusion of water protons becomes more limited, thus decreasing the ADC (Poussaint *et al.*, 2016; Swartz *et al.*, 2018). If brain tumours become necrotic or cystic, the interstitial space is increased as tumour cells and/or microenvironment components are removed, allowing freer movement of water protons and increasing the ADC (Asao *et al.*, 2005).

Lastly, FLAIR MRI is a T_2-weighted approach used to suppress signal from the cerebral spinal fluid to allow clearer visualisation of pathology within the brain. Furthermore, FLAIR MRI along with DWI can facilitate the detection of oedema in brain metastases (Fink and Fink, 2013).

1.2.1.2 Advanced clinical MRI techniques

Clinical MR perfusion is a technique that relies on the injection of contrast agents to determine the amount of blood present in a brain voxel. Often, this is performed by dynamic-susceptibility contrast (DSC) MRI, a T_{2*}-weighted technique based on the susceptibility-induced signal loss that occurs when gadolinium-based contrast agents (GBCAs) circulate though the tissue capillary bed (Rempp *et al.*, 1994). This signal loss is proportional to the amount of GBCA in the capillary bed, and, thus, to the cerebral blood volume (CBV) present. DSC MRI can provide relative cerebral blood flow (rCBF) values as well as CBV measurements in the brain, which together can be used to calculate the mean transit time (MTT; MTT = CBV/CBF) of blood in brain regions such as brain metastases (reviewed in (Østergaard, 2005)). Another option for perfusion MRI is dynamic contrast-enhanced (DCE) MRI, a T_1-weighted approach looking at the accumulation of GBCAs in brain tissue through its shortening effect on T_1 relaxation times (Tofts, 2010).

DTI provides information on the orientation, location and anisotropy of the brain white matter tracts (reviewed in (Mori and Van Zijl, 2002) and (Basser and Jones, 2002). Through DTI, the ADC can be determined as well as the fractional anisotropy (FA) representing the anisotropy, or directionality, of the diffusion process. DTI has been demonstrated to

differentiate glioma grades in the brain as well as gliomas from brain metastases (Suh *et al.*, 2018).

Finally, MRS can identify variations in the metabolic profile of brain metastases (Chernov *et al.*, 2006) and has been shown to differentiate brain metastases from high-grade gliomas, as well as identifying the presence of necrosis within brain metastases (Bulakbasi *et al.*, 2003; Hollingworth *et al.*, 2006).

1.3 Arterial spin labelling MRI

Arterial spin labelling (ASL) is another perfusion MRI technique that has yet to be implemented into clinical practice but shows great potential, and is the primary focus of this thesis. This technique was developed in the 1990s (Detre *et al.*, 1992; Williams *et al.*, 1992a; Alsop and Detre, 1996), allowing imaging of tissue blood flow in a non-invasive manner. In ASL MRI, blood flow information is obtained through the selective magnetic inversion of blood water protons as they pass through a geographically located labelling plane. Then, the labelled blood water protons are allowed to exchange with tissue water protons, creating negative contrast in areas of blood perfusion when the tissue of interest is imaged after a certain delay. The subtraction of an image acquired with blood labelling from one acquired without labelling provides a relative blood flow map, reflecting regions where water exchange from the labelled blood, or perfusion, has occurred. The brain, being an isolated organ with a defined set of inflowing arteries and being less sensitive to motion than other organs of the body, was initially chosen for the development of this subtractive technique. The labelling plane is, therefore, placed along the neck, perpendicular to the blood flow of the carotid and vertebral arteries to homogeneously

label the brain inflowing blood. A simplified schematic of ASL imaging and analysis is presented in Figure 1.5.

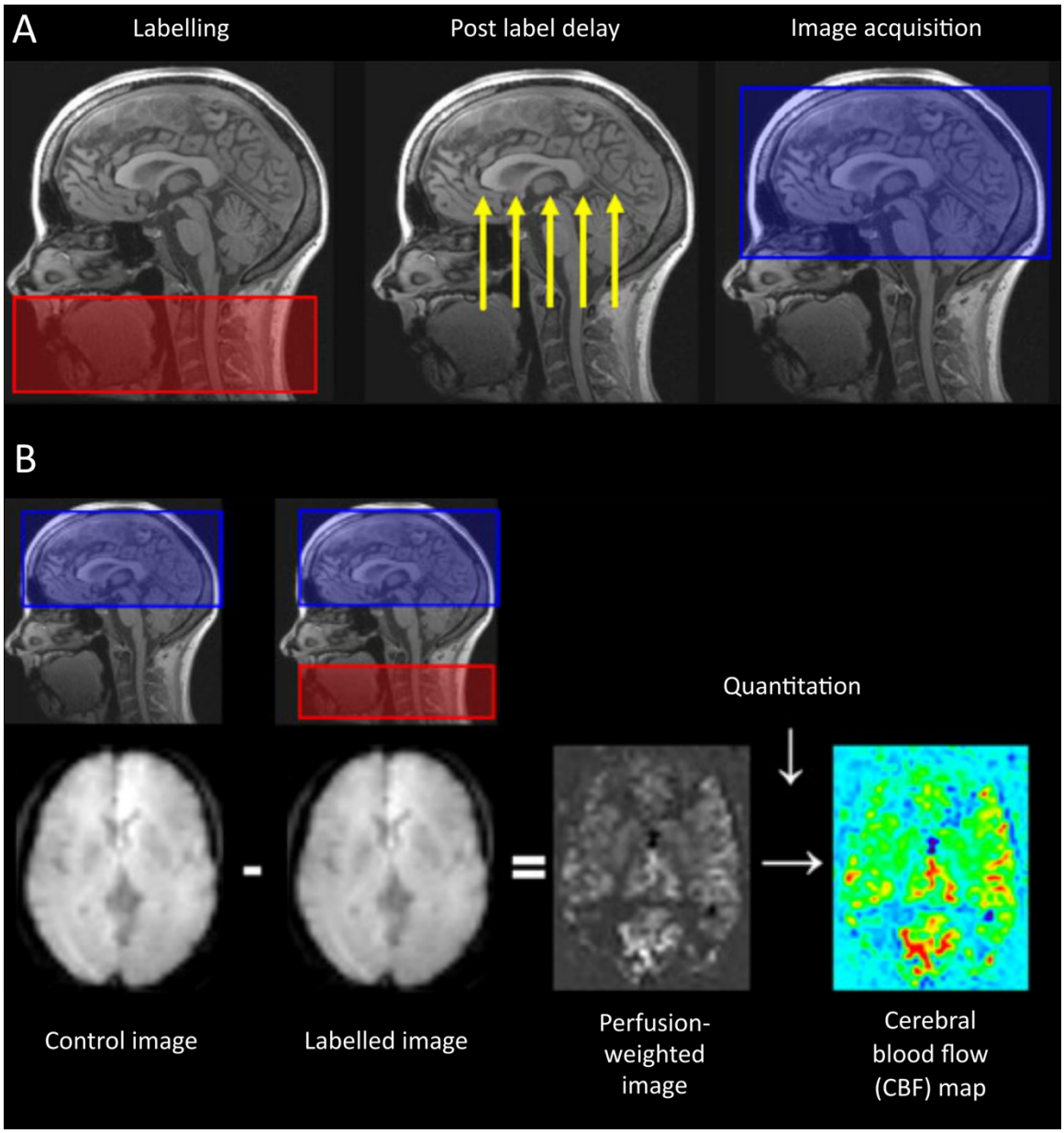

Figure 1.5: Arterial spin labelling acquisition and quantitation. **A** Schematic of the three steps of ASL MRI in humans with the labelling plane positioned as for CASL or pCASL labelling. **B** Simplified analysis of ASL MRI with the subtraction of the labelled image from the control image to get a perfusion-weighted image and finally a CBF map. Figures were modified with permission from Ferré *et al.*, 2013.

1.3.1 Labelling strategies in ASL MRI

Three main blood labelling strategies for ASL MRI have been proposed: continuous ASL (CASL), pulsed ASL (PASL) and pseudo-continuous ASL (pCASL). CASL MRI was the labelling method first presented in 1992, in which the flow-driven adiabatic inversion of blood water spins is accomplished by a constant low amplitude radiofrequency (RF) pulse lasting 1-3 s at a thin slice through the subject's neck (Williams *et al.*, 1992b). Although, CASL MRI provides the highest perfusion contrast among the ASL MRI labelling techniques, it comes at the detriment of high levels of energy deposition in the tissue and of magnetisation transfer (MT) effects, reducing the signal contribution from water protons (Pekar *et al.*, 1996; Wang *et al.*, 2002). Furthermore, the clinical translation of CASL MRI is complicated by the requirement for additional hardware, used in the transmission of continuous RF pulses, not typically present on clinical MRI scanners (Pollock *et al.*, 2009).

In contrast, PASL MRI uses short RF pulses of 5-20 ms to invert spins in a large labelling plane proximal to the imaging region. Three main subtypes of PASL MRI exist, EPISTAR, FAIR and PICORE, each using a single inversion pulse for the magnetic labelling of the blood water proton spins (Edelman, Darby and Nobre, 1994; Kim and Tsekos, 1997; Wong, Buxton and Frank, 1997). Owing to the large volume occupied by the labelling plane, the inversion efficiency of PASL MRI (~95 %) is greater than that achieved in CASL MRI (~85 %). However, the short temporal width of the label for blood water spins reduces the SNR in PASL MRI.

Thirdly, pCASL MRI was proposed by Garcia and colleagues in 2005 as an alternative approach using a labelling train of short RF pulses, over a similar duration to the continuous labelling pulse in CASL MRI, for the flow-driven adiabatic inversion of blood

water spins inflowing to the brain (Garcia, de Bazelaire and Alsop, 2005). This labelling method is compatible with imaging on clinical scanners, possesses the high SNR and imaging efficiency of CASL MRI without the considerable MT effects or the high RF power energy deposition in tissues. However, pCASL MRI has an increased sensitivity to magnetic field inhomogeneities (Jahanian, Noll and Hernandez-Garcia, 2011).

1.3.2 Obstacles in the clinical implementation of ASL

Although ASL MRI provides a contrast-free method of obtaining brain perfusion imaging, it has struggled to get implemented into routine clinical practice. Some researchers believe that the many types and subtypes of ASL labelling may have led to a confusion about the selection of the appropriate labelling scheme for clinical use and could be one of the reasons why ASL has not been readily adopted in clinical practice. Yet, techniques such as DCE MRI, which require the use of paramagnetic contrast agents, were quickly accepted despite the associated potential for toxicity (Malayeri *et al.*, 2016). To rectify this confusion, the ASL MRI 'white paper' was published in 2014 with recommendations for the use of ASL MRI in the clinic in an attempt to standardise this technique across centres and scanners and promote its incorporation into routine clinical imaging (Alsop *et al.*, 2014). This article considered many aspects of ASL MRI, from hardware requirements to the type of ASL, the time delay between labelling and imaging, readout approaches and post-processing methods. Although ASL MRI is increasingly being used in clinical trials and for clinical and preclinical research, it has yet to be implemented in routine clinical practice.

To date, only a few clinical research studies have used ASL MRI in brain metastases; some focusing on the differentiation between primary and secondary brain tumours

through CBF measurements (Weber *et al.*, 2006; Sunwoo *et al.*, 2016) or looking at the predictive treatment outcome of patients based on tumour blood flow (Weber *et al.*, 2004). Moreover, a study by Soni and colleagues demonstrated a strong correlation between the tumour blood flow and healthy tissue CBF measurements obtained from ASL MRI and DSC MRI, and encouraging the replacement of current perfusion MRI techniques requiring GBCA administration by ASL MRI (Soni *et al.*, 2017).

1.4 Novel treatment strategies of brain metastases

In recent years, novel treatment strategies and therapeutic agents have shown promise for the treatment of brain metastases. Clinically, the use of systemic drug delivery for targeted therapies, specific to the primary tumour type of the brain metastasis, have been used. For example, the inhibition of epithelial growth factor receptor (EGFR) by tyrosine kinase inhibitors (TKIs), e.g. gefitinib or erlotinib, have been successful in the treatment of intracranial lesions of non-small cell lung cancer (NSCLC) with EGFR mutations in clinical trials (Porta *et al.*, 2011; Iuchi *et al.*, 2013). Furthermore, AZD3759 and osimertinib, third generation EGFR TKIs, have been proposed as potential substitutes to brain radiation in NSCLC, since they were more effective and less neurotoxic both in preclinical models and clinical trials (Kim *et al.*, 2015; Ahn *et al.*, 2016; Ballard *et al.*, 2016). Reports have also demonstrated effects of targeted therapy in HER2+ (human epidermal growth factor receptor 2) breast cancer brain metastasis using a combination of capecitabine and lapatinib (Morikawa *et al.*, 2015). However, the effects were variable and drug delivery to the brain metastasis tissue was too weak to be effective in some cases. Also, the combination of SRS and immunotherapy, such as anti-PD1 (programmed cell death

protein 1) therapy or anti-CTLA-4 (cytotoxic T-lymphocyte-associated protein 4) antibodies, in melanoma brain metastasis treatment has demonstrated an increased overall survival in patients (Choong *et al.*, 2017).

Another suggested improvement to the current treatment of brain metastases is the incorporation of 5-aminolevulinic acid (5-ALA) as an intraoperative fluorescent marker of brain metastases to improve the accuracy of surgical resection. 5-ALA-induced fluorescence was detected in regions of 32 brain metastases out of 52 (62 %) in a study by Kamp and colleagues and was independent of the primary origin of the brain metastases (Kamp *et al.*, 2012).

Preclinically, imaging advances for the earlier detection of brain metastases have been proposed by using molecular imaging techniques targeting cellular adhesion molecules (CAMs) present on vessels at sites of extravasation of brain metastatic cells (Serres *et al.*, 2012; Soto *et al.*, 2014; Cheng *et al.*, 2019). This approach is accomplished by the addition of antibodies targeting CAMs to micron-sized particles of iron oxide (MPIO), injection of these MPIOs into the systemic circulation and, subsequent detection of hypointense regions in the brain on $T_{2}*$-weighted MRI where the MPIO have bound to CAMs. Following earlier detection of brain micrometastases, the presence of an intact BBB at this stage of development still poses a problem for their effective treatment. On this basis, research on the selective permeabilisation of the BBB for the treatment of brain micrometastases has been undertaken. Potential strategies for selective and transient BBB permeabilisation include treatment with TNF (tumour necrosis factor) or lymphotoxin, and the localised disruption of the BBB though cavitation of microbubbles by ultrasound, among others (E. Konofagou *et al.*, 2012; Connell *et al.*, 2013). Permeabilisation of the BBB using TNF enabled a significant increase in intracranial trastuzumab delivery in a

mouse model of brain metastasis (Connell *et al.*, 2013). As for the localised BBB disruption using microbubbles, an added feature of this technique is that the microbubbles can be coupled to antibodies on their surface and loaded with therapeutic agents for a localised treatment delivery at the site of microbubble accumulation in the brain (Acosta *et al.*, 2008; Carugo *et al.*, 2015).

1.5 Tumour angiogenesis and anti-angiogenic therapy

One area of particular interest in cancer treatment, which has, thus far, had very little application in brain metastases, is anti-angiogenic and vascular normalisation therapies. As briefly related to in section 1.1.1, angiogenesis is a hallmark of solid tumours. Angiogenic activity of a tumour does not directly correlate to its aggressiveness but has been demonstrated to be associated with a poor prognosis and invasiveness in certain tumours, such as breast cancer, colorectal cancer and melanoma (Ahmad *et al.*, 2001; Bergers and Benjamin, 2003; Sfiligoi *et al.*, 2003; Imanishi *et al.*, 2007; Helfrich *et al.*, 2009). The high proliferation rates present in cancers make them increasingly dependent on blood vessels in order to sustain their survival through oxygen and nutrient delivery, and solid tumours use a number of mechanisms to facilitate this (Figure 1.6): (1) the formation of new vessels, sprouting from existing vessels (angiogenesis; Carmeliet and Jain, 2000); (2) the re-appropriation of pre-existing blood vessels to the tumour (vascular co-option; reviewed in Donnem *et al.*, 2013); (3) the recruitment of bone-marrow-derived endothelial cells to form entirely new vessels (bone marrow-derived vasculogenesis; Ribatti *et al.*, 2001); (4) the separation of a blood vessel into two (intussusception; Patan, Munn and Jain, 1996; Baum *et al.*, 2010; Gianni-Barrera *et al.*, 2011); and (5) tumour cells

themselves form vessel-like structures (vascular mimicry; reviewed in Paulis *et al.*, 2010). The first two mechanism are the most commonly observed in tumours and will be discussed briefly below.

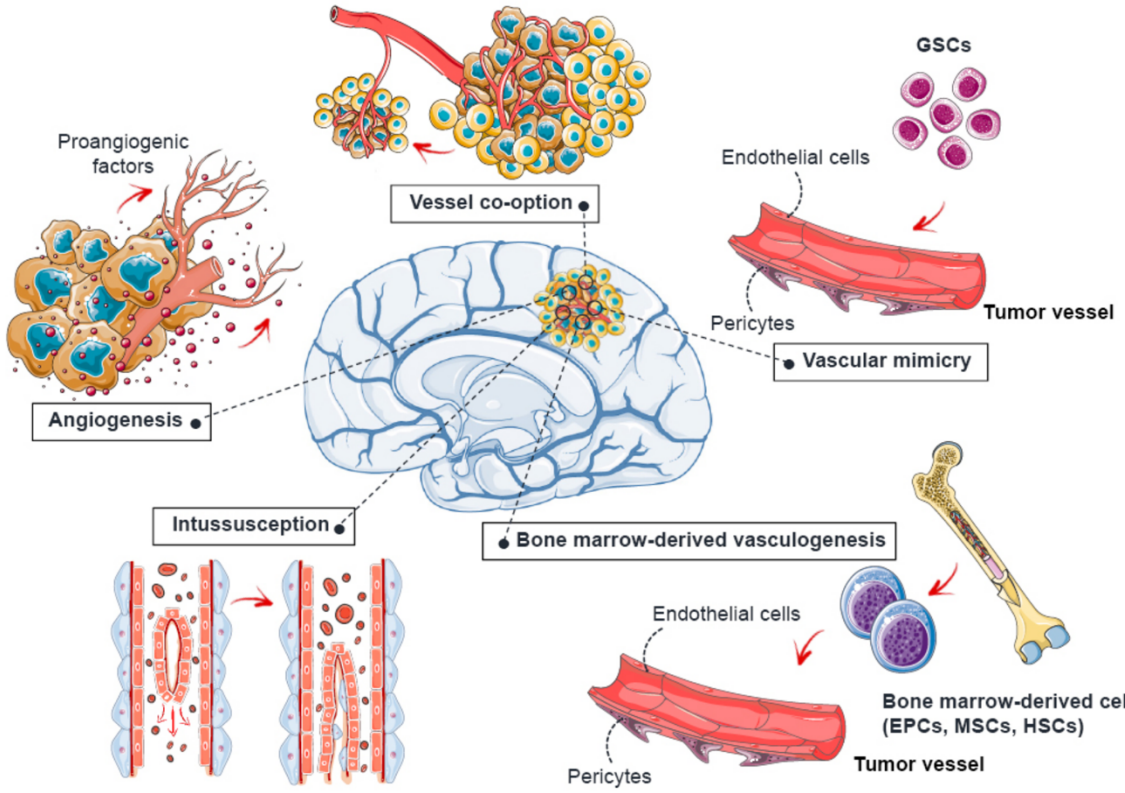

Figure 1.6: Tumour-associated vessels. Five mechanisms by which tumours (glioblastoma in this case) obtain blood for oxygenation and nutrient delivery, obtained with permission from Clavreul *et al.*, 2019 (EPCs: endothelial progenitor cells; GSCs: glioblastoma stem-like cells; HSCs: hematopoietic stem cells; MSCs: mesenchymal stem cells).

1.5.1.1 Angiogenesis

When a tumour is initiating its growth, it is avascular, relying on proximal vessels of the surrounding healthy tissue for oxygen and nutrients. Once the tumour diameter reaches 1-2 mm, the tumour may become dormant or establish a steady-state, in which proliferating tumour cells replace cells undergoing apoptosis in the tumour (Bergers and Benjamin, 2003). Tumours could remain at this stage forever, however, the cells most

distant to the blood supply may become hypoxic and trigger the angiogenic switch (Bergers and Benjamin, 2003). This angiogenic switch, or the vascular phase, can lead to an exponential growth of the tumour and increases the metastatic potential of solid tumours. The angiogenic switch can be triggered at any stage in tumour development, yet is often correlated with a distance exceeding 70 µm between tumour cells and the most proximal blood vessel (Thomlinson, 1977; Folkman, 1995; Hanahan and Folkman, 1996). A reduced activity of the prolyl hydroxylase domain (PHD) oxygen sensing proteins in the hypoxic cancer cells will lead to inhibition of the degradation of the hypoxia-inducible factors (HIF) 1 and 2, allowing the transcription of HIF-driven hypoxia-related genes, such as the vascular endothelial growth factor (VEGF; Semenza and Wang, 1992; Wang and Semenza, 1995; Kaelin and Ratcliffe, 2008; Mazzone *et al.*, 2009). VEGF is a pro-angiogenic factor that binds to VEGF tyrosine kinase receptors (VEGFR) 1, 2, or 3, although VEGFR2 is the most prominent receptor used in angiogenesis (Terman *et al.*, 1992; Millauer *et al.*, 1993). Other pro-angiogenic factors involved in tumour angiogenesis include angiopoietin-2 (Ang-2) acting on the Tie2 receptor, the fibroblast growth factor (FGF) acting on the FGF receptor, the placental growth factor (PlGF) acting on the PlGF receptor, and the platelet-derived growth factor (PDGF) acting on the PDGF receptor (Holash *et al.*, 1999; Vajkoczy *et al.*, 2002; Fischer *et al.*, 2007; Raica and Cimpean, 2010). The expression of VEGF has been shown to induce vasodilation and increase the permeability of pre-existing blood capillaries to allow the extravasation of plasma proteins, which form a scaffold-like structure for the arrival of endothelial cells (Benjamin *et al.*, 1999; Inai *et al.*, 2004; Tong *et al.*, 2004). Ang-2 mediates the loosening or detachment of perivascular cells (pericytes and vascular smooth muscle cells) following binding to Tie2, a selectively expressed receptor on endothelial cells (Holash *et al.*, 1999;

Yancopoulos *et al.*, 2000; Morikawa *et al.*, 2002). This loosening of the perivascular cells facilitates the movement of endothelial cells to form new vessels.

Newly formed vessels in the tumour are structurally different from vessels in healthy tissue. The imbalance between pro- and anti-angiogenic factors in tumours result in the presence of disorganised, dilated, hyperpermeable, tortuous and saccular vessels with weakened tight junctions between endothelial cells (Less *et al.*, 1991; Yuan *et al.*, 1996; Hashizume *et al.*, 2000; Nagy *et al.*, 2002; Jain, 2005). Tumour subregions can also possess areas of high or low vascular density, with increased vessel shunting and a loss of vessel diameter control (Pries *et al.*, 2009, 2010). The thickness of vascular basement membranes is reportedly high in brain tumours, while being very thin or non-existent in many other tumour types (Bosnian, Havenith and Cleutjens, 1985; Baluk *et al.*, 2003). This vascular organisation leads to spatial and temporal heterogeneity in tumour blood flow and oxygenation and an increased interstitial pressure, which all contribute towards poor efficacy of immunotherapy, chemotherapy and radiotherapy (Helmlinger *et al.*, 1997; Less *et al.*, 1997; Fukumura *et al.*, 2010; Goel *et al.*, 2011).

1.5.1.2 Vascular co-option

Vascular co-option is observed when the cells of a tumour extend along existing vasculature and use it to supply the nutrients required for tumour growth. In these co-opted blood vessels, the vessels are mature and covered by perivascular cells (Donnem *et al.*, 2013). The appearance of the vasculature is hierarchical, as in healthy tissues. Many tumour types have displayed an initial vascular co-option phenotype, during the 'avascular' phase mentioned in the previous section followed by a switch to angiogenesis

by the overexpression of VEGF and Ang-2 at the onset of hypoxic regions or vessel regression (Holash *et al.*, 1999), e.g. NSCLC subtypes (Pezzella *et al.*, 1996, 1997), lymphoma (Passalidou *et al.*, 2003), glioblastoma (Wesseling *et al.*, 2009), and metastatic lung (Sardari Nia *et al.*, 2007) and liver cancer (Vermeulen *et al.*, 2001; Stessels *et al.*, 2004), lymph nodes (Naresh, Nerurkar and Borges, 2001) and brain tumours, including brain metastases (Küsters *et al.*, 2002; Kienast *et al.*, 2010). The initial co-option phenotype in brain metastases maintains the integrity of the BBB and is, in part, responsible for the late detection of these tumours, as discussed in section 1.1.3, upon onset of the angiogenic switch. In some instances, vessel co-option can be observed in the rim of tumours, while the tumour core will be angiogenic. Interestingly, the major factors reported to be involved in vessel co-option are also VEGF, VEGFR and Tie-2, therefore, the same pathways between angiogenesis and vessel co-option could potentially be activated (Donnem *et al.*, 2013).

1.5.2 Anti-angiogenic treatment and vascular normalisation

The dependence of tumours on angiogenesis has instigated the substantial research into anti-angiogenic cancer treatments in an attempt to prevent the formation of new vessels or cause vascular regression and to either starve the tumour to death or maintain them in a dormancy state (Sherwood and Parris, 1971). Preclinical studies performed in the early 1990's appeared to support this hypothesis and displayed a significant reduction in microvessel density and tumour growth when mouse xenograft models of glioblastoma, rhabdomyosarcoma and leiomyosarcoma were treated with an antibody targeting VEGF (Kim *et al.*, 1993). Yet, the anti-angiogenic treatment of tumours in the

clinic as a monotherapy produced underwhelming results and provided no improvement in overall survival in phase III clinical trials (Jain *et al.*, 2006). However, when anti-angiogenic therapy was combined with conventional chemotherapies, an improved overall survival of patients was observed when compared to chemotherapy as a monotherapy (Hurwitz *et al.*, 2004; Sandler *et al.*, 2006; Saltz *et al.*, 2008; Reck *et al.*, 2009; Tebbutt *et al.*, 2010). In 2001, Rakesh Jain proposed the 'vascular normalisation' hypothesis to explain the paradoxical results between anti-angiogenic mono- and combination therapy (Jain, 2001).

Vascular normalisation in tumours is defined by a reversion of the disorganised tumour vessels to a more organised and 'normal' phenotype. An attenuation of the hyperpermeability of the vasculature, a maturation of tumour vessels with an increased presence of perivascular cells, a tightening of connections between endothelial cells and a more normal basement membrane are also observed in the tumour (Jain, 2005; Goel *et al.*, 2011). Vascular normalisation typically occurs when anti-angiogenic treatments are given at optimal doses and for a limited amount of time (Figure 1.7). At higher or more prolonged doses, anti-angiogenic treatment could result in toxicity to normal tissue or to extensive vessel pruning. It is believed that vascular normalisation restores the balance between pro- and anti-angiogenic factors in the tumour microenvironment, which in turn improves blood flow in tumour regions and reduces hypoxia (Jain, 2001). Furthermore, many studies have demonstrated a decrease in metastasis incidence, owing to the increased difficulty of intra- and extravasation processes (Yano *et al.*, 2000; Bergers and Benjamin, 2003; Kim *et al.*, 2004; Kienast *et al.*, 2010). As a result of vascular normalisation, the sensitivity to radiotherapy and the efficiency of chemotherapies is increased during the vascular normalisation window. This therapeutic time window is

transient and has been demonstrated to typically occur as early as 1-2 days after initiation of vascular normalisation therapy and is followed by an eventual loss of normalisation features (Goel *et al.*, 2011). The detection of vascular normalisation in the clinic and in preclinical models most commonly relies on the decreased permeability of the tumour, measured by the transfer constant K^{trans}, the permeability factor from DCE MRI (Jackson *et al.*, 2007). Other detection methods include the decrease in microvessel density and increased vessel coverage by perivascular cells, both determined by histological analysis (Goel *et al.*, 2011).

The five main types of vascular normalisation agents proposed for this therapy target either VEGF itself, the VEGFRs, the Ang-2/Tie2 angiogenesis pathway, integrins involved in angiogenesis or PlGF. The most popular vascular normalisation agent has been bevacizumab, a humanised monoclonal antibody targeting VEGF. VEGF targeted therapies inhibit the binding of VEGF to its receptors, preventing the activation of this angiogenic pathway. The use of bevacizumab in combination treatments is now implemented in the standard of care for several tumour types. TKIs for VEGFRs are also widely used in preclinical and clinical research, and although they allow binding of VEGF to its cognate receptors, receptor activity is inhibited. Targeting the Ang-2/Tie2 pathway has proven more unreliable, since angiopoietins can exert a pro- or anti-tumourigenic response, depending on the tumour or cell type (Cascone and Heymach, 2012).

In some instances, treatment with bevacizumab has increased the occurrence of vascular co-option in tumour types, including melanoma (Leenders *et al.*, 2004), glioblastoma (Rubenstein *et al.*, 2000) and brain-metastatic lung cancer (Kienast *et al.*, 2010). The degree of vessel co-option in tumours could explain the efficacy of vascular

normalisation treatment. However, additional research is still needed in this area to confirm this hypothesis.

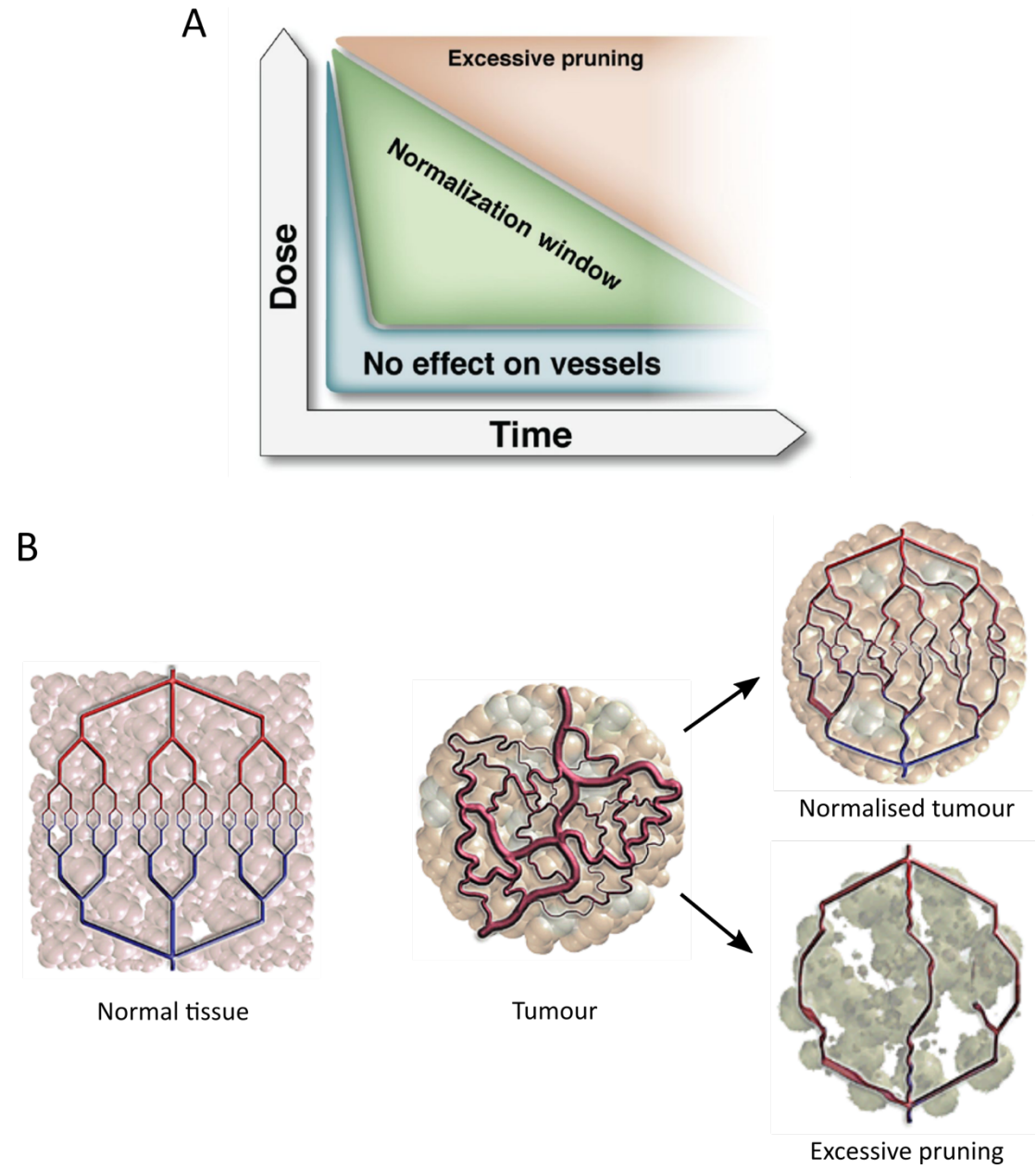

Figure 1.7: Vascular normalisation of tumour vessels. **A** Relationship between dose of anti-angiogenic agent and time, obtained with permission from Huang *et al.*, 2013. **B** Representation of the hierarchical structure present in normal healthy tissues compared with tumour vasculature. With anti-angiogenic treatment, tumour vessels are initially normalised but over time or at high doses, excessive pruning can occur. Modified with permission from Jain, 2001.

1.6 Preclinical models of brain metastasis

Preclinical research on brain metastases allows the testing of novel detection strategies, the improvement of imaging techniques and the assaying of novel therapeutics *in vivo* prior to their clinical translation. Preclinical models of disease must recapitulate, at least in part, the brain metastasis pathological situation seen in patients to be translated and potentially advantageous.

The range of rodent models of brain metastasis spans from spontaneous models, to ectopic and orthotopic cell implantations with syngeneic or xenogeneic origins and to genetically-engineered models (reviewed in Daphu *et al.*, 2013). Moreover, these rodent brain metastasis models originate from a variety of primary tumour types in rodents and humans, known to metastasise to the brain. The selection of preclinical brain metastasis model varies greatly between research groups based on the scientific focus and specific aims of the group. Here is a brief summary of a few popular rodent models in brain metastasis research.

Spontaneous tumours in rodents have been isolated and dissociated to form cell lines that can then be injected ectopically or orthotopically to generate brain metastases. The advantage of these models is that they can be performed in immunocompetent rodents to also get unbiased information on the rodent's immune response to the brain metastases. The route of inoculation of tumour cells for brain metastasis models is selected based on the tropism of the cell line used and the purpose of the study. To improve model success and reliability, brain-seeking tumour cells have been generated through the repeated injection and cell isolation of brain metastases formed in preclinical models (Yoneda *et al.*, 2001). Tumour cells can be inoculated ectopically through the

vasculature, either through tail vein injection, intracardiac injection or intracarotid injection (Figure 1.8). Tail vein inoculations will result in cells first passing through the lung vasculature, then the brain and remainder of the body whereas intracardiac injections of tumour cells will first pass through the brain and body before the lungs. In both these cases, administered cells should possess a high brain-tropism to ensure preferential colonisation of the brain. In contrast, the intracarotid inoculation is recommended for cells with a low brain-tropism since they will pass by the brain before both the body and the lungs. Conversely, tumour cells may be directly injected into the brain parenchyma by intracerebral injection to minimise the risk of extracranial tumours in rodents. Yet, brain metastasis models involving haematogenous dissemination of cells are more clinically relevant as the trajectory of tumour cells involves more steps of the metastatic cascade – tumour cell survival in the circulation, extravasation and colonisation of the brain parenchyma – and can lead to the formation of multiple micrometastases *in vivo.* Alternatively, if the research interest is focused on a point where brain metastases are already established colonies in the brain, a direct implantation brain metastasis model can be more informative, reproducible and reliable.

Another rodent brain metastasis model is the orthotopic model where cells are injected at the site of the primary tumour (e.g. skin, mammary fat pad, lungs) and, subsequently, metastasises to the brain. Genetically-engineered animal models of brain metastasis are similar to the orthotopic model since they rely on the formation of a primary tumour through inducible oncogene expression *in vivo,* followed by metastatic dissemination. Although the entirety of the metastatic cascade is undertaken in these models, which makes them ideal models of human disease, the major problems are the low incidence of

metastasis and the rapid development of the primary tumours and, thus, early study endpoint.

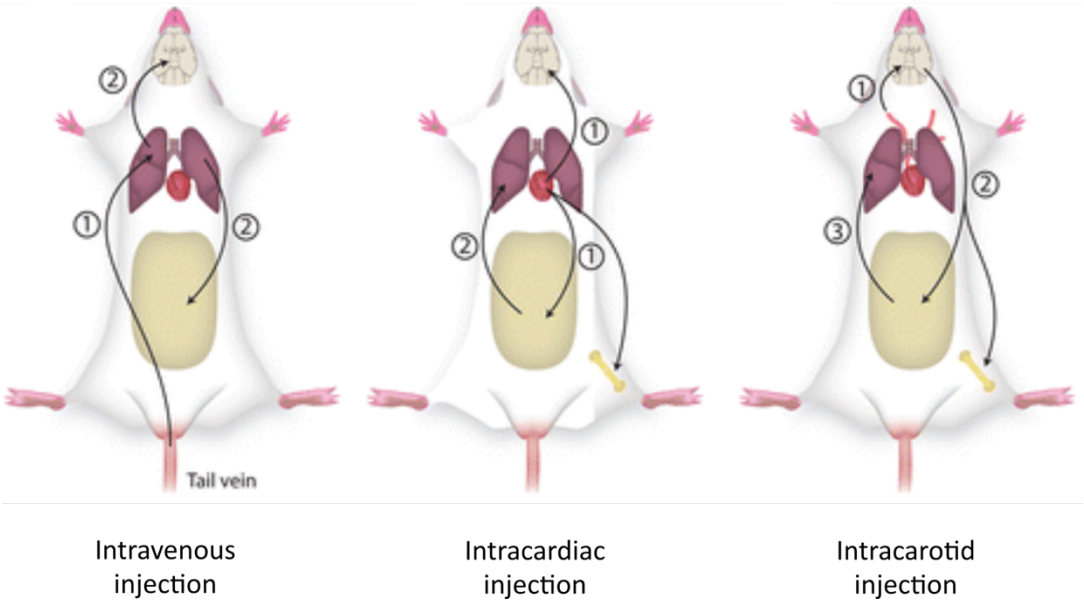

Figure 1.8: Ectopic injections for brain metastasis models. Representation of three sites of injection with the order of delivery to organs of interest in metastasis models, modified with permission from Daphu *et al.*, 2013.

1.6.1 Preclinical ASL MRI

Once brain metastases are established in preclinical models, a variety of treatment options and imaging techniques can be used. As proposed in section 1.3, ASL MRI could be applied to these preclinical models of brain metastases to determine tumour blood flow and predict treatment outcome. Since its development, ASL MRI has been widely used in preclinical research for measurement of cerebral blood flow (CBF) in a variety of brain anomalies and disease models, including brain tumours (Lindner *et al.*, 2018) as well as stroke (Shen and Duong, 2016) and dementia (Shen *et al.*, 2018). However, similar to the clinical setting, individual research groups or centres appear to possess their own

labelling approach or analysis method for CBF determination. The differences in ASL MRI techniques stem not only from the different labelling approaches available but also from the translation of the method from humans to small research animals, like mice and rats. The variability of the ASL MRI method used between preclinical research studies have led to a wide range of CBF values reported in the literature. Moreover, preclinical studies are rarely performed on multiple MRI scanners or in different imaging centres, a factor which has delayed the standardisation of this perfusion MRI technique. Preclinical ASL MRI would clearly benefit from a standardisation, as was proposed for its clinical application, and likely from an optimisation for use in small rodents to allow better clinical translation of ASL MRI preclinical findings.

1.7 Thesis aims

As outlined in this chapter, there is an unmet need for improvements in the detection and treatment of brain metastases to increase the duration and quality of life in patients. The addition of ASL MRI to brain metastasis imaging could provide a better insight into the biological characterisation of brain metastases and be a useful tool in treatment planning and in assessing treatment response. Additionally, vascular normalisation has yet to be performed in most brain metastasis tumour types and could lead to improved radiotherapy outcomes in patients.

Based on the above, the aims of this thesis are the following:

1- To optimise and validate preclinical ASL MRI in rats, thus, providing accurate and reliable measurements of CBF for the preclinical standardisation of this method;

2- To use ASL MRI to reproducibly measure CBF in rats with brain metastases over time and to assess its sensitivity changes in metastasis blood flow and tumour location as compared to currently used clinical MRI techniques, as well as histology; and

3- To assess the effects of anti-angiogenic drugs in a rat brain metastasis model and to evaluate ASL MRI as a detection method for vascular normalisation therapy that could potentially replace MRI methods relying on contrast agent administration.

CHAPTER 2

Methods and materials

Methods used in this thesis can be found either in the present chapter, when used for multiple chapters or in chapter-specific methods sections, when the methods were only relevant for the chapter.

2.1 Cell lines and *in vitro* cell culture

ENU1564 cells (*N*-ethyl-*N*-nitrosourea-induced rat mammary adenocarcinoma isolated from a BDIV rat; referred to as ENU) were received as a gift from Professor G. Stoica, Texas A & M University. Cells were cultured in monolayers in ventilated flasks (Corning Life Sciences, UK) in Dulbecco's Modified Eagle Medium (DMEM; Sigma-Aldrich, UK) supplemented with 10 % (v/v) foetal bovine serum (FBS; Labtech International, UK) and 1 % (v/v) L-glutamine (45 µg/mL; Sigma-Aldrich, UK) at 37 ˚C in a humidified atmosphere of 95 % air and 5 % carbon dioxide. Characterisation of ENU1564 cells is described in these

two articles (Hal and Stoica, 1994; Hall and Stoica, 1994). For ENU cell injection into rats, confluent flasks of cells were washed in sterile phosphate-buffered saline (PBS) before trypsinisation of the cells (Sigma-Aldrich, UK) at 37 ˚C. Tryspin was de-activated once ENU cells no longer adhered to the culture flask by the addition of DMEM with FBS and L-glutamine. This solution was centrifuged at ~300 $\times$ *g* (1200 rpm in TX-750 rotor, Heraeus Megafuge 40R; Thermo Fischer, UK) for 5 minutes. The supernatant was subsequently removed, and the cell pellet resuspended in PBS. ENU cells were counted using Countess II automated counter (Invitrogen, UK) by trypan blue exclusion method and the PBS volume was adjusted to yield 1×10^6 cells per mL.

2.2 Animals

All animal experiments were approved by the UK Home Office (Animals [Scientific Procedures] Act 1986) and conducted in accordance with the University of Oxford Policy on the Use of Animals in Scientific Research and the ARRIVE guidelines (Kilkenny *et al.*, 2013; Oxford, 2019). Animals were housed in individually ventilated cages under a 12-hour light/12-hour dark cycle with food and water *ad libitum*. All animals were housed in cages of two to five animals, depending on body mass. Female, as opposed to male, rats were used owing to the breast primary tumour of the brain metastasis model. Information pertaining to animal experimental plans are found in the chapter of interest.

2.2.1 Preclinical intracerebral brain metastasis model

ENU1564 cells were injected into the left striatum of female Berlin-Druckrey IX (BDIX) rats. Cells were prepared as described in section 2.1 and kept in a sterile cold box to

prolong cell survival. Cells were injected ≤ 2 hours post-trypsinisation to ensure viable cell counts.

Rats were anaesthetised in a 30:70 O_2:N_2O gas mixture with 3 % isoflurane and anaesthesia was maintained with 1.5-2.5 % isoflurane. The head was shaved and then rats were laid prone on a stereotactic frame (Stoetling Co., USA), with EMLA cream (5 %; Aspen Global Inc., AstraZeneca, UK) as analgesic placed on the ear bars, atop a homeothermic pad, and body temperature was maintained at 37 ˚C using a rectal temperature probe with a feedback loop to the homeothermic pad (Harvard Apparatus U.K.; Cambourne, UK). 100 µL of Marcain (0.25%; Aspen Global Inc., AstraZeneca, UK) was injected sub-dermally as analgesic followed by a 5 minute wait. The head was sterilised using 70 % ethanol wipes with chlorohexidine (1 %), and the rat covered with a sterile surgical drape with an opening for the surgical area, comprising of the top of the head. The sterile procedure commenced using sterile surgical gowns, surgical masks and latex gloves, as well as autoclaved surgical tools. A small incision was made using a size 15 scalpel blade (Swann-Morton, Sheffield, UK) at the midline of the top of the skull. Bregma was identified using a stereoscopic surgical microscope and a burr hole drilled in the skull 1 mm anterior and 3 mm lateral to the left of bregma (Mains powered drill (240V), World Precision Instruments, Hitchin, UK, and 1.4 mm drill bit, Fine Science Tools, Heidelberg, Germany). ENU cells (1×10^6 cells/mL) were resuspended using a 23 gauge needle fixed to a 1 mL syringe, and loaded into a pulled glass capillary with a 70 µm diameter tip using a 27 gauge needle fixed to a 1 mL syringe. The capillary was cleaned using chlorohexidine solution and then rinsed in saline (0.9 %) before being attached to the stereotactic frame. 1 µL of cells (1000 cells) were injected at a depth of 3.5 mm, into the left striatum, by increased pressure through the capillary with a syringe full of air, connected via a short

length of tubing to the top of the injection capillary. The capillary remained at a depth of 3.5 mm for 5 minutes for the increased pressure inside the brain to reach equilibrium and, thus, to prevent cells from flowing out of the injection site. The capillary was then raised by 0.5 mm followed by a 2 minute wait, before full extraction of the capillary. The injection area was rinsed several times with saline (0.9 %) to remove any cells that could be present at the entrance to the injection site or extracranially. The rat scalp was subsequently sutured (Vicryl, Ethicon, Germany) with sutures positioned approximately every 2 mm. Sterility was broken at this point to remove the rat from the stereotactic frame and rat nails were clipped to prevent scratching and removal of head stitches. Rats were allowed to recover from the surgical anaesthesia in a warmed ventilated cage. Rats were fed mash immediately after surgery.

In PBS-injected animals, the same procedure was performed with the injection of 1 µL of PBS without cells.

2.2.2 Perfusion-fixation

In brain metastasis-bearing rats, three hours prior to killing the rats, each was injected intraperitoneally with 60 mg/kg of pimonidazole hydrochloride (Hypoxyprobe, Burlington, USA) to identify regions of hypoxia histologically.

In all rats, whose brains would be used for immunohistochemistry, at time of killing, rats were injected intraperitoneally with an overdose of pentobarbitone followed by transcardial perfusion-fixation with heparinised saline (0.9 % with 1 unit heparin per mL) followed by PLP_{light} (75 µM L-lysine HCl (Sigma-Aldrich, UK), 10 mM sodium phosphate, dibasic (Sigma-Aldrich, UK), 10 mM sodium metaperiodate (VWR, UK), 10 %

paraformaldehyde (w/v; Sigma-Aldrich, UK), 0.0025 % glutaraldehyde (w/v; Sigma-Aldrich)) using a perfusion pump (Watson-Marlow bredel pump, Falmouth, UK) at a rate of 18 mL/minute. Following perfusion, rat brains were isolated and post-fixed for 4-6 hours in PLP_{light} at 4 ˚C, before being transferred to a 30 % sucrose solution (w/v in dH_2O; Sigma-Aldrich, UK) for cryoprotection, until brains sank to the bottom of the tube. Cryoprotected rat brains were thinly embedded in OCT (Pyramid Innovation, UK) in isopentane with dry ice and stored at -20 ˚C until cryo-sectioned.

2.3 Magnetic resonance imaging

Rats were anaesthetised with 3 % isoflurane in a 10 % oxygen and 90 % air gas mixture and laid prone on an in-house built homeothermic pad with their head secured using ear bars. Rats were imaged using a horizontal-bore 9.4 T spectrometer (Agilent, UK) with a 72 mm transmit-receive volume coil and a 4-channel surface receive array (Rapid Biomedical, Rimpar, Germany). Anaesthetic depth was monitored and breathing rate was maintained between 40 and 60 breaths per minutes by adjusting isoflurane concentration between 1.5-2.5 %. In rats used for Chapters 4, 5 and 6, a saline-filled cannula was positioned in a tail vein prior to imaging, allowing the intravenous injection of contrast-agents during imaging.

2.3.1 Multiphase pCASL MRI[1]

The multiphase pCASL (MP-pCASL) MRI sequence was a developed by Dr. James Meakin (Meakin, 2014).The phase increments were varied through radio-frequency (RF) pulses in the labelling plane between 0˚ and 315˚ through eight steps of 45˚. In accordance with the results of Chapter 3, the labelling plane thickness of 6.2 mm was used at an angle of 45˚ relative to the bore of the spectrometer. A label duration of 2.4 s was used, corresponding to a repetition time (TR) of 5 s (experimental time (T_{exp}) = 1 min 51 s) to maximise MP-pCASL MRI imaging efficiency in single-average acquisitions. A post-label delay (PLD) of 650 ms was used. The MP-pCASL imaging region consisted of ten 1 mm thick slices with an axial orientation, acquired in an anterior-posterior direction and starting directly behind the sulcus of the olfactory bulbs to cover the tumour site.

MP-pCASL MRI was performed using a multi-slice spin-echo echo planar imaging (EPI) readout with a field of view (FOV) of 32 × 32 mm and a 64 × 64 matrix, giving an in-plane resolution of 500 × 500 µm, and an echo time (TE) of 28.7 ms. Proton-density calibration images with the same parameters as described above were acquired for absolute quantitation of cerebral blood flow (CBF), for all rats, by omitting labelling pulses and using both the surface receive array (1 average; 31 s) and the volume coil (8 averages; 4 min 4 s) and using a TR of 7.6 s. Apparent CBF measurements were calculated as described in section 3.3.3.2, using an in-house built code[2] calling the FSL tool 'fabber' (Chappell *et al.*, 2009), Quantiphyse for supervoxel generation (Irving *et al.*, 2016) and a

[1] The MP-pCASL MRI parameters here were used for Chapters 4, 5, and 6. The MP-pCASL MRI parameters for the sequence optimisation are present in Chapter 3.
[2] Code built by Dr. James Larkin and myself.

custom version of BASIL for oxford_asl (Chappell *et al.*, 2009; Groves, Chappell and Woolrich, 2009), both available through the FMRIB Software Library.

2.3.2 Diffusion-weighted MRI

Diffusion-weighted imaging is widely used in stroke and brain tumour imaging and exploits the random motion of water particles for tumour characterisation and ischaemic stroke boundary determination. The diffusion of water particles is followed in brain tissue voxels and the resulting apparent diffusion coefficient (ADC) reports on the impedance of water particles in tissue, based on tissue cellularity (proximity of cells from one another) and the presence of intact cell membranes. Here, diffusion-weighted images were acquired in three separate orthogonal directions for b = 0 s/mm² and b = 1000 s/mm² in ten 1 mm slices, acquired in the rostral-caudal direction, using an EPI readout, a FOV of 32 × 32 mm and a 64 × 64 matrix, giving an in-plane resolution of 500 × 500 µm. A TR of 3 s and TE of 43.2 ms were used for a T_{exp} = 31 s. ADC maps were generated according to the following formula:

$$ADC(x,y,z) = \ln\left(\frac{S_2(x,y,z)}{S_1(x,y,z)}\right) \Big/ (b_1 - b_2) \quad , \tag{2.1}$$

where S_2 and S_1 represent the signal from images acquired with b = 1000 s/mm^2 and b = 0 s/mm^2, respectively, in each direction, and b_1 and b_2 represent the b-values 0 s/mm^2 and 1000 s/mm^2, respectively.

2.3.3 T_1-weighted imaging

T_1-weighted imaging was performed in brain metastasis-bearing rats before and after the injection of gadodiamide contrast agent (150 µL of 0.5 mmol/mL; Omniscan, GE Healthcare, Oslo, Norway), as part of DCE MRI (section 2.3.5), to detect areas of BBB breakdown in the brain metastases. T_1-weighted acquisitions had a FOV = 32 × 32 mm and a 256 × 256 matrix, giving an in-plane resolution of 125 × 125 µm, with TR = 0.5 s and TE = 20 ms were used for a T_{exp} = 4 min 16 s. The same slice pattern was used, as for the EPI readout methods.

2.3.4 T_2-weighted imaging

2.3.4.1 For MP-pCASL MRI labelling plane position

Routine sagittal scans for MP-pCASL MRI label plane positioning were acquired using a T_2-weighted fast spin-echo readout at a single 2 mm slice at the brain midline using FOV = 50 × 50 mm, data matrix = 256 × 256, TR = 1 s, effective TE (TE_{eff}) = 40 ms and T_{exp} = 34 s.

2.3.4.2 High resolution for tumour volume approximations

Using a T_2-weighted fast spin-echo readout, anatomical imaging was performed in brain metastasis-bearing rats to obtain tumour size approximations and detect regions of cystic necrosis, together with brain anatomical information. T_2-weighted acquisitions had a FOV = 32 × 32 mm and a 256 × 256 matrix, giving an in-plane resolution of 125 × 125 µm,

with TR = 3 s and TE_{eff} = 51.26 ms were used for a T_{exp} = 3 min 18 s. The same slice pattern was used, as for the EPI readout methods.

2.3.5 Dynamic contrast-enhanced MRI

DCE MRI was performed to determine outflow kinetics of the injected bolus of gadodiamide contrast agent (150 µL of 0.5 mmol/mL; Omniscan, GE Healthcare, Oslo, Norway) by acquiring rapid sequential T_1-weighted images, following intravenous contrast agent injection, to determine vascular permeability of brain metastasis foci by K^{trans}. Acquisitions of DCE MRI used a gradient echo 3D readout with FOV = 64 × 32 × 32 mm and a 128 × 64× 64 matrix, giving an isotropic 500 µm. A flip angle of 5˚ was used, together with a TR = 2 s, TE = 0.93 ms for a frame rate = 8.3 s. The frame rate was repeated 60 times, with the bolus injection of gadodiamide occurring at the start of the 11th repetition, for a T_{exp} = 8 min 23 s. K^{trans} maps were generated from an in-house built code[1].

2.3.6 Relaxometry

T_1 relaxation time was obtained using a T_1 inversion recovery method with inversion times increasing in nine logarithmic steps from 0.013 to 8 s, with TR = 10 s allowing a complete recovery between steps and T_{exp} = 3 min 21 s. T_2 relaxation times were obtained through a multi-echo approach with TE varying from 30 to 160 ms in ten logarithmic steps, also

[1] Code was built by Dr. P. Danny Allen of the Pre-Clinical Imaging Scientific Research Facility of the Department of Oncology, University of Oxford.

with TR = 5 s and a T_{exp} = 1 min 51 s. Readouts for both the T_1 and T_2 relaxation time acquisitions were spin-echo EPI as for the MP-pCASL MRI acquisitions. Relaxation times were determined on a voxel-wise basis by fitting to a non-linear least squares fitting method using an in-house code[1], using equation 2.2 for determining T_1 relaxation time and equation 2.3 for T_2 relaxation time.

$$M = M_0 \left(1 - 2e^{-\frac{t}{T_1}}\right), \tag{2.2}$$

$$M = M_0 \times e^{-\frac{t}{T_2}}, \tag{2.3}$$

where M is the magnetisation at time t, M_0 is the initial magnetisation of 1, and T_1 and T_2 are the T_1 and T_2 relaxation times, respectively.

2.3.7 Chemical exchange saturation transfer MRI

CEST MRI was performed in rats to detect chemical exchanges of labile protons in biomolecules with water protons present in the tissue. In this thesis, the CEST MRI was preferentially selective to the amide proton transfer (APT) of the CEST profile, sensitive to the exchange between protons on the side chains and backbone of proteins and water molecules present in the brain tissue. The previous work of Dr. Kevin Ray from our group discusses in detail the tumour pH and protein concentration changes that can be detected in the rat model of brain metastasis used here (Ray, 2017; Ray *et al.*, 2019[2]).

The pulse saturation scheme used for CEST MRI was preferentially selective to amide protons (3.5 ppm) at a pH of 7.02 *in vivo* and consisted of 34 saturation pulses (offset

[1] Code written by Dr. Kevin Ray and Dr. James Larkin.
[2] I have contributed to this work.

frequencies relative to water: -300, -5, -4, -3.8, -3.5, -3.2, -2.9, -2.6, -2.3, -2, -1.5, -1, -0.8, -0.5, -0.3, 0, 0.3, 0.5, 0.8, 1, 1.6, 1.8, 2, 2.2, 2.4, 2.7, 3, 3.2, 3.4, 3.6, 3.8, 4, 5, 300 ppm). Each pulse was comprised of a Gaussian radiofrequency (RF; 20 ms) with a flip angle of 184˚ followed by a crusher gradient (20 ms), for a total duration of 2 s with equivalent continuous wave power of 0.55 mT. Following saturation, 10 slices of 1 mm thickness were acquired in the rostral-caudal direction using a multi-slice spin-echo EPI readout with a FOV of 32×32 mm and a 64×64 matrix, giving an in-plane resolution of 500×500 µm. A TR of 5 s and TE of 27 ms were used for a T_{exp} = 7 min 51 s. Data were quantified using the QuantiCEST widget in Quantiphyse (offset frequency of 3.5 ppm, exchange rate of 30 Hz, water T_1 relaxation of 1.8 s and water T_2 relaxation of 100 ms) to generate amide proton transfer ratio (APTR*) brain maps (Chappell *et al.*, 2013, 2017).

2.3.8 Segmentation of regions of interest in the brain

Regions of interest (ROI) in the brain from MRI acquisitions were segmented in ITK-SNAP (Yushkevich *et al.*, 2006) on T_2-weighted anatomical images for the brain metastasis foci and on spin echo EPI images for the corresponding contralateral area, tumour rim and tumour core in all ENU- and PBS-injected rats used; for PBS-injected rat, a tumour region from a metastasis-bearing rat from the same time point was applied to the same brain region. The brain metastasis foci segmentation was initially drawn on the higher resolution images to determine estimates of volume for the brain metastasis foci and increase the precision of the ROI. These segmentations were down-sampled to the 500×500 µm in-plane resolution of spin-echo EPI MRI and adjusted slightly in some areas to account for the different artefacts or shifts between the acquisition readouts. The brain

metastasis rim region was determined geographically using a one-voxel wide region at the outer margins of the tumour segmentation on MRI images with an in-plane resolution of 500 × 500 µm. The brain metastasis core region was obtained from the subtraction of the rim region from the entire brain metastasis segmentation. Examples of these segmentation are presented in Figure 2.1

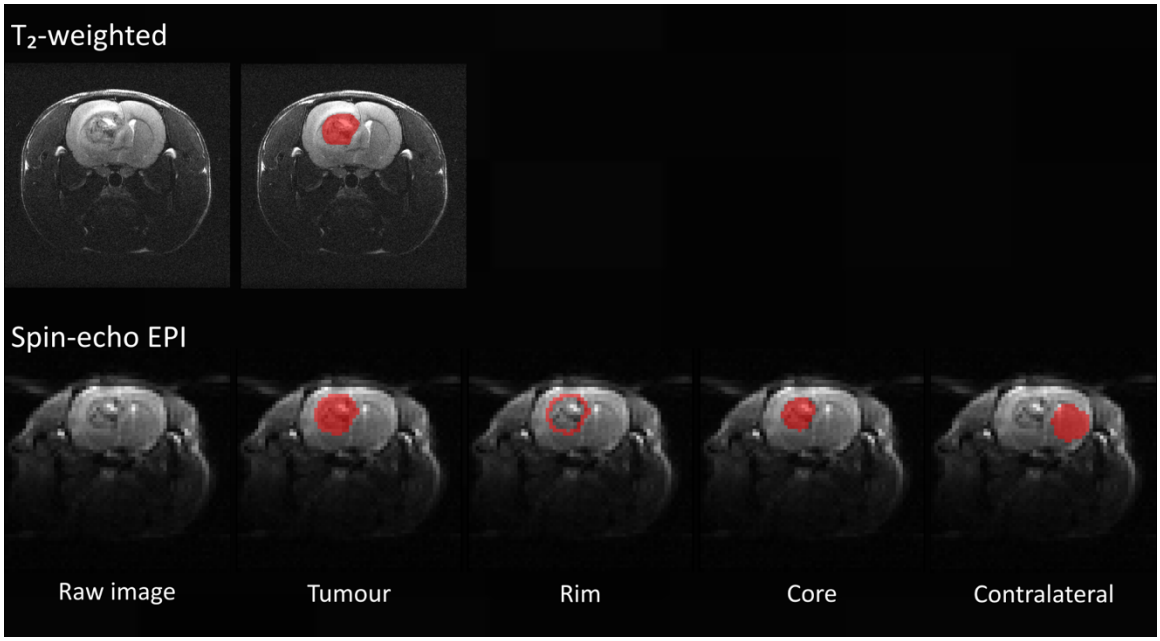

Figure 2.1 Segmentation of brain regions of interest on MRI. The brain metastasis region is first drawn on T_2-weighted images, of higher resolution, then applied to the lower resolution spin-echo EPI images and divided into the rim and core regions. The contralateral ROI is drawn so as to not overlap with the tumour ROI, and approximately of the same size.

2.4 Immunohistochemistry

2.4.1 Tissue sectioning

Cryoprotected brains covered with OCT from section 2.2.2 were affixed to a Leica CM1950 cryostat (Leica, UK) sample platform with OCT and cut in 20 µm thick brain section. Sections were collected on glass slides (SuperFrost Plus, Menzel Gläser, Braunschweig,

Germany) at 200 µm intervals on each slide. Consecutive slides possessed the immediately adjacent brain tissue sections. Sections were stored at -20 ˚C. until stained.

2.4.2 Antigen retrieval protocol

For α-smooth muscle actin (αSMA) immunohistochemistry (IHC), antigen retrieval was necessary to obtain reproducible staining. Sections were warmed to room temperature prior to antigen retrieval and rinsed twice in PBS (Oxoid, Thermo Fisher Scientific, UK) for 5 minutes. Next, slides were bathed in sodium citrate buffer (pH = 6.0) with 0.1 % Tween-20 (Sigma-Aldrich, UK) and microwaved twice for 5 minutes, replacing the citrate buffer between sessions. Slides were cooled to room temperature and then carried on the standard IHC protocol outlined below.

2.4.3 Standard immunohistochemistry protocol

Sections were warmed to room temperature prior to IHC protocol initiation. Sections were rinsed in PBS twice for 5 minutes then quenched in methanol (Sigma-Aldrich, UK) with hydrogen peroxide (H_2O_2; 1 % (v/v); Sigma-Aldrich, UK) for 20 minutes on a shaker (KS250 IKA Labortechnik, IKA England, Oxford, UK). Then, sections were washed three times for 5 minutes in PBS with tween (PBST; 0.05 % Tween-20) and slides containing rat brain sections were assembled with clips and loaded onto the Sequenza IHC system (Thermo, UK). 150 µL of 10 % blocking buffer in PBST was administered to each slide and incubated for 1 hour at room temperature. Subsequently, 150 µL of primary antibody solution with 1 % blocking buffer in PBST was added and slides were kept at 4 ˚C

overnight. The following day, slides, still in the Sequenza system, were rinsed three times with PBST and 150 µL of the secondary antibody in PBST was added for 1 hour at room temperature. Slides were rinsed three times with PBS and 150 µL of avidin/biotin complex-horseradish peroxidase (HRP) system (VectaStain Elite ABC detection kit, Vector Laboratories Ltd, Burlingame, USA), prepared 45 minutes earlier, was added to each slide. Again, slides were rinsed three times with PBS and Sequenza clips were disassembled. Brain sections were then exposed to 3,3'-diaminobenzidine tetrahydrochloride hydrate (DAB; Acros Organics, Fisher Scientific, UK) with 0.04 % H_2O_2 to visualise staining. Sections were then counter-stained with cresyl violet acetate. To do so, sections were acidified in H_2O with 0.05 % acetic acid glacial (Thermo Fisher Scientific, UK) for 30 s then exposed to cresyl violet acetate (0.5 %, w/v in H_2O; Sigma-Aldrich, UK) until cell nuclei were easily identifiable (20 s to 2 min). Sections were dehydrated in ethanol baths of increasing concentration (75 %, 95 %, 100 %) then left in ethanol for 5 minutes. Sections were transferred sequentially through three xylene baths, each with a 5 minute incubation, then coverslips were mounted using DPX mountant (Sigma-Aldrich, UK).

2.4.4 IHC analysis

IHC sections were digitised at 200× on an Aperio CS2 Scanscope (Leica Biosystems, Germany). Using the ImageScope software (v12.3.2.8013; Leica Biosystems, Germany), brain metastases, brain metastasis core and the healthy contralateral striatum were segmented. Subsequently, the Positive Pixel Count v9 algorithm was used to obtain the number of stained pixels within the selected area. Threshold parameters were selected

subjectively based on the intensity of the DAB staining and cresyl violet acetate counterstain, which could account for some differences in the final quantitation. Where possible, most IHC staining was performed for all brain sections simultaneously for each antibody selected, in order to minimise variability in staining intensity. Nevertheless, baseline levels of staining were subtracted from both brain metastasis rim and core regions to correct for the variability in staining intensity and background staining observed between batches of staining. No differences could be visually detected between the contralateral striata of metastasis-bearing rats of any treatment group compared to PBS-injected rats or naïve rats. Areas of positive staining were calculated using the positive pixel counts generated and image pixel size for the selected brain region. An example of the segmentation of brain metastasis rim and core regions can be found in Figure 2.2.

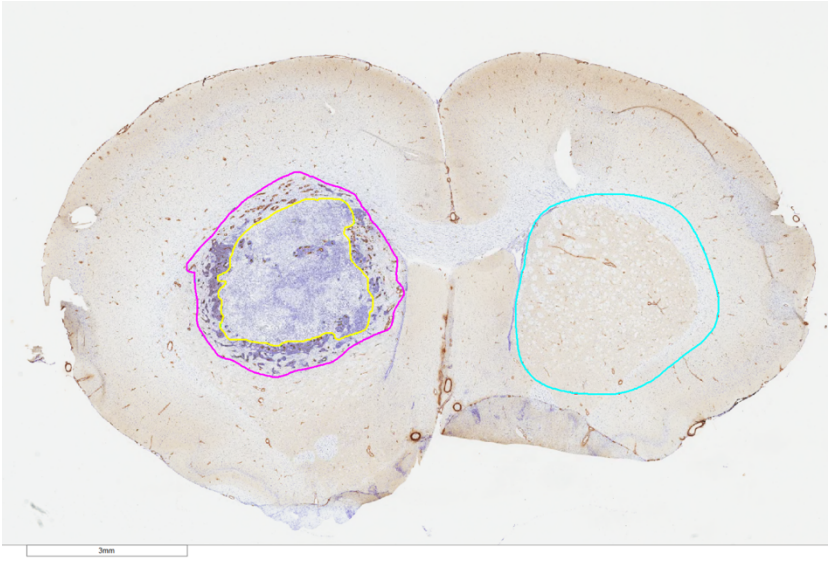

Figure 2.2 Brain regions of interest in IHC. A representative brain section of αSMA IHC with the brain metastasis core region outlined in yellow, the brain metastasis rim region outlined in pink and yellow, and the contralateral striatum in turquoise.

CHAPTER 3

Optimisation of preclinical arterial spin labelling in rats

3.1 Introduction

3.1.1 Clinical recommendations for arterial spin labelling (ASL)

In 2014, the ASL white paper was published and recommended a set of guidelines for the use of ASL MRI in the clinic (Alsop *et al.*, 2014). This seminal article reviewed previous implementations of ASL MRI in humans with the purpose of standardising this technique across clinical scanners and centres. In summary, ASL MRI should be performed on clinical scanners of at least 1.5 T and use a pseudo-continuous arterial spin labelling (pCASL) approach. In humans, the labelling plane should be positioned perpendicular to the brain feeding arteries either by placing it 85 mm inferior to the anterior commissure/posterior

The majority of the conception, execution and analysis of the results presented in this chapter was performed equally by Dr. James R. Larkin and myself. Many of the results have also been published into a peer-reviewed journal article (Larkin *et al.*, 2018), where Dr. Larkin and I were co-first authors (Appendix I).

commissure line or just below the cerebellum. The label duration should be of 1.8 s followed by a post-label delay (PLD) of 2000 ms in adults. Background suppression is recommended for 3D and single slice 2D acquisitions to increase signal-to-noise ratio. The recommended readout is a 3D segmented readout when available, otherwise a multi-slice single-shot echo planar imaging (EPI) readout is suggested. Finally, cerebral blood flow (CBF) should be shown in mL/100g/min and calculated according to the image signal intensity, the blood:brain partition coefficient and the T_1 relaxation time of blood (Alsop *et al.*, 2014).

3.1.2 Preclinical ASL MRI

Preclinical rodent models of disease are of great importance to many fields of research and accurate non-invasive measurement of CBF in these models is paramount in many studies. The clinical recommendations outlined above cannot simply be applied to preclinical ASL MRI to produce high quality CBF data. Anatomical differences are immense between humans and rodents, and the technical equipment available in the clinic and in preclinical research facilities varies greatly. One of the major problems with ASL MRI in the preclinical setting relates to the higher magnetic field strength used for research ($\geq$ 7 T) and the small anatomical features, and their organisation, in the neck of rodents. Good magnetic field homogeneity in the labelling plane in the neck along with the imaging region is required for high quality ASL MRI acquisitions. Yet, the proximity of air-filled cavities, such as the throat, oesophagus, nasal cavities and mouth, to the labelling plane and imaging region result in magnetic susceptibility artefacts, as well as off-resonance effects, in the brain feeding arteries, arising from poor magnetic field homogeneity at

higher magnetic field strengths. These off-resonance effects and susceptibility artefacts may lead to differing labelling efficiency of each vessel at the labelling plane, resulting in error-prone CBF measurements in traditional label-control pCASL MRI. The limitations outlined above have contributed to the wide array of unrealistic CBF values observed in the literature for rodents (e.g. > 300 mL/100g/min; (Hendrich *et al.*, 2001; Kim and Kim, 2005; Thomas *et al.*, 2006; Wells *et al.*, 2010; Debacker *et al.*, 2017) that are not in agreement with gold-standard autoradiography CBF measurements (Sakurada *et al.*, 1978; Maeda *et al.*, 2000; Orzi, Capone and Mangiardi, 2006). Of note, inhalation anaesthetics are commonly used in preclinical studies, of which, halogenated agents are most common; isoflurane, halothane, sevoflurane, desflurane, enflurane. These halogenated inhalation anaesthetics are known to possess vasodilating properties, which have been shown to increase CBF (Iida *et al.*, 1998; Shen, 2008; Satuito and Tom, 2016; Eis and Kramer, 2019). However, the gold-standard autoradiography measurements, along with the other studies referred to above have all used halogenated anaesthetic agents, and should, therefore, all demonstrate similar CBF values. There is clearly a need to improve preclinical application of ASL MRI in rodents and to establish a standardisation across centres as has now been implemented clinically.

3.1.3 Multiphase pCASL MRI

Multiphase pCASL (MP-pCASL) MRI is a variant of traditional label-control pCASL MRI, where instead of acquiring images at 180˚ and 0˚ (representing the label and control images, respectively) images are acquired with radiofrequency (RF) pulses at multiple phase increments, thereby increasing the likelihood of detecting the maximal inversion

of protons, while decreasing the impact of off-resonance effects (Jung, Wong and Liu, 2010). These increments span an entire 360˚ enabling the fitting of the data to an expected function, rather than performing a simple subtraction of the label from the control pCASL MRI images (Figure 3.1). By increasing the sampling from two phases, the possibility of obtaining no signal at all is eliminated, as would be the case for the green squares, 90˚ off-resonance, in Figure 3.1A. However, MP-pCASL MRI increases the scan time relative to a single-average label-control ASL MRI acquisition by a factor of $N_\phi/2$, where N_ϕ represents the number of phases. Nonetheless, in the worst-case scenario of an 8-phase multiphase acquisition (Figure 3.1B), 22.5˚ off-resonance, would still theoretically yield 93.4 % of the signal. In the case of pCASL MRI at higher magnetic field strength or with smaller subjects, where the likelihood of off-resonance effects is increased, the use of MP-pCASL MRI allows for *post-hoc* correction of off-resonance effects in the labelling plane to provide an increased accuracy in values of CBF.

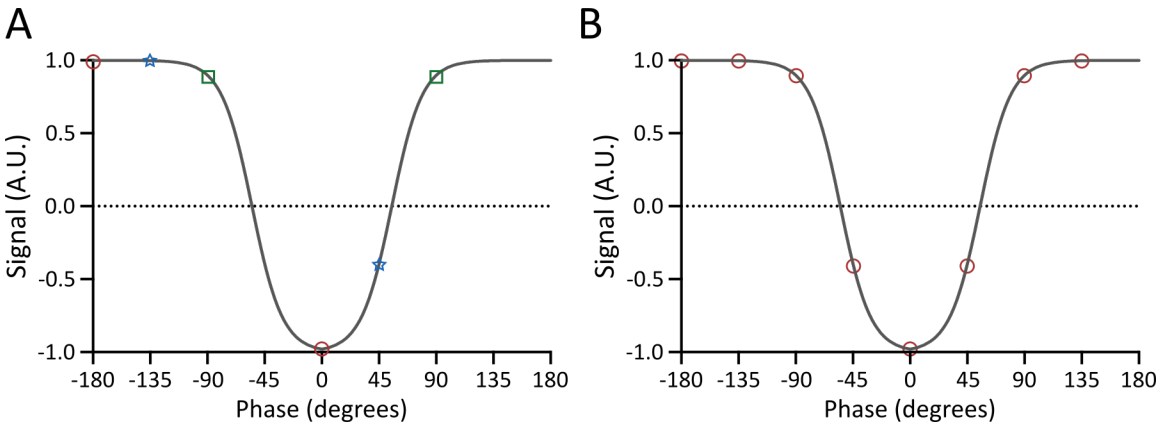

Figure 3.1 Advantage of multiphase pCASL MRI over traditional label-control pCASL MRI. Fermi function curves (α = 55, β = 21) representing the signal fluctuation during traditional label-control pCASL MRI (**A**) and multiphase pCASL MRI (**B**). **A** Traditional label-control pCASL MRI is performed using phase angles of -180˚ and 0˚ (red circles). Blue stars represent the signal with a 45˚ phase offset (77.8 % of optimal signal variation) and green squares represent the signal with a 90˚ phase offset (zero signal variation). **B** MP-pCASL MRI acquires signal from multiple phases, 8 phase sampling is shown by red circles.

An alternative to MP-pCASL MRI has recently been proposed by Hirschler and colleagues, where dedicated pre-scans attempt to solve the problem of off-resonance (Hirschler *et al.*, 2017). The authors used large voxels across each hemisphere, with a high SNR, then rapidly iterated through a multitude of phase offsets. These pre-scans then enabled the optimal acquisition parameters for the upcoming pCASL MRI acquisition to be determined. The drawbacks to this approach are, firstly, that if the vertebral and carotid arteries feeding one brain hemisphere possess different phase offsets, a single offset will be chosen for both vessels and, secondly, analysis of the optimal parameters must be performed while the rodent is in the spectrometer. In contrast, MP-pCASL MRI allows for a voxel-wise or brain vessel territory-wise phase offset selection and the entire analysis can be performed *post-hoc*, reducing total imaging time.

3.1.4 Chapter aim and hypotheses

3.1.4.1 Aim

The aim of this chapter was to establish optimal parameters for ASL MRI in rat brain to provide reproducible and robust quantitative cerebral blood flow measurements.

3.1.4.2 Hypotheses

(1) MP-pCASL MRI improves CBF quantitation compared to traditional label-control pCASL MRI by allowing for correction of off-resonance effects in vessels at the labelling plane.

(2) CBF measured from MP-pCASL MRI is in agreement with gold-standard CBF results from [^{14}C]-iodoantipyrine autoradiography.

3.2 Methods

3.2.1 Animals

Female Sprague-Dawley (SD; *n* = 7; 230-403 g), Wistar (*n* = 7; 180-230 g), and Berlin-Druckrey IX (BDIX; *n* = 7; 196-295 g) rats were used. SD and Wistar rats were chosen as they are commonly used in scientific research for various disease models. BDIX rats were also selected since a syngeneic model of breast cancer brain metastasis exists for this rat strain and will be used in later chapters of this thesis.

3.2.2 Power Doppler ultrasound

Power Doppler ultrasound detects frequency changes in high frequency sound waves based on the Doppler effect to non-invasively determine the velocity of fluids in the body. In this chapter, it was used to determine the velocity of blood moving toward the brain in rats. Rats (*n* = 3 per strain) were anaesthetised with 3 % isoflurane in a 10 % oxygen and 90 % air gas mixture and laid supine on an ultrasound stage. Anaesthesia was maintained using 1.5-2.5 % isoflurane. Body temperature was maintained at 37 ˚C using a homeothermic pad under the animal (Harvard Apparatus U.K.; Cambourne, UK). Rat fur at the neck was removed using depilatory cream (Nair, Boots, UK) and electro-cardiac probes were inserted subcutaneously below the ribcage for recording of the heart and respiration rates. Aquasonic 100 ultrasound transmission gel (Parker Laboratories, USA) was applied to the neck and the MX550D probe couple to a Vevo 3100 ultrasound (Visualsonics, Toronto, Canada) was used in the Rat Cardiology (large) setting (rat set-up shown in Figure 3.2A). Blood supply in the brain occurs through the carotid and vertebral

arteries. Since the carotid arteries are larger in the neck, the velocity of blood flowing through it was determined using Power Doppler ultrasound in SD, Wistar and BDIX rats. Carotid and vertebral artery location was determined by a 3-dimensional coloured Power Doppler acquisition across the neck. Once the right carotid artery was located, the angle of the artery was defined (Figure 3.2B) and 30 s clips of B-mode Power Doppler giving blood velocity were acquired at 10-12 respiration rates between 40 and 65 breaths per minute in each rat. The blood velocity was calculated using

$$f_{Doppler} = \frac{2 \cdot f_0 \cdot v_{blood} \cdot \cos\theta}{c} \quad , \tag{3.1}$$

where $f_{Doppler}$ is the Doppler frequency, f_0 is the transmitted ultrasound frequency, v_{blood} is the blood velocity, c is the speed of sound in tissue (1540 m/s) and θ is the angle between the probe and the blood vessel.

Clip velocity graphs were converted to 2-dimensional graphs with the *x*-axis spanning the entire clip duration in Fiji (Schindelin *et al.*, 2012) and were digitised using a threshold-based image-to-data tool (Web Plot Digitizer (Rohatgi, 2010)) to extract velocities at every 10 ms. Mean blood velocity and large peak velocity were calculated from the data with each clip representing one data point for each rat strain (Figure 3.2C). Respiration rate was manually counted in each clip as a proxy for anaesthetic depth.

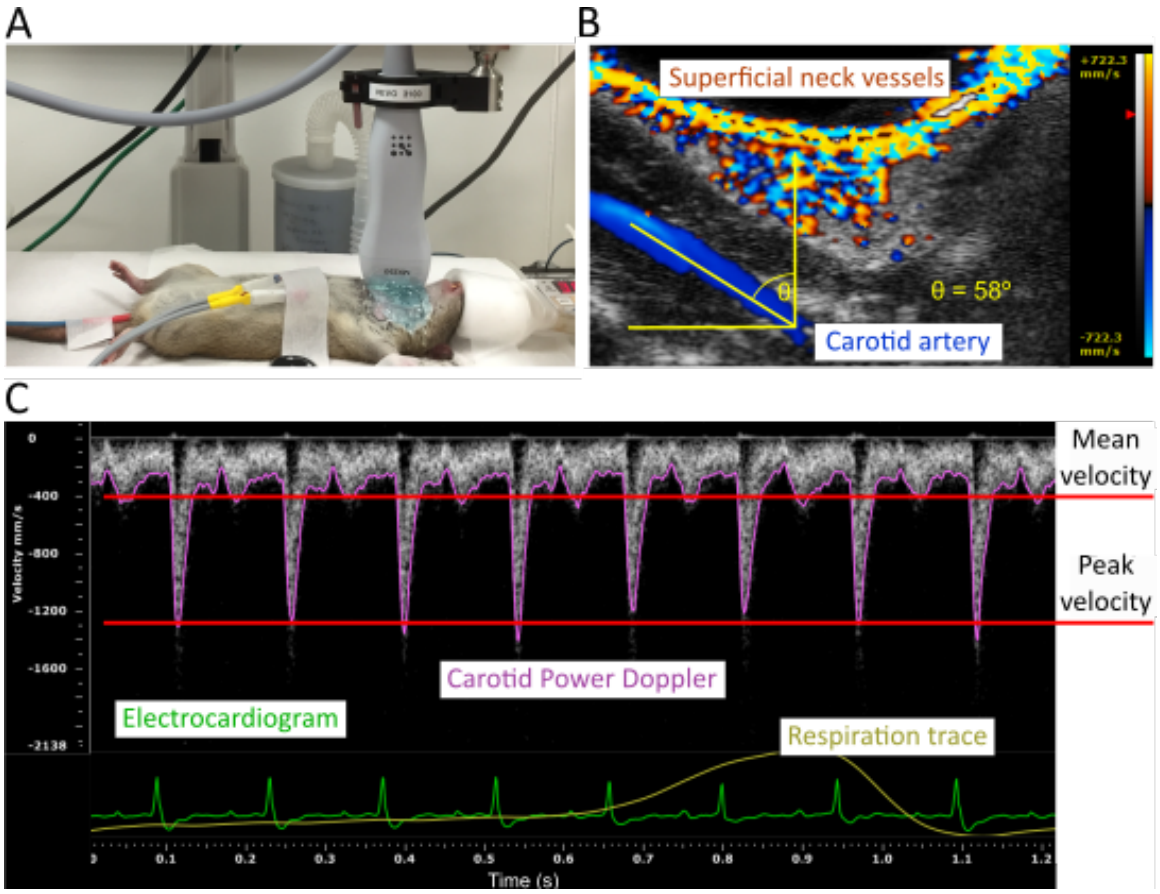

Figure 3.2 Measuring carotid blood velocity in rats using Power Doppler ultrasound. **A** Carotid artery Power Doppler ultrasound set-up of a BDIX rat. **B** Example of Power Doppler image for positioning of the probe and selecting alignment of carotid artery (blue vessel) with blood velocity going away from the probe (negative values). **C** Typical Power Doppler blood velocity trace graph over time along with electrocardiogram and respiration trace of a rat (SD) with identification of mean and peak velocities.

3.2.3 Bloch simulations

The Bloch equations were defined in 1946 by Felix Bloch to calculate the nuclear magnetisation as a function of time, dependent on the longitudinal (M_z) and transverse (M_x and M_y) relaxation times, T_1 and T_2, respectively (Bloch, 1946). Numerical simulations using the Bloch equations were conducted from previously developed code by Dr. Thomas Okell (Okell, 2011), in MATLAB (MathWorks®, Natick, USA). These simulations were used to determine the optimal flip angle for RF pulses of the adiabatic inversion in MP-pCASL MRI, the optimal labelling plane thickness and the expected blood water

inversion efficiency at relevant carotid blood velocities. Of note, the relationship between the maximal gradient (G_{max}) and the labelling plane thickness (Thk_{lab}) is given by

$$Thk_{lab} = \frac{BW_{trans}}{\gamma_0 \cdot G_{\max}} \quad , \tag{3.2}$$

where BW_{trans} is the transmitted RF bandwidth (4.3 kHz) and γ_0 is the proton gyromagnetic ratio (42.58 MHz/T).

3.2.4 Magnetic resonance imaging

MRI was performed on all rats, as described in section 2.3.

3.2.4.1 Multiphase pseudo-continuous arterial spin labelling

The multiphase pCASL MRI sequence was a developed by Dr. James Meakin (Meakin, 2014).The phase increments were varied through radio-frequency (RF) pulses in the labelling plane between 0˚ and 315˚ through eight steps of 45˚. A labelling plane with a thickness of 6.2 mm and at a 45˚ angle relative to the bore of the spectrometer was used. For the assessment of optimal labelling plane location, a reference labelling plane was positioned directly caudal to the notch behind the gracile fasciculus immediately rostral to the C1 vertebra. From the labelling plane reference position, 0 mm, the labelling plane was displaced up to 6 mm in 2 mm increments, in both the rostral (positive) and caudal (negative) directions in the three strains of rat studied (Figure 3.3).

As for the assessment of optimal label duration, durations of 0.4 s, 0.9 s, 1.4 s, 2.4 s, 3.7 s and 5.0 s were chosen to cover a range of physiologically sensible values. The repetition time (TR) of 4 s was used for label durations of 0.4 s, 0.9 s and 1.4 s for a total experimental time (T_{exp}) of 1 min 29 s. TR was increased to 5 s (T_{exp} = 1 min 51 s), 6.3 s

(T_{exp} = 2 min 20 s) and 7.6 s (T_{exp} = 2 min 48 s) with label durations of 2.4 s, 3.7 s and 5.0 s, respectively, to maintain a minimum post-saturation recovery period (Figure 3.4).

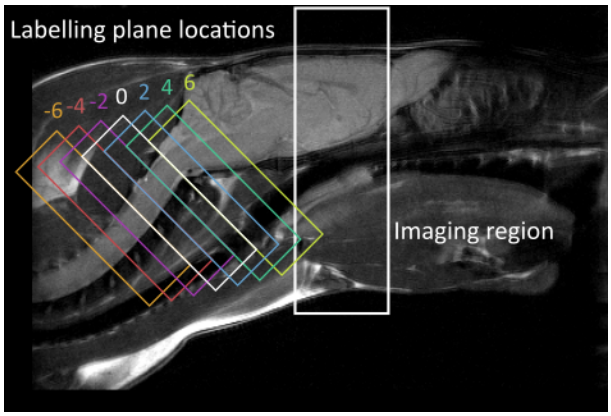

Figure 3.3 MP-pCASL MRI labelling plane locations. Labelling plane locations, shown on a T_2-weighted sagittal acquisition of the head midline, tested for optimal location with labelling planes spaced 2 mm apart at up to 6 mm caudal or rostral to the reference location, 0 mm.

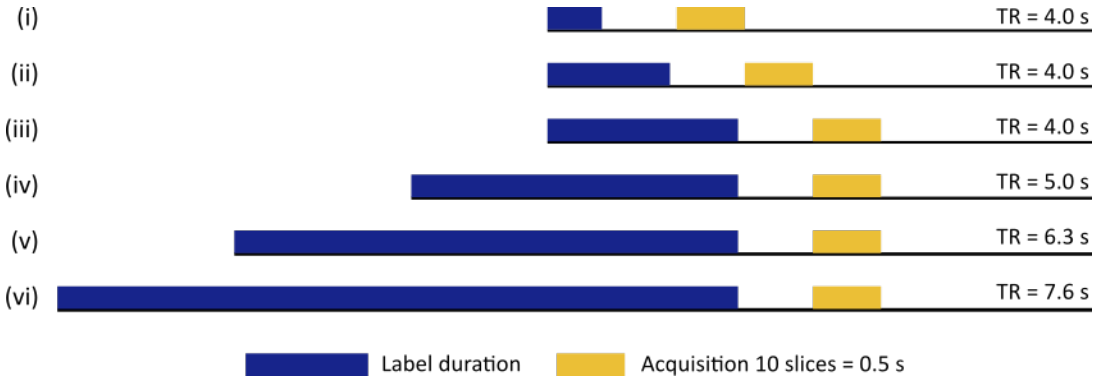

Figure 3.4 MP-pCASL MRI sequence at varying label durations. Schematic of increasing label durations of MP-pCASL MRI from 0.4 s (i), to 0.9 s (ii), 1.4 s (iii), 2.4 s (iv), 3.7 s (v) and 5.0 s (vi) with an increase in TR to allow sufficient T_1 recovery. A post-label delay of 550 ms is assumed between the label duration and image acquisition here.

The MP-pCASL MRI imaging region consisted of ten 1 mm thick slices with an axial orientation acquired in an anterior-posterior direction and starting at a position 1 mm behind the sulcus of the olfactory bulbs in the brain. This region was selected to cover the striatum of the rat brain as it is the location of choice for intracerebral injections in most rodent brain tumour models (Candolfi *et al.*, 2007; Garcia *et al.*, 2014; Serres *et al.*, 2014).

Multi-post-label delay (PLD) MP-pCASL MRI was performed in SD, Wistar and BDIX rats to determine the blood arrival time to the rat brain using 12 PLDs ranging from 10 ms to 1000 ms, to obtain blood arrival time maps (PLDs = 10, 15, 20, 25, 30, 50, 100, 200, 300, 500, 750, 1000 ms; T_{exp} = 14 min 41 s). Since image acquisition takes 50 ms per 2D MRI slice, only the anterior and posterior slices of the standard 10 slice imaging volume were selected for blood arrival time determination. Additionally, the posterior slice of the brain was acquired prior to the anterior slice to account for the shorter travel time and earlier arrival of blood to this slice.

Finally, MP-pCASL MRI was performed using a multi-slice spin-echo EPI readout with a FOV of 32 × 32 mm and a 64 × 64 matrix, giving an in-plane resolution of 500 × 500 µm, and a TE of 28.7 ms. Proton-density calibration images with the same parameters as described above were acquired for absolute quantitation of CBF, for all rats, by omitting labelling pulses and using both the surface receive array (1 average; 31 s) and the volume coil (8 averages; 4 min 4 s) and using a TR of 7.6 s. Apparent CBF measurements were calculated as described in 3.3.3.2 using an in-house built code[1] calling the FSL tool 'fabber' (Chappell *et al.*, 2009), Quantiphyse for supervoxel generation (Irving *et al.*, 2016) and a custom version of BASIL for oxford_asl (Chappell *et al.*, 2009; Groves, Chappell and Woolrich, 2009), both available through the FMRIB Software Library.

3.2.4.2 Background suppression MP-pCASL MRI

Selection of the static tissue selective saturation and inversion times was determined with an assumed tissue T_1 relaxation time of 1.5 s and with the following equation for

[1] Code built by Dr. James Larkin and myself.

magnetisation according to longitudinal recovery time. For tissue T_1 saturation, the magnetisation can be determined using

$$M = M_0 \left(1 - e^{-\frac{t}{T_1}}\right) \ , \tag{3.3}$$

where M is the magnetisation at time t, M_0 is the initial magnetisation of 1, and T_1, in this case, is the T_1 relaxation time of our static tissue (1.5 s). For tissue T_1 inversions, the magnetisation can be determined using equation 2.2. The factor of 2 in this equation comes from the complete inversion of M_0 to a net magnetisation of -1, instead of the net magnetisation of 0 in the case of a saturation.

These equations were used to minimise the signal of static tissue in the brain and, thus, to increase the MP-pCASL MRI signal during single-slice and multi-slice imaging by first saturating the brain tissue at the imaging region and then through a series of inversions (Figure 3.5). The initial saturation at the imaging region was performed at the beginning of the scan, followed by slice selective inversions at 1.0 s, 2.4 s and 2.95 s; directly on either side of the MP-pCASL MRI labelling (1.4 s, starting 1 s after scan initiation) and following the PLD (550 ms) immediately prior to either a single- or multi-slice acquisition.

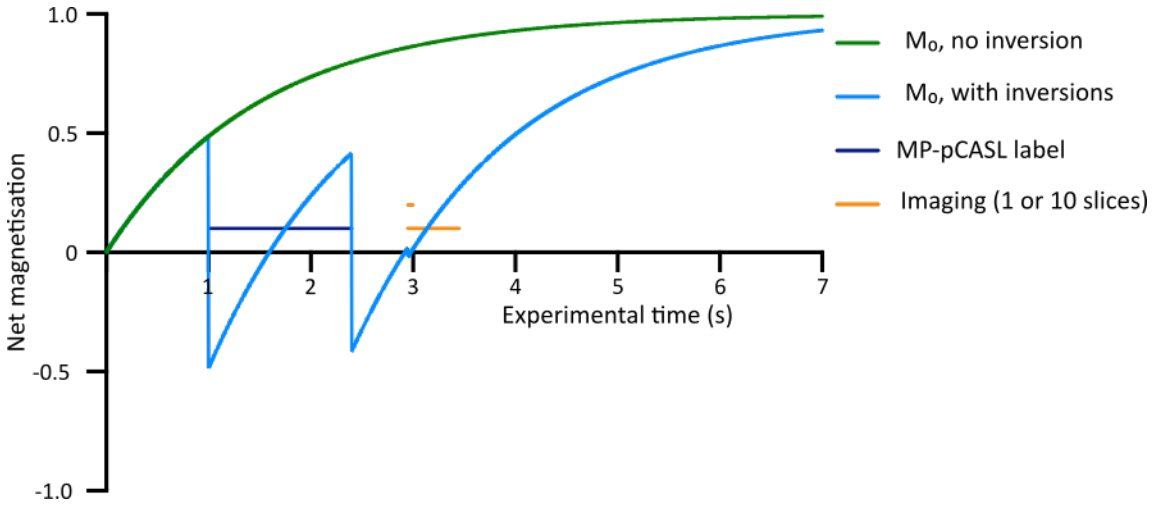

Figure 3.5 Schematic of background suppression in MP-pCASL MRI. Schematic of net magnetisation of static tissue with a T_1 relaxation time of 1.5 s following saturation and inversions at the imaging region to achieve background suppression (blue curve). A saturation at time 0 s is followed by selected inversions at 1.0 s, 2.4 s and 2.95 s before single or multi-slice MP-pCASL MRI acquisition. MP-pCASL MRI label begins 1.0 s after the initial saturation and is not interrupted by inversions.

3.2.4.3 Label-control pCASL MRI

MP-pCASL MRI and traditional label-control pCASL MRI were compared by acquiring MP-pCASL MRI data and extracting the first and fifth phases, corresponding to the 180˚ and 0˚ of traditional label-control pCASL MRI. These phases were averaged through 4 separate MP-pCASL MRI acquisitions for fair comparison to a one-average MP-pCASL MRI acquisition, to have an equivalent experimental time. CBF quantitation from label-control images was determined using the voxel-wise calculation recommended in the white paper (Alsop *et al.*, 2014),

$$CBF = \frac{6000 \cdot \lambda \cdot (SI_{control} - SI_{label}) \cdot e^{\frac{PLD}{T_{1,blood}}}}{2 \cdot \alpha \cdot T_{1,blood} \cdot SI_{PD,Str} \cdot \left(1 - e^{-\frac{\tau}{T_{1,blood}}}\right)}, \quad (3.4)$$

where λ is the brain/blood partition coefficient of water (0.9 mL/g) (Herscovitch and Raichle, 1985), $SI_{control}$ and SI_{label} are the signal intensities of the control and label images,

α is the inversion efficiency for pCASL MRI (0.85) (Dai *et al.*, 2008), $SI_{PD,Str}$ is the mean signal intensity of the striatum in the proton density-weighted reference image without labelling pulses, and τ is the label duration.

3.2.4.4 Time of flight angiography

Time of flight (TOF) angiography was used to visualise the location and geometry of the vessels in the neck and head. This sequence was developed by the Pre-Clinical Imaging Scientific Research Facility of the Department of Oncology at the University of Oxford. The imaging readout is a T_1-weighted 3D gradient echo with a FOV = 40 × 40 × 60 mm and a matrix = 128 × 128 × 192, giving an isotropic resolution of 313 × 313 × 313 µm, TR = 30 ms, flip angle (FA) of 30˚ and an axial excitation slab for a T_{exp} = 12 min 17 s. The acquired 3D volume was processed with Fiji (Schindelin *et al.*, 2012) to obtain a maximal-intensity projection along the left-right axis in order to visualise all rat head vessels simultaneously.

3.2.4.5 Anatomical MRI

Routine sagittal scans for label plane positioning were acquired using a T_2-weighted fast spin-echo readout at a single 2 mm slice at the brain midline using FOV = 50 × 50 mm, data matrix = 256 × 256, TR = 1 s, TE_{eff} = 40 ms and T_{exp} = 34 s. High resolution sagittal scans were acquired with FOV = 40 × 60 mm, matrix = 128 × 192, TE_{eff} = 10 ms and T_{exp} = 2 min 8 s.

3.2.4.6 Relaxometry of rat brain tissue and blood

Relaxometry of rat brain tissue was performed in living rats, whereas rat blood relaxometry values were obtained from post-mortem anti-coagulated blood of a female Wistar rat re-oxygenated in a 15 mL falcon tube with oxygen and heated to 37 ˚C using a heated water jacket sample holder to maintain the temperature. Oxygenation of the blood was confirmed as complete using an i-STAT blood-gas analyser with a G3+ cartridge (Table 3.1; Abbott, Maidenhead, UK). For rat brains and blood, T_1 and T_2 relaxation times were obtained as described in section 2.3.6.

Table 3.1 Blood gas analysis results from i-STAT G3+ cartridge.

Parameter	*Value*
pH	7.88
Partial pressure of carbon dioxide (pCO_2)	1.41 kPa
Partial pressure of oxygen (pO_2)	37.7 kPa
Base excess in extracellular fluid compartment (BEEcf)	3 mmol/L
Concentration of bicarbonate (HCO_3)	19.7 mmol/L
Concentration of total carbon dioxide (TCO_2)	20 mmol/L
Saturation of oxygen (sO_2)	100 %

3.2.4.7 Calculation of signal-to-noise ratio (SNR)

The SNR can be calculated using

$$SNR = 0.655 \cdot \frac{SI}{\sigma} \ , \tag{3.5}$$

where *SI* is the signal intensity of a region or interest (ROI) and σ is the standard deviation of the noise. The 0.655 factor takes into account the Rician distribution of the noise,

because the noise variation is only represented in positive values, which artificially reduces σ (Gudbjartsson and Patz, 2018).

3.2.4.8 Regions of interest in the brain

Regions of interest (ROI) in the brain were segmented in ITK-SNAP (Yushkevich *et al.*, 2006) on spin-echo EPI images for the whole brain, striatum and cortex in all naïve rats used. These segmentations were applied to CBF and relaxometry maps to obtain relevant values.

3.2.5 [^{14}C]-Iodoantipyrine autoradiography

Quantitative CBF was determined autoradiography in 3 rats of each of the three strains studied using gold-standard [^{14}C]-iodoantipyrine autoradiography ([^{14}C]-IAP AR), either directly after MP-pCASL MRI or less than 24 hours after MRI. Rats were anaesthetised with 3 % isoflurane in a 10 % oxygen and 90 % air gas mixture or maintained under anaesthesia if taken straight from the MRI and laid in a supine position. The tail vein was first cannulated using an in-house built 27 gauge cannula connected to a saline filled syringe. A small incision of about 1 cm was made before the left hind leg using a cautery iron (Accu-Temp®, BVI Medical, Abingdon, UK) and the femoral vein was isolated and cannulated using saline-filled 0.4 mm internal diameter polyethylene tubing (Fischer Scientific, UK) fixed to a 25 gauge needle on a 1 mL syringe. The femoral vein cannulation was secured by two independent threads on the vessel and with cyanoacrylate tissue glue (Loctite, Düsseldorf, Germany). The tubing was further secured along the left hind leg with two sutures. The right femoral artery was then cannulated by the same procedure.

Once both the rat femoral vein and artery were cannulated, 4[N-methyl-^{14}C]-iodoantipyrine ([^{14}C]-IAP; 0.1 mCi/mL; specific activity = 55 mCi/mmol; Hartmann Analytics, Germany) was infused into the femoral vein at a linear continuous rate of 0.5 mL/min (the dead volume of the femoral vein cannula, which leads to delayed arrival of the [^{14}C]-IAP to the vein, was taken into account). Arterial blood was removed from the rat through the femoral artery cannula as [^{14}C]-IAP was being introduced into the bloodstream to maintain a constant blood volume in the rat. The rat was killed by intravenous pentobarbitone overdose through the tail vein, immediately decapitated and the head frozen in isopentane (Fischer Scientific, UK) on dry ice. The rat head was stored at -80 ˚C. The brain was removed from the head at -20 ˚C prior to sectioning of the brain at a 20 µm thickness using a Leica CM1950 cryostat (Leica, UK). Brain sections at 200 µm intervals were dried at 60 ˚C for 10 min and then exposed to Carestream® Kodak® Biomax® MR Film (Sigma-Aldrich, UK) along with carbon-14 standards (0-35 µCi/g; Hartmann Analytics, Germany) for 72 hours in a dark cassette before being developed (Xograph Compact x4 X-ray film processor, Stonehouse, UK). Developed autoradiograph films were scanned using the Epson Expression 10000 XL transmittance scanner (Epson, UK) at a resolution of 2400 pixels/inch. Each film was scanned 3 times and those scans averaged to account for acquisition noise. Background signal was determined by averaging eight areas of the background and subtracting it from the image in Fiji (Schindelin *et al.*, 2012). Then, autoradiographs were calibrated to the standards using the Fiji 'Calibrate' function, fitting to an exponential curve and omitting standards that were over-exposed. Conversion to absolute CBF values was performed using the following equation,

$$C_i(T) = \lambda K \int_0^T C_A e^{-K(T-t)}\, dt \ , \tag{3.6}$$

where C_i is the concentration of the tracer at final time (*T*), λ is the tissue:blood partition coefficient, C_A is the concentration of the tracer in the artery at time *t*, and *K* is a constant that incorporated blood flow into the tissue with

$$K = \frac{m \cdot F}{W \cdot \lambda} \ , \tag{3.7}$$

where *m* is the diffusion equilibrium between blood and tissue (assumed to be 1), and *F/W* is the flow of blood per unit mass (Reivich *et al.*, 1969).

From equation 3.6, C_i can be found in the calibrated brain autoradiographs, and λ is of 0.8 for [^{14}C]-IAP as determined by Sakurada and colleagues (Sakurada *et al.*, 1978). C_A can also be determined based on the linear accumulation of [^{14}C]-IAP in the blood assuming a total blood volume dependent on body weight of 78.4 mL/kg in SD rats (Probst *et al.*, 2006) and of 62 mL/kg for BDIX rats as an estimate of blood volume, since no strain specific blood volume value was found; thus, the median of estimated rat blood volume was used. In Wistar rats, the blood volume was determined according to Lee and Blaufox (Lee and Blaufox, 1985) to be *BV = 0.06 x BW + 0.77*, where *BV* is the blood volume of the rat in mL and *BW* is the body weight in kg. With this information, equation 3.6 can now be simplified:

$$C_A(t) = At \ , \tag{3.8}$$

$$C_i(T) = \lambda K \int_0^T At \cdot e^{-K(T-t)}\, dt \ , \tag{3.9}$$

$$C_i(T) = \lambda KA \int_0^T t \cdot e^{-KT} \cdot e^{Kt}\, dt \ , \tag{3.10}$$

$$C_i(T) = \lambda KA \cdot e^{-KT} \int_0^T t \cdot e^{Kt}\, dt \ , \tag{3.11}$$

$$C_i(T) = \lambda A \cdot \left(1 - \frac{1}{K} + \frac{1}{K} e^{-K}\right) \ . \qquad (3.12)$$

Equation 3.12, was solved numerically to obtain CBF values for each calibrated pixel in the brain autoradiographs. Finally, autoradiographs were aligned with respective MP-pCASL MRI CBF maps using a manual perspective transform for individual slices. Finally, MR-resolution autoradiography-derived maps of CBF were constructed for easier comparison. Whole brain, cortex and striatum segmentations, initially drawn on MRI images, were used to determine blood flow in each region as found by autoradiography.

3.3 Results

3.3.1 Considerations prior to starting pCASL MRI

3.3.1.1 Bloch simulations of MP-pCASL MRI

Simulations of the Bloch equations were used to determine the magnetisation of protons at specific times based on the longitudinal (T_1) and transverse (T_2) relaxations of the signal. These simulations can be used to determine the optimal MP-pCASL MRI parameters for labelling the inflowing rat blood using a 9.4 T. To use these equations, several parameters first needed to be determined, either specific to the MP-pCASL MRI sequence or to the three strains of rats used in this study (blood velocity in the neck and T_1 and T_2 relaxation times of rat arterial blood).

3.3.1.1.1 Sequence of MP-pCASL MRI

The Bloch simulations are dependent upon sequence specific information such as the RF pulse duration, 600 µs, the RF separation, 1200 µs, and the RF pulse shape, Hanning (sequence shown in Figure 3.6B). Additionally, the gradient amplitude (G_{amp}) and mean gradient in the *z* direction (20-fold lower as per the sequence) were varied to determine the optimal pCASL MRI parameters.

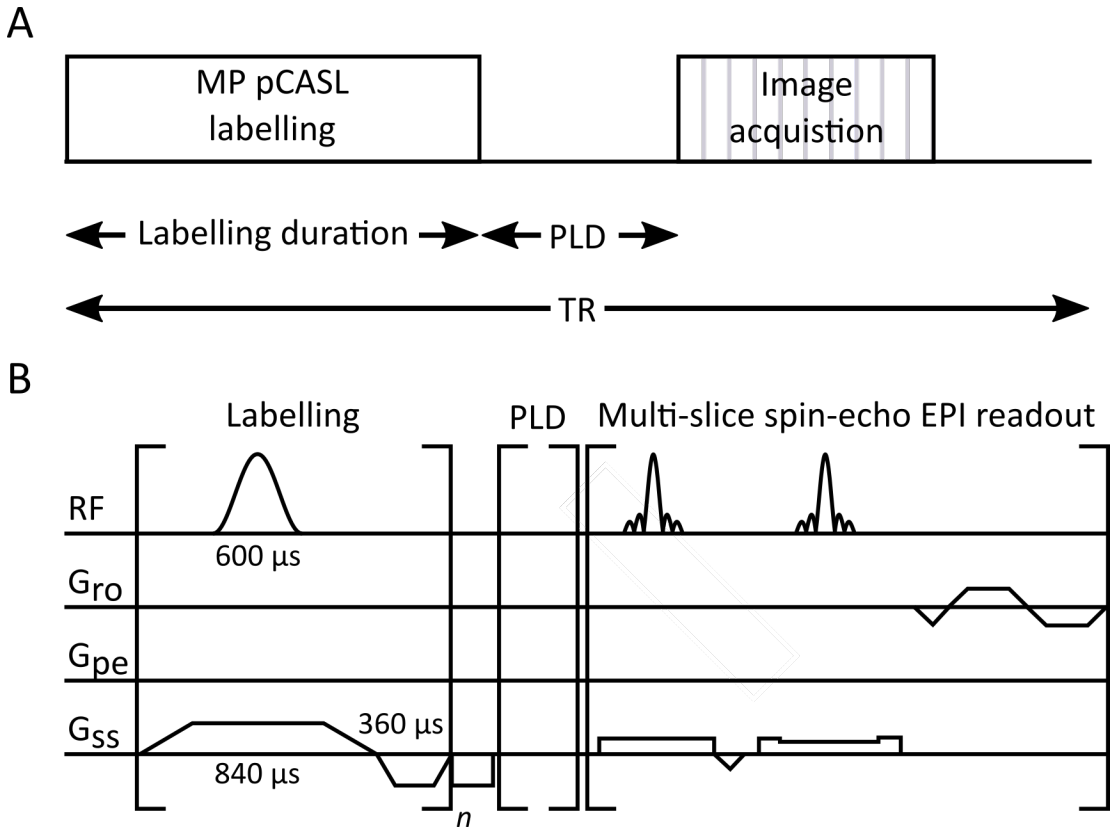

Figure 3.6 Pulse sequence of MP-pCASL MRI. **A** Schematic of the MP-pCASL MRI pulse sequence components. **B** MP-pCASL MRI pulse sequence with RF and gradient information (RF: radiofrequency; G_{ro}: readout gradient; G_{pe}: phase encoding gradient; G_{ss}: slice selective gradient). This figure was modified from the JCBFM publication arising from the work performed in this chapter (Larkin, Simard *et al.*, 2018).

3.3.1.1.2 Blood velocity in the carotid artery

The mean carotid blood velocity as measured by Power Doppler ultrasound was highest in SD rats, 47.4 ± 7.5 cm/s, compared to Wistar and BDIX rats, 35.3 ± 7.0 cm/s and 30.3 ± 4.6 cm/s, respectively (Figure 3.7A). Peak velocity, corresponding to minimum inversion efficiency, was 146.5 ± 22.8 cm/s in SD, 112.9 ± 11.5 cm/s in Wistar and 82.2 ± 10.1 cm/s in BDIX. Anaesthetic depth, corresponding to a breath rate of 40 breaths per minute (bpm) at the deepest anaesthetic depth and 65 bpm at the lightest, did not significantly affect the carotid blood velocity in SD or Wistar rats (slopes of -0.24 and 0.20, respectively; Figure 3.7B). However, in BDIX rats, carotid blood velocity increased with

respiration rate and when fit with a linear regression, possessed a slope statistically significantly different to zero (slope of 0.29; $p = 0.0078$).

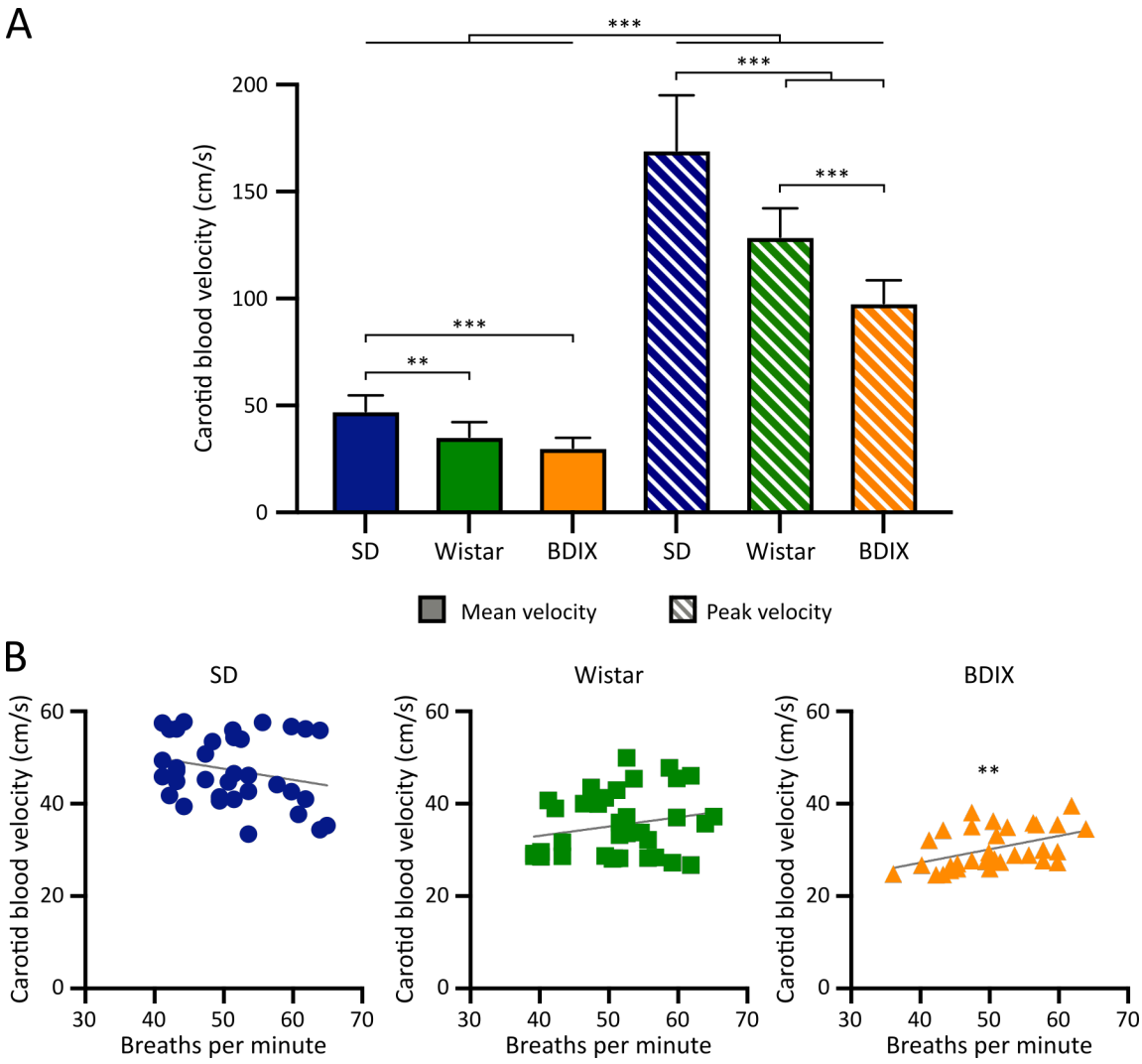

Figure 3.7 Carotid blood velocity in naïve rat strains. **A** Mean and peak carotid blood velocities in three strains of rat ($n = 3$ rats per strain, 10-12 measurements per rat; one-way ANOVA with Tukey's multiple comparisons, ** $p < 0.01$, *** $p < 0.001$; error bars represent standard deviation from the mean). **B** Mean carotid velocity as a function of anaesthetic depth represented by breathing rate with linear regression (grey line; SD, $n = 35$; Wistar, $n = 35$; BDIX, $n = 32$).

3.3.1.1.3 Rat blood relaxometry

A good estimate of oxygenated rat blood relaxometry values is crucial for the Bloch simulations as it will determine the relaxation times of our labelled blood water protons

as they move to the brain and exchange with tissue water protons. Relaxometry MRI on oxygenated Wistar rat blood at 37 ˚C was performed and using voxel-wise fitting analysis, a T_1 relaxation time of 2.10 ± 0.02 s and a T_2 relaxation time of 33.15 ± 0.026 ms were calculated (Figure 3.8).

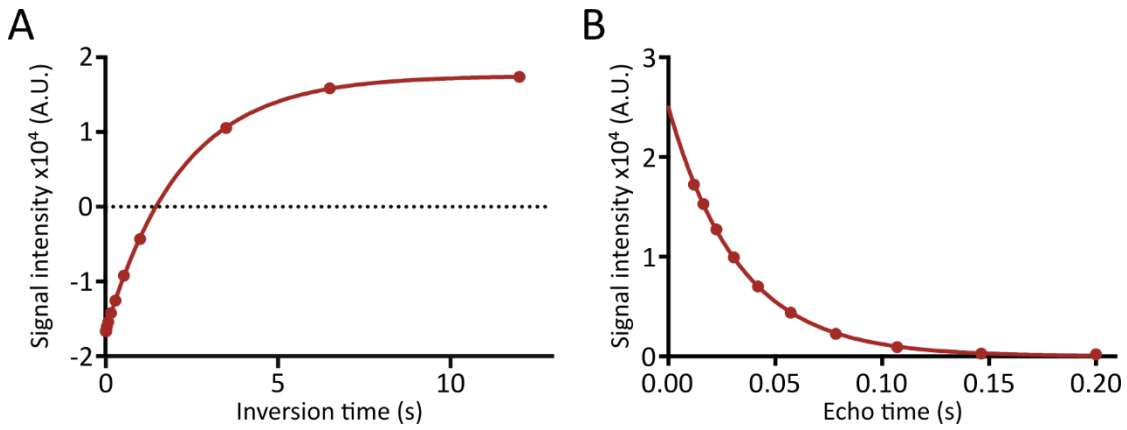

Figure 3.8 Relaxometry of oxygenated rat blood at 37 ˚C at 9.4 T. T_1 (**A**) and T_2 (**B**) relaxation over time of oxygenated rat blood at 37 ˚C from a female Wistar rat.

3.3.1.1.4 Bloch simulations

Bloch simulations were performed, using the input parameters of Table 3.2 with varying flip angle for adiabatic inversion (RF_{amp}), labelling plane thickness (G_{amp}) and blood velocity. Labelling efficiency varied as a function of these three parameters and this relationship is shown in Figure 3.9A for a blood velocity of 37 cm/s, chosen as the mean blood velocity for SD, Wistar and BDIX rats (n = 3 per strain). The inversion efficiency was not significantly altered between the mean blood velocities of the three rat strains studied; 75.3 %, 84.5 % and 86.9 % for SD, Wistar and BDIX rats, respectively (Figure 3.9B). Based on these results, a flip angle of 40˚ was selected for the adiabatic inversions and a labelling plane thickness of 6.2 mm was chosen, corresponding to an RF_{amp} of 4 µT and a G_{amp} of 4.4 µT/m. This yielded an inversion efficiency of 82.2 % at 37 cm/s.

Table 3.2 Bloch simulation input parameters.

Parameter	Value(s)
RF pulse duration	600 µs
RF pulse separation	1200 µs
RF pulse shape	Hanning
Flip angle (RF_{amp})	1˚-90˚ in 1˚ steps (0.1-7.4 µT)
Labelling plane thickness (G_{amp})	0.1-10 mm in 0.1 mm steps (10-1 mT/m)
Mean G_Z	1/20 G_{amp}
Blood T_1 relaxation	2.10 s
Blood T_2 relaxation	33.15 ms
Blood velocity	1-100 cm/s in 1 cm/s steps

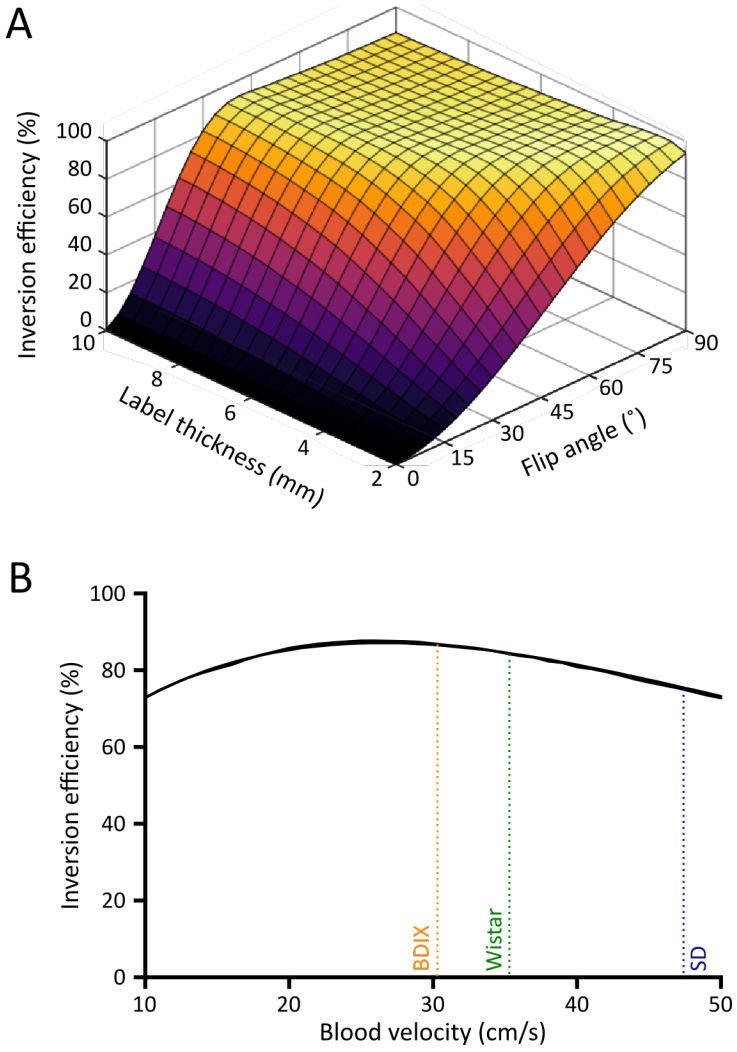

Figure 3.9 Inversion efficiency of multiphase pCASL MRI determined by Bloch simulations. **A** Bloch simulation results of theoretical labelling efficiency as a function of label thickness (G_{amp}) and flip angle (RF_{amp}) at a blood velocity of 37 cm/s (mean velocity from SD, Wistar and BDIX rats). **B** Theoretical inversion efficiency as a function of blood velocity for a flip angle of 40˚ and a labelling thickness of 6.2 mm. Mean velocity from each of the three strains of rats are indicated.

3.3.1.2 Effect of spin-echo echo-planar imaging parameters on SNR

As the MP-pCASL MRI method used here has a 2D SE-EPI readout approach, the effect of bandwidth and TE on the SNR of images was determined to optimise the readout approach. Both bandwidth and TE have an inverse relationship with SNR and should, therefore, be kept as low as possible (Figure 3.10). However, a narrow bandwidth is more likely to result in spatial distortions and an increased chemical shift. Furthermore, narrow bandwidths require longer TE, thus imaging time, and therefore a bandwidth of 250 kHz with a corresponding TE of 28 ms were selected for the spin echo EPI imaging readout of MP-pCASL MRI, resulting in an SNR of 72.8.

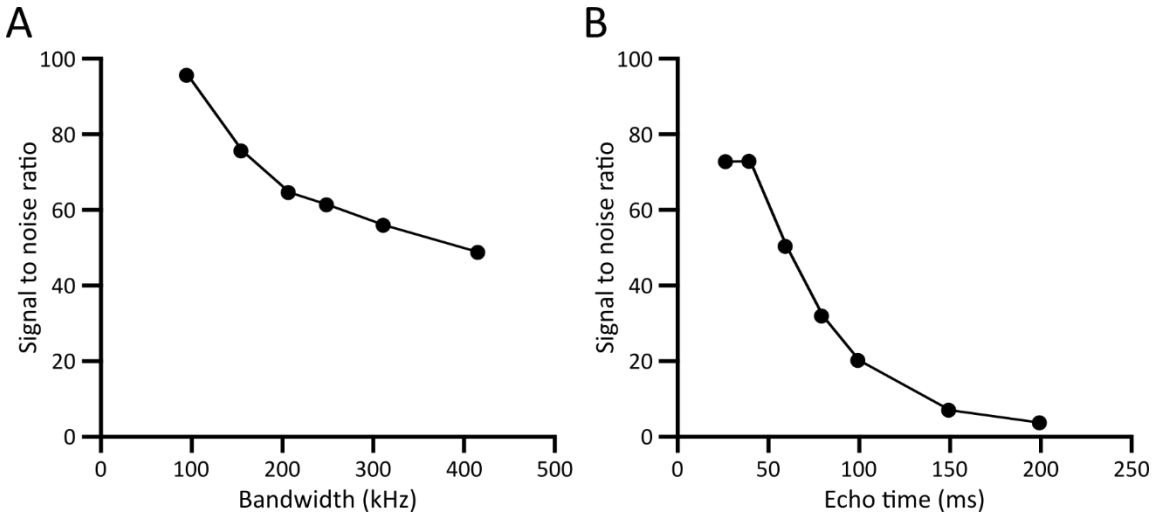

Figure 3.10 Selection of bandwidth and echo time at 9.4 T based on signal to noise ratio in EPI MRI. SNR as a function of bandwidth (**A**) and TE (**B**) for selection of EPI parameters for MP-pCASL MRI.

3.3.2 MP-pCASL MRI optimisation

3.3.2.1 Labelling plane position

The positioning of rodents in the scanner as well as the spatial anatomy of the brain feeding arteries differs to that of humans. Rats are typically placed in a prone position

during MRI with the head slightly raised and, therefore, the carotid and vertebral arteries in the neck are at an angle as shown by time-of-flight (TOF) angiography MRI in Figure 3.11. The angles of the arteries feeding the brain with respect to the frontal plane, as determined by TOF angiography MRI in all three strains of rats, were of $42 \pm 6^{\circ}$ for carotid arteries and $44 \pm 7^{\circ}$ for vertebral arteries. These angles were not significantly different between strains of rat or between smaller and larger rats. Since flow-driven adiabatic inversion is most efficient when the labelling plane is perpendicular to vessels, we compared the CBF values obtained using a parallel (0° angle) and a 45° angled labelling plane in three BDIX rats (Figure 3.11). The resulting CBF was significantly higher when using the 45° labelling plane and the variability of the CBF within the brain was significantly reduced (Figure 3.11F). For all subsequent MP-pCASL MRI acquisitions, the labelling plane was positioned at a 45° angle.

The position of this angled labelling plane along the neck could influence the measured CBF and will increase or delay the arterial transit time or arrival of the labelled blood to the brain tissue. Thus, the selection of a standard and optimal labelling plane location is recommended. A 0 mm reference position was defined at the last point at which the vertebral arteries are perpendicular to the labelling plane, as shown in Figure 3.11C. No significant difference was evident in CBF when comparing the all labelling plane positions between -6 mm and 0 mm (Figure 3.12). However, as the labelling plane moved further forward, it overlapped with the imaging plane and was no longer perpendicular to the vertebral arteries, resulting in an artificially decreased CBF in all rat strains studied. Since the notch behind the gracile fasciculus immediately rostral to the C1 vertebra is an easily identifiable anatomical marker and its position can be determined through a rapid

T_2-weighted anatomical scan, it was selected as the optimal position for the 6.2 mm thick 45˚-angled labelling plane in rats.

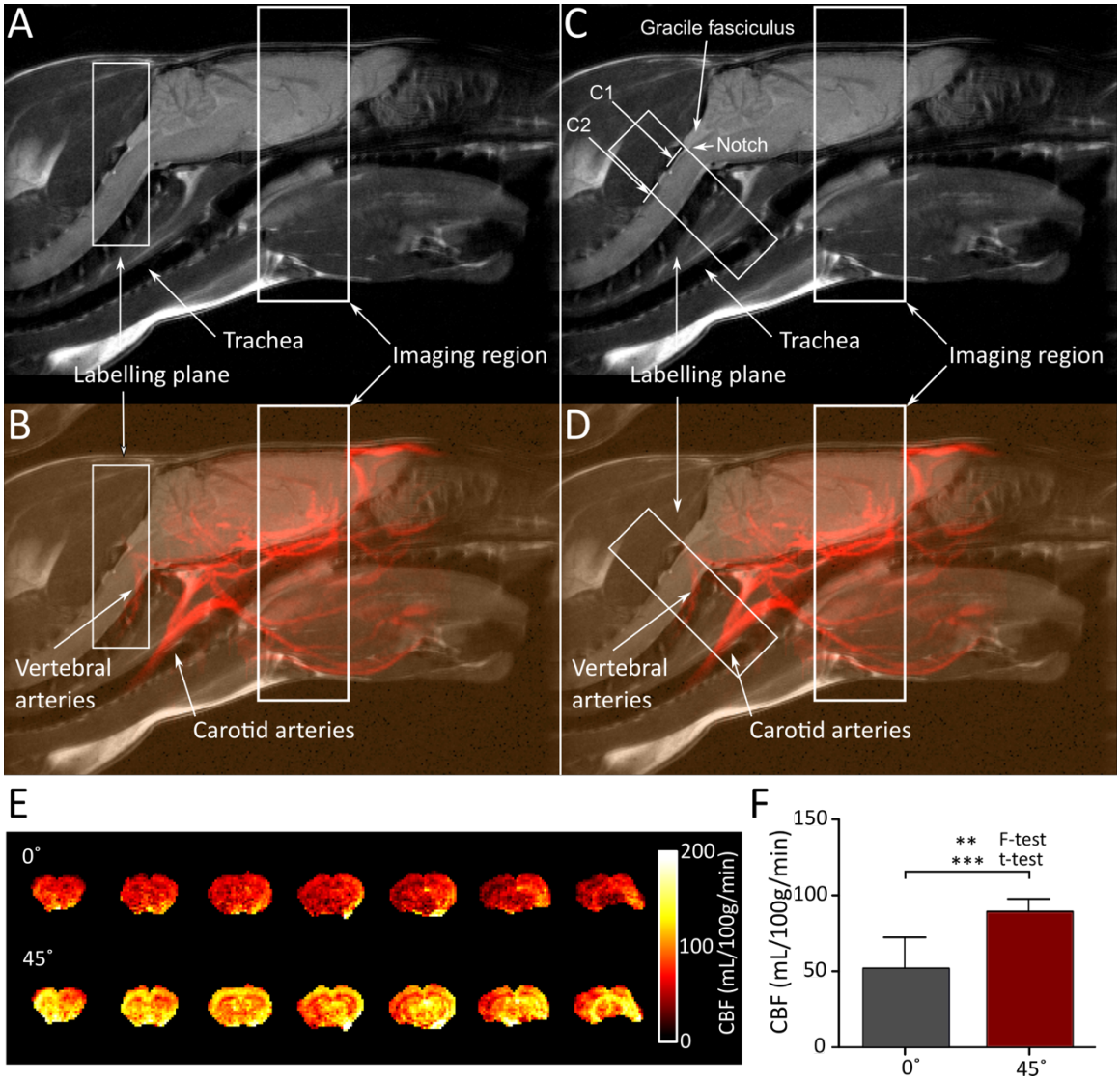

Figure 3.11 Angled labelling plane in MP-pCASL MRI leads to improved inversion and robust CBF output. **A, C** Sagittal T_2-weighted anatomical image of a rat head with location of the MP-pCASL imaging region and parallel (**A**) or angled labelling planes (**C**). Also highlighted in these images are a few anatomical features such as the trachea, gracile fasciculus and the C1 vertebra. **B, D** TOF angiography MRI showing larger vasculature in the rat head (SD) is superimposed onto the anatomical images from **A** and **C**. **E** Example CBF maps from four averages of MP-pCASL MRI from a BDIX rat with a labelling plane parallel to the imaging region (0˚) or at a 45˚ angle. **F** Apparent CBF quantitation for both straight and angled labelling planes (n = 3 BDIX rats; Student's t-test for CBF values, *** $p < 0.001$; F-test for variance, ** $p < 0.01$; error bars represent standard deviation from the mean).

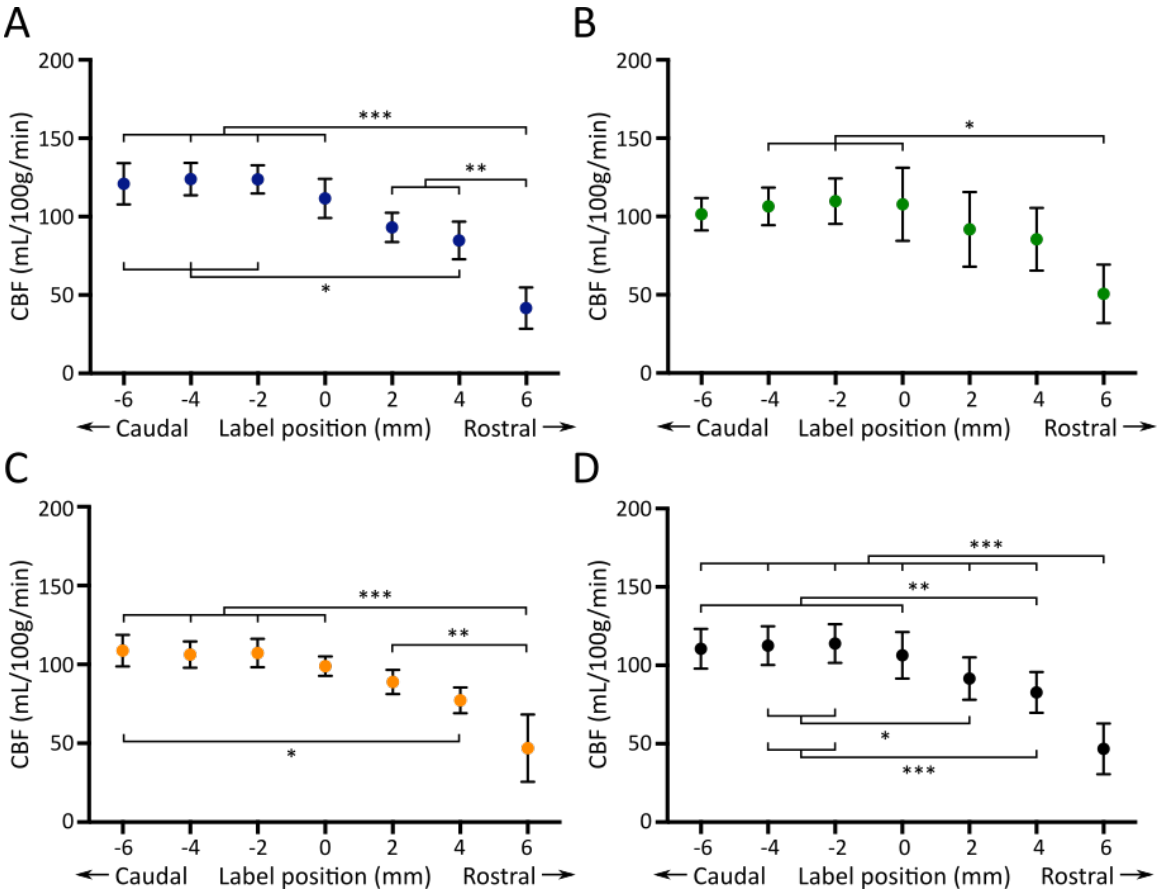

Figure 3.12 Effect of location of angled labelling plane in MP-pCASL MRI on rat CBF. Labelling plane location along the neck of SD (**A**), Wistar (**B**), and BDIX (**C**) rats ($n = 3$ per strain) or all rats combined (**D**). The 0 mm position is that of *Figure 3.11 B,D* with negative positions moving closer to the tail and positive positions closer to the nose (one-way ANOVA with Tukey's multiple comparisons, * $p < 0.05$, ** $p < 0.01$, *** $p < 0.001$; error bars represent standard deviation from the mean).

3.3.2.2 Duration of MP-pCASL MRI labelling

The duration of labelling in MP-pCASL MRI affects the amount of labelled blood present in the brain and, therefore, will influence the signal difference between the different phases in MP-pCASL MRI. Overall, the variation of label duration between 0.4 s and 5.0 s did not significantly affect the measured CBF in the different rat strains, except for the comparison of the smallest and two largest label durations in SD rats (Figure 3.13). The measured CBF resulting from label durations of 0.9 s to 5.0 s were consistent within each strain and when all rat strains were treated as a group.

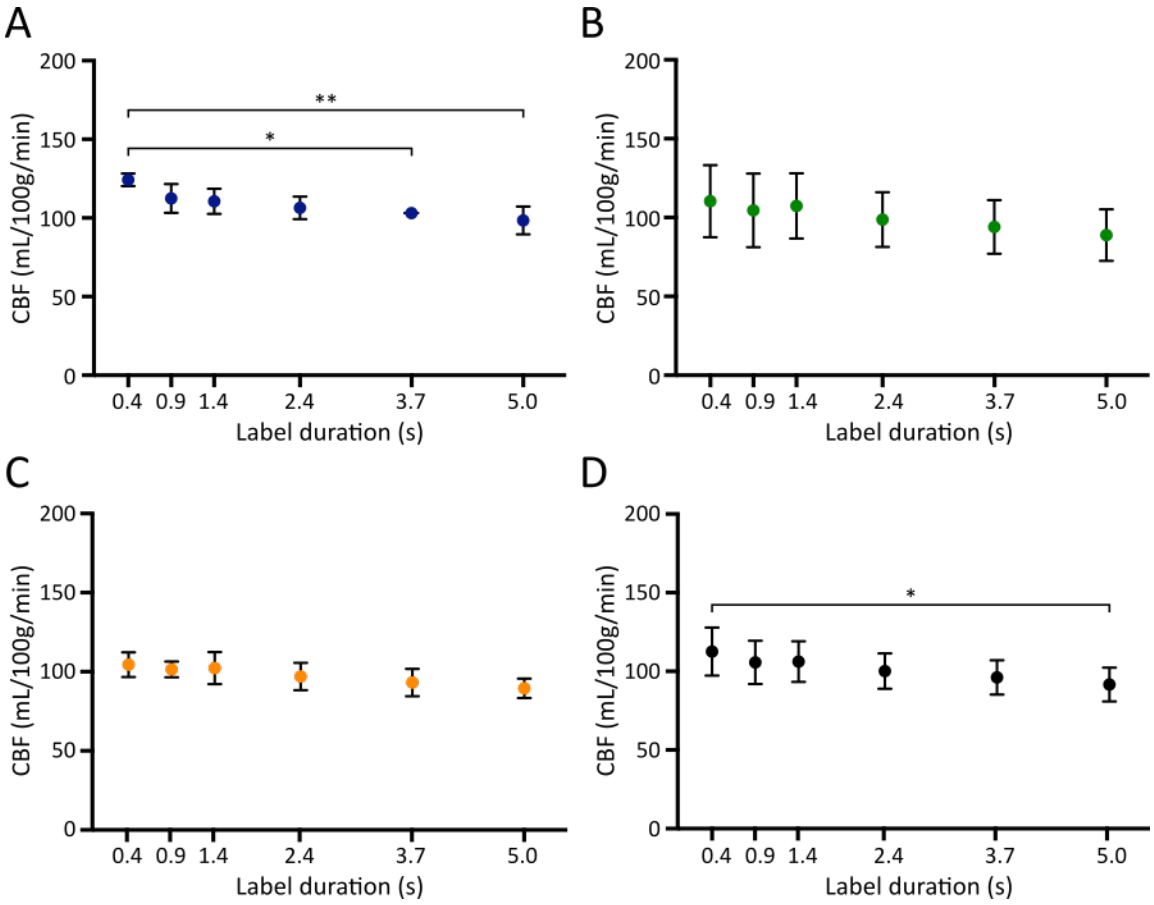

Figure 3.13 Effect of MP-pCASL MRI label duration on rat apparent CBF. Labelling duration of MP-pCASL MRI in SD (**A**), Wistar (**B**) and BDIX (**C**) rats (n = 3 per strain) or all rats combined (**D**; one-way ANOVA with Tukey's multiple comparisons, * $p < 0.05$, ** $p < 0.01$; error bars represent standard deviation from the mean).

Theoretically, the ASL MRI signal increases with longer label durations (Figure 3.14A), yet so does the experimental time owing to the increased TR at longer label durations (Figure 3.14B). In practice, imaging efficiency, defined by signal/(experimental time)$^{0.5}$, was affected by blood T_1 relaxation and outflow kinetics of the labelled protons. The incorporation of these factors results in a sharp increase in imaging efficiency between 0.4 s and 1.4 s, which then remains constant at longer label durations (Figure 3.14C). As the imaging efficiency plateau was evident from a label duration of 1.4 s, which has a shorter TR (Figure 3.14B), this label duration was selected to allow a shorter imaging time.

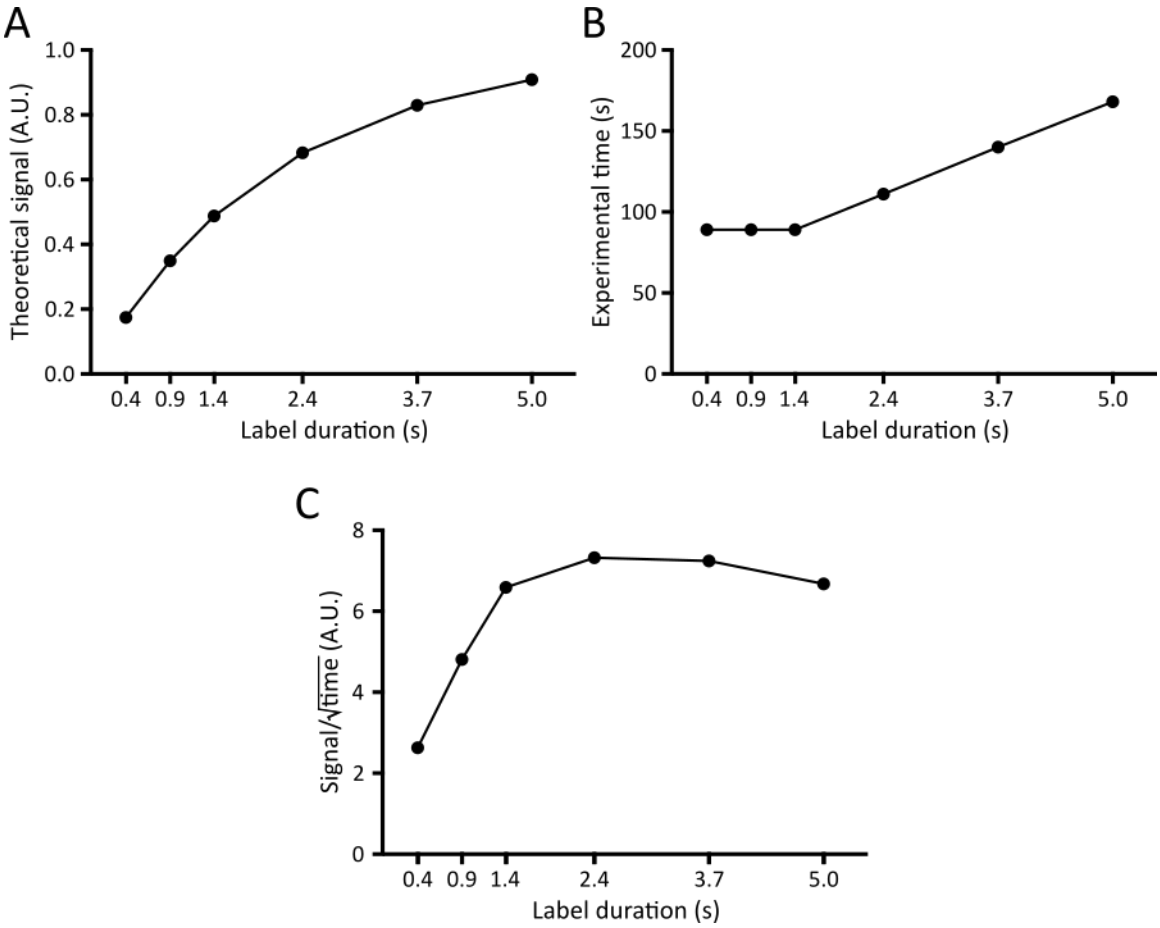

Figure 3.14 Imaging efficiency of MP-pCASL MRI according to label duration. Comparison between theoretical signal accumulation of MP-pCASL MRI as a function of increasing label durations including T_1 relaxation (**A**), the experimental time required for MP-pCASL MRI acquisitions at different label durations (**B**) and experimental MP-pCASL MRI signal over the square root of experimental time for increasing label durations (**C**).

3.3.2.3 Blood arrival time and selection of MP-pCASL MRI PLD

Optimal PLD selection in ASL MRI is essential for maximal signal variation during imaging. If a PLD is too short, the labelled blood will still be circulating in the brain vasculature during image acquisition, resulting in artificially increased CBF measurements. Conversely, if a PLD is too long, T_1 relaxation of the labelled blood will lead to loss of overall pCASL MRI signal and SNR reduction in an already low SNR MRI method. Multi-PLD MP-pCASL MRI (Figure 3.15A) performed in SD, Wistar and BDIX rats,

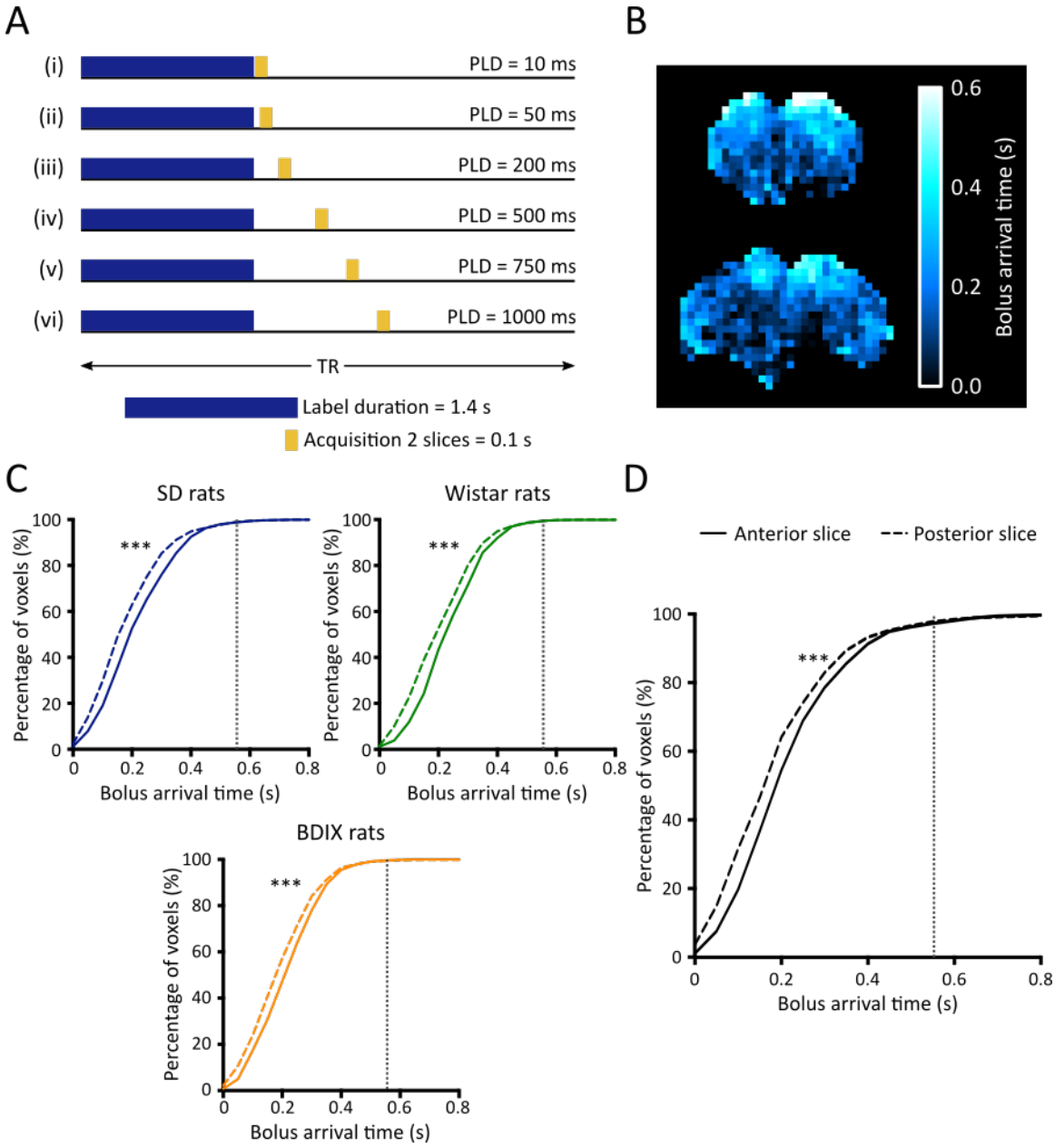

Figure 3.15 Labelled blood arrival time and selection of optimal post-label delay. **A** Schematic of MP-pCASL MRI sequence with six of the twelve PLDs used to determine blood arrival time to brain tissue. **B** Representative blood arrival maps to the anterior and posterior slices of the MRI imaging region of a BDIX rat. **C** Percentage of voxels with blood arrival over time for the anterior (full line) and posterior slices of the MP-pCASL imaging region in three strains of rats (SD, $n = 6$; Wistar, $n = 7$; BDIX, $n = 5$) and in all rats combined (**D**; Kolmogorov-Smirnov test, *** $p < 0.001$). Dotted vertical lines represent the PLD of 0.55 s, at which over 98 % of voxels from all rats combined had received labelled blood.

demonstrated that blood arrival in brain voxels occurred significantly earlier in the posterior slice compared to the anterior slice ($p < 0.001$, Kolmogorov-Smirnov test; Figure 3.15C). After 550 ms, blood arrival had taken place in > 98% of voxels from all rat brains

Figure 3.15D); > 98% in SD, > 99% in Wistar and > 99% in BDIX (Figure 3.15C). A PLD of 550 ms was selected for further MP-pCASL MRI acquisitions in naïve rats because labelled arterial blood transit had already occurred in most of the brain at this time.

3.3.2.4 Background suppression

The static brain tissue signal contribution is of little interest to ASL imaging, yet it accounts for most of the signal in the images acquired. Background suppression of this static brain tissue is recommended in clinical ASL MRI for 3D and single-slice 2D ASL MRI acquisitions (Alsop *et al.*, 2014). Background suppression in multi-slice acquisitions is not often performed as brain T_1 relaxation occurs in the delay between acquiring the first and last slices, which increases the static signal contribution over time, complicating the analysis. In our rat imaging, the MP-pCASL MRI signal variation between phases accounted for approximately 3 % of the signal in the image (Figure 3.16B). By performing a selective saturation followed by a series of inversions at the site of the imaging plane, the static tissue contribution to the imaging signal was reduced and the MP-pCASL MRI signal variation between phases in the image was increased to over 30 % in a single-slice 2D acquisition (Figure 3.16B). However, with a 2D imaging readout, relaxation of the static tissue occurs during the image acquisition (50 ms per MRI slice), meaning that the background tissue net magnetisation would be around 13-fold greater in the 10^{th} acquired slice compared to the first, for a tissue T_1 relaxation value of 1.5 s. Furthermore, although the MP-pCASL MRI signal variation between phases significantly increased with background suppression, a significant decrease in measured CBF was also observed – to unphysiologically low values for naïve rat brains (Figure 3.16D). Since the imaging readout

used in this chapter is a multi-slice 2D acquisition and, given the decrease in apparent CBF present in single-slice background suppressed MP-pCASL MRI, background suppression was not incorporated for further MP-pCASL MRI acquisitions.

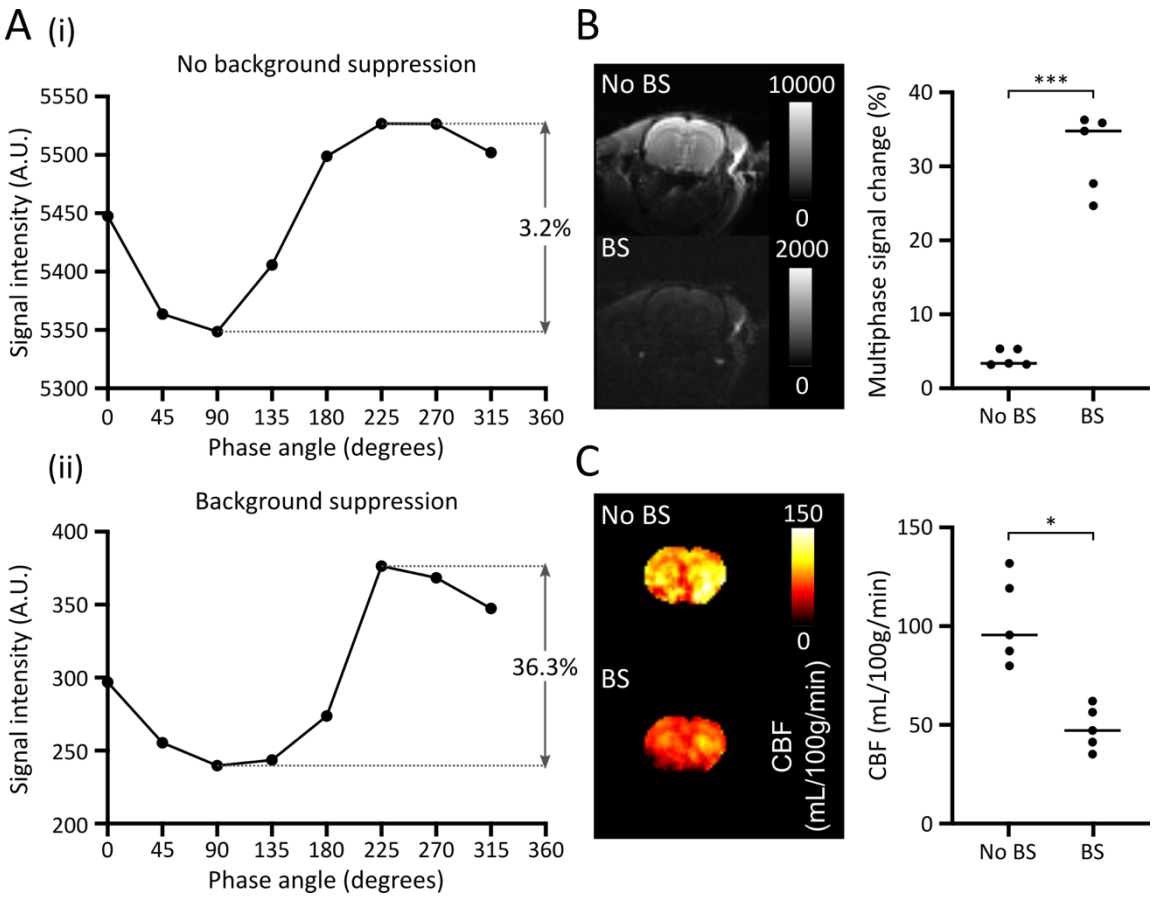

Figure 3.16 Background suppression in 2D MP-pCASL MRI. **A** Representative MP-pCASL MRI signal variation between phases in a single slice without (i) and with background suppression (ii). **B** Comparison of MP-pCASL MRI signal variation between phases in raw images without and with background suppression in single-slice MP-pCASL MRI (SD, $n = 3$; Wistar, $n = 2$; Student's paired t-test, *** $p < 0.001$). **C** Comparison of MP-pCASL MRI generated CBF maps and apparent CBF measurements in single-slice MP-pCASL MRI (SD, $n = 3$; Wistar, $n = 2$; Student's paired t-test, * $p < 0.05$).

3.3.3 Post-processing of MP-pCASL MRI

3.3.3.1 Selection of representative parameters for Fermi function

The multiphase acquisition data were fit to a modified Fermi function,

$$f(\phi) = Mag\left(-2\left[\frac{1}{1+e^{\frac{|\phi|-\alpha}{\beta}}}\right]\right) + Off \ , \qquad (3.15)$$

where ϕ is the phase angle in degrees, *Mag* is the magnitude (amplitude), *Off* is the offset from 0, and α an d β are parameters that will determine the shape and amplitude of the function. The best fit of MP-pCASL MRI data from SD, Wistar and BDIX rats (n = 7 per strain) to the Fermi function was determined to select the optimal α and β for naïve rat brain imaging (Figure 3.17A). Two rats were excluded based on an ambiguous fit for one and a Z-score > 5 for the other. The mean α and β of the remaining 19 rats were 68 ± 20 and 22 ± 9, respectively, with a mean R^2 of 0.91 ± 0.10. Of these, the 12 rats with an $R^2 > 0.90$ to the Fermi function yielded a statistically significant increase in precision of α and β ($p < 0.05$), compared to the original 19 rats, with $\alpha = 70 \pm 11$, $\beta = 19 \pm 4$ and a mean R^2 of 0.97 ± 0.02 (Figure 3.17B). These parameters were used for all future MP-pCASL MRI analysis.

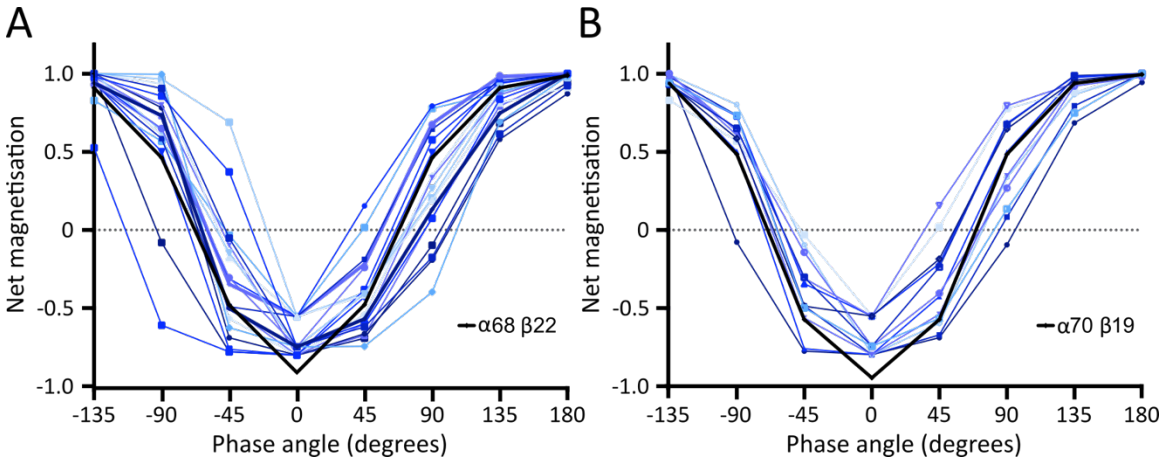

Figure 3.17 Selection of α and β in modified Fermi function for MP-pCASL MRI analysis. **A** Net magnetisation as a function of MP-pCASL MRI 8 labelling phases in 19 rats (SD, Wistar and BDIX, n = 7 per strain). α and β were determined from the best fit to the Fermi function for each rat. **B** Rats with $R^2 > 0.9$ (n = 12) to the Fermi function were averaged to obtain an optimal α and β of 70 and 19, respectively (black curve).

3.3.3.2 MP-pCASL MRI analysis

The acquired MP-pCASL MRI images were firstly fitted to the Fermi function, using the Variational Bayesian algorithm within the FSL tool 'fabber' in the FMRIB Software Library, to obtain the magnitude of the MP-pCASL MRI signal. This produced voxel-wise estimates for phase, magnitude and offset. However, at shorter label durations an overestimation of the magnitude may occur, owing to lower signal arising from the labelling of a smaller total blood volume than at longer label durations (Figure 3.14A). The resulting over-estimation of the magnitude leads to increased noise present in the images, which translates to abnormally increased apparent CBF measurements at shorter label durations. (Figure 3.18, red curve). However, the actual CBF does not change, yet its measurement across label durations is inconsistent. By clustering the raw phase maps using a supervoxel approach with four supervoxels (Irving *et al.*, 2016), a high-precision prior of phase in brain regions could be determined, which decreased the biological noise in the acquired images to provide more consistent CBF measurements (Figure 3.18).

Four supervoxels were chosen as there are four brain feeding arteries and a smoothing factor of 0.8 and compactness of 0.1 were selected based upon qualitative supervoxel organisation in the brain of 3 SD rats (Figure 3.19). The supervoxel ROIs could roughly represent the brain regions of where inflowing blood mainly originates from the right and left vertebral and carotid arteries, respectively.

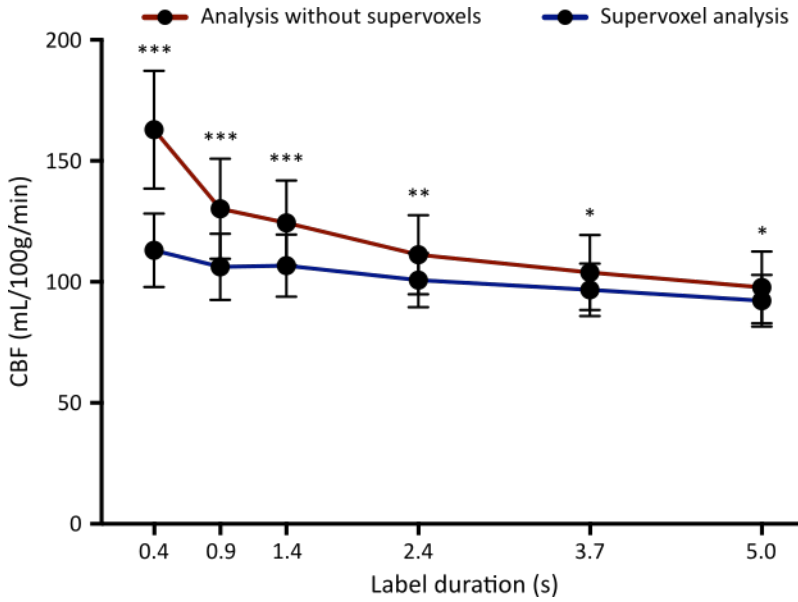

Figure 3.18 Supervoxel analysis improves CBF measurements. Comparison of MP-pCASL MRI analysis with (blue) and without supervoxel ROI phase priors in SD, Wistar, and BDIX rats (n = 9, 3 rats from each strain; Student's paired t-test, * $p < 0.05$, ** $p < 0.01$, *** $p < 0.001$, error bars represent standard deviation from the mean).

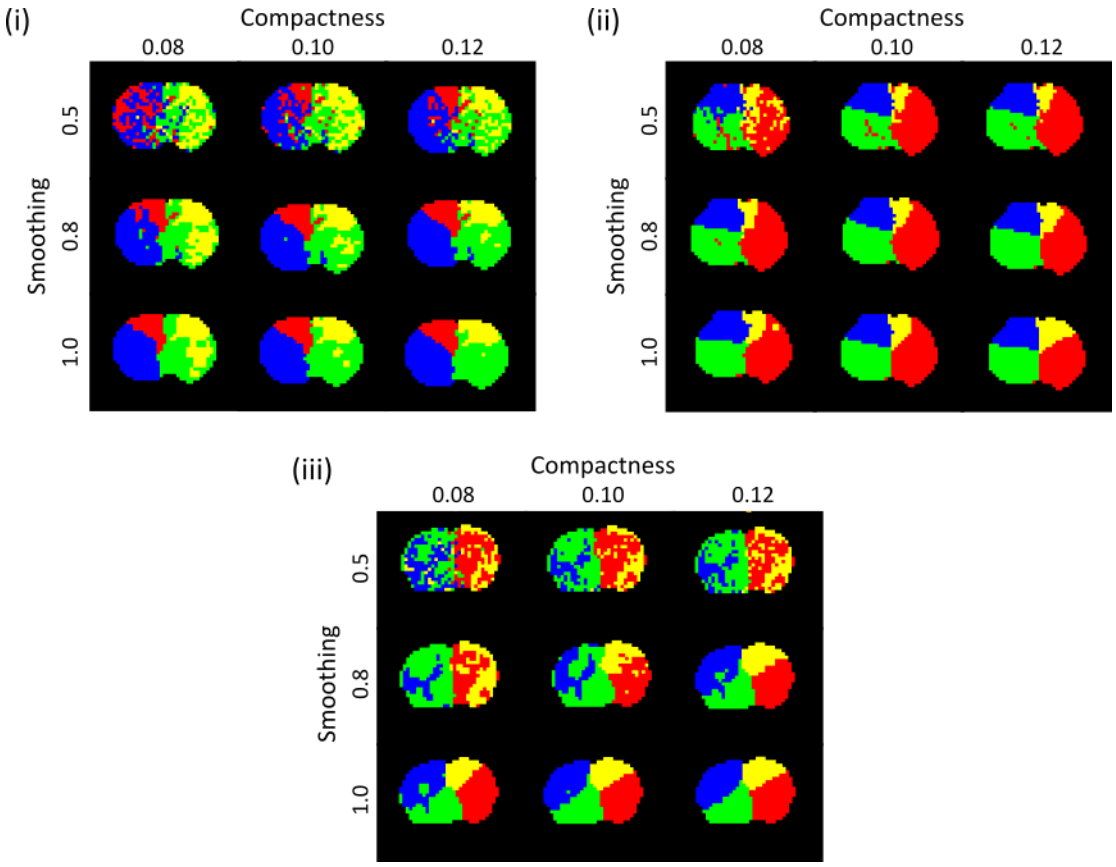

Figure 3.19 Supervoxel parameter selection for MP-pCASL MRI analysis. Variation of compactness and smoothing for selection of supervoxel parameters in SD rats (n = 3; I, ii, and iii, respecitvely).

For each supervoxel, the data from the original MP-pCASL MRI images were averaged for all voxels across each phase, providing a dataset with a higher SNR. This dataset was then fitted to the Fermi function a second time to obtain a phase prior map with a single optimal phase value for each of the four supervoxels. Finally, these phase values were used as high-precision priors for the final fitting of the original MP-pCASL MRI data to obtain voxel-wise maps of magnitude and offset. These maps are equivalent to the traditional label-control subtracted images and represent the presence of labelled water on a voxel-wise basis. These maps were processed with oxford_asl (part of the FMRIB Software Library (Chappell *et al.*, 2009; Groves, Chappell and Woolrich, 2009)) according to the one-compartment kinetic model of Buxton and colleagues (Buxton *et al.*, 1998) to generate relative CBF maps.

Next, these maps were corrected for coil sensitivity inhomogeneity, using the ratio of proton density images acquired with the surface receive array and the volume coil, respectively. Calibration of these maps to absolute CBF units was performed in oxford_asl using the striatum as a reference region M_0 value. The striatum was selected as an alternative to the clinically-used cerebral spinal fluid (CSF) since the latter possesses a small volume in rats, which would lead to partial volume effects in the few voxels containing CSF. The striatum T_1 and T_2 relaxation values of 1.47 ± 0.16 s and 40.4 ± 7.8 ms, respectively, used for the CBF quantitation were calculated from 20 rats; SD (n=7), Wistar (n=7), BDIX (n=6). A striatum-specific tissue:blood partition coefficient of 0.97 (Leithner *et al.*, 2010) of water and an inversion efficiency of 82.2 % determined from Bloch simulations in 3.3.1.1.4 were also used.

Finally, other relaxation parameters used for CBF quantitation were the T_1 and T_2 relaxation times of blood (3.3.1.1.3) and whole brain T_1 relaxation of 1.56 ± 0.25 s,

determined in the same 20 rats as for the striatal relaxation values. A simplified summary of this analysis is shown in Figure 3.20.

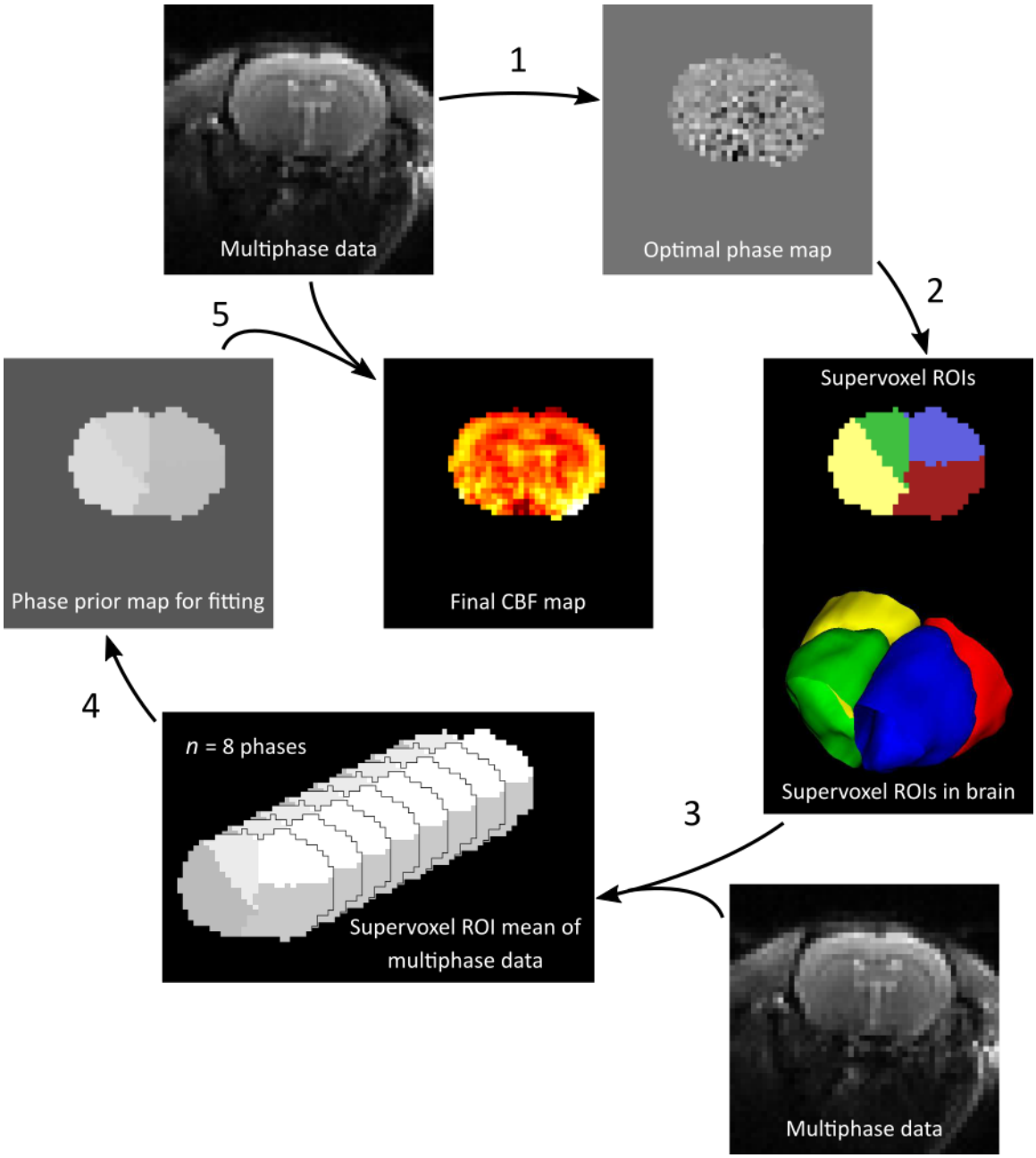

Figure 3.20 MP-pCASL MRI analysis pipeline. Briefly, raw MP-pCASL MRI data is fit to the Fermi function to yield a raw phase map (step 1), which is then smoothed and clustered to supervoxels (step 2). These supervoxel ROIs are applied to the raw MP-pCASL MRI data to obtain high SNR supervoxel ROI means of the data (step 3), which are fit once again to the Fermi function to yield a high precision phase map (step 4). This phase map is applied to the raw MP-pCASL MRI data to generate the final CBF maps (step 5).

3.3.3.2.1 Supervoxel phases offsets

The mean phases in the four supervoxels were compared between rats to determine whether they varied significantly based on specific rat anatomy and/or position within the scanner. This analysis demonstrated that the phase angle varied for each of the supervoxels (Figure 3.21A; $n = 21$ rats, 7 rats per strain). Moreover, while the phase offsets from the four supervoxels was similar in some rats, this was not observed in all animals (Figure 3.21B). The addition of supervoxel clustering to the MP-pCASL MRI analysis added 13.9 s to the total analysis; 8.6 ± 0.2 s for analysis without supervoxels and 22.5 ± 4.3 s ($n = 4$ cases each).

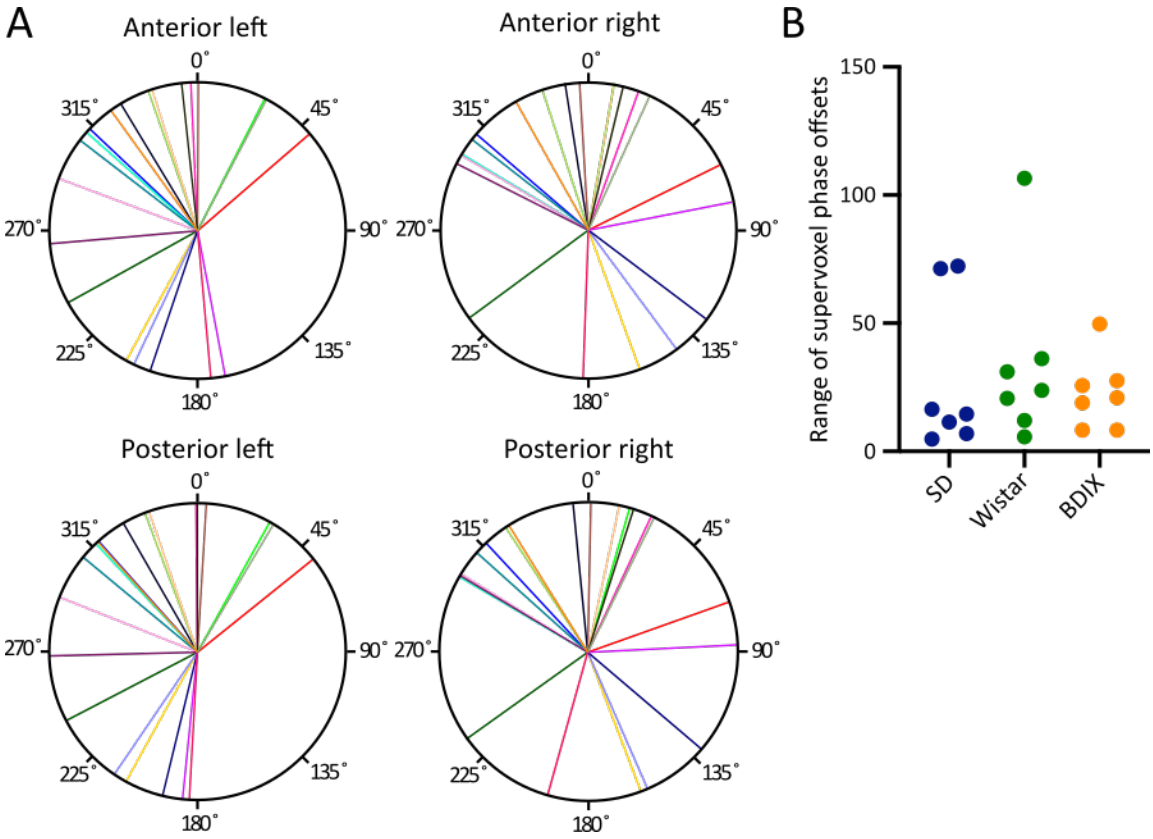

Figure 3.21 Optimal phase offsets in each supervoxel ROI in rats. **A** Phase offsets for all 21 rats in the study (SD, Wistar and BDIX, $n = 7$ per strain) in each of the four supervoxel ROIs. Each colour represents a different rat. **B** The range of supervoxel phase offsets present in each rat in the four rat strains studied. Each dot represents a different rat.

3.3.4 Comparison of MP-pCASL MRI to other CBF measurement methods

3.3.4.1 Traditional label-control pCASL MRI comparison

Representative label-control and MP-pCASL MRI CBF maps are shown in Figure 3.22. Label-control pCASL MRI and MP-pCASL MRI were performed in the 21 rats studied (SD, Wistar and BDIX, n = 7 per strain). Although the quality of the CBF maps was clearly greater in for the MP-pCASL MRI data, no significant differences were found in CBF quantitation between the two methods for either the cortex or striatum in the three strains of rat studied. However, a significantly lower measured CBF for the whole brain was found in SD and BDIX rats using label-control pCASL MRI, but not in Wistar rats (paired Student's t-test: SD, $p < 0.01$; BDIX, $p < 0.05$; Figure 3.23A).

The intra-brain inter-voxel coefficient of variation in CBF was 0.30 ± 0.06 in SD, 0.32 ± 0.04 in Wistar and 0.26 ± 0.06 in BDIX rats using MP-pCASL MRI, and 0.66 ± 0.13 in SD, 0.65 ± 0.11 in Wistar and 0.63 ± 0.10 in BDIX rats using label-control pCASL MRI analysis (Figure 3.23B). Thus, variance was significantly higher in SD, Wistar and BDIX rats for the label-control analysis (n = 7 rats per strain; $p < 0.001$). This variation and increased standard deviation to the mean brain CBF is present in the CBF maps of Figure 3.22, where the label-control CBF maps have regions of very low perfusion that were not observed in MP-pCASL MRI CBF maps. Whole brain CBF values from label-control pCASL MRI and MP-pCASL MRI are summarised in Table 3.3.

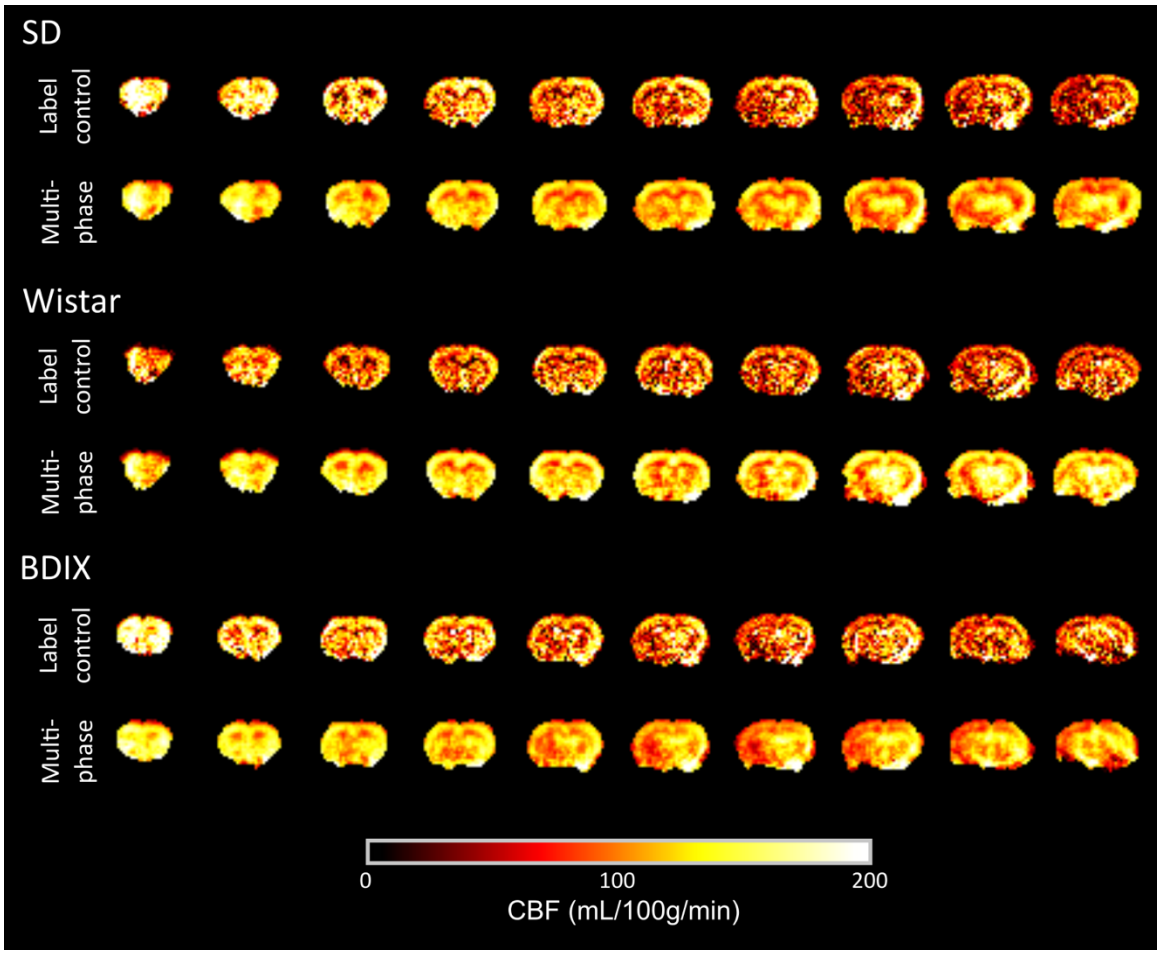

Figure 3.22 CBF map comparison between of traditional label-control pCASL MRI and MP pCASL MRI. Four averages of traditional label-control pCASL MRI apparent CBF maps were compared to a single average MP-pCASL MRI maps in three strains of rat as they require the same imaging time (1 min 29 s). Label-control pCASL MRI apparent CBF maps appear more heterogeneous with areas of little perfusion compared to MP-pCASL MRI apparent CBF maps in all three rat strains studied.

*Table 3.3 CBF measurements from whole brain in label-control pCASL MRI and MP-pCASL MRI. Mean ± standard deviation to the mean (*n *= 7 per strain)*.

Strain	Label-control CBF (mL/100g/min)	MP-pCASL CBF (mL/100g/min)
SD	85 ± 30	109 ± 25
Wistar	83 ± 25	112 ± 21
BDIX	83 ± 25	106 ± 12

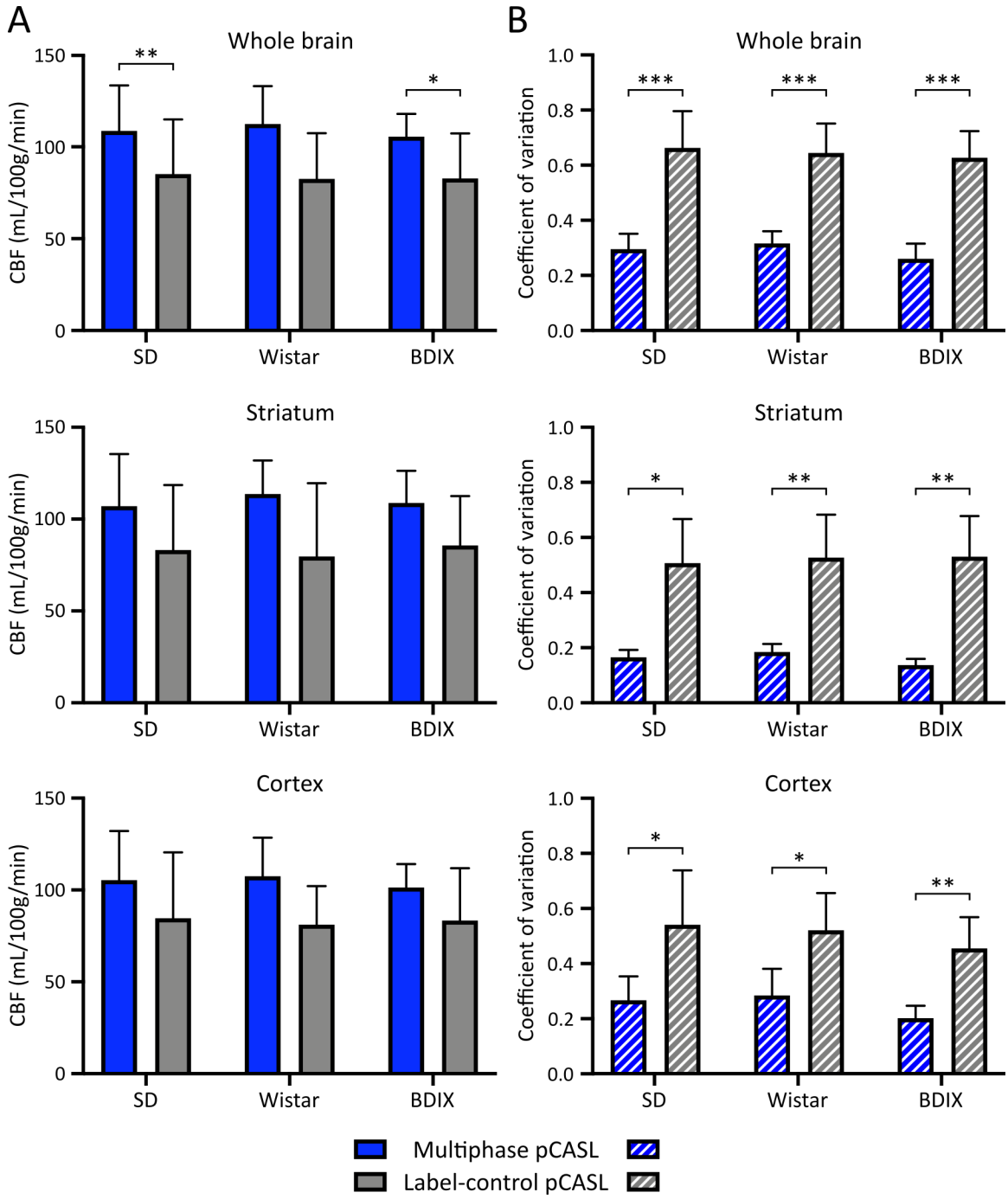

Figure 3.23 Measured CBF and coefficient of variation comparison between traditional label-control pCASL MRI and MP-pCASL MRI. **A** CBF quantitation from label-control pCASL MRI and MP-pCASL MRI in whole brain, striatum and cortex of three strains of rat (SD, Wistar and BDIX, $n = 7$ per strain). **B** Coefficient of variation (CV) across the same three brain regions for the CBF quantitation from label-control pCASL MRI and MP-pCASL MRI (Student's paired t-test, * $p < 0.05$, ** $p < 0.01$, *** $p < 0.001$; error bars represent standard deviation from the mean CBF and CV).

3.3.4.2 [^{14}C]-Iodoantipyrine autoradiography

[^{14}C]-iodoantipyrine autoradiography ([^{14}C]-IAP AR) was developed in the late 1960s by Reivich and colleagues (Reivich *et al.*, 1969; Sakurada *et al.*, 1978) and to this day remains a gold-standard for preclinical CBF measurements. Representative CBF maps from both [^{14}C]-IAP AR and MP-pCASL MRI are presented in Figure 3.24. CBF quantitation for the two methods was not significantly altered in any of the brain regions of interest for SD, Wistar or BDIX rats (Figure 3.25). Comparison of whole brain CBF measurements between the two methods is shown in Table 3.4.

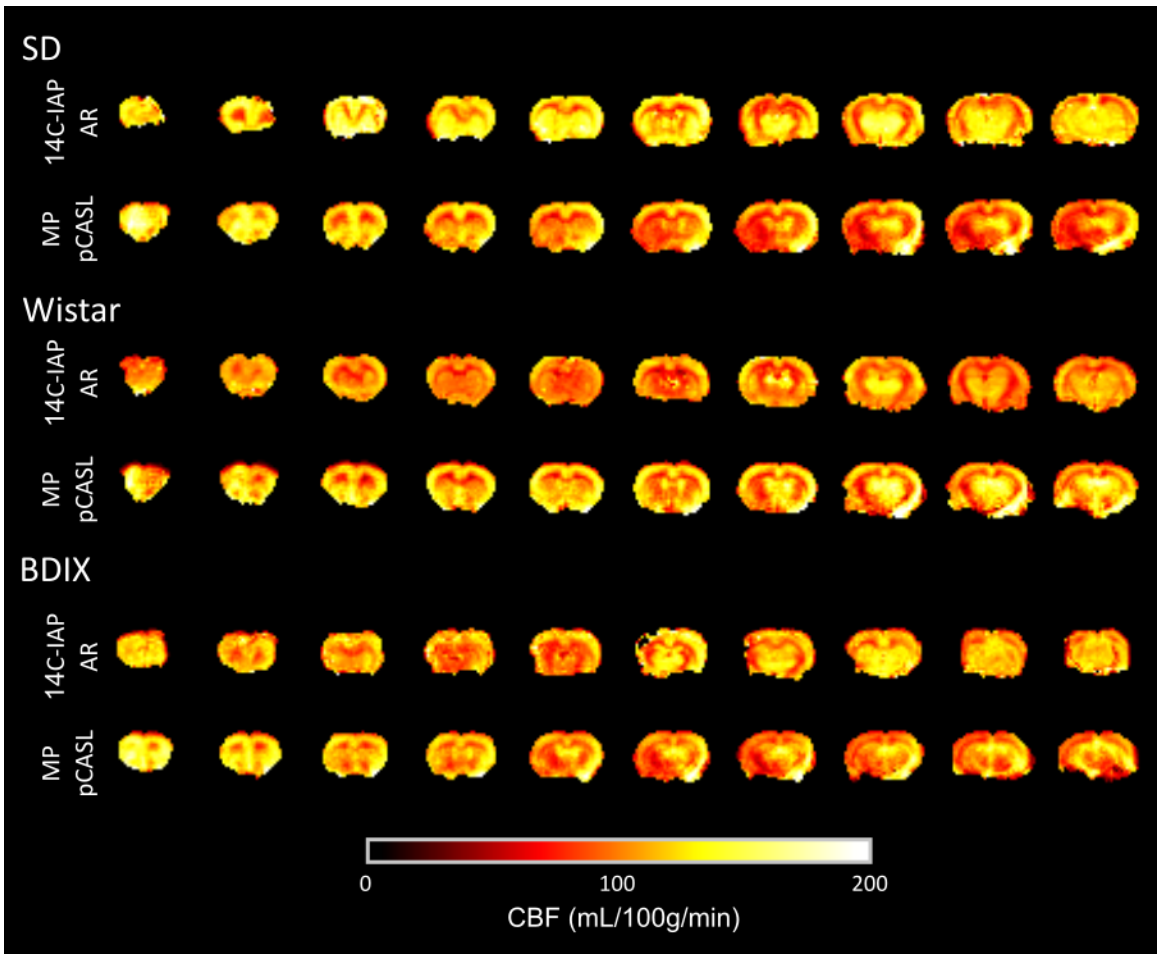

Figure 3.24 CBF maps from gold-standard [14C]-iodoantipyrine autoradiography and MP pCASL MRI. Example of [^{14}C]-IAP AR generated CBF maps compared to apparent CBF maps from eight averages of MP-pCASL MRI in three strains of rat.

*Table 3.4 CBF measurements from whole brain in [14C]-IAP AR and MP pCASL MRI. Mean ± standard deviation to the mean (*n *= 3 per strain).*

Strain	[^{14}C]-IAP AR CBF (mL/100g/min)	MP-pCASL CBF (mL/100g/min)
SD	112 ± 24	125 ± 10
Wistar	99 ± 16	118 ± 26
BDIX	106 ± 21	114 ± 9

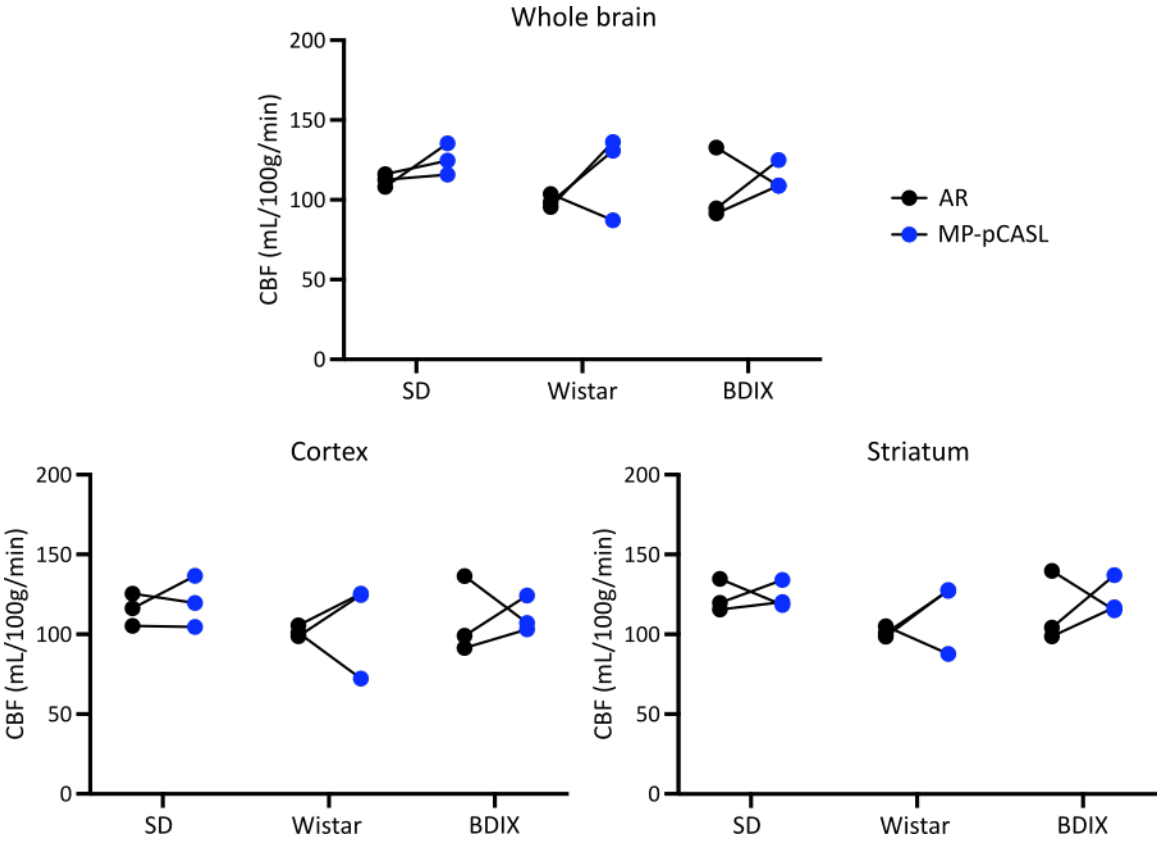

Figure 3.25 CBF quantitation of gold-standard [^{14}C]-iodoantipyrine autoradiography and MP-pCASL MRI. [^{14}C]-IAP AR and MP-pCASL MRI CBF quantitation in three strains of rats (*n* = 3 rats per strain).

3.3.4.3 One- and two-compartment kinetic model comparison of MP-pCASL MRI

In complex analyses such as this, the selection of an appropriate kinetic model is key to accurate measurement of CBF. A comparison of the one-compartment model from Buxton and colleagues (Buxton *et al.*, 1998) and the Parkes and Tofts (Parkes and Tofts,

2002) two-compartment kinetic model was performed in the subset of rats used for autoradiography for SD, Wistar and BDIX strains (n = 3 per strain). The two-compartment model incorporates an extravascular water pool along with the blood compartment water pool, present in the one-compartment model, and possesses two solutions; slow and fast. The slow solution assumes that the labelled water never leaves the tissue voxel, whereas the fast solutions assumes the venous blood has the same magnetisation as the blood in the voxel. CBF measurements from the fast solution of the two-compartment kinetic model were significantly increased in all rats (n = 9, 3 rats each from SD, Wistar and BDIX strains) when compared to the slow solution of the same model, the one-compartment model and to CBF from [^{14}C]-IAP AR ($p < 0.001$; Figure 3.26). No statistically significant difference in CBF measurements was observed between the gold-standard CBF and the one-compartment model or the slow solution to the two-compartment model. Therefore, both these models could be used in the analysis of MP-pCASL MRI to obtain accurate quantitative CBF measurements.

3.3.4.4 Comparison of CBF between naïve strains of rat

Representative maps of CBF for each rat strain and quantitation of CBF in the whole brain, cortex and striatum from the 21 rats studied (SD, Wistar and BDIX, n = 7 per strain) are shown in Figure 3.27. A significant difference in apparent CBF could be observed between Wistar rats and SD and BDIX rats, with significantly greater CBF in all brain regions of Wistar rats.

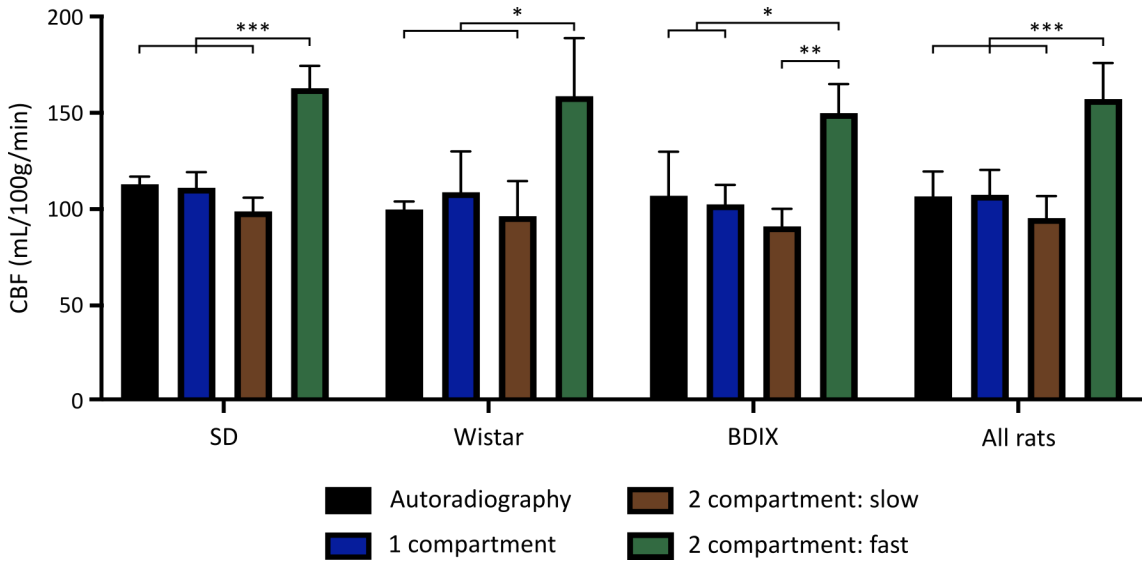

Figure 3.26 CBF quantitation comparison of [^{14}C]-iodoantipyrine autoradiography and 1- and 2-compartment model analyses of MP-pCASL MRI data. CBF quantitation from MP-pCASL MRI analysis using a one-compartment model and the slow and the fast solutions of a two-compartment model are compared to [^{14}C]-IAP AR CBF measurements in SD, Wistar and BDIX rats (n = 3 rats per strain; one-way ANOVA with Tukey's multiple comparisons, * $p < 0.05$, ** $p < 0.01$, *** $p < 0.001$; error bars represent the standard deviation from the mean).

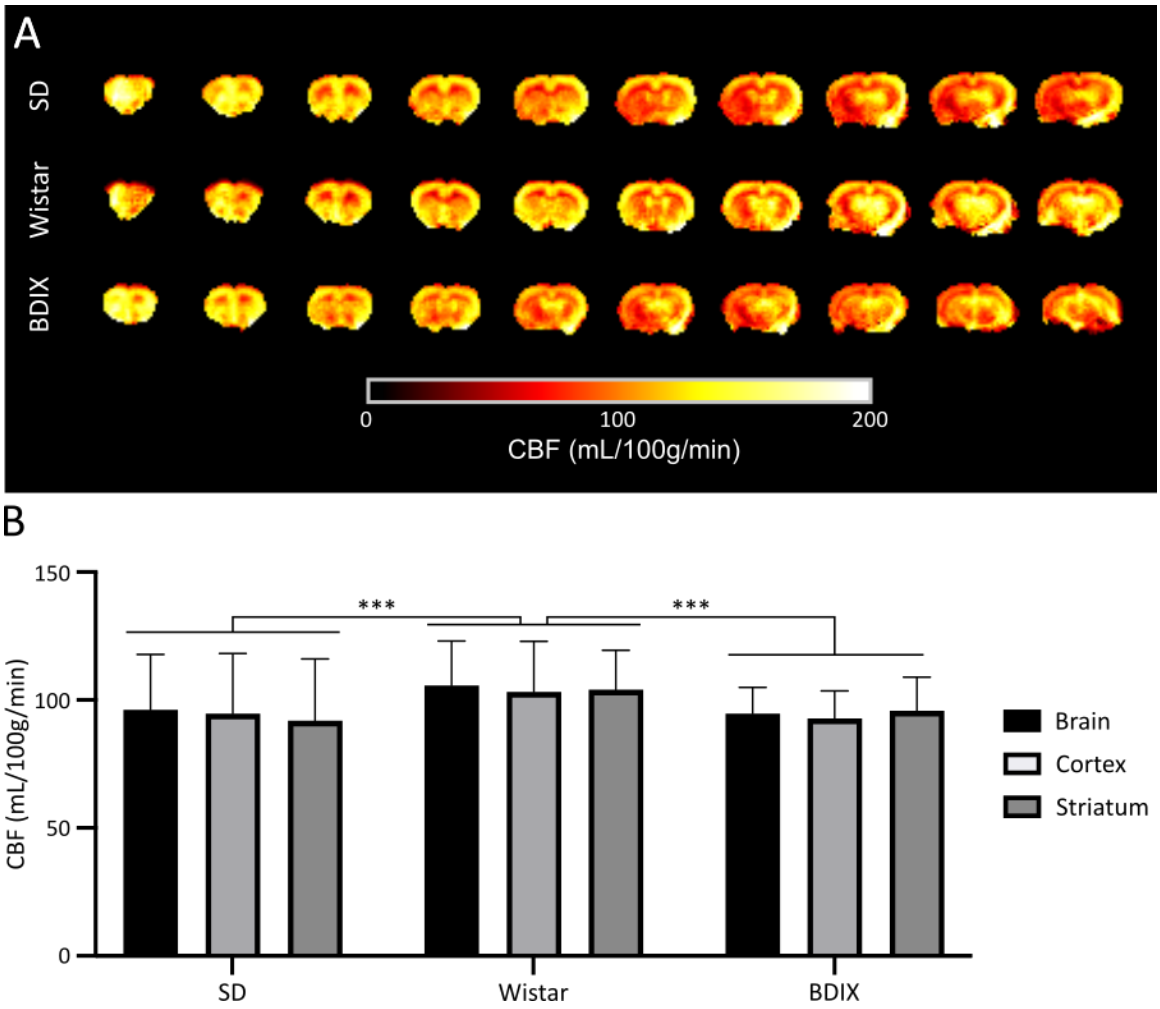

Figure 3.27 Example CBF maps and measurements from MP-pCASL MRI in rat brain. **A** Representative MP-pCASL MRI apparent CBF maps obtained using a one-compartment model for each strain of rat studied. **B** CBF quantitation in three brain regions of SD, Wistar and BDIX rats (n = 7 per strain; one-way ANOVA with Tukey's multiple comparisons of rat strains, *** $p < 0.001$; error bars represent the standard deviation from the mean).

3.4 Discussion

3.4.1 Parameter selection for MP-pCASL prior to MRI

The simulations of the Bloch equations performed prior to MP-pCASL MRI allowed the determination of optimal parameters for the efficient labelling of the inflowing blood water proton spins. With a labelling plane thickness of 6.2 mm and a flip angle of 40˚ for adiabatic inversion RF pulses, an inversion efficiency of 82.2 % could theoretically be achieved, which is similar to the 85 % inversion efficiency expected for pCASL MRI in humans (Dai *et al.*, 2008). Rat carotid blood velocity increased slightly when anaesthetic depth was deepened (lower respiration rate) in SD rats, while a decrease in blood velocity occurred in Wistar and BDIX rats but was only significantly altered in BDIX rats. The tighter agreement of the velocity between Power Doppler ultrasound measurements in BDIX rats could explain the greater slope found in this rat strain. Nevertheless, the variation of carotid blood velocity for all strains with varying anaesthetic depth will have little effect on the inversion efficiency achieved as highlighted in Figure 3.9B.

The selection of a bandwidth of 250 kHz and of an echo time of 28 ms for the MP-pCASL MRI acquisition, enabled high SNR in acquired images and an ASL MRI signal percentage variation of approximately 3 % between phases in all animals. This value is greater than that typically achieved in clinical ASL, where signal variations of < 1 % are common (Alsop *et al.*, 2014). The increase in ASL signal variation between phases is likely to, in part, reflect the increased blood flow present in rats compared to humans and, in part, the use of a higher magnetic field strength (9.4 T) than that used in the clinic (1.5 or 3.0 T, or 7.0 T in some experimental settings). Furthermore, the addition of multiple phase offsets from MP-pCASL MRI increases coverage along the adiabatic inversion curve and allows for a

better estimation of the true signal variation between phases. Altogether, the high SNR and increased ASL signal variation between phases obtained with MP-pCASL MRI in rats compares favourably to that seen in humans.

3.4.2 MP-pCASL MRI optimisation

3.4.2.1 Labelling plane parameters

The position of the labelling plane is crucial for efficient labelling of blood through brain feeding arteries. For optimal blood labelling, the labelling plane should be oriented perpendicularly to the flow in the carotid and vertebral arteries in the neck and, therefore, these arteries should not be bent in the labelling plane. Firstly, the effect of the labelling plane angle was investigated, and a 45˚ angle proved advantageous compared to the traditional use of a labelling plane parallel to the imaging region and perpendicular to the bore of the spectrometer. This angled labelling plane decreased the error associated with CBF measurements and increased the apparent CBF values with a close agreement to the autoradiography gold-standard data.

As for the location of the labelling plane along the rat neck, TOF angiography MRI informed the initial positioning of the labelling plane behind the gracile fasciculus, the most rostral point where the brain feeding arteries were straight. Moving the labelling plane further toward the tail proved not to affect CBF measurements in any of the rat strains studied. However, if the labelling plane was moved in the rostral direction, the apparent CBF measurements markedly decreased to unphysiological levels. The decreased apparent CBF in these locations can be explained by the bend of the vertebral arteries closer to the back of the brain leading to inefficient blood labelling and, in part,

by the super-positioning of labelling plane onto the imaging region. Since TOF angiography MRI is a lengthy scan (> 12 minutes), we proceeded to select an anatomical reference, directly behind the notch of the gracile fasciculus present in all rats to enable reproducible positioning of the labelling plane with a reduced imaging time, as suggested for humans in the white paper (Alsop *et al.*, 2014).

Contrary to the labelling plane location, the label duration had a minimal effect on CBF measurements, except in the comparison between the shortest (0.4 s) and two longer label durations (3.7 s and 5.0 s) in SD rats when using the supervoxel generated phase prior MP-pCASL MRI analysis. When compared to the apparent CBF results from MP-pCASL MRI without the supervoxel generated phase priors, the apparent CBF at shorter label durations was markedly decreased. However, it is possible that the supervoxel incorporation into MP-pCASL MRI analysis does not perfectly correct for the increased noise present in acquired images at shorter label durations. Furthermore, it may be that the small decrease in apparent CBF measurements at longer label durations was caused by outflow of a higher proportion of labelled protons from the brain tissue. MP-pCASL MRI imaging efficiency is dependent on the increased signal at longer label durations, but this is offset by ongoing T_1 relaxation, creating a plateau in efficiency at longer labelling times. The imaging efficiency is particularly low at label durations below 1.4 s, but remains high at label durations between 1.4 s and 5.0 s. Yet, as the label duration increases, so does the imaging time required. For this reason, a label duration of 1.4 s was selected for MP-pCASL MRI in naïve rats.

3.4.2.2 PLD selection from arrival time information

The selection of a PLD is a trade-off between loss of signal with longer PLDs due to T_1 relaxation of blood and inaccurately elevated CBF measurements at shorter PLDs owing to compromise of signal by circulating labelled blood. Through multi-PLD MP-pCASL MRI, a PLD of 550 ms was selected as the best compromise for maximal signal without brain circulating arterial blood contamination, since over 98 % of brain voxels from SD, Wistar and BDIX rats had received labelled blood in the both the most anterior and most posterior imaging slices. Only two imaging slices were acquired to minimise acquisition delay between slices and as these represent the edges of the imaging region, blood arrival time to intervening slices should fall within the arrival times measured. The posterior slice was acquired first since the labelled blood arrives at this slice earlier than the anterior brain slice. Furthermore, the 50 ms delay between the two slice acquisitions is less likely to affect the anterior slice than the posterior slice as it is located further from the labelling plane.

Brain pathologies such as cancer and stroke are likely to affect the brain vasculature and thereby blood arrival time to the brain, suggesting that multi-PLD MP-pCASL MRI should be performed prior to MP-pCASL MRI to determine an appropriate PLD for each model.

3.4.2.3 Background suppression in rat 2D MP-pCASL MRI

Background suppression in ASL MRI is recommended for clinical use to increase ASL signal variations and decrease noise from subject motion (Alsop *et al.*, 2014). Unfortunately, background suppression works best if the entire imaging region is

acquired simultaneously, as is the case in 3D imaging readouts and single-slice 2D acquisitions. In the current work, as the acquisition of each imaging slice took 50 ms, the final slice acquisition will begin 450 ms later than the first imaging slice. During this time, background tissue that was initially suppressed in the overall imaging signal will begin to progressively contribute more over time and lead to increasingly erroneous CBF measurements across the imaging volume. Further, the decreased apparent CBF from background suppressed single-slice MP-pCASL MRI acquisitions could be caused by inversion of some labelled blood already present in the brain imaging region during the spatially selective inversion immediately following the MP-pCASL MRI labelling. This spatially-selective inversion would, therefore, erase tissue:blood exchanges occurring during the labelling period. Yet, since the aim of this work is to acquire multi-slice MP-pCASL MRI data, the increasing background signal contribution during multi-slice image acquisition together with the lower CBF values obtained in single-slice background suppression MP-pCASL MRI led to the decision not to pursue this technique further.

3.4.3 Impact of analysis on MP-pCASL MRI CBF measurements

The analysis pipeline must be constructed to accurately represent the species and method used. Selection of the α and β parameters for the fitting to the Fermi function allows the optimal fitting model for empirically observed MP-pCASL MRI data. Another important aspect of the analysis is the selection of the correct phase priors for this fitting. In three parameter models such as the one used herein (magnitude, phase and offset), addition of noise results in an over-estimation of the amplitude (Alegria, 2009). In MP-pCASL MRI with short label durations, noise is increased since less labelled blood is

present in the imaging region. Consequently, the MP-pCASL MRI signal variation between phases is similar to acquisition and biological noise floors. If the correct phase priors are not present, an artificially increased CBF is obtained through the over-estimation of the magnitude. Supervoxel ROI addition into the analysis pipeline, for the generation of phase priors in brain vascular territories, increased the SNR and circumvented this over-estimation of magnitude at the expense of spatial resolution (Msayib *et al.*, 2019[1]). The use of supervoxels with phase prior information is justified as phase estimates should not vary on a voxel-wise basis within a brain vascular territory. The phase offsets from each supervoxel ROI varied between all animals, indicating that this is dependent on vessel location within the rat and within the bore of the spectrometer. Supervoxel ROI phase priors must be determined in each acquisition to ensure accurate phase prior selection. Addition of supervoxel clustering increased analysis time by 13.9 s. However, considering data organisation from the MRI and segmentation of the brain requires approximately 1 min and 3 min, respectively, the increased analysis time is negligible.

3.4.4 Comparisons of CBF from MP-pCASL MRI with other CBF measurement methods

3.4.4.1 MP-pCASL *vs.* traditional label-control pCASL MRI

The acquisition time for MP-pCASL MRI acquisitions with 8 phases is equivalent to four traditional label-control pCASL MRI averages but provides a trade off in bias and variance with improved image quality. MP-pCASL MRI provides a qualitative and quantitative

[1] I have contributed to this work.

advantage over traditional label-control pCASL MRI. Uncorrected off-resonance effects present in the different vessels at the labelling plane are easily seen in label-control CBF maps in areas of apparently very little perfusion signal, whereas CBF maps from MP-pCASL MRI of the same rat show no evidence of this apparently decreased perfusion. Moreover, label-control pCASL MRI data exhibits an increase in CBF variability across the brain when compared to MP-pCASL MRI data and apparent CBF maps, a variability not present in the gold-standard autoradiography CBF maps and quantitation. Overall, MP-pCASL MRI presents itself as a clear improvement over traditional label-control pCASL MRI in rats imaged at a high magnetic field strength.

3.4.4.2 Validation of MP-pCASL MRI CBF measurements with gold-standard values and model comparisons

[^{14}C]-Iodoantipyrine autoradiography has been used as a gold-standard for perfusion measurements in animals for the past several decades (Reivich *et al.*, 1969; Sakurada *et al.*, 1978; Ewing *et al.*, 2003). However, it is a complex, invasive and terminal procedure, and quantitation is a lengthy process, which limits its application. Yet, it remains the best calibration point for a technique such as MP-pCASL MRI in a preclinical study. CBF maps and quantitation from the three rat strains show close agreement between the two methods. Comparisons between CBF values from [^{14}C]-IAP AR and MP-pCASL MRI analysed using Buxton's one-compartment (Buxton *et al.*, 1998) and both solutions of the Parkes and Tofts (Parkes and Tofts, 2002) two-compartment models were performed to determine the optimal kinetic modelling to use. The fast solution of the two-compartment model may be over-estimating CBF as it does not incorporate a complete venous outflow factor, likely to be significant at higher flow rates. Both the slow solution

of the two-compartment model and Buxton's one-compartment model are in close agreement to each other and to the gold-standard autoradiography, thus either model could be used for quantitative CBF measurements of MP-pCASL MRI. For simplicity and because no significant difference existed between the models, the MP-pCASL MRI performed in the majority of this chapter, and in subsequent chapters of this thesis, used the one-compartment kinetic model, which was already implemented in BASIL and oxford_asl of the analysis pipeline.

3.4.5 Optimised MP-pCASL MRI in naïve rats

3.4.5.1 CBF measurement comparison in naïve rat strains

Three preclinically relevant strains of rat were used throughout this chapter to test the reliability and robustness of MP-pCASL MRI between strains and to determine whether strain-specific CBF differences are present. Wistar rats possessed significantly greater apparent CBF from MP-pCASL MRI than the other two strains in all three regions of interest of the brain. This increased CBF does not appear to be linked to the inflowing blood velocity, as Wistar rats possessed a carotid blood velocity inferior to that observed in SD rats, yet greater than that of BDIX rats.

3.4.5.2 Summary of optimised MP-pCASL MRI in rats and comparison with clinical recommendations for ASL MRI

The optimisation of MP-pCASL MRI in naïve rats has been described throughout this chapter. To summarise, Bloch simulations determined that a flip angle of 40˚ for adiabatic inversion of inflowing blood water spins through a 6.2 mm thick labelling plane provided

an inversion efficiency greater than 80 %, according to the mean carotid blood velocity of SD, Wistar and BDIX rats. The labelling plane benefits from being perpendicular to the brain feeding arteries, at a 45˚ angle to the bore of the spectrometer for preclinical imaging with rats positioned prone and with the head raised and secured through ear bars. Reproducible positioning of the labelling plane is facilitated by placing it immediately behind the gracile fasciculus, rostral to the C1 vertebra, which is an easily identifiable anatomical marker. MP-pCASL MRI label duration is recommended to be $\geq$ 1.4 s and up to 5.0 s, and TR should be adjusted in relation to label duration to allow sufficient relaxation time. In naïve rats, a PLD of 550 ms is sufficient to allow blood arrival to the whole brain, yet remains short enough to retain good pCASL MRI signal variation between phases in the brain. Background suppression is not recommended for either 2D multi-slice acquisitions or single-slice imaging, since a significant decrease in apparent CBF was detected. For 8-phase MP-pCASL MRI analysis, an α of 70 and β of 19 is recommended for fitting to the Fermi function. The inclusion of clustering using four supervoxels for phase offset in vascular territories within the brain creates high-precision phase priors and reduces biological noise in MP-pCASL MRI CBF measurements. During the MP-pCASL MRI analysis, a one-compartment model or the slow solution of the two-compartment model yield quantitative CBF measurements in agreement with gold-standard autoradiography CBF values. Finally, MP-pCASL MRI provides an advantage over traditional label-control pCASL MRI for CBF measurements. Table 3.5 demonstrates a comparison between the recommended clinical application of ASL MRI from the white paper (Alsop *et al.*, 2014) and the optimised MP-pCASL MRI in rats.

Table 3.5 Recommended clinical and preclinical ASL parameters.

	Clinical ASL	Preclinical ASL
Hardware considerations	Field strength > 1.5 T when available	9.4 T was used here, although other field strengths could also be used, albeit with potential changes in acquisition parameters
ASL labelling approach	pCASL	MP-pCASL
Labelling plane location	Perpendicular to brain feeding arteries either by placing it 85mm inferior to anterior commissure posterior commissure (AC-PC) line or just below inferior border of the cerebellum	Directly behind notch of gracile fasciculus and at a 45˚ angle to be perpendicular to brain feeding arteries
Bolus duration	1.8 s	1.4 or 2.4 s (up to 5.0 s, with increasing imaging time)
Post label delay	Should be just longer than blood arrival time. Set to 2000 ms in adults	Determined arrival time to be lower than 550 ms in naïve rats
Background suppression	Performed in 3D or in single-slice 2D acquisitions	Not recommended for multislice 2D EPI[1]
Readout	Segmented 3D readout when available, if not multislice single-shot 2D EPI	Single-shot 2D SE-EPI, either single or multi-slice[1]
Post-processing method	Calculated according to image signal intensity, blood:brain partition coefficient and T_1 of blood	CBF quantified by oxford_asl in BASIL dependent on signal intensity, supervoxel-derived phase priors, blood:brain partition coefficient, T_1 of blood and brain tissue, slice acquisition delay, TE, TR, reference images (transmit & receive arrays)

[1] 3D MP-pCASL MRI acquisitions were not attempted in the current study.

3.5 Conclusion

In the present chapter, MP-pCASL MRI was optimised in three strains of rat to improve preclinical ASL MRI at high magnetic field strengths. A multiphase pCASL MRI approach provided a clear advantage over traditional label-control pCASL MRI, allowing for corrections of off-resonance effects present in vessels at the labelling plane. Optimal parameters for the labelling plane such as its position and angle were selected to obtain an efficient blood inversion, and the label duration was determined to yield maximum imaging efficiency. A PLD with minimal arterial blood contamination was identified and CBF maps were generated. Optimised MP-pCASL MRI was confirmed to produce accurate quantitative CBF measurements by gold-standard [^{14}C]-IAP AR and, thus, is a rapid, robust and reproducible method of measuring CBF non-invasively in rats.

CHAPTER 4

Multiphase pCASL MRI in a rat model of breast cancer brain metastasis

4.1 Introduction

4.1.1 Clinical research applications of arterial spin labelling MRI

Clinically, ASL MRI can provide valuable information on brain perfusion, a feature often dysregulated in physiological and psychological disorders. Since its inception, an increasing amount of clinical and preclinical research on ASL MRI is being performed every year (Figure 4.1). Although clinical ASL MRI applications are currently limited to the research setting, ASL MRI has been used to characterise cerebral blood flow (CBF) anomalies in patients with a stroke (Siewert *et al.*, 1997), tumours (Qiao *et al.*, 2015), dementia (Schuff *et al.*, 2009), schizophrenia (Ota *et al.*, 2014), epilepsy (Pendse *et al.*, 2010) and even post-traumatic stress disorder (Schuff *et al.*, 2011), among others.

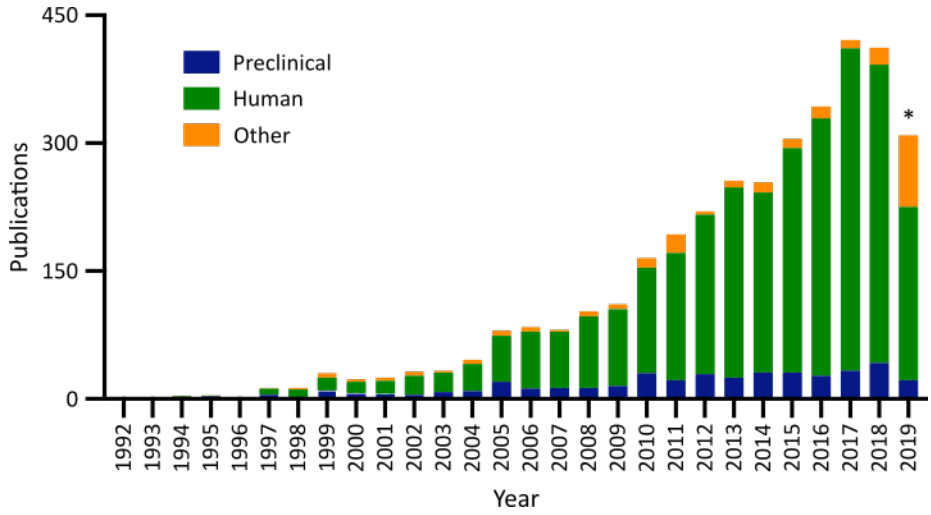

*Figure 4.1 Arterial spin labelling MRI publications over time.*Yearly publications on preclinical ASL MRI in rodents (blue),clinical human ASL MRI (green) or other ASL MRI applications (orange) as of August, 2019 according to a search in Scopus (www.scopus.com). An asterisk (*) is used to highlight the fact that the 2019 year is ongoing.

In brain tumours, tumour blood flow obtained from ASL MRI can be used for tumour staging and can inform treatment planning and predictive outcome (Lu *et al.*, 2017; Abdel Razek and Nada, 2018; Liu *et al.*, 2019). Brain metastases represent the majority of brain tumours in adults (Nayak, Lee and Wen, 2012) and commonly arise from lung, breast, melanoma or colon primary tumours (Wen and Loeffler, 2000). Previously, ASL MRI in brain tumours have shown that increased CBF measurements correlate with histopathologic vascular density of the tumour, and that CBF decreases from ASL MRI have been shown to be predictive of positive treatment outcome in brain metastasis patients having undergone stereotactic radiosurgery (Weber *et al.*, 2004; Noguchi *et al.*, 2008).

One of the main advantages of ASL MRI compared to currently performed MRI techniques in brain tumours is the absence of contrast agent required for measurement of CBF. Gadolinium-based contrast agents (GBCAs) are often used in the clinic for brain tumour imaging, but have been shown to deposit in the brain and other tissues such as

the liver, skin and bone (Malayeri *et al.*, 2016; Guo, Yang and Zhang, 2018) and are linked to cases of nephrogenic systemic fibrosis (Marckmann *et al.*, 2006). Therefore, administration of GBCAs is not recommended in patients with co-morbidities involving the kidneys and MRI techniques involving injection of GBCAs should not be repeated frequently in order to minimise gadolinium deposits in humans. Thus, the replacement of some GBCA-based MRI techniques with ASL would be beneficial from a health stand-point and would enable MRI to be performed as often as required.

4.1.2 ASL in rodent brain metastasis

Since ASL is an MRI technique with an inherently low SNR, it would not be useful for the detection of brain tumours including metastases. However, once metastases have colonised a sufficient volume in the brain to cause BBB disruption, ASL MRI could be useful in the biological characterisation of this tumour. Consequently, direct implantation of tumour cells into the brain parenchyma can provide a useful and relevant test bed for demonstrating the application of ASL MRI for tumour characterisation in rodent models of brain metastasis. The intracerebral ENU1564 rat breast cancer brain metastasis model is such a model and has previously demonstrated similarities to human brain metastasis including metastasis growth mediated through vascular co-option and the presence of necrotic areas (Serres *et al.*, 2014). Excluding research performed by our group (Buck *et al.*, 2018; Larkin *et al.*, 2018), ASL MRI has never been performed in rodent models of brain metastasis.

4.1.3 Chapter hypotheses and aims

In this chapter, clinically-relevant MRI methods described in section 1.2.1 (T_2-weighted, pre- and post-contrast T_1-weighted, DWI and MR perfusion) were performed throughout the progression of a rat model of breast cancer brain metastasis together with rat optimised MP-pCASL MRI. MRI results were compared to *ex vivo* histology for vessel density, hypoxic fraction, and angiogenesis in the rat brain metastasis model.

4.1.3.1 Main hypothesis

MP-pCASL MRI yields accurate CBF measurements in brain metastases, which could replace current MRI techniques for perfusion requiring GBCAs and provide valuable information for brain metastasis treatment planning.

4.1.3.2 Aims and aim-specific hypotheses

(1) Apply MP-pCASL MRI to a rat breast cancer brain metastasis model to quantitatively determine CBF changes during tumour progression.
    a. MP-pCASL MRI bolus arrival time increases in brain metastases compared to healthy tissue owing to vascular dysregulation and, therefore, the MP-pCASL PLD MRI will need to be increase.
    b. CBF differences between healthy brain tissue and brain metastases are detected by MP-pCASL MRI.

(2) Compare MP-pCASL MRI CBF results to those obtained from clinically-relevant MRI techniques over time in a rat model of brain metastasis.

a. MP-pCASL MRI CBF measurements yields valuable information on tumour biology in brain metastases and can inform treatment planning when added to current clinically recommended MRI techniques.

(3) Compare histological findings with MRI results in a rat model of brain metastasis.

a. MP-pCASL MRI CBF measurements reflects histological findings with respect to vessel density and hypoxic regions.

4.2 Methods

4.2.1 Rat intracerebral brain metastasis model

Details concerning the implantation of cells into the brain parenchyma for the rat breast cancer brain metastasis model are found in section 2.2.1.

4.2.1.1 Rat brain metastasis model experimental plan

Following intracerebral injection of ENU cells, rats were allowed to recover for two weeks prior to the initial MRI session. Initially, rats (PBS-injected, $n = 5$; ENU-injected, $n = 6$) were imaged every two weeks with an MRI protocol consisting of T_2-weighted anatomical imaging, T_1 and T_2 relaxometry imaging, diffusion-weighted imaging, T_1-weighted imaging pre- and post-gadolinium injection and MP-pCASL (Figure 4.2A). Rats were killed six weeks following intracerebral injection, except for 3 ENU-injected rats demonstrating symptoms of distress between four and six weeks, which were culled upon symptom presentation. For this reason, along with the cystic necrosis of the brain metastases present at six weeks post tumour injection, the revised end-point for the rat brain metastasis model was moved to four weeks post-injection.

In subsequent rats, the MRI protocol was as previously described with the addition of an intravenous injection of ultra-small super-paramagnetic iron oxide (USPIO) particles and T_2 relaxometry before and after this injection for the construction of relative cerebral blood volume (rCBV) maps (Figure 4.2B). Rats were killed at each time-point by pentobarbitone overdose and perfusion-fixation (details in section 2.2.2) for histological analysis at biweekly time points during brain metastasis progression.

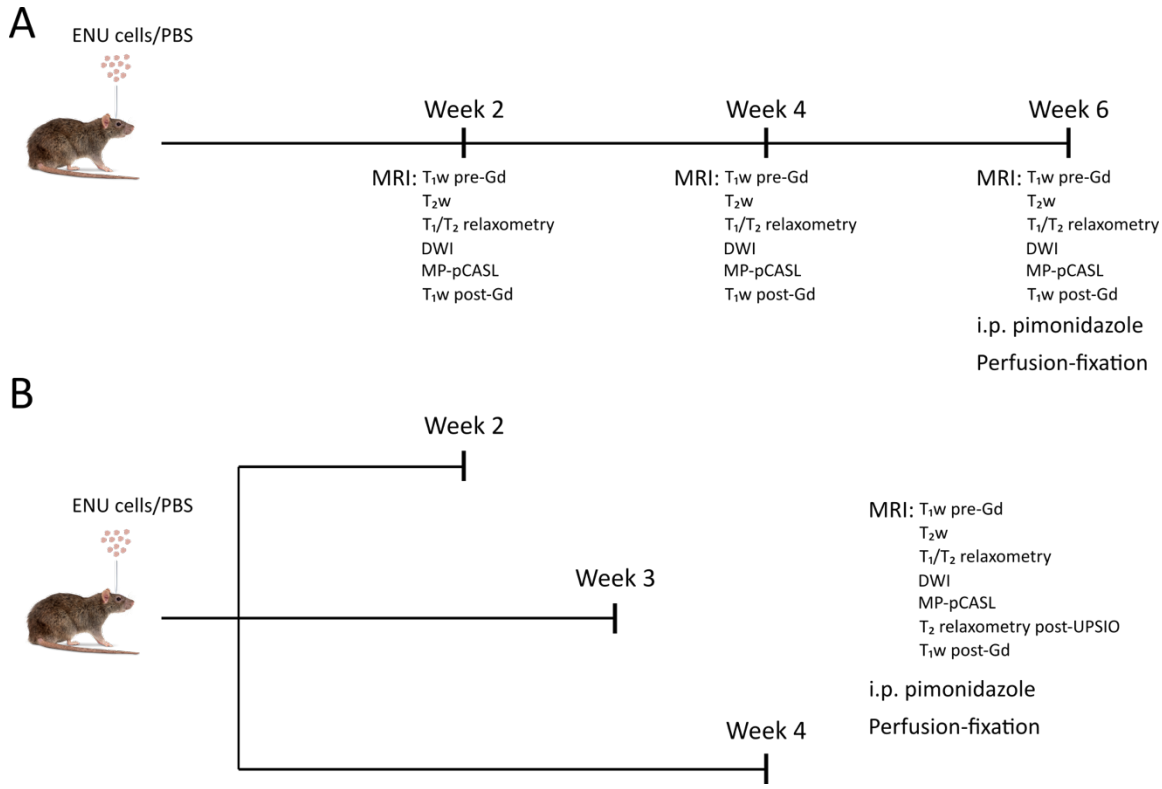

Figure 4.2 Rat experimental plan imaging of brain metastasis progression. **A** Pilot study experimental plan. Rats underwent MRI every 2 weeks, starting at 2 weeks post-injection until the six week time point. **B** Experimental plan for all subsequent rats, with addition of UPSIO-injection and T_2 relaxometry post-USPIO injection in the MRI protocol.

4.2.2 Magnetic resonance imaging

All MRI acquisitions were performed as described in section 2.3.

4.2.2.1 T_1-weighted and T_2-weighted anatomical imaging

Please refer to section 2.3.3 and section 2.3.4 for details of T_1-weighted and T_2-weighted anatomical MRI, respectively, used herein.

4.2.2.2 T_1 and T_2 relaxometry

Please refer to section 2.3.6 for details of T_1 and T_2 relaxometry used herein.

4.2.2.3 Diffusion-weighted imaging

Detailed diffusion-weighted MRI methods and analysis description are found in section 2.3.2.

4.2.2.4 USPIO and rCBV

T_2 relaxometry MRI (section 2.3.6) was performed before and after the injection of 100 µL of ultra-small paramagnetic iron oxide particles (USPIO; 10.6 mg iron/mL), a blood pooling agent, through the tail vein of rats while in the spectrometer to obtain blood volume weighted data. Relative cerebral blood volume (rCBV) was calculated using an in-house build code[1], using the USPIO particle specific relaxivity in blood at 37 ˚C of 1822.9 Hz/(mg/mL) and an assumed blood volume of 62 mL/kg of BDIX rats. Briefly, a relaxation rate difference map was created by subtracting the relaxation rate of the brain at baseline from the relaxation rate following USPIO injection. Subsequently, a map of iron concentration was generated by dividing the difference map by the relaxivity of USPIO particles. Finally, this iron concentration map was divided by the blood iron concentration, obtained using the assumed blood volume of BDIX rats and the injected volume and concentration of the USPIO solution, to yield rCBV maps.

4.2.2.5 Multiphase pseudo-continuous ASL MRI

MP-pCASL MRI acquisitions and analysis were performed as described in section 2.3.1. Multi-PLD MP-pCASL MRI was performed in ENU-injected BDIX rats three weeks post-

[1] Code built by Dr. James Larkin.

injection to determine the blood arrival time to the region of brain metastases and healthy striatum using 12 PLDs ranging from 10 ms to 1000 ms, to obtain blood arrival time maps: PLDs = 10, 15, 20, 25, 30, 50, 100, 200, 300, 500, 750, 1000 ms; TR = 5 s; T_{exp} = 18 min 21 s.

4.2.2.6 Regions of interest in the brain

Brain ROIs were generated as described in section 2.3.8.

4.2.3 Immunohistochemistry

IHC was performed targeting the endothelial marker CD31 (AF3628, R&D Systems, Abingdon, UK), the hypoxia gold-standard marker pimonidazole HCl (Hypoxyprobe, Burlington, USA) and the angiogenesis marker Tie2 (bs-1300R, Insight Biotechnology Ltd, London, UK) as described in section 2.4.3. All secondary antibodies were purchased from Vector Laboratories Ltd (Burlingame, USA).

Table 4.1 Immunohistochemistry antibodies and concentrations

IHC antigen	*Blocking solution*	*Primary antibody concentration*	*Secondary antibody and concentration*
CD31 Polyclonal goat IgG	Normal horse serum	1:200	Goat raised in horse; 1:200
Pimonidazole HCl Monoclonal mouse IgG	Normal horse serum	1:100	Mouse raised in horse; 1:200
Tie2 Polyclonal rabbit IgG	Normal goat serum	1:200	Rabbit raised in goat; 1:200

IHC analysis was performed according to the method outlined in section 2.4.4.

4.3 Results

4.3.1 ENU brain metastasis progression imaged with clinically relevant MRI techniques

4.3.1.1 T_1-weighted and T_2-weighted MRI

ENU brain metastases in BDIX rats, each comprised of many metastatic foci as previously shown (Serres *et al.*, 2014), could be detected by hyperintense and heterogeneous regions on T_2-weighted anatomical MRI in 6 out of 13 rats two weeks post-intracerebral injection of ENU cells and in all rats at weeks three, four, and six following injection (Figure 4.3A). Tumour volumes estimated from T_2-weighted MRI acted as a surrogate measure of ENU brain metastasis and were significantly increased as time progressed (Figure 4.3C). All ENU tumours presented cystic necrosis six weeks post-injection (bright tumour on T_2-weighted images, Figure 4.3A). BBB breakdown, detected by gadolinium-enhancement on T_1-weighted MRI acquisitions, occurred in 3 out of 13 rats at week two post-injection, and increased to 8 out of 9 rats at week three. All 9 ENU-injected rats showed BBB breakdown at week four. Gadolinium-derived hyperintensities were detected in 2 out of 3 rats six weeks post-injection. No hyperintensities from gadolinium extravasation were detected in T_2-weighted MRI of PBS-injected rats at any time-points assessed (Figure 4.3B).

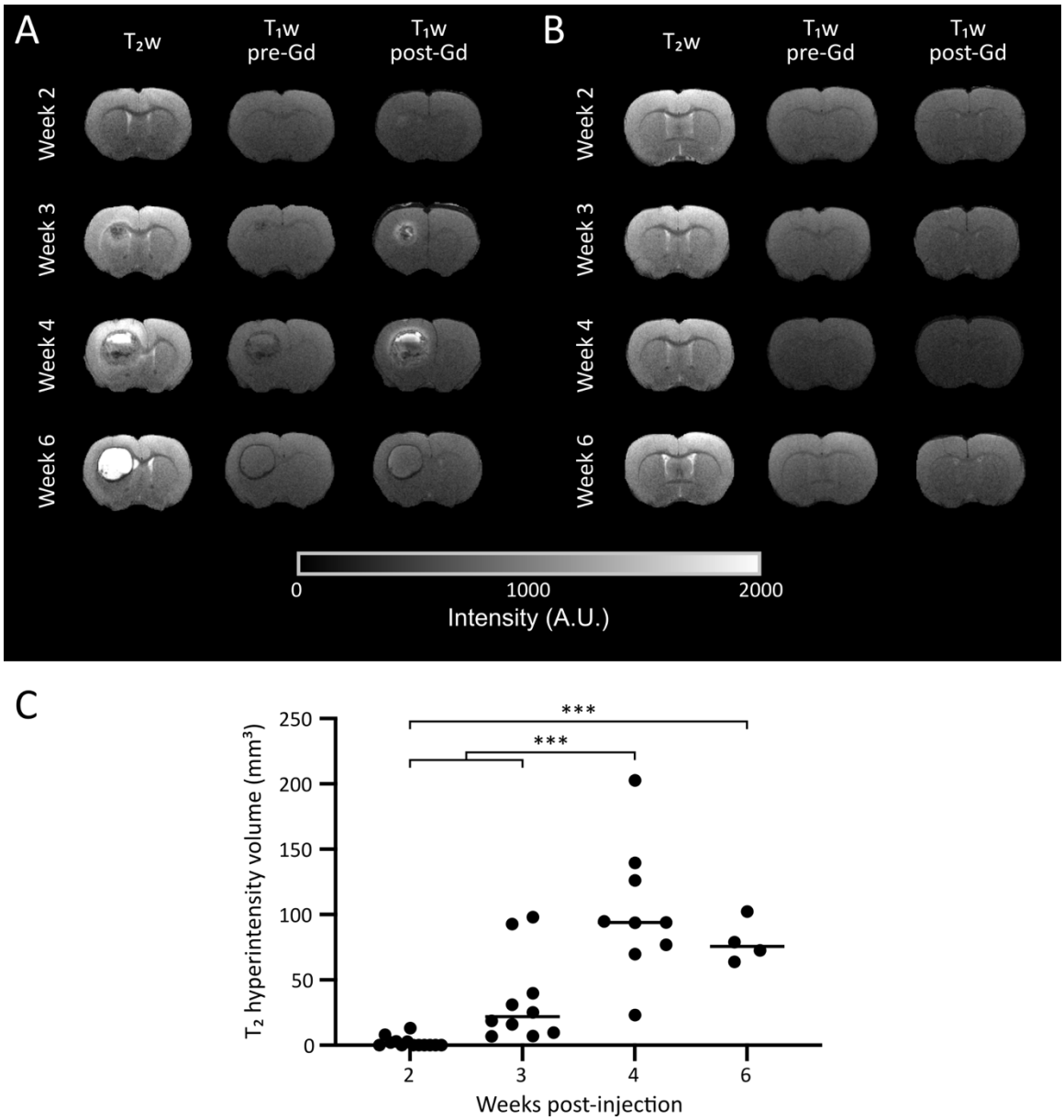

Figure 4.3 Anatomical imaging of ENU brain metastasis progression in BDIX rats. Brain metastasis progression in T_2-weighted and T_1-weighted representative acquisitions pre- and post-gadolinium contrast injection in ENU- (**A**) and PBS-injected (**B**) BDIX rats at two, three, four and six weeks post-injection. **C** ENU tumour volume measured on T_2-weightedMRI images at two weeks (n = 13), three weeks (n = 10), four weeks (n = 9) and six weeks (n = 4) post-injection (one-way ANOVA with Tukey's multiple comparisons, *** $p < 0.001$).

4.3.1.2 Brain cellularity assessment by measurement of the apparent diffusion coefficient

Apparent diffusion coefficient (ADC), was used as an indirect measure of cellularity, where a lower ADC represents higher cellularity and a higher ADC represents decreased

voxel cellular content. A significantly increased ADC was measured in ENU brain metastases as when compared to the contralateral striatum at weeks three ($p < 0.01$) and four ($p < 0.001$) post-injection (Figure 4.4C) and when compared to the PBS-injected striatum at weeks three ($p < 0.01$), four ($p < 0.05$), and six ($p < 0.05$) post-injection. No significant differences in ADC values were present between the injected and contralateral striata of PBS-injected rats at any time point during (Figure 4.4B).

Lastly, the brain metastasis region was separated into rim and core regions to assess whether these regions differed owing to a higher likelihood of an invading tumour rim and of a necrotic tumour core over time. A significant decrease in ADC was observed in the core of ENU brain metastasis foci compared to the rim region at week three ($p < 0.05$) indicating increased tissue cellularity in this region (Figure 4.4D). Overall, ADC results increased progressively during brain metastasis development in rats.

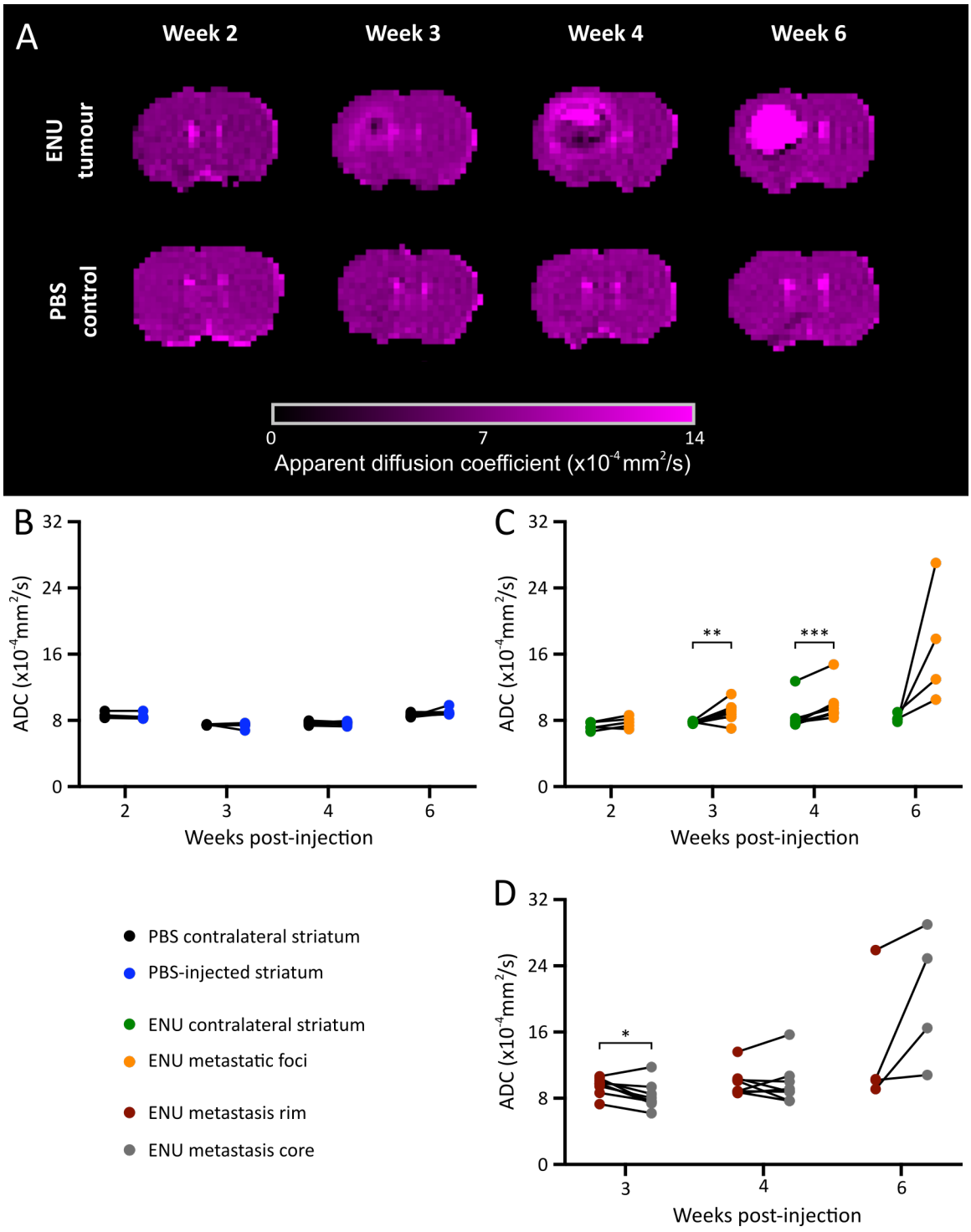

Figure 4.4 Apparent diffusion coefficient of ENU brain metastases during tumour progression in BDIX rats. **A** Representative ADC maps from ENU- and PBS-injected BDIX rats during tumour progression. Comparisons of ADC values in the injected and contralateral striata of PBS-injected rats (**B**; n = 5, 6, 7, 5 for weeks two, three, four and six, respectively) and of ENU-injected rats (**C**; n = 5, 9, 8, 4, for weeks two, three, four and six, respectively) over time. **D** ADC of ENU metastasis rim and core at three (n = 9), four (n = 8), and six weeks (n = 4) post-injection. Paired Student's t-tests were performed for striata of each group (* $p < 0.05$, ** $p < 0.01$, *** $p < 0.001$). Unpaired Student's t-tests were performed for comparison of PBS and ENU-injected striata and significant increases in ADC values were detected in the tumour group compared to the PBS group at weeks three ($p < 0.01$), four ($p < 0.05$) and six ($p < 0.05$).

4.3.1.3 Decreased cerebral blood volume present in rat brain metastasis

rCBV measurements, were used to determine approximate blood volume present in healthy brain tissue voxels and in ENU brain metastases. In the ENU rat brain metastasis model, a significant decrease in rCBV was detected in brain metastases three weeks post-injection compared to the contralateral ROI ($p < 0.05$; Figure 4.5A,C) or to the PBS-injection control rats ($p < 0.01$, respectively). At this time point, a significant reduction in rCBV was also observed in the ENU tumour core compared to the tumour rim ($p < 0.05$; Figure 4.5D). Although a decrease in rCBV in brain metastasis foci was present compared to the contralateral striatum, and especially in the tumour core, rCBV measurements were only performed in 3 rats and the decrease was not statistically different. Moreover, rCBV measurements were not performed in PBS-injected control BDIX rats two weeks post-injection or in any rats at six weeks owing to the delayed addition of this technique in the MRI protocol. The presented results demonstrate that decreased rCBV is a feature of this rat brain metastasis model, especially at a later stage in tumour growth.

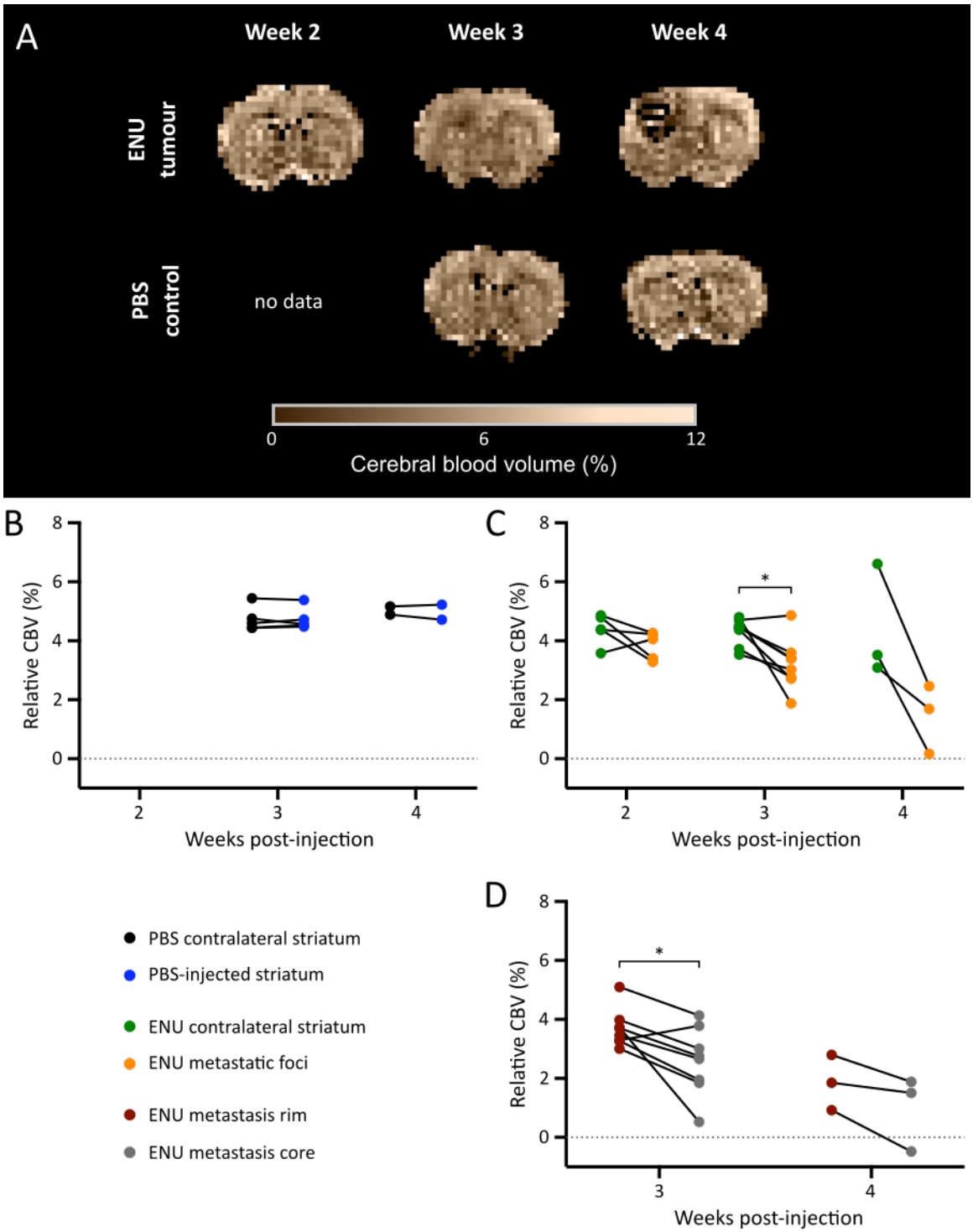

Figure 4.5 Relative cerebral blood volume of ENU brain metastases during tumour progression in BDIX rats. **A** Representative rCBV maps from ENU- and PBS-injected BDIX rats during tumour progression. Comparisons of rCBV values in the injected and contralateral striata of PBS-injected rats (**B**; $n = 5$ and 2 for weeks three and four, respectively) and of ENU-injected rats (**C**; $n = 5$, 8 and 3, for weeks two, three and four, respectively) over time. **D** rCBV of ENU metastasis rim and core at three ($n = 8$) and four weeks ($n = 3$) post-injection. Paired Student's t-tests were performed for striata of each group (* $p < 0.05$). Unpaired Student's t-tests were performed for comparison of PBS and ENU-injected striata and significant decreases in rCBV were detected in the tumour group compared to the PBS group at week three post-injection ($p < 0.01$).

4.3.2 Effect of brain metastasis on brain tissue relaxation times

4.3.2.1 T_1 relaxation time increases in ENU brain metastases

T_1 brain relaxation times were significantly increased by the presence of brain metastasis foci in rats at the tumour site, but not in the contralateral hemisphere at three and four weeks post-injection ($p < 0.001$; Figure 4.6A,C). Similarly, upon comparison with the PBS-injected striatum, T_1 relaxation times of the brain metastasis foci were significantly increased from three weeks post-injection onwards ($p < 0.001$ at weeks three and four, and $p < 0.01$ at week six). No significant differences were detected between the striata of PBS-injected rats at any time-point (Figure 4.6B). A significant increase T_1 relaxation time was present in the core of the brain metastasis foci compared to its rim at three and four weeks after tumour cell injection ($p < 0.01$; Figure 4.6D). The presence of brain metastasis foci caused a progressive increase in T_1 relaxation time in rat brains, which highlights its clinical prevalence in brain tumour imaging.

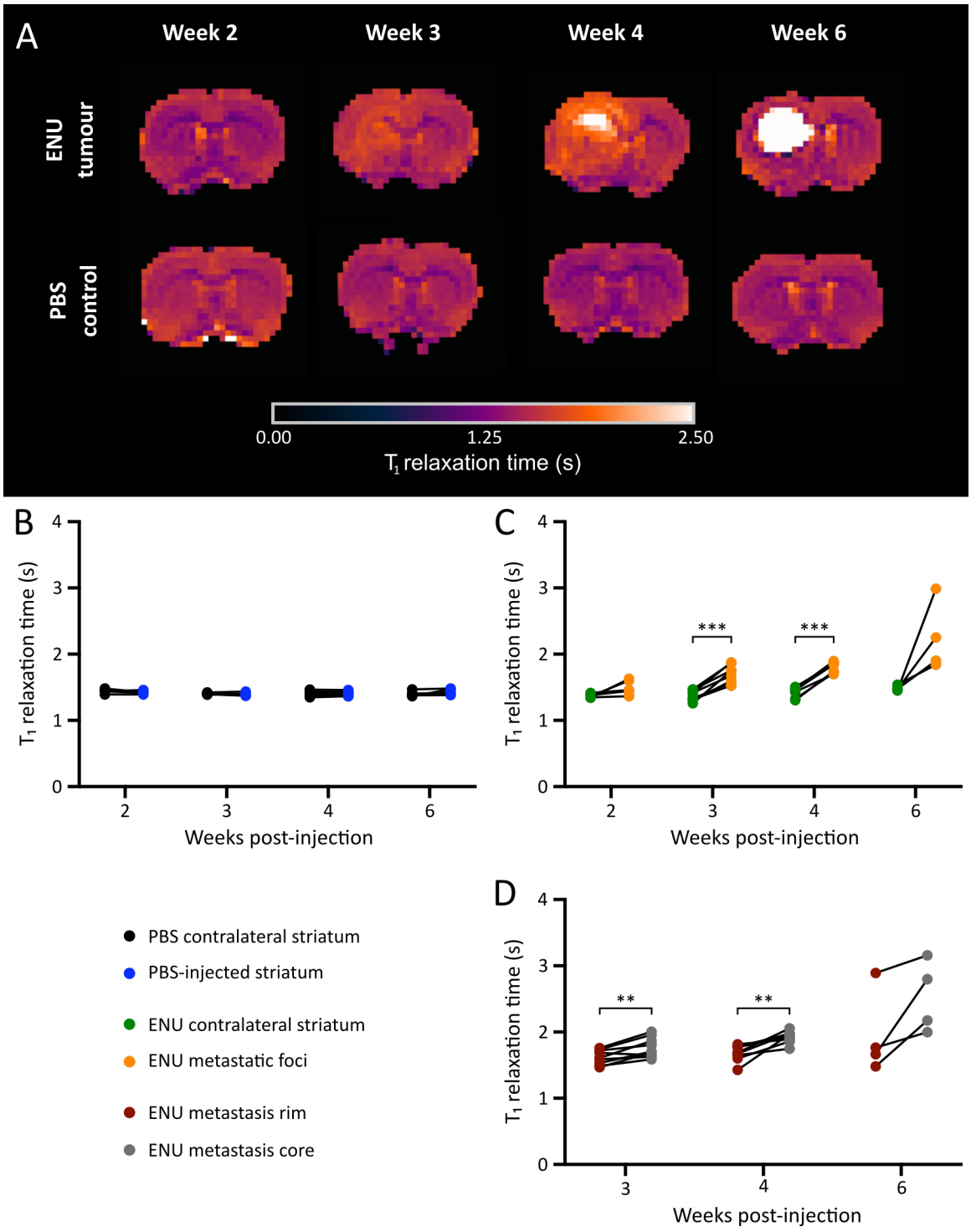

Figure 4.6 T_1 *relaxation time of ENU brain metastases during tumour progression in BDIX rats.* **A** Representative T_1 relaxation maps from ENU- and PBS-injected BDIX rats during tumour progression. Comparisons of T_1 relaxation times in the injected and contralateral striata of PBS-injected rats (**B**; n = 5, 6, 7, 5 for weeks two, three, four and six, respectively) and of ENU-injected rats (**C**; n = 5, 9, 8, 4, for weeks two, three, four and six, respectively) over time. **D** T_1 relaxation times of ENU metastasis rim and core at three (n = 9), four (n = 8), and six weeks (n = 4) post-injection. Paired Student's t-tests were performed for striata of each group (** $p < 0.01$, *** $p < 0.001$). Unpaired Student's t-tests were performed for PBS and ENU-injected striata and significant increases in T_1 relaxation times were detected in the tumour group compared to the PBS group at weeks three ($p < 0.001$), four ($p < 0.001$) and six ($p < 0.01$).

4.3.2.2 Changes of T_2 relaxation time in ENU brain metastases

T_2 brain relaxation times were significantly decreased in the brain metastasis foci compared to the contralateral striatum of ENU-injected rats following two weeks of tumour growth ($p < 0.05$) and when compared to the PBS-injected striatum ($p < 0.01$). In contrast, T_2 brain relaxation times were significantly increased in the tumour four post-injection in comparison with the contralateral striatum ($p < 0.05$; Figure 4.7A,C). This increased T_2 relaxation time at the four week time point was significantly greater in the tumour core than in the rim ($p < 0.05$; Figure 4.7D). Overall, changes in T_2 relaxation time were minimal in rat brain metastases, except when cystic necrosis was present in the tumour core.

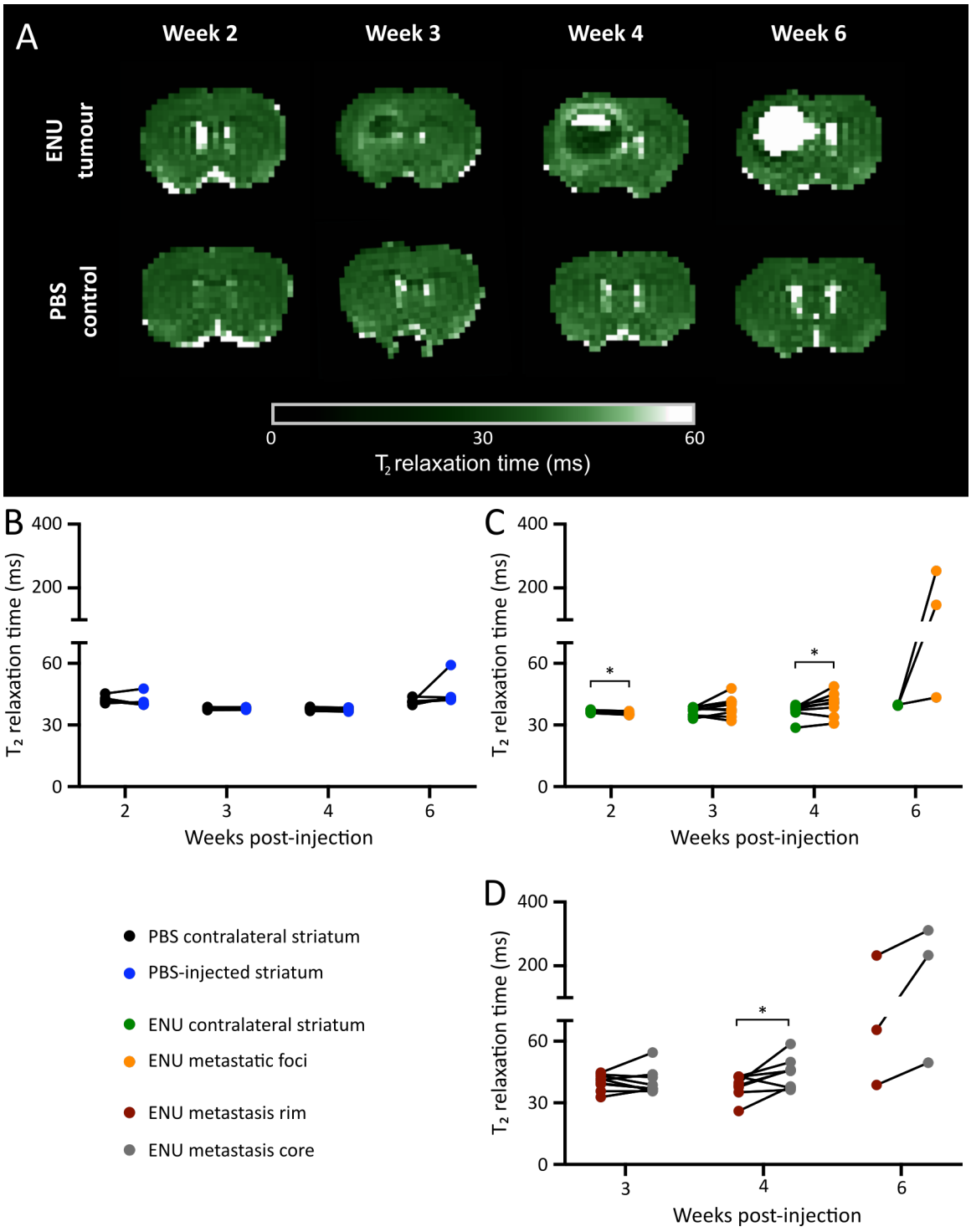

Figure 4.7 T_2 *relaxation time of ENU brain metastases during tumour progression in BDIX rats.* **A** Representative T_2 relaxation maps from ENU- and PBS-injected BDIX rats during tumour progression. Comparisons of T_2 relaxation times in the injected and contralateral striata of PBS-injected rats (**B**; n = 5, 6, 7, 5 for weeks two, three, four and six, respectively) and of ENU-injected rats (**C**; n = 5, 9, 8, 3, for weeks two, three, four and six, respectively) over time. **D** T_2 relaxation times of ENU metastasis rim and core at three (n = 9), four (n = 8), and six weeks (n = 3) post-injection. Paired Student's t-tests were performed for striata of each group (* $p < 0.05$). Unpaired Student's t-tests were performed for PBS and ENU-injected striata and a significant decrease in T_2 relaxation times were detected in the tumour group compared to the PBS group at week two of tumour growth ($p < 0.01$).

4.3.3 MP-pCASL MRI of ENU brain metastases

4.3.3.1 Bolus arrival time is increased in tumours

Arrival time of MP-pCASL MRI labelled blood from RF pulses applied in the neck was significantly delayed in ENU brain metastases three weeks post-injection of tumour cells in the left striatum compared to the blood arrival in contralateral striatum ($p < 0.001$; Figure 4.8). At 650 ms following the end of the labelling pulse train, over 97 % of voxels in the contralateral striatum had received the bolus of labelled blood compared to 85 % of the ENU brain metastasis. Since blood arrival might not occur in all tumour voxels, owing to the dysregulated blood flow often observed in tumours and the increasing loss of MP-pCASL MRI signal from the relaxation of protons at longer PLDs, a PLD of 650 ms was selected for MP-pCASL MRI in this rat model.

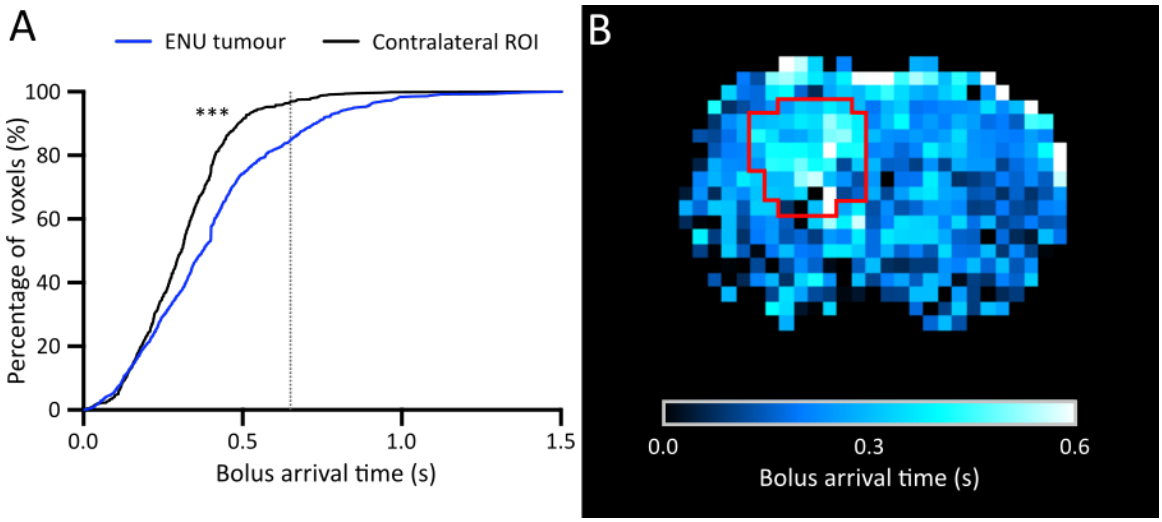

Figure 4.8 Arrival time of MP pCASL MRI labelled blood in ENU brain metastases at three weeks post-injection. **A** Percentage of voxels with blood arrival over time for the ENU tumour (blue line) and the contralateral ROI (black line) in two tumour-containing MRI slices of the MP-pCASL MRI imaging region ($n = 13$; Kolmogorov-Smirnov test, *** $p < 0.001$). Dotted vertical line represents the PLD of 650 ms, at which over 97 % of healthy brain voxels and 85 % of ENU tumour voxels had received labelled blood. **B** Representative arrival map of an ENU tumour-containing slice with the tumour area outlined in red.

4.3.3.2 Cerebral blood flow decreases as brain metastasis growth progresses

CBF was measured using the MP-pCASL MRI method described in Chapter 3. A few parameters were modified to account for the presence of dysregulated blood flow in the brain, namely, a longer PLD of 650 ms (4.3.3.1), a label duration of 2.4 s to maximise imaging efficiency and the addition of T_1 relaxation time voxel-wise priors (4.3.2.1) to the analysis of MP-pCASL MRI. In brain metastases. A significant reduction of apparent CBF in brain metastasis foci was present from three weeks post-injection of ENU-cells when compared to the contralateral ROI ($p < 0.001$ at weeks three and four, $p < 0.01$ at week six; Figure 4.9C) or to the PBS-injection control ROI ($p < 0.001$ for weeks three, four and six). This decreased perfusion in the metastasis region can clearly be observed in later weeks on CBF maps (Figure 4.9A). The reduction in CBF was significantly pronounced in the core of the ENU brain metastasis foci compared to the tumour rim at three ($p < 0.05$), four ($p < 0.001$), and six weeks post-injection ($p < 0.01$; Figure 4.9D). No significant difference in CBF could be observed in the PBS-injected rats between the injected and contralateral striata (Figure 4.9B). On the whole, CBF decreased progressively during brain metastatic growth in rats.

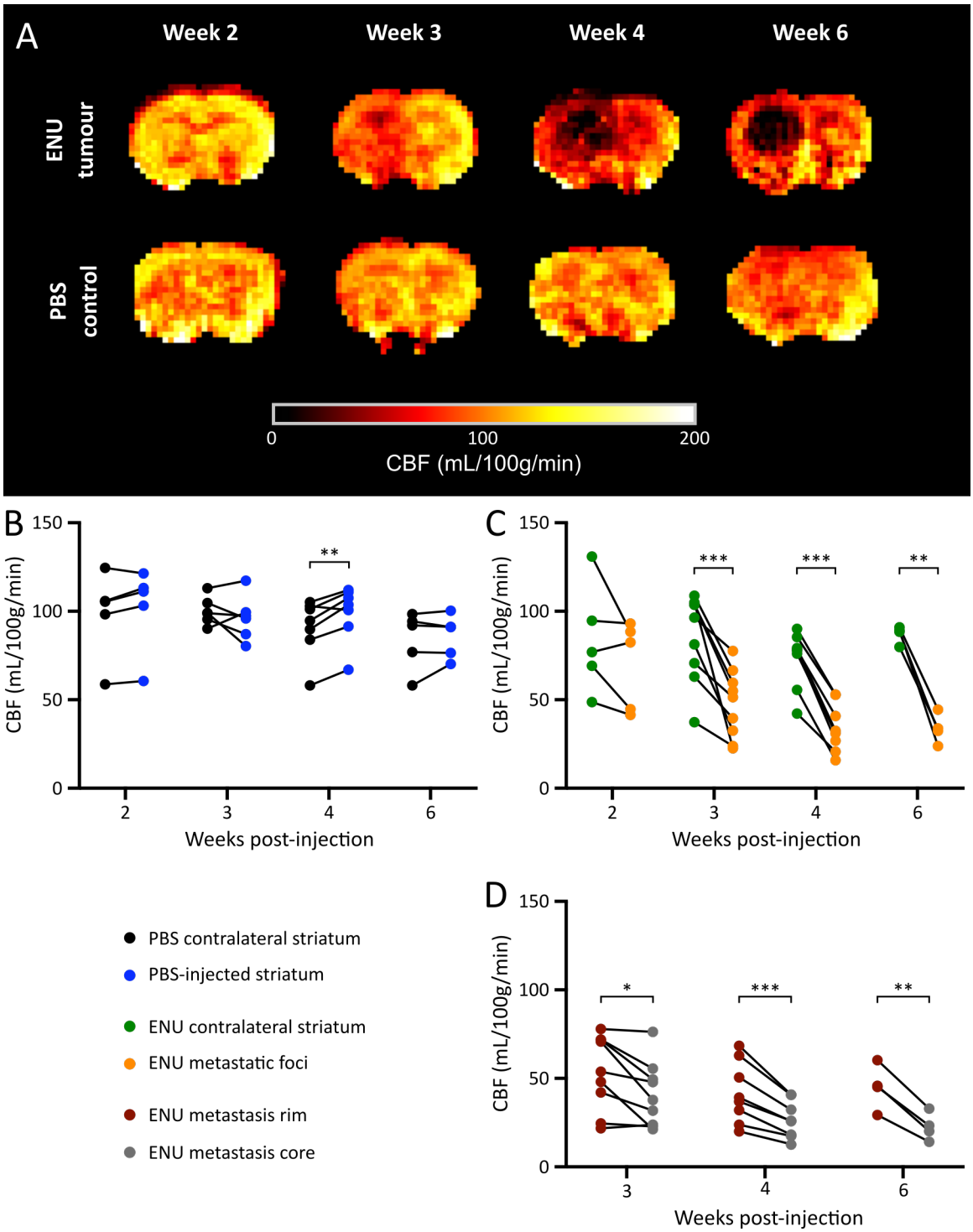

Figure 4.9 Cerebral blood flow of ENU brain metastases during tumour progression in BDIX rats. **A** Representative CBF maps of ENU- and PBS-injected BDIX rats during tumour progression. Comparisons of apparent CBF measurements in the injected and contralateral striata of PBS-injected rats (**B**; n = 5, 6, 7, 5 for weeks two, three, four and six, respectively) and of ENU-injected rats (**C**; n = 5, 9, 8, 4, for weeks two, three, four and six, respectively) over time. **D** Apparent CBF measurements of ENU metastasis rim and core at three (n = 9), four (n = 8), and six weeks (n = 4) post-injection. Paired Student's t-tests were performed for striata of each group (* $p < 0.05$, ** $p < 0.01$, *** $p < 0.001$). Unpaired Student's t-tests were performed for PBS and ENU-injected striata and a significant decrease in apparent CBF were detected in the tumour group compared to the PBS group at weeks three, four and six of tumour growth ($p < 0.001$).

4.3.4 Histological findings during ENU brain metastasis growth

4.3.4.1 Histological assessment of microvessel density

Brain metastasis microvessel density, measured by CD31 immunohistochemistry, was significantly increased in the ENU brain metastasis rim region at all weeks and in the core region at week three post-ENU cell injection compared to a healthy-appearing contralateral ROI (Figure 4.10B). As brain metastasis growth progressed to four weeks post-injection, a decrease in microvessel density in the brain metastasis core was observed between the week three and four timepoints (Figure 4.10B). Moreover, microvessel density was greater in the tumour rim compared to the tumour core after four weeks of tumour growth. Representative CD31 histology can be seen in Figure 4.10A with the higher CD31 staining (brown) present at the tumour rim and the increasing ENU tumour size (highlighted in Figure 4.10C).

4.3.4.2 Increasing hypoxic fraction during rat brain metastasis progression

The hypoxic fraction of brain metastases, detected though pimonidazole injection and subsequent immunohistochemistry, was significantly increased in the brain metastasis rim region following four weeks of tumour growth compared to the healthy contralateral ROI ($p < 0.01$; Figure 4.11B). The presence of pimonidazole staining was appeared increased in the tumour rim than its core at weeks three and four post-injection, yet this was not statistically significant. Although a trend toward an increasing pimonidazole-stained fraction can be observed during the brain metastasis progression, pimonidazole staining was not significantly increased over time. No apparent pathological hypoxic

fraction was observed in the healthy-appearing contralateral brain tissue, which was regarded as baseline levels of staining and was subtracted from the brain metastasis quantitation.

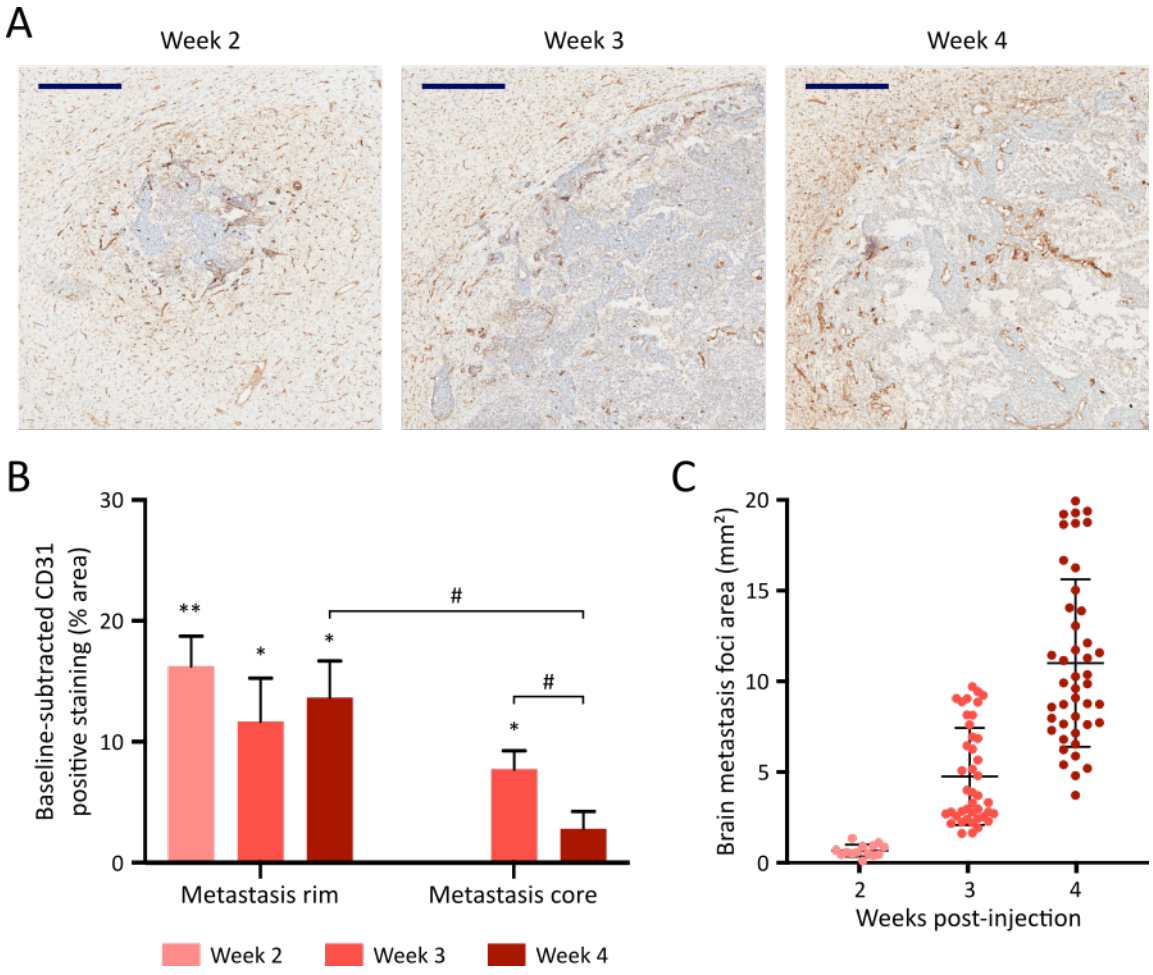

Figure 4.10 Vessel density in ENU brain metastases in BDIX rats over time. **A** CD31 immunohistochemistry (brown stain) of ENU brain metastases in BDIX rats at weeks two, three and four post-ENU cell injection, counterstained with cresyl violet (blue; scale bar = 500 µm). **B** Quantitation of baseline-subtracted CD31 positive pixels in the rim and core of brain metastasis foci by subtracting baseline contralateral in each analysed section (n = 3 rats per time-point). The entire metastasis region was considered as rim at week two (Asterisks represent statistical significance from contralateral ROI, * $p < 0.05$, ** $p < 0.01$; rim: One-way ANOVA with Tukey's multiple comparisons; core: unpaired Student's t-test; rim and core: paired Student's t-test; # $p < 0.05$). **C** ENU brain metastasis foci area of the analysed sections.

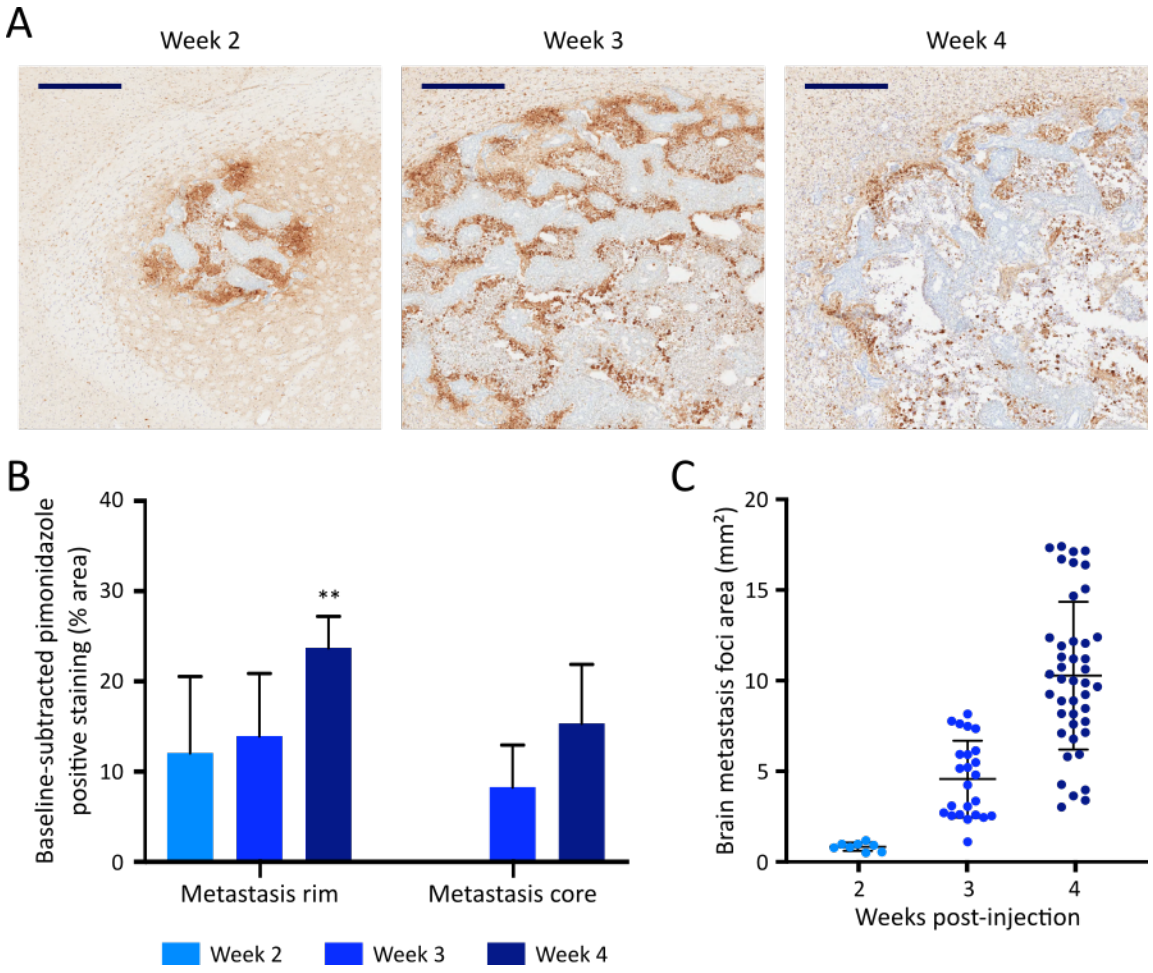

Figure 4.11 Hypoxic fraction in ENU brain metastases in BDIX rats over time. **A** Pimonidazole (pimo) immunohistochemistry (brown stain) of ENU brain metastases in BDIX rats at weeks two, three and four post-ENU cell injection, counterstained with cresyl violet (blue; scale bar = 500 µm). **B** Quantitation of baseline-subtracted pimonidazole positive pixels in the rim and core of brain metastasis foci by subtracting baseline contralateral in each analysed section (n = 3 rats per time-point). The entire metastasis region was considered as rim at week two (Asterisks represent statistical significance from contralateral ROI, ** $p < 0.01$; rim: One-way ANOVA with Tukey's multiple comparisons; core: unpaired Student's t-test; rim and core: paired Student's t-test). **C** ENU brain metastasis foci area of the analysed sections.

4.3.4.3 Histological assessment of angiogenesis in rat brain metastases

Angiogenesis in the ENU rat brain metastasis model, measured through Tie2 IHC, was significantly increased in ENU brain metastases, both in the rim and core, compared to the contralateral striatum ($p < 0.001$). In the rim region of the brain metastasis foci, the highest levels of Tie2 staining were present at the week three time point, yet these levels were not significantly greater than those present at weeks two and four post-injection in

the brain metastasis rim region (Figure 4.12B). However, a significant decrease in Tie2 levels was present in the brain metastasis core region at week four compared to week three and to the rim region at week four post-injection ($p < 0.05$, in both cases). The increased angiogenic profile observed at week three was independent of tumour size, as the tumour area per brain section continued to increase as a function of time (Figure 4.12C).

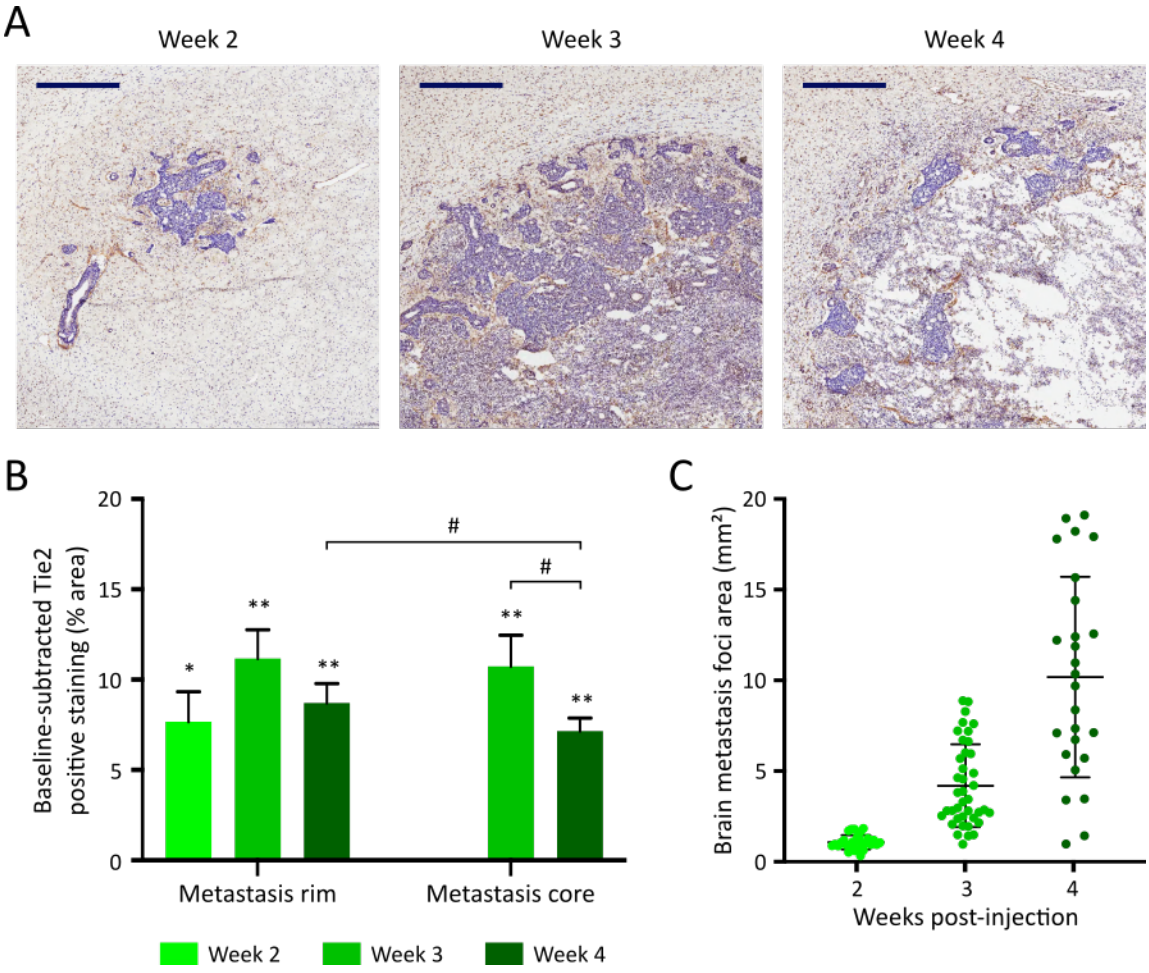

Figure 4.12 Angiogenesis in ENU brain metastases in BDIX rats over time. **A** Tie2 immunohistochemistry (brown stain) of ENU brain metastases in BDIX rats at weeks two, three and four post-ENU cell injection, counterstained with cresyl violet (blue; scale bar = 500 µm). **B** Quantitation of baseline-subtracted Tie2 positive in the rim and core of brain metastasis foci by subtracting baseline contralateral in each analysed section ($n = 3$ rats per time-point). The entire metastasis region was considered as rim at week two (Asterisks represent statistical significance from contralateral ROI, * $p < 0.05$, ** $p < 0.01$; rim: One-way ANOVA with Tukey's multiple comparisons; core: unpaired Student's t-test; rim and core: paired Student's t-test; # $p < 0.05$). **C** ENU brain metastasis foci area of the analysed sections.

4.4 Discussion

4.4.1 Clinically relevant MRI methods for imaging brain metastases

T_1-weighted pre- and post-gadolinium-based contrast agent injection in the vasculature as well as T_2-weighted anatomical MRI scans were performed here to mirror MRI methods used in the clinic for the detection and follow-up of brain metastases. These acquisitions allowed the detection of BBB breakdown and a surrogate measure of tumour volume from T_2-weighted hyperintensities in the rat brain metastasis model. Tumour volume approximations, initially increased over time yet, remained constant a later time-points, when the formation of a necrotic cyst was easily identifiable on T_2-weighted MRI images. Interestingly, BBB breakdown was not observed in all tumours at week six, likely reflecting the fact that very little tumour tissue was still present other than the tumour rim. Furthermore, fewer rats were available at week six of tumour growth since many reached the humane endpoint prior to this time. Although T_1-weighted and T_2-weighted MRI scans yield valuable information on the size and location of brain metastases, they do not provide much biological information other than the incidence of the BBB breakdown, which is why further MRI acquisitions are required in brain tumour and metastasis imaging in clinical practice and preclinical research.

The ADC from diffusion MRI is another routinely performed acquisition in clinical practice as the diffusion of water protons provides information on the interstitial space and cellularity of tissue. Decreased cellularity, indicated by elevated ADC values, was characteristic of tumour regions, but not of the healthy contralateral brain tissue, particularly at later time points. This finding is in line with the T_2-weighted acquisitions,

indicative of cystic necrosis, a feature of our model and of poor-prognosis in clinical brain metastases (Serres *et al.*, 2014; Sun *et al.*, 2016). Additionally, an increased cellularity in the tumour area was evident through a significant decrease in ADC values in the core of brain metastases at week three post-injection, and also occurred in some metastatic regions at week four. However, especially at smaller volumes, the combination of an increased ADC in the rim of the tumour and of the decreased ADC in the tumour core could potentially lead to overall tumour ADC values similar to that of healthy tissue. At larger tumour volumes, this issue is less problematic since the resolution of the tumour improves and such heterogeneity in ADC values across the tumour can be resolved.

Lastly, rCBV measurements are performed in the clinic by perfusion dynamic-susceptibility contrast (DSC) MRI or dynamic-contrast enhanced (DCE) MRI to inform on voxel blood content. Here, a slightly different approach was used, involving a blood pooling agents (USPIO) instead of a GBCAs, which is more common in preclinical MRI settings to determine the percentage of voxel that is blood (Simonsen *et al.*, 1999; Kim and Kim, 2005; Perles-Barbacaru *et al.*, 2012; Kim *et al.*, 2013). Significant decreases in rCBV were detected in the brain metastasis region when compared to healthy brain tissue, either from the contralateral ROI or PBS-injection control brains. Of note, four weeks following tumour injection, the tumour also became more heterogeneous with the appearance of necrotic areas, which may account for the increased variability observed at this time point. Biologically, this decrease in rCBV translates to a lack of perfused blood vessels in the tumour as it progresses and could, therefore, be a sign of hypoxia, necrosis or a combination of both within the brain metastasis. Such measures of rCBV, however, as noted in Chapter 3, require the injection of a contrast agent and could be dismissed for non-invasive perfusion MRI methods such as MP-pCASL MRI, especially in cases where

co-morbidities involving the kidneys are present in a patient. However, it is important to note that CBV and CBF, although related, are different aspects of perfusion MRI with CBV representing the blood *volume* (units: mL/100g) present in a voxel instead of the blood *flow* (units: mL/100g/min), which is time-dependent.

4.4.2 Brain metastases affect brain tissue relaxation times

From all MRI methods performed in this chapter, only T_2 relaxation times were significantly altered in brain metastases as early as week two post-tumour cell injection. Although the T_2 relaxation times of brain metastases foci were significantly decreased compared to those of the contralateral striatum and the PBS-injected, all relaxation times fell within a range of normal T_2 relaxation times for brain tissue at 9.4 T (De Graaf *et al.*, 2006). In this study, the brain and tumour T_2 relaxation times did not provide additional information on the brain metastasis as the presence of a cyst could already be detected on T_2-weighted anatomical images.

As for the impact on T_1 relaxation times from the presence of brain metastasis foci, a progressive increase was observed during tumour growth. This result combined with an increase in ADC values, suggested a decreased cellularity and an increased stromal or necrotic portion of the brain metastasis region over time, since T_1 relaxation times are increased in water compared to cellular tissue.

4.4.3 MP-pCASL MRI as a non-invasive method for perfusion measurement in brain metastases

As the optimisation of MP-pCASL MRI had previously been performed in naïve rat brains, some parameters required optimisation before its application to the rat brain metastasis model. Firstly, the presence of a brain metastasis in the brain leads to dysregulated blood flow in that region, which will affect the blood arrival time. However, upon exiting the labelling plane, inverted blood water protons initiate their recovery to re-align with the magnetic field. A short PLD is recommended in ASL MRI to retain higher levels of contrast between labelling conditions (label-control or multiphase), but without the circulation of labelled blood still present in the brain capillaries. The assessment of blood arrival time to the tumour was performed three weeks post-injection since ENU tumours were all visible at this point and fewer tumours possessed cystic necrosis when compared to later time points. A PLD of 650 ms was selected since over 97 % of the contralateral striatum had received labelled blood, and 85 % of the tumour. As the brain metastasis encompasses a region of dysregulated blood flow, with some voxels potentially never receiving blood in the case of hypoxia or necrosis, this PLD was deemed acceptable. The selection of a longer PLD, although allowing for increased blood arrival in brain metastasis voxels would come at the detriment of signal loss. However, by selecting a PLD shorter than the arrival time of blood in some tumour voxels, blood flow may be overestimated in these voxels owing to circulation of labelled blood in this region. Interestingly, although the CBF was altered in the tumour, it was through a significant decrease, not increase, in perfusion from three weeks following ENU-injection. As a result, we can confirm that MP-pCASL MRI derived CBF in tumours provides biologically relevant information on rat brain metastases with respect to the vascular changes occurring during

brain metastasis growth. In addition to the longer PLD, a label duration of 2.4 s was used in MP-pCASL MRI for brain metastasis-bearing rats, since the peak MP-pCASL MRI imaging efficiency was previously determined to be at this label duration (Chapter 3, Figure 3.14). Furthermore, since tissue T_1 relaxation values were affected in the present of brain metastases, a T_1 map image prior was incorporated in the MP-pCASL MRI analysis to utilise voxel-specific T_1 relaxation values in the analysis to obtain more accurate CBF measurements by accounting for the relaxation rate in tissue following the proton exchange with circulating blood.

4.4.4 Relating histological findings of ENU brain metastasis progression to MRI results

The microvessel density of brain metastasis foci was increased compared to the contralateral striatum, a finding which agrees with the typical angiogenic profile of tumours. However, this increased presence of vasculature did not correlate with the decreased perfusion detected by MRI. Although the CD31 staining levels were globally increased in the brain metastasis region compared to the contralateral striatum, it is possible that these tumour associated vessels were non-perfused. To investigate this possibility, the injection of tomato lectin through a tail vein of the rats, prior to perfusion-fixation, was attempted, in order to only detect perfused vessels of the tumour. However, owing to BBB breakdown, there was an accumulation of dye within the brain metastasis, increasing the level of background noise to the extent that perfused vessels were not detected accurately (Appendix II). Alternatively, since only a positive pixel count was performed in these histological sections, it could be that the increase in CD31 positive staining is not attributed to a higher number of blood vessels, but rather an increase in

vessel size within the brain metastases or a combination of the two. Further analysis would need to be performed looking at the number and size of vessels present in the tumour before drawing further conclusions. Additionally, it is possible that the MRI resolution used was too poor to detect the increased perfusion in areas of the brain metastasis foci, especially since the large metastasis region is essentially an aggregate of many micrometastases.

The ENU brain metastases were found to possess greater levels of pimonidazole staining over time, which correlated with the decreasing microvessel density as well as the decreased rCBV and CBF MRI measurements. Interestingly, a greater number of pimonidazole staining was detected in the rim of the tumour compared to the core, although not significant; this reflected the presence of cystic necrosis in the core of these tumours leading to an absence of tumour cells in this region and, thus, lower accumulation of pimonidazole.

Finally, the angiogenic profile of the brain metastases was determined to further characterise this brain metastasis model in order to determine its potential response to anti-angiogenic treatments in subsequent chapters (Chapters 5 and 6). The number of Tie2 positive pixels was significantly increased compared to healthy tissue in the contralateral striatum, indicating an increase in angiogenesis in the brain metastasis region. Of note, the ENU brain metastases were significantly more angiogenic at three weeks post tumour cell injection in the brain metastasis core than at week four post-injection. No significant decrease in microvessel density had yet been observed by this time point, possibly indicating the angiogenic profile of the growing brain metastases. Further, brain metastasis foci were still relatively small after two weeks of growth and less likely to require the additional nutrients brought forth by angiogenesis. Moreover, by

four weeks of growth, the brain metastases were increasingly necrotic and/or cystic and, therefore, a smaller fraction of the tumour cells could promote angiogenesis at this time compared to one week prior. Thus, in the ENU rat brain metastasis model, the application of anti-angiogenic therapy or vascular normalisation at this time point in tumour progression may yield a maximal effect (see Chapters 5 and 6).

4.5 Conclusion

In the present chapter, the characterisation of a rat brain metastasis model through focal injection in the striatum was performed by multi-parametric MRI and histological analysis at several time-points across tumour progression. This experimental platform enabled the comparison of the rat optimised MP-pCASL MRI method described in Chapter 3 to clinically relevant MRI methods. In summary, T_1-weighted and T_2-weighted anatomical MRI scans were effective for the detection of brain metastasis location and size, but provided little biological information on the tumour for treatment planning purposes and required the use of exogenous contrast agents. Diffusion MRI, as currently performed in clinical practice for ADC determination, exhibited a biphasic effect of ADC increase and decrease in this brain metastasis model, which could potentially mask the tumour if it were to occupy a small volume in the brain. Perfusion MRI was performed by two separate techniques to yield rCBV and CBF measurements and both showed decreases in brain metastasis perfusion over time. The determination of brain metastasis rCBV required the use of GBCAs, and variability between brain metastasis results was greater than that observed in CBF, although smaller samples sizes available for this imaging technique and could be responsible for this variability. In comparison, MP-pCASL MRI provided a non-invasive way to determine cerebral and tumour blood flow and was adjusted to better fit this tumour model with (i) a longer PLD allowing labelled blood arrival to the tumour, and (ii) the incorporation of voxel-wise T_1 relaxation time image prior in the analysis to accurately represent the biological changes taking place in tumour tissue.

The MRI results from brain metastasis foci were compared to the contralateral striatum in the same rats as well as to PBS-injected striata, both of which represented healthy tissue. Overall, as there was little difference observed between the contralateral striatum from ENU-injected rats and the PBS-injected striata, the contralateral striatum was selected as healthy tissue to provide an internal standard during imaging and to reduce the total number of rats required for brain metastasis studies.

Histological results of pimonidazole staining over time were in agreement with the decreases in rCBV and CBF observed by MRI, present at times of reduced microvessel density and increasing tumour hypoxic fractions. Finally, histological analysis for angiogenesis showed that these brain metastases are angiogenic, particularly at three weeks post-injection, which is in agreement with the microvessel density and hypoxia findings at this time point, since these were not significantly altered from the two week post-injection time point, even though the size of the brain metastasis region was increased. The increase in angiogenesis at this time point and tumour size was used to inform future therapeutic experiments in this brain metastasis model (Chapters 5 and 6).

In conclusion, MP-pCASL MRI was shown to reliably and reproducibly detect decreases in brain metastasis blood flow and could be used as a replacement for current MR perfusion methods requiring injection of exogenous contrast agents, such as blood-pooling agent-derived, and potentially DSC-MRI derived, rCBV measurements. MP-pCASL MRI measurements were decreased in hypoxic regions of the brain metastases, assessed histologically, and thus could provide valuable biological information for treatment planning of brain metastasis.

CHAPTER 5

Vascular normalising effects of bevacizumab treatment in rat brain metastases

5.1 Introduction

5.1.1 Vascular normalisation

Vascular normalisation was previously described in section 1.5.2. Briefly, it consists of an anti-angiogenic therapy whereby the disorganised, leaky and newly formed immature vessels of tumours are normalised to more closely resemble the hierarchical structure of healthy tissue vasculature through an inhibition of neo-angiogenesis (reviewed in Goel *et al.*, 2011). This normalisation of the tumour vasculature allows the maturation of existing vessels by increasing the coverage of vessels with perivascular cells, such as pericytes and end-feet of astrocytes in the brain, for a more intact blood-brain barrier (Benjamin *et al.*, 1999; Carmeliet and Jain, 2011; Fakhrejahani and Toi, 2012). This maturation of tumour vasculature is often accompanied by an increase in tumour oxygenation and reduction in tumour hypoxia. The vascular normalisation therapeutic window is typically of short

duration since prolonged administration of anti-angiogenic agents or administration of high doses of anti-angiogenic treatment will exert negative effects on treatment outcome (Jain, 2005). During the vascular normalisation therapeutic window, an improved delivery of chemotherapeutic agents to the tumour and an improved response to radiotherapy have been detected (Goel *et al.*, 2011).

5.1.2 Bevacizumab

Bevacizumab, also known under the trade name Avastin®, is the most commonly used clinical vascular normalisation agent. Bevacizumab is a recombinant humanised monoclonal IgG1 antibody that targets the vascular endothelial growth factor A (VEGF-A). Bevacizumab blocks the interaction between VEGF-A and the VEGF receptors 1 and 2 (VEGF-R1 and VEGF-R2), thereby inhibiting the neo-angiogenesis signalling cascade. According to NICE technology appraisal guidance, bevacizumab is used in the clinic as a vascular normalising agent in combination therapies for the treatment of metastatic colorectal cancer (TA118, TA212 & TA242), metastatic breast cancer (TA214 & TA263), advanced ovarian cancer (TA284), platinum-sensitive advanced ovarian cancer (TA285) and advanced and/or metastatic renal cell carcinoma (TA178; NICE 2019). Bevacizumab has also been approved by the United States Food and Drug Administration (FDA) as part of the treatment regime for glioblastoma (Iwamoto and Fine, 2010), providing evidence that it can successfully cross a compromised BBB.

Preclinical research using bevacizumab in mice has reported similar findings, with an improvement of glioblastoma oxygenation and an increased tumour sensitivity to ionising radiation (McGee *et al.*, 2010). Preclinical tumour model studies with bevacizumab have also demonstrated that the vascular normalisation window occurs rapidly (≤ five days

following treatment) in mice and rats (Dings *et al.*, 2007; McGee *et al.*, 2010; Pishko *et al.*, 2015). Upon vascular normalisation, Dickson and colleagues have demonstrated a decrease in microvessel density in neuroblastoma xenografts treated with bevacizumab together with an increased pericyte coverage of existing tumour vasculature, increasing the vascular maturation index; defined as vessels covered by perivascular cells such as pericytes (Dickson *et al.*, 2007). The increased intratumoural vessel coverage and, thus, maturation, also leads to a decreased vascular permeability and results in improved delivery of chemotherapeutic agents, such as topotecan, paclitaxel, irinotecan and temozolomide (Frumovitz *et al.*, 2017; Lu *et al.*, 2019). Preclinical treatment with bevacizumab has also shown a reduction in the rate of tumour growth in mice with soft tissue sarcoma, squamous cell carcinoma and breast cancer, among others (Okada *et al.*, 2010; Yoshida *et al.*, 2018; Gu *et al.*, 2019).

5.1.3 Current detection method of vascular normalisation in tumours

In the clinic, vascular normalisation, either through treatment with bevacizumab or another vascular normalisation agent, is currently detected by dynamic contrast-enhanced (DCE) MRI. As the name suggests, this MRI technique requires the injection of a gadolinium-based contrast agent (GBCA) in the vasculature and follows the rate at which this GBCA exits the vasculature through the disrupted BBB at the site of the tumour. The accurate detection of vascular normalisation in tumours is of the utmost importance as the therapeutic treatment window, where the tumour would benefit from radio- or chemotherapy, is short lived. As mentioned in Chapter 4, the use of GBCAs can be contraindicated for repeated imaging or in patients with comorbidities involving the

kidneys. Therefore, a new detection method for vascular normalisation without the required injection of exogenous contrast agents would provide a clear advantage over the current clinical MRI detection method.

In the present chapter, the effects of bevacizumab, in the previously described rat brain metastasis model, were assessed by imaging before and after bevacizumab or saline control treatment. The MRI protocol consisted of the MRI techniques performed in Chapter 4, with the exception of cerebral blood volume measurements and T_2 relaxation maps, as the former was be replaced by MP-pCASL MRI, as the perfusion MRI technique, and the latter showed no significant difference between brain metastases and healthy brain tissue. DCE MRI was conducted as a vascular normalisation detection control and to allow comparison of the proposed non-invasive MP-pCASL MRI with the current clinical detection method.

Additionally, chemical exchange saturation transfer (CEST) MRI was carried out to detect changes in tumour protein concentration and/or pH potentially occurring following treatment with bevacizumab. Briefly, CEST MRI is a non-invasive technique, in which the chemical exchange of protons between water and macromolecules, after radiofrequency saturation pulses, enables the quantitation of macromolecule ratios or concentrations in the tissue, which would normally be too small to detect (reviewed in Van Zijl and Yadav, 2011; Wu *et al.*, 2016). Through a series of saturation pulses at a resonant frequency specific to one type of macromolecule, such as the amide protons in the backbone of proteins or peptides or amine protons in protein side chains, an increasing saturation of protons in the water pool will occur, based on the proton exchange rate between the macromolecules and water. The exchange rate itself is

dependent on factors such as the concentration of the macromolecules in the tissue, the temperature and the tissue pH. CEST MRI has shown to be able to differentiate between brain tumour grades, and tumours from oedema and radiation necrosis through elevated protein concentrations (Zhou *et al.*, 2003, 2011; Zhao *et al.*, 2013; Togao *et al.*, 2014; Park *et al.*, 2015).

Following the imaging studies, histological analysis of brain metastasis tissue was performed to detect possible changes in microvessel density, pericyte coverage and the vascular maturation index, as well as changes in the hypoxic fraction following treatment with bevacizumab.

5.1.4 Chapter aims

The main aims of this chapter were to establish vascular normalisation in a rat breast cancer brain metastasis model and to determine the sensitivity of MRI techniques that do not require the injection of GBCAs, such as MP-pCASL MRI, CEST MRI, diffusion MRI or T_1 relaxation mapping, for detection of this vascular normalisation

5.1.4.1 Hypotheses

(1) Bevacizumab can normalise the vasculature of rat brain metastases within two days post-treatment.

(2) As a consequence of vascular normalisation from treatment with bevacizumab,

   a. K^{trans}, the permeability factor measured by DCE MRI decreases in brain metastases owing to the maturation of existing tumour vessels, while remaining stable in saline control brain metastases;

b. CBF measurements from brain metastases remain stable or increase, while those from saline control-treated brain metastases, decrease progressively;

c. APTR* values from brain metastases remain stable or increase, while those from saline control-treated brain metastases, decrease progressively;

d. ADC values decrease resulting from a greater tumour cell density surrounding mature tumour vasculature, while those from saline control brain metastases progressively increase;

e. tumour T_1 relaxation values decrease in brain metastases to more closely resemble those of healthy tissue, while remaining elevated in saline control brain metastases;

f. histologically, the microvessel density of the brain metastases decreases owing to the inhibition of neo-angiogenesis, while remaining stable in saline control brain metastases;

g. pericyte coverage of existing vessels increases upon vascular normalisation compared to saline control brain metastases, thereby increasing the vascular maturation index;

h. a reduction in pimonidazole positive staining in brain metastases indicates a decrease in hypoxic levels, while hypoxic levels in saline control brain metastases increase.

5.2 Methods

5.2.1 Rat breast cancer brain metastasis model

Please refer to section 2.2.1 for rat brain metastasis injection protocol.

5.2.2 Experimental plan

Brain metastasis progression was followed closely through T_1-weighted and T_2-weighted imaging twice a week from two weeks post-intracerebral injection. Once the observed T_2 hyperintensity volume in the injected rat brain hemisphere exceeded 10 mm^3, rats were assigned to the control or bevacizumab treatment group based on brain metastasis volume estimates, to ensure tumours were evenly distributed between groups.

Preliminary results, performed in 8 rats (4 per treatment group) indicated a decreased K^{trans} 2 days following treatment with bevacizumab, with K^{trans} values increasing following this time point, as previously suggested in the literature (reviewed in Goel *et al.*, 2011).

Prior to treatment, baseline rat MRI was performed: MP-pCASL MRI, CEST MRI, diffusion MRI, T_1 relaxation mapping, DCE MRI, T_2-weighted imaging and T_1-weighted pre- and post-gadolinium imaging. This MRI session was immediately followed by the injection of 10 mg/kg of bevacizumab (or equivalent volume of saline in control rats) through the tail vein cannula. MRI was performed once again 2 days after treatment, subsequently, a subset of rats from each group was injected with pimonidazole-HCl and, 3 hours later were killed by exsanguination with perfusion-fixation (section 2.2.2) for histological analysis at this time point. The remaining rats were imaged one final time at 5 days post-

treatment and injected with pimonidazole-HCl 3 hours before being culled by perfusion-fixation. This later time point was selected based on the humane end point of this tumour model and to determine if the vascular normalisation effects could be retained over a few days or very transient. A schematic of this animal experimental plan is shown in Figure 5.1.

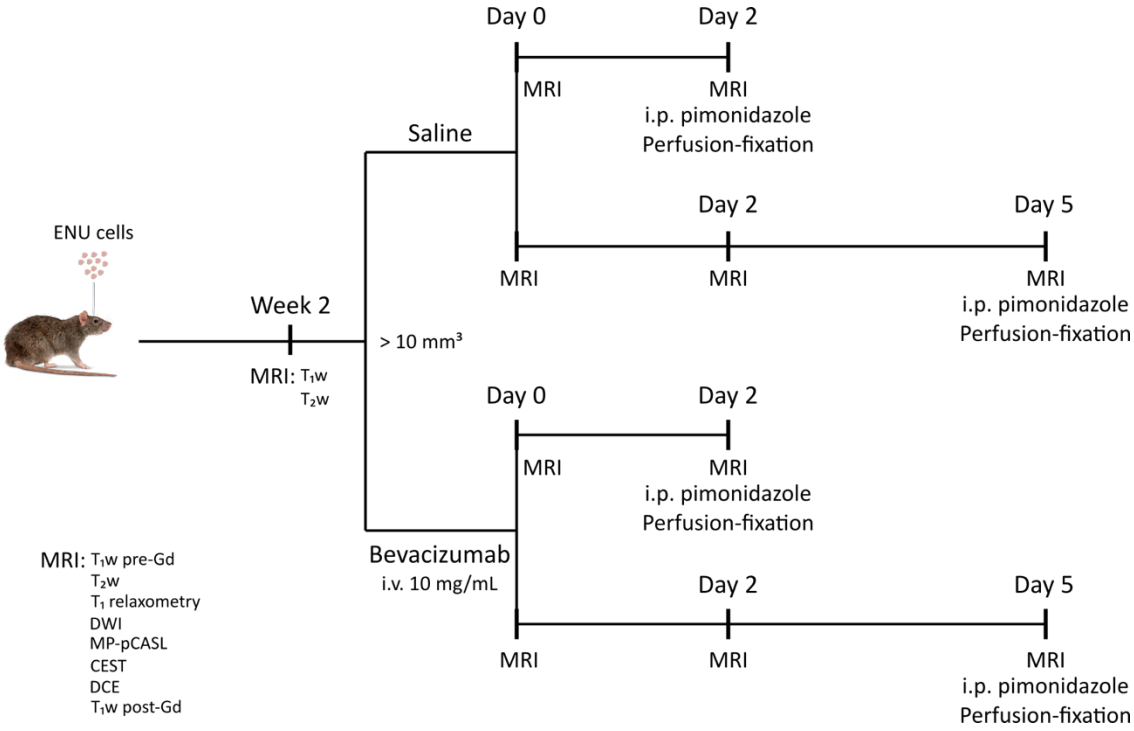

Figure 5.1 Rat experimental plan for bevacizumab treatment and imaging in brain metastases. Rats were followed from 2 weeks post-injection onwards, until tumour volume estimates from T_2-weighted MRI were greater than 10 mm^3. Bevacizumab treatment or saline control were administered after MRI on Day 0.

5.2.3 Bevacizumab

Bevacizumab (Avastin®, Roche), was obtained from the Pharmacy Distribution Department of the Oxford University Hospitals NHS Foundation Trust (Churchill Hospital, Oxford, UK). The treatment dose and regime were selected based on the European Medicines Agency's (EMEA) Avastin® information document and previous rat brain

tumour bevacizumab studies (European Medicines Agency, 2005; Yang *et al.*, 2018). According to EMEA, bevacizumab possesses a bioavailability of 69 % when administered intraperitoneally or subcutaneously; consequently, the antibody was injected intravenously in the present study. Furthermore, the EMEA Avastin® information document reports that following an intravenous injection of 10 mg/kg in rats, the half-life of bevacizumab is of 12.3 $\pm$ 3.2 days, therefore, a single injection of bevacizumab was selected for a study duration of five days post-treatment. Thus, bevacizumab treatment was administered in a single dose of 10 mg/kg intravenously following baseline MRI. Rats were monitored by observation twice a day and weighed daily following bevacizumab injection to detect whether secondary effects of the drug were present; no secondary effects were noticed in any bevacizumab-treated rat.

5.2.4 Magnetic resonance imaging

MRI was performed on all rats as described in section 2.3. Methods and analyses for the MRI techniques used herein are described in the sections presented in Table 5.1.

Table 5.1 Location of MRI technique-specific methods and analysis protocols.

MRI technique	Section
T_2-weighted imaging	2.3.4
T_1-weighted imaging (pre/post-gadolinium)	2.3.3
Diffusion MRI	2.3.2
T_1 relaxation mapping	2.3.6
MP-pCASL MRI	2.3.1
CEST MRI	2.3.7
DCE MRI	2.3.5

5.2.5 Immunohistochemistry

5.2.5.1 Immunohistochemistry protocol and antibodies

IHC was performed targeting the endothelial marker CD31 (AF3628, R&D Systems, Abingdon, UK), the hypoxia gold-standard marker pimonidazole HCl (Hypoxyprobe, Burlington, USA) and pericytes using α-smooth muscle actin (ab7817, Abcam, Cambridge, UK).

Table 5.2 Immunohistochemistry antibodies and concentrations

IHC antigen	*Blocking solution*	*Primary antibody concentration*	*Secondary antibody and concentration*
CD31 Polyclonal goat IgG	Normal horse serum	1:200	Goat raised in horse; 1:200
Pimonidazole HCl Monoclonal mouse IgG	Normal horse serum	1:100	Mouse raised in horse; 1:200
αSMA Monoclonal mouse IgG	Normal horse serum	1:100	Mouse raised in horse; 1:200

Please refer to section 2.4.3 for the standard IHC protocol and to section 2.4.2 for the antigen-retrieval protocol used for αSMA, prior to standard IHC protocol.

5.2.5.2 Immunohistochemistry analysis

Analysis of stained sections was performed as described in section 2.4.4. Brain sections, every 200 μm across the brain metastasis region were selected for each antibody IHC. Mean brain metastasis foci positive staining was determined for each rat (13 ± 5 sections per rat, depending on brain section quality and tumour volume) and averaged for analysis and comparison between treatment groups at each time point. Baseline levels of staining were subtracted from both brain metastasis rim and core regions to correct for the

variability in staining intensity and background staining observed at different days. No differences could be visually detected between the contralateral striata of metastasis-bearing rats of any treatment group compared to PBS-injected rats or naïve rats, used in previous chapters.

5.3 Results

Rat brain metastasis volume approximations were measured on T_2-weighted anatomical images (Figure 5.2A) and relative tumour growth was calculated as tumours progressed following treatment with bevacizumab or saline as vehicle control injection. No significant differences were present between the estimated brain metastasis volumes between treatment groups or in relative tumour growth between groups at either time point (Figure 5.2B). However, brain metastasis volumes significantly increased from two days to 5 days after treatment in both groups (Figure 5.2C).

5.3.1 Dynamic contrast-enhanced MRI for detection of vascular normalisation with bevacizumab

DCE MRI, the current clinical detection method for vascular normalisation, was performed to generate K^{trans} maps, representing the leakiness of brain metastases within the brain parenchyma. No significant differences in K^{trans} were detected in either the bevacizumab treatment group or the control group at baseline or at any time point following treatment (Figure 5.3). This finding suggests that vascular normalisation did not take place in this model, or that the vascular normalisation window did not overlap with the selected time points. However, other clinically-relevant MRI techniques as well as MP-pCASL MRI were performed to determine whether other changes were evident between groups.

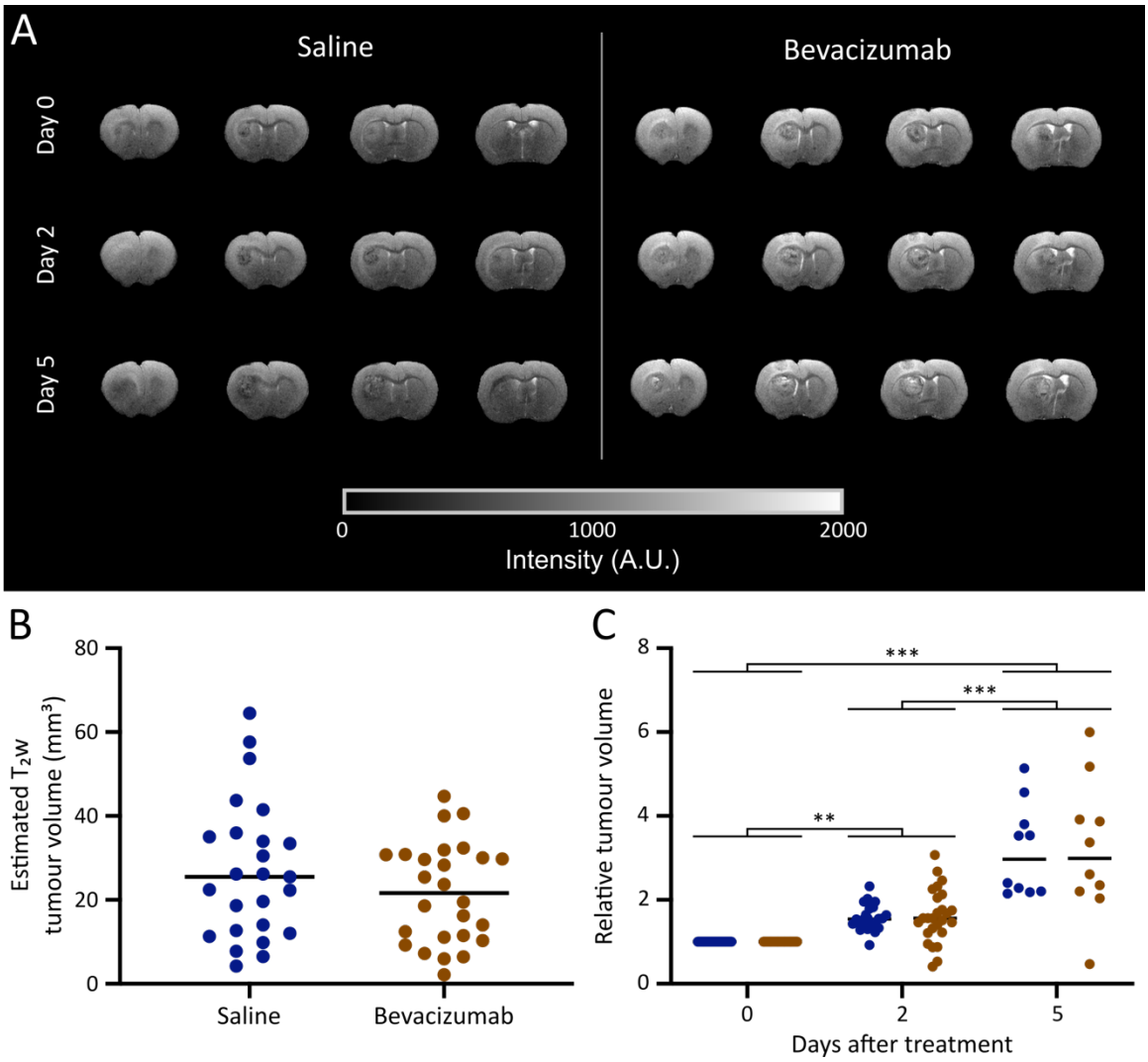

Figure 5.2 Anatomical changes in brain metastases treated with bevacizumab. **A** Representative T_2-weighted anatomical images from saline or bevacizumab-treated (10 mg/kg i.v.) rats before treatment (day 0) or 2 and 5 days after treatment. Images were taken from the same rat at different time points. **B** Detectable tumour volume on T_2-weighted MRI images prior to treatment. Each point represents one brain metastasis bearing rat (n = 25 for saline control; n = 26 for bevacizumab). **C** Relative growth of brain metastases over time compared to starting volume measured on T_2-weighted images (n = 25 and 10 for saline control at days 2 and 5, respectively; n = 26 and 10 for bevacizumab at days 2 and 5, respectively; *** $p < 0.001$; Student's t-test).

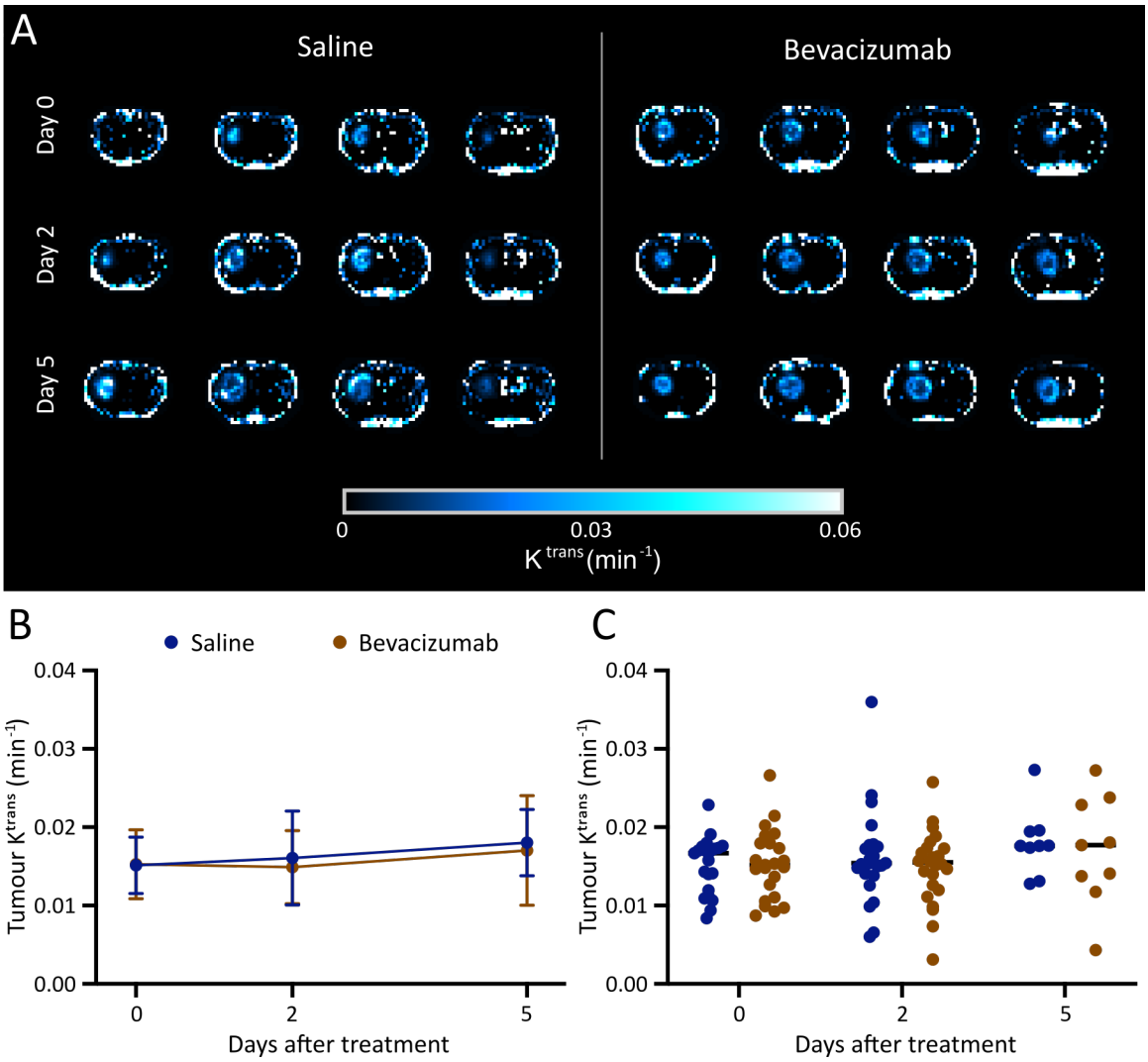

Figure 5.3 Brain metastasis permeability following bevacizumab treatment. **A** Representative K^{trans} maps calculated from DCE MRI in saline (left) and bevacizumab (right) treated rats at baseline, 2 days and 5 days after treatment (10 mg/kg i.v.). K^{trans} maps shown were taken from the same rat at different time points in each treatment condition. **B-C** K^{trans} measurements in saline and bevacizumab-treated brain metastases over time. Data are represented as the mean ± standard deviation (**B**) and for each individual metastasis-bearing rat (**C**; from left to right, n = 21, 23, 24, 24, 9, 9).

5.3.2 GBCA-free MRI of bevacizumab-treated rat brain metastases

CBF measurements from MP-pCASL MRI (Figure 5.4) together with amine proton transfer ratio (APTR*) from CEST MRI (Figure 5.5) yielded no significant differences between the bevacizumab and control-treated rat brain metastasis groups at baseline or

at either the two day or five day time points following treatment. Small, but not significant decreases could be observed for both CBF and APTR* over time. Similarly, the ADC (Figure 5.6) and T_1 relaxation times (Figure 5.7) of brain metastases did not display significant differences between treatment groups at any time point and remained unchanged over the treatment period.

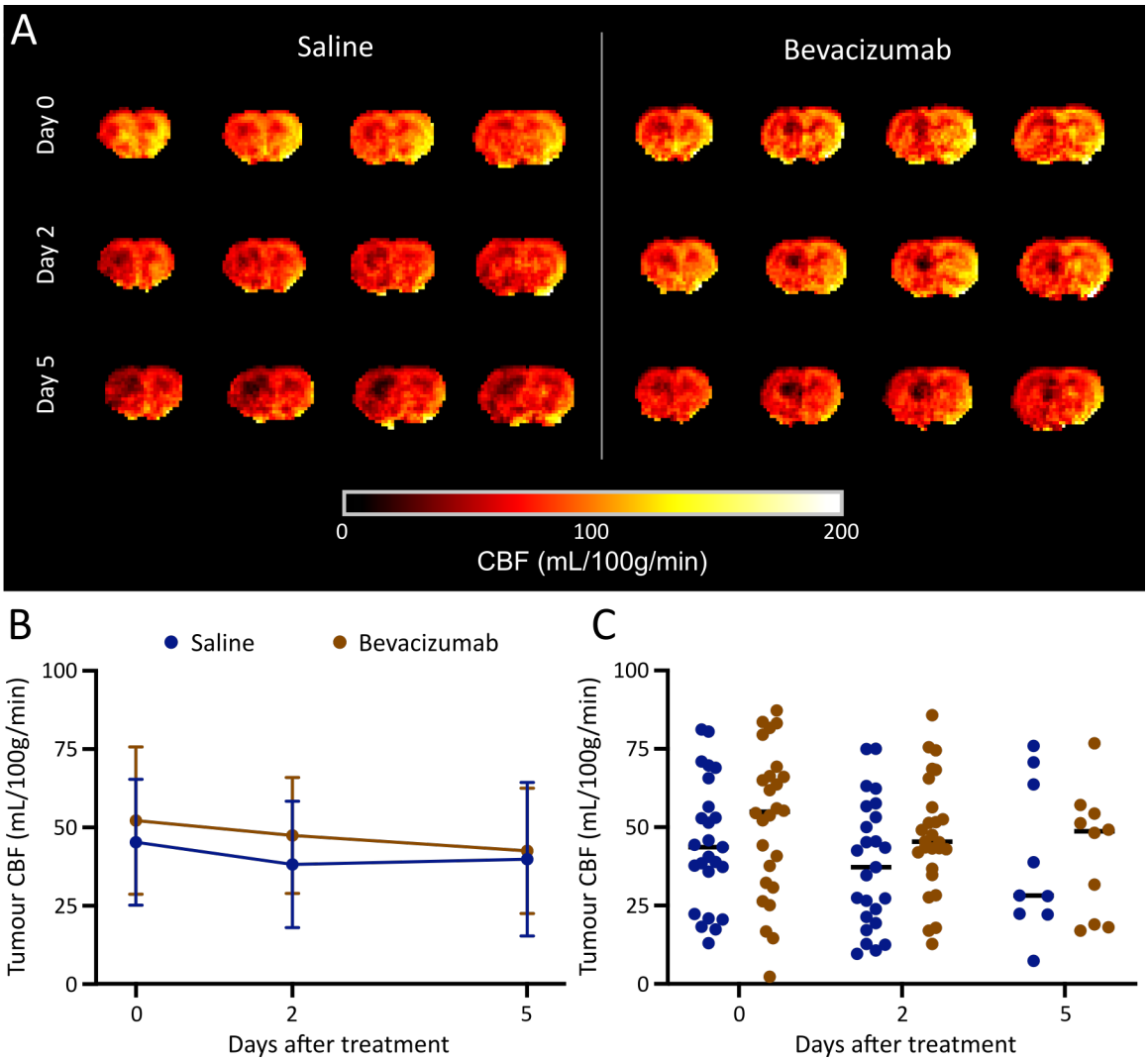

Figure 5.4 Cerebral blood flow in bevacizumab-treated brain metastases over time. **A** Representative apparent CBF maps from a saline (left) and bevacizumab (right; 10 mg/kg i.v.) treated rat over time. **B-C** CBF measurements over time shown as mean ± standard deviation (**B**) and for each individual metastasis-bearing rat (**C**; from left to right, n = 25, 26, 25, 26, 9, 10).

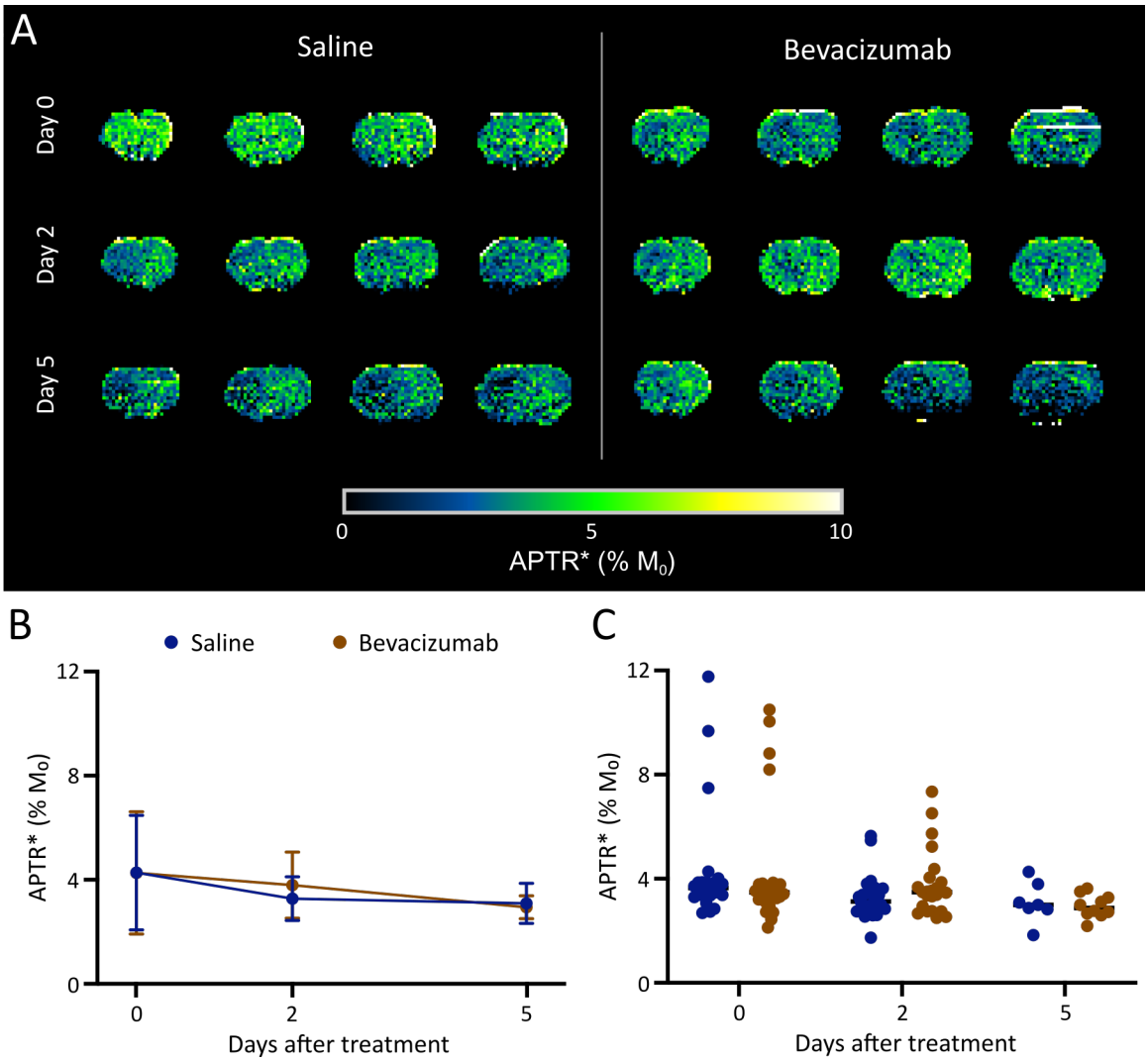

Figure 5.5 Variations in APTR signal of brain metastases treatment with bevacizumab.* **A** Representative APTR* maps from CEST MRI from a saline (left) and bevacizumab (right; 10 mg/kg i.v.) treated rat over time. **B-C** APTR* measurements over time shown as mean ± standard deviation (**B**) and for each individual metastasis-bearing rat (**C**; from left to right, n = 24, 25, 25, 23, 7, 10).

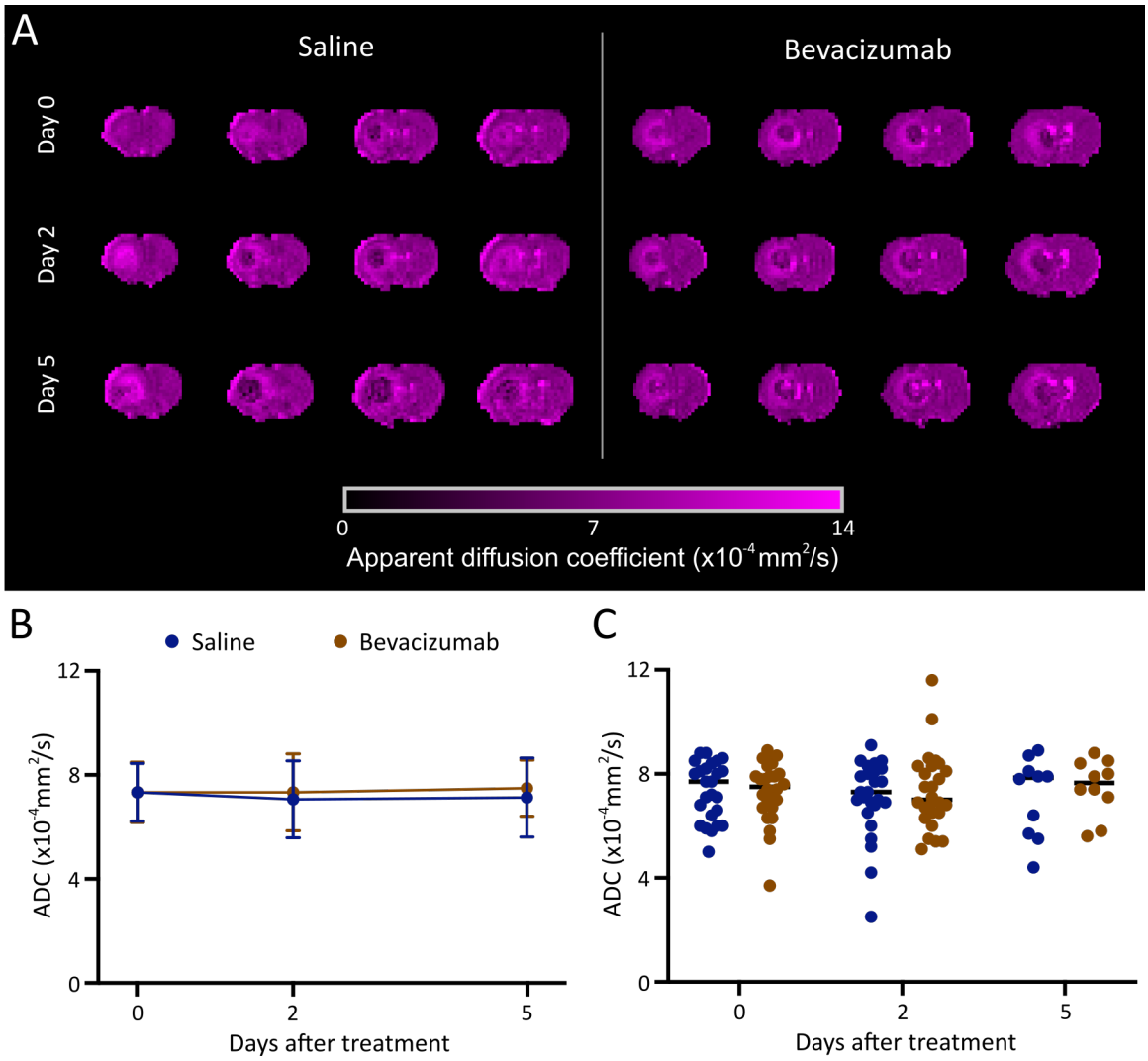

Figure 5.6 Tissue water diffusion in bevacizumab-treated brain metastases. **A** Representative ADC maps generated from diffusion MRI acquisitions from a saline (left) and bevacizumab (right; 10 mg/kg i.v.) treated rat over time. **B-C** ADC values over time shown as mean ± standard deviation (**B**) and for each individual metastasis-bearing rat (**C**; from left to right, n = 25, 26, 25, 26, 10, 10).

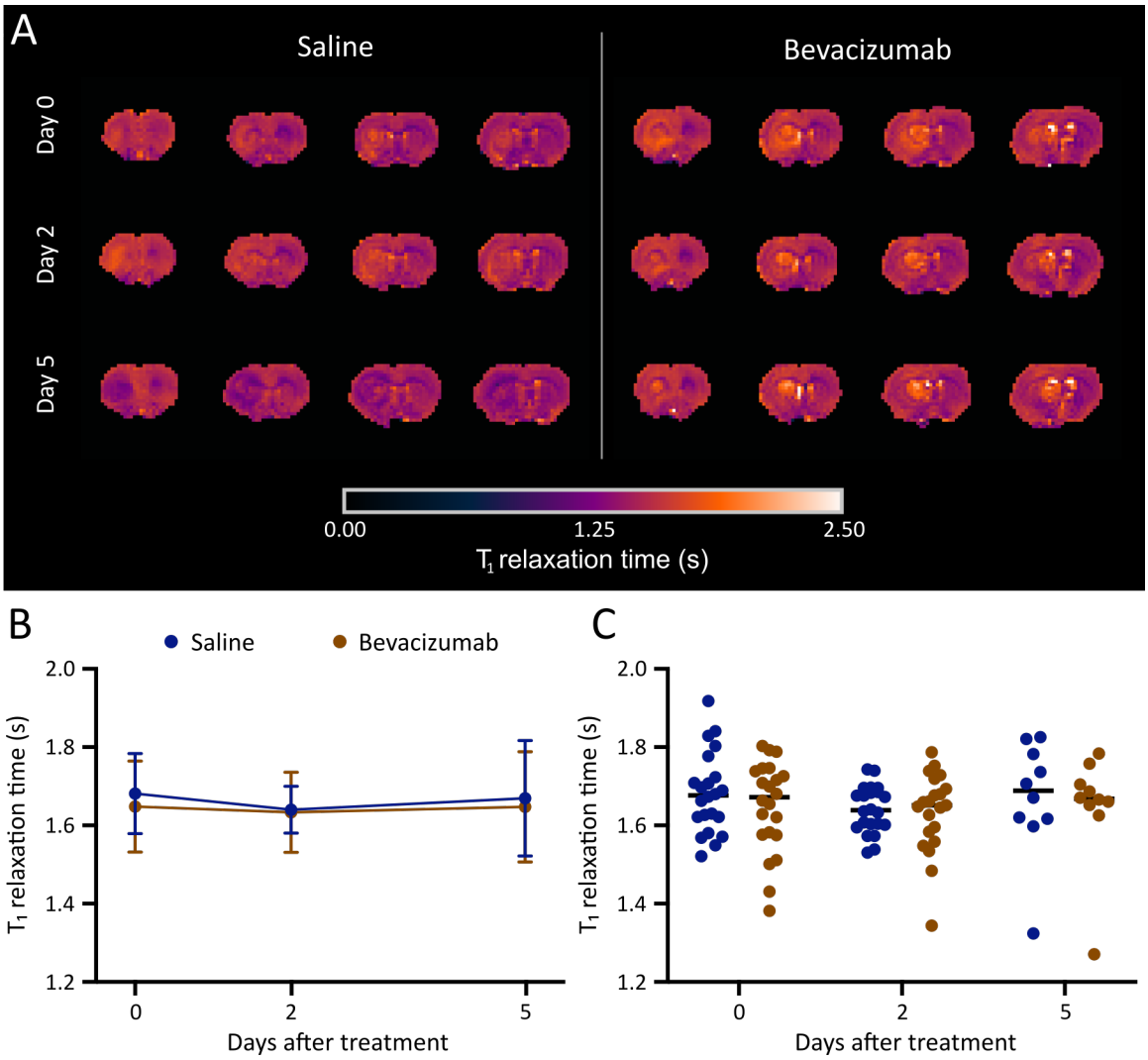

Figure 5.7 T_1 *relaxation measurements in bevacizumab-treated brain metastases.* **A** Representative T_1 relaxation maps from a saline (left) and bevacizumab (right; 10 mg/kg i.v.) treated rat over time. **B-C** T_1 relaxation times over time shown as mean ± standard deviation (**B**) and for each individual metastasis-bearing rat (**C**; from left to right, n = 22, 22, 22, 21, 10, 10).

A summary heatmap of all MRI results, relative to the baseline imaging, for both control and bevacizumab treatment groups at two and five days post-treatment are found in Figure 5.8 for each brain metastasis-bearing rat. No consistent changes were observed for any MRI technique, except for T_1 relaxation values in all rats for both treatment groups and time points, where essentially no changes were evident. Most CBF results, especially at day five post-treatment, exhibited a decrease compared to baseline values and similar

observations could be made for APTR* results, with one exception in each treatment group.

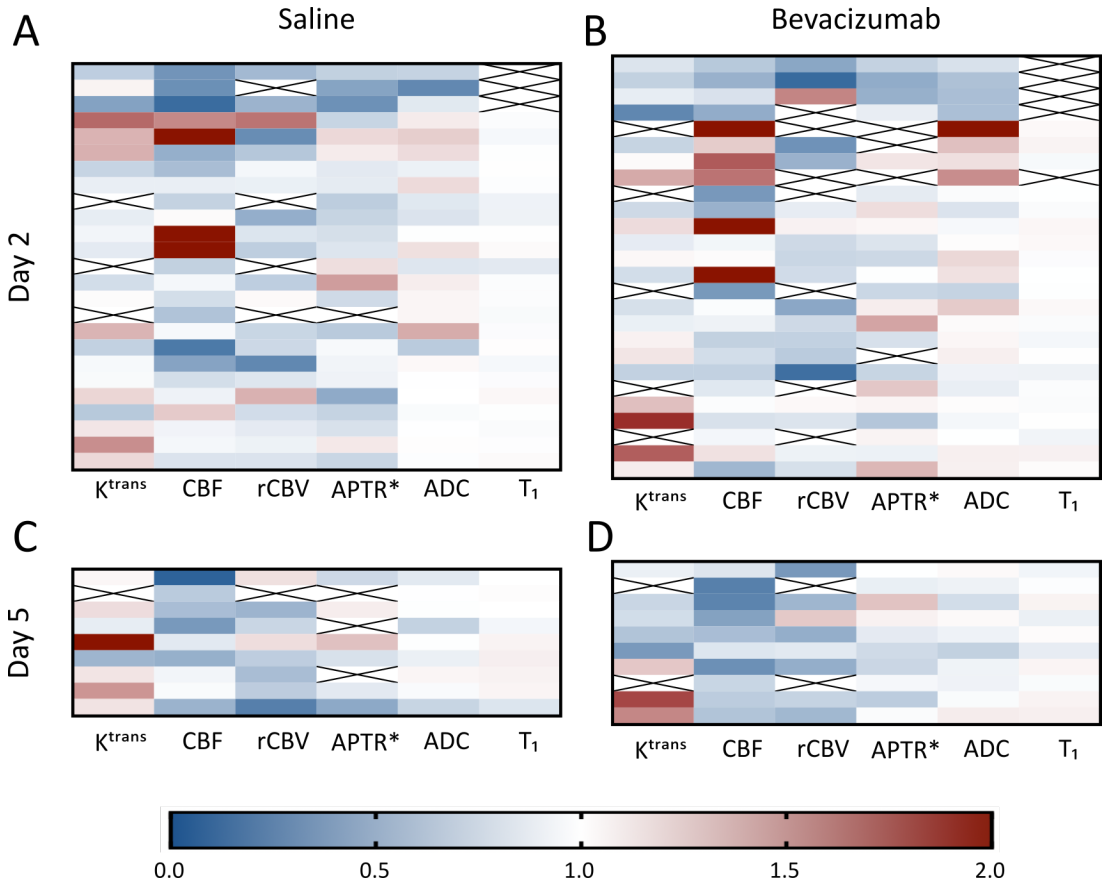

Figure 5.8 Summary of MRI findings for bevacizumab treatment in rat brain metastases. Heatmaps of changes in saline (**A**, day 2; **C**, day 5) and bevacizumab-treated (**B**, day 2; **D**, day 5) rat brain metastases in relation to baseline MRI data. Each line represents an individual rat. Increases are shown in red, decreases in blue and no change in white. Absence of result is represented by an X.

5.3.3 Effects of bevacizumab treatment on brain vasculature histology and brain metastasis hypoxia levels

Upon bevacizumab treatment of rat brain metastases, no significant change could be observed in microvessel density, as determined by positive CD31 histology, when compared to control-treated brain metastases (Figure 5.9B). However, significant increases in microvessel density were apparent between two and five days post-treatment in both groups. Furthermore, the rim region of the brain metastasis foci

possessed a significantly higher microvessel density than the core, and also when compared to the healthy contralateral striatum, in both groups and at both time points. Moreover, significant increases in microvessel density were observed in all rat brain metastases (rim and core of metastatic foci) between day two and day five post-treatment, suggesting that angiogenesis was still taking place in these tumours. This increased microvessel density was not observed in the contralateral striatum.

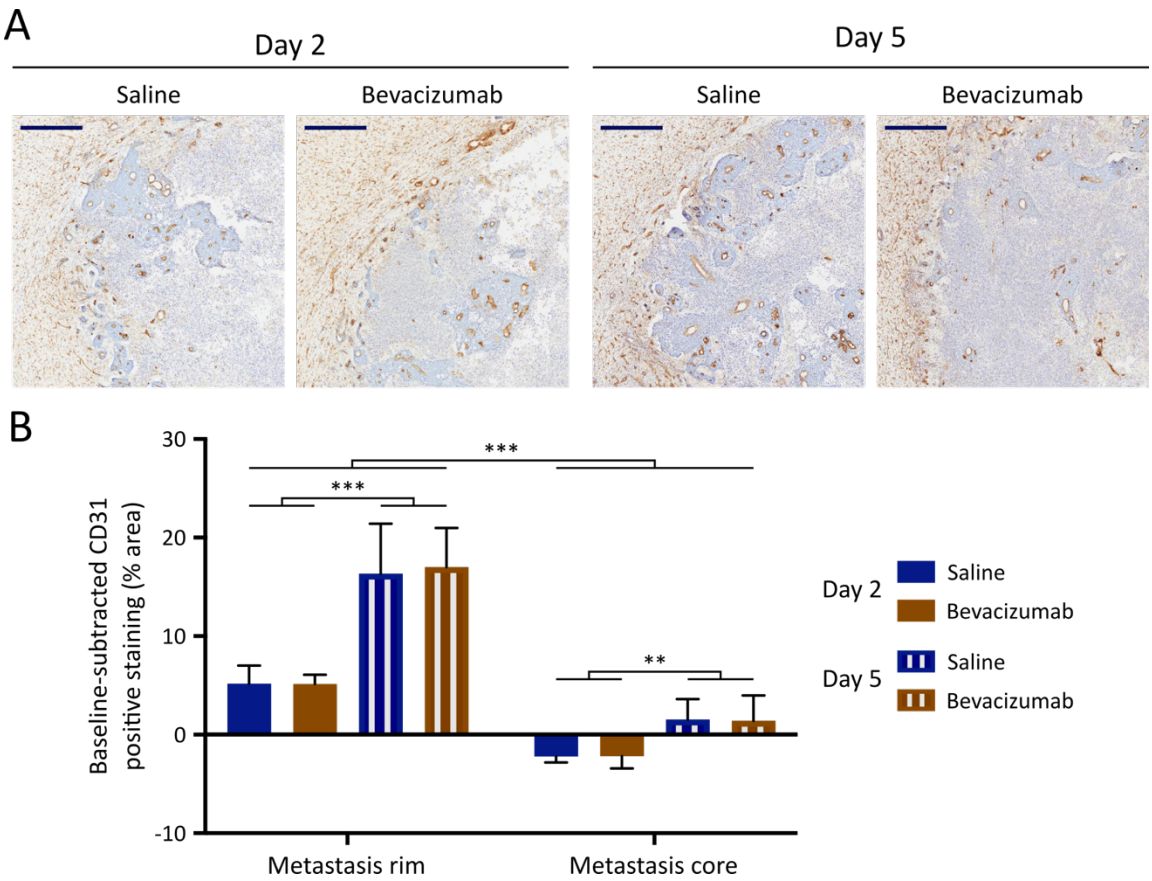

Figure 5.9 Microvessel density in brain metastases treated with bevacizumab. **A** Representative sections of CD31 IHC (brown stain), representing vasculature, in brain metastases treated with saline or bevacizumab (10 mg/kg i.v.) at 2 days and 5 days post-treatment. **B** Percentage of baseline-subtracted (contralateral striatum) CD31 positive staining in the brain metastasis foci of rats treated with saline or bevacizumab at days 2 (n = 7 per condition) and 5 (n = 9 per condition) post-treatment (2-way ANOVA; ** $p < 0.01$, *** $p < 0.001$).

The vascular maturation index (VMI) was determined for rat brain metastases by calculating the pericyte coverage of vessels in the tumour foci, through αSMA histology,

in relation to the microvessel density. Firstly, αSMA histological results exhibited a significantly greater pericyte positive staining in the rim of the metastatic foci in both treatment groups and at all time points, when compared to either the core or to healthy striatum (Figure 5.10B), similar to that observed for the microvessel density. The metastasis core region showed levels of staining in line with baseline levels on day two post-treatment with bevacizumab and, in fact were decreased at the later time point compared to healthy tissue. In contrast to the microvessel density findings, the αSMA positive area for the rim and the core regions of the metastatic foci significantly decreased in both treatment groups over time. This decrease is indicative of an increased presence of immature vessels (i.e. newly formed through angiogenesis) in the brain metastases as they progressed after treatment. The decreased pericyte coverage observed, together with the increased microvessel density at the later time point, led to a significantly lower VMI in brain metastasis foci five days post-treatment compared to the earlier time point in both control and bevacizumab-treated groups, (Figure 5.10C). The VMI was only determined for the rim of the brain metastasis region since in the core, the negative values of microvessel density and/or αSMA staining following baseline subtraction, resulted in predominantly negative VMI ratios, which did not accurately represent the situation in this highly stromal and necrotic tumour area.

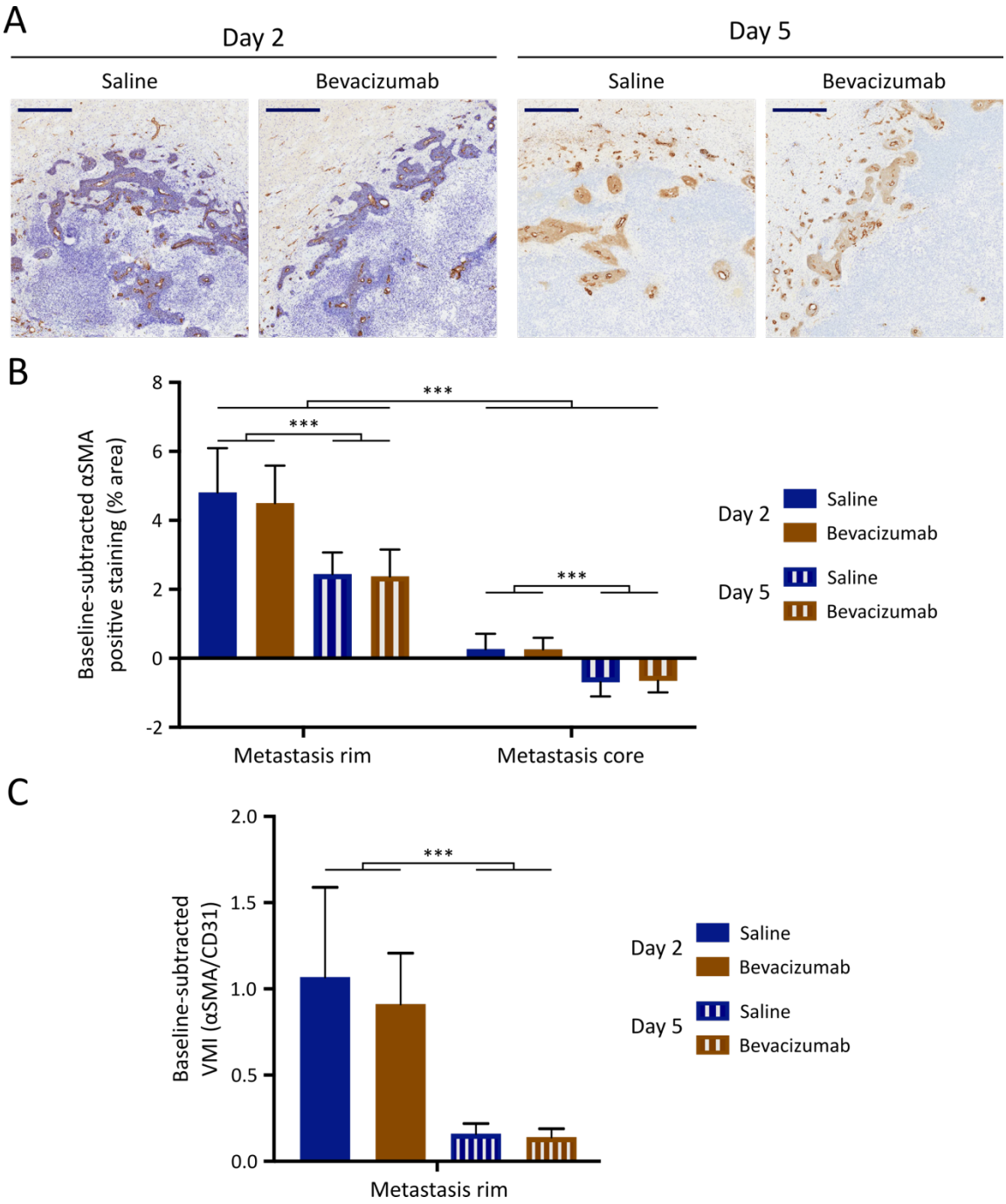

Figure 5.10 Vascular maturation index following bevacizumab treatment in brain metastases. **A** Representative sections of α-smooth muscle actin (αSMA) IHC (brown stain), representing pericytes, in brain metastases treated with saline or bevacizumab (10 mg/kg i.v.) at 2 days and 5 days post-treatment. **B** Percentage of baseline-subtracted (contralateral striatum) αSMA positive staining in the brain metastasis foci of rats treated with saline or bevacizumab at days 2 (n = 7 per condition) and 5 (n = 9 per condition) post-treatment. **C** Vessel maturation index (αSMA positive pixels / CD31 positive pixels) of the rim region of brain metastases treated with saline or bevacizumab at days 2 (n = 7 per condition) and 5 (n = 9 per condition) post-treatment (**B**-**C**: 2-way ANOVA; * $p < 0.05$, ** $p < 0.01$, *** $p < 0.001$).

Following treatment with bevacizumab, rat brain metastases showed no significant difference in their levels of hypoxia compared to the saline-treated control group (Figure 5.11B). A trend towards a decreased hypoxic fraction was determined in the core of the metastatic foci compared to the rim region in both groups and at both time points, but was not significant. All brain metastases exhibited significantly greater levels of hypoxia than healthy contralateral striata, in which positive staining was observed in less than 1 % of the striatum area, likely representing background levels of staining.

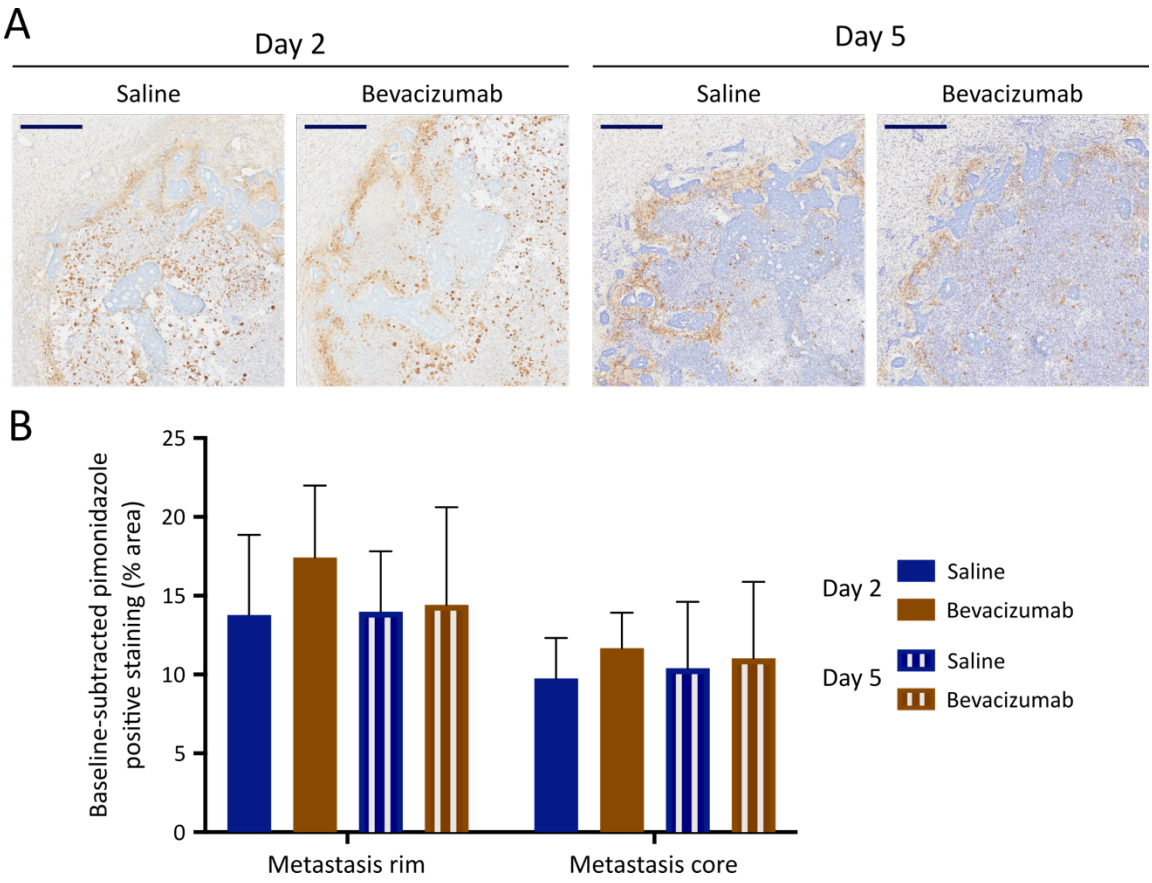

Figure 5.11 Effect of bevacizumab treatment on the hypoxic fraction of rat brain metastases. **A** Representative sections of pimonidazole IHC (brown stain), representing hypoxia, in brain metastases treated with saline or bevacizumab (10 mg/kg i.v.) at 2 days and 5 days post-treatment. **B** Percentage of baseline-subtracted (contralateral striatum) pimonidazole positive staining in the brain metastasis foci of rats treated with saline or bevacizumab at days 2 (n = 7 per condition) and 5 (n = 9 per condition) post-treatment (2-way ANOVA; * $p < 0.05$, *** $p < 0.001$).

Overall, histological findings for microvessel density, VMI and hypoxia were unchanged between bevacizumab-treated rat brain metastases compared to the control group, suggesting that inhibition of angiogenesis by bevacizumab treatment did not occur.

5.4 Discussion

5.4.1 Bevacizumab treatment of rat brain metastases did not result in a normalisation of the tumour vasculature

MRI results demonstrated no significant differences between bevacizumab-treated brain metastases and control brain metastases with regards to the relative apparent brain metastasis volume (approximated from T_2-weighted MRI), K^{trans}, CBF, APTR*, ADC or T_1 relaxation over five days. The only significant difference post-treatment was a significant increase in estimated tumour volume, as detected by T_2-weighted anatomical imaging, between two and five days in both treatment groups.

Histological analysis of the rat brain metastases was performed to determine whether the MRI performed was not sensitive enough to detect vascular normalisation. However, no significant differences between bevacizumab-treated brain metastases and the control group were evident. In contrast, evidence of brain metastasis growth was detected through the significant increase in CD31 staining five days post-treatment compared to the earlier two days post-treatment time point, irrespective of treatment. This finding suggests that angiogenesis was still occurring in the both groups. Furthermore, a decrease in pericyte coverage of the brain metastatic foci was detected through lower αSMA positive staining five days post-treatment, indicating the immaturity of the newly formed tumour vasculature. MRI results and histological results seem to suggest that vascular normalisation did not occur in this brain metastasis model.

The increased microvessel density, together with the decreased pericyte coverage of tumour vasculature, translated to a decreased VMI in the rim region of brain metastases

at five days post bevacizumab treatment, further evidence that vascular normalisation did not occur in this rat brain metastasis model.

Finally, histological analysis demonstrated no difference in the brain metastasis hypoxia profile over time in either the control or bevacizumab-treated rats. Decreased hypoxia levels were detected in both treatment groups and at both time points in the core of the metastasis foci but did not reach significance, as had been the case in Chapter 4 during later stages of tumour progression. Moreover, if vascular normalisation had occurred, an overall decrease in hypoxia would be expected in bevacizumab-treated brain metastases.

Comparison of MRI and histological results shows a lack of agreement since an increase in microvessel density is observed at the five day post-treatment time point, while the tumour blood flow is decreasing. As mentioned it Chapter 4, this could potentially be attributed to the *de novo* generation of blood vessels through angiogenesis that are redundant or yet to be perfused. However, the hypoxic phenotype in the brain metastases, treated either with bevacizumab or with saline control, although it remained unchanged over time, correlated with the decreased blood flow measured by MP-pCASL MRI. In conclusion, the results obtained from both MRI and histological analyses strongly suggest that vascular normalisation did not occur in this rat brain metastasis model.

5.4.2 Shortcomings of bevacizumab treatment in rat brain metastases

Many previous studies have demonstrated positive and therapeutic effects of bevacizumab in rat models of retinal ischemia, Achilles tendon repair and C6 glioma (Kohen *et al.*, 2018; Tempfer *et al.*, 2018; Yang *et al.*, 2018, respectively). Nevertheless, in this study, no effects could be seen in brain metastases following a single treatment of

10 mg/kg at either two or five days after treatment either by MRI or histological analyses. However, since bevacizumab is a humanised antibody targeting human VEGF-A, it possesses a significantly lower binding affinity to rat VEFG-A compared to human, primate or rabbit VEGF-A (Lin *et al.*, 1999; Ferrara *et al.*, 2004). This lower affinity is caused by the replacement of a glycine in position 88 in humans, essential to its binding, to a serine in mouse and rat bevacizumab binding sites (Muller *et al.*, 1998). The poor binding of bevacizumab to rat VEGF-A could, therefore, be the cause of the continued angiogenesis and lack of vascular normalisation in the rat model of brain metastasis used, herein.

It is unlikely that the size of the bevacizumab antibody, approximately 149 kilodaltons (kDa), was a limiting factor in this study since bevacizumab is a monoclonal immunoglobulin 1 (IgG1) antibody (Presta *et al.*, 1997) and IgG antibodies are often used in research as a marker for BBB breakdown in rodents. BBB breakdown was present in all treated rats as assessed by gadolinium enhancement in the brain metastasis region.

In conclusion, the likely cause of the failure of vascular normalisation in this study was the decreased binding affinity of bevacizumab to rat VEGF-A. The absence of vascular normalisation in brain metastases using bevacizumab made it impossible to determine whether MP-pCASL MRI could potentially replace DCE MRI as the current clinical detection method for vascular normalisation. Since bevacizumab has previously been shown to work in rats, one option to try to achieve vascular normalisation would have been to test multiple doses and at additional time points to find a combination that could achieve this. This approach, however, would be quite time consuming and ultimately has a relatively high chance of failure. Therefore, it was decided to opt for an alternative anti-angiogenic agent, with more evidences of success in rat, and to use this to test the

vascular normalisation hypotheses set in section 5.1.4. Thus, in the following chapter, cediranib, a small molecule inhibitor of VEGFR2, was used.

5.5 Conclusion

Vascular normalisation of rat breast cancer brain metastases was attempted using bevacizumab as a vascular normalising agent. No significant differences could be detected by either DCE MRI, MP-pCASL MRI, CEST MRI, diffusion MRI or in T_1 relaxation times between bevacizumab and control-treated brain metastases at days two and five post-treatment. On the microscopic scale, no significant differences were observed between treatment groups with regards to microvessel density, pericyte coverage, VMI or hypoxia levels of the brain metastasis foci in rats. However, an increase in microvessel density and a decrease in pericyte coverage of vessels was present between days two and five post-treatment, indicating that neo-angiogenesis was ongoing in these tumours. Thus, I conclude that vascular normalisation with bevacizumab did not occur in this tumour model likely owing to low binding affinity of bevacizumab to rat VEGF-A.

CHAPTER 6

Vascular normalisation in rat brain metastases using cediranib

6.1 Introduction

Cediranib, also known as Recentin™ and AZD2171, is an orally active small molecule inhibitor of vascular endothelial growth factor receptor (VEGFR) 1, 2 and 3, which inhibits angiogenesis, neovascular survival, vascular permeability and lymphangiogenesis (Wheeler *et al.*, 2003; Wedge *et al.*, 2005; Heckman *et al.*, 2008). Cediranib has been used as a vascular normalising agent either as a monotherapy or in combination therapies in multiple clinical trials, such as ovarian cancer, recurrent glioblastoma, colorectal cancer and non-small cell lung cancer, among others (Batchelor *et al.*, 2010, 2013; Ramalingam *et al.*, 2010; Kato *et al.*, 2012; Ledermann *et al.*, 2016). Dose regimes requires no adjustment for patients presenting with mild or moderate hepatic or renal impairments and can be used regardless of age or weight of patients. Its known side effects in long-

term exposure include fatigue, hypertension and diarrhoea (Dietrich, Wang and Batchelor, 2009; Tang *et al.*, 2017).

Cediranib has been shown to be a substrate of P-glycoprotein (P-gp), a drug transport protein found on the apical membrane of endothelial cells of the body, including those of the BBB (Schinkel, 1999; Wang, Agarwal and Elmquist, 2012). In mice with an intact BBB, P-gp restricts the brain distribution of cediranib by active efflux of the drug back into systemic circulation (Wang, Agarwal and Elmquist, 2012). Yet, no studies have been performed looking at cediranib concentration in circumstances of BBB disruption. Moreover, the presence of brain tumours, and the associated BBB breakdown, were previously shown to alter the function of P-gp in the brain, with an increased activity of P-gp in primary brain tumours but a significantly decreased activity in lung (40 % of normal activity) and melanoma (5 %) brain metastases (Régina *et al.*, 2001). Finally, several preclinical studies have also shown that cediranib is responsible for a reduction in tumour growth and decrease of microvessel density in tumours (Medinger *et al.*, 2009; Siemann, Brazelle and Jürgensmeier, 2009; Kendrew *et al.*, 2013).

Overall, cediranib is a clinically-relevant anti-angiogenic agent used for vascular normalisation therapy in both clinical and preclinical settings. Following the lack of effect of bevacizumab treatment in Chapter 5, the overall goal of this chapter was to determine the effect of cediranib as a monotherapy in rat breast cancer brain metastases, as performed for bevacizumab. In addition, the effect of cediranib withdrawal was evaluated for two days, after three days of treatment, to discern whether its vascular normalising effects were long lasting or transient. Furthermore, cediranib distribution in the brain was measured to determine whether inhibition of P-gp, as recommended by Wang and colleagues, is required for vascular normalisation in breast cancer brain metastases with

a compromised BBB. Lastly, the histological effects of cediranib on rat brain metastases was determined for microvessel density, vascular maturation index and levels of hypoxia.

6.1.1 Chapter aims

Similar to Chapter 5, the overall aims of this chapter were to establish vascular normalisation using cediranib in a rat breast cancer brain metastasis model and to determine whether this vascular normalisation could be detected by MRI techniques that do not require the injection of GBCAs, such as MP-pCASL MRI, CEST MRI, diffusion MRI or T_1 relaxation mapping as well as the current detection method, DCE MRI.

6.1.1.1 Hypotheses

(1) Cediranib can normalise the vasculature of rat brain metastases;

(2) Distribution of cediranib in brain metastases across a permeable BBB does not require the co-injection of a P-gp inhibitor;

(3) As a consequence of vascular normalisation with cediranib treatment,

   a. K^{trans}, the permeability factor measured by DCE MRI, decreases in brain metastases owing to the maturation of existing tumour vessels, while remaining stable in vehicle control brain metastases;

   b. CBF measurements from brain metastases remain stable or increase, while those from vehicle control-treated brain metastases decrease progressively;

c. APTR* values from brain metastases in remain stable or increase, while those from vehicle control-treated brain metastases decrease progressively;

d. ADC values decrease resulting from a greater tumour cell density surrounding mature tumour vasculature, while those from vehicle control brain metastases progressively increase;

e. tumour T_1 relaxation values decrease in brain metastases to more closely resemble those of healthy tissue, while remaining elevated in vehicle control brain metastases;

f. histologically, the microvessel density of the brain metastases decreases, owing to the inhibition of neo-angiogenesis, while remaining stable in vehicle control brain metastases;

g. pericyte coverage of existing vessels increases upon vascular normalisation compared to vehicle control brain metastases, thereby increasing the vascular maturation index;

h. a reduction in pimonidazole positive staining in brain metastases indicates a decrease in hypoxia levels, while hypoxia levels in vehicle control brain metastases increase;

i. MRI and histological results in the cediranib withdrawal group maintain some effect of vascular normalisation, while showing evidence of reverting back to the vehicle control levels, to some extent.

6.2 Methods

6.2.1 Rat breast cancer brain metastasis model

Please refer to section 2.2.1 for rat brain metastasis injection protocol.

6.2.2 MRI and treatment plan

Brain metastasis progression was followed closely through T_1-weighted and T_2-weighted imaging twice a week from two weeks post intracerebral injection. Once the apparent brain metastasis volume exceeded 10 mm^3, as determined by regions of heterogeneity in T_2-weighted images, rats were assigned to the vehicle or cediranib treatment groups, based on brain metastasis volume estimates, to ensure tumours were evenly distributed among groups, with twice as many rats in the cediranib group since it will be divided to determine effects of cediranib withdrawal. Prior to first treatment dose, baseline rat MRI was performed: MP-pCASL MRI, CEST MRI, diffusion MRI, T_1 relaxation mapping, DCE MRI, T_2-weighted imaging and T_1-weighted pre- and post-gadolinium imaging. Cediranib injection was then performed daily (at 24 hours intervals) at a dose of 4 mg/kg, 2 hours prior to blood sampling and MRI, for up to 5 days of repeated treatment. In a subset of rats, MRI was only performed at baseline and on day 3 of treatment. Rats were injected intraperitoneally with pimonidazole-HCl 3 hours prior to being killed by exsanguination with perfusion-fixation (section 2.2.2) for histological analysis or saline perfusion only for HPLC-MS analysis. A schematic of this animal experimental plan is shown in Figure 6.1 and Table 6.6.1 displays the number of rats in each treatment group at each time point. The size of group in each treatment branch varied for multiple reasons,

as follows. In the initial cediranib pilot study, cediranib treatment was administered for 1 or 2 days, with some rats culled after 1 day of treatment. Also, once day 3 was selected as the time point of choice for the full study, some rats were only imaged at baseline and day 3. Finally, issues with the MRI spectrometer occurred during day 4 imaging and MRI could not be performed for 1 rat from each treatment group at this time point.

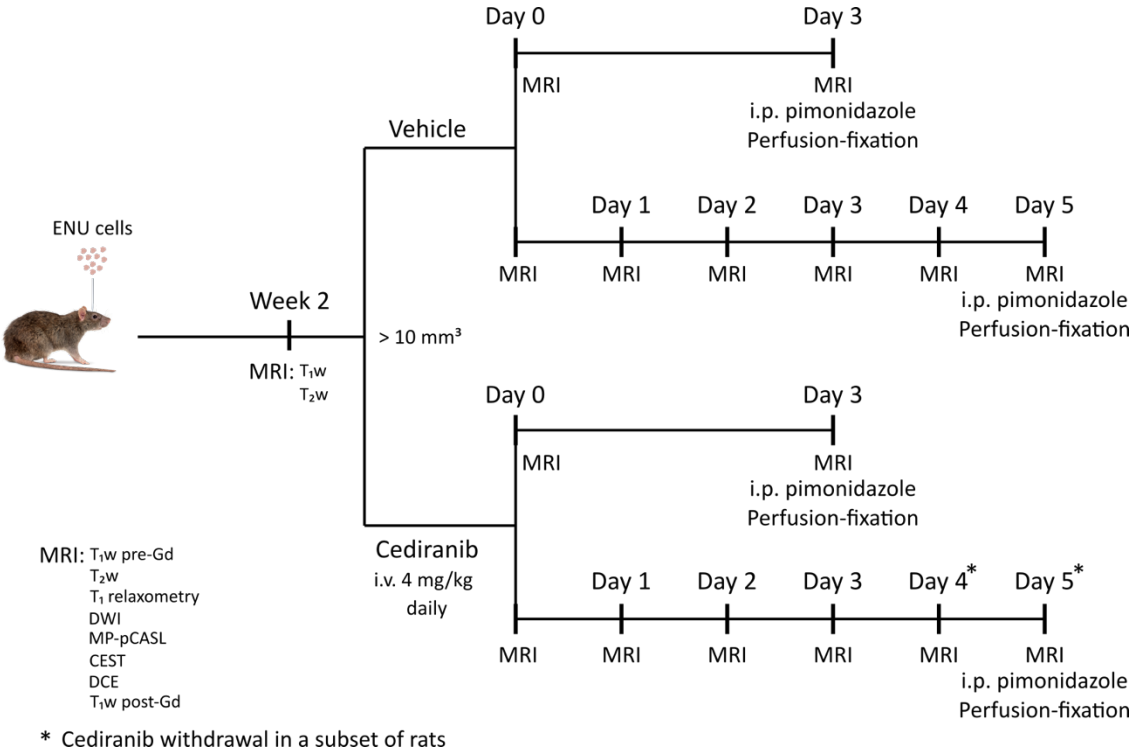

Figure 6.1 Rat experimental plan for cediranib treatment and imaging in brain metastases. Rats were followed from 2 weeks post-injection onwards, until tumour volume estimates from T_2-weighted MRI were greater than 10 mm^3. First treatment dose was administered after MRI on Day 0. On subsequent days, at 24 hour intervals, cediranib or vehicle were injected 2 hours prior to MRI.

Table 6.6.1 Number of brain metastasis-bearing rats in treatment groups at each time point.

Treatment group	Baseline	Day 1	Day 2	Day 3	Day 4	Day 5
Vehicle	13	10	10	9	5	6
Cediranib	29	22	19	20	5	6
Withdrawal	-	-	-	-	6	7

6.2.3 Cediranib

Cediranib (IUPCAC chemical name, 4-[(4-fluoro-2-methyl-1H-indol-5-yl)oxy]-6-methoxy-7-[3-(pyrrolidin-1-yl) propoxy]quinazoline; molecular weight, 450.5 g/mol; melting point, 199 ˚C) is normally administered orally by oral gavage in mice or rats in preclinical studies. However, it has been shown to exhibit food-drug interactions and its administration is recommended to be performed either 1 hour before or 2 hours after food ingestion (Tang *et al.*, 2017), which is more difficult to control in rodents than in humans. Thus, in order to provide a more reliable dosing scheme for cediranib, improve its bioavailability (~75 % orally for female rats (European Medicines Agency, 2016)) and reduce food-drug interactions, cediranib was administered intravenously in rats with breast cancer brain metastases. Cediranib was injected at a dose of 4 mg/kg, according to the dose used by Wang and colleagues, and slightly lower than the dose typically used when administered orally (Wang, Agarwal and Elmquist, 2012). Cediranib was suspended in 1 % Tween-80 (Sigma-Aldrich, UK) in ddH_2O at a concentration of 8 mg/mL, sonicated using a Sonics Vibra-Cell™ ultrasonic liquid processor (Jencons-PLS, Southampton, UK) for approximately 10 seconds to dissociate aggregates and, finally, vortexed prior to injection via a rat tail vein, using a 31 gauge insulin syringe to ensure cediranib aggregates were not injected. Vehicle solution injection (1 % Tween-80 in ddH2O) was injected daily via a tail vein of metastasis-bearing rats as a control. Rats were monitored by observation twice a day and weighed daily following cediranib injection. No secondary effects were noticed in any cediranib-treated rat.

6.2.4 Magnetic resonance imaging

Methods and analyses for the MRI techniques used herein are described in the sections presented in Table 6.6.2.

Table 6.6.2 Location of MRI technique-specific methods and analysis protocols.

MRI technique and analysis	Section
T_2-weighted imaging	2.3.4
T_1-weighted imaging (pre/post-gadolinium)	2.3.3
Diffusion MRI	2.3.2
T_1 relaxation mapping	2.3.6
MP-pCASL MRI	2.3.1
CEST MRI	2.3.7
DCE MRI	2.3.5

6.2.5 High-performance liquid chromatography and mass spectrometry

The high-performance liquid chromatography and mass spectrometry (HPLC-MS) to determine cediranib concentrations in rat plasma and brain tissues was performed by Lisa Folkes and Alix Hampson in the Bioanalysis Scientific Research Facility of the Department of Oncology, University of Oxford. The HPLC-MS method was modified from Wang and colleagues (Wang, Oberoi and Elmquist, 2011), according to the equipment available.

6.2.5.1 Plasma and brain metastasis and striatum isolation

Plasma samples were obtained from the rat tail vein prior to MRI using a short, open ended butterfly cannula (27 gauge, Vygon Venoflux, Swindon, UK) with a small amount of saline heparin (1000 units/mL; Wockhardt, Wrexham, UK) or from the heart immediately before perfusion using a 1 mL syringe with a 23 gauge needle with a small amount of

heparin saline. Blood samples were placed in a 1.5 mL tube and centrifuged using a table-top microcentrifuge (StarLabs Ltd, Milton Keynes, UK) for 10 minutes. Plasma, the top layer, was pipetted into a clean 1.5 mL tube, then placed on dry ice until storing at -80 ˚C.

The brain was isolated following a saline perfusion. The rat brain was sliced using a rat brain slicer matrix (Zivic, Pittsburgh, USA) and razor blades (VWR, UK) positioned caudal and rostral to the brain metastasis region. Brain metastasis region and contralateral striatum were isolated using the wide end of P200 pipette tips, then dropped into pre-weighed 1.5 mL tubes and flash frozen in liquid nitrogen. Brain samples were stored at -80 ˚C until processed.

6.2.5.2 HPLC-MS materials and standard preparation

AG1478 (epidermal growth factor receptor inhibitor; internal standard; IS) was received from Enzo life sciences, UK. Cediranib stock solution was prepared at 1 mg/mL in dimethyl sulfoxide (DMSO); IS stock solution was prepared at 1 mg/ml in DMSO. A calibration curve was prepared in surrogate matrix (5 % bovine serum albumin (w/v) in PBS) for brain homogenates and in control BDIX plasma for plasma analysis.

6.2.5.3 Cediranib concentration quantitation

Plasma samples were analysed as received. Weighed brain samples were homogenised with a Mikro dismembrator (B Braun, Biotech Int.) with ice cold surrogate matrix to give a four-fold dilution. The plasma sample or plasma standard, 20 µL was mixed with 20 µL of 400 ng/ml IS (prepared in water from 1 mg/ml stock) prior to the addition of 0.2 mL ethyl acetate. Samples were mixed for 15 s and centrifuged at 13,000 *g* for 1 min.

Subsequently, 190 µL of the ethyl acetate layer (top layer) was dried down in a centrifugal evaporator (Thermo Scientific, UK). For brain homogenates 50 µL of homogenate or surrogate matrix standard was mixed with 50 µL IS and extracted into 0.5 mL ethyl acetate. 0.49 mL was dried down, as above, and reconstituted in 50 µL reconstitution solution, as above. Samples were reconstituted in 50 µL 40 % acetonitrile + 60 % 20 mM ammonium acetate containing 0.1 % formic acid. HPLC analysis was carried out on a Waters Acquity H-Class Quarternary Solvent Manager. Following a 5 µL injection separation was achieved on an Acquity UPLC C18, 1.7 µm, 100 × 2.1 column (Waters, UK) maintained at 35 °C. Samples were eluted in 60 % 20 mM ammonium formate in 0.1 % formic acid with 40 % acetonitrile with a flow rate of 0.4 mL/min and a run time of 3 min. Cediranib and IS were detected by mass spectrometry with a Waters Acquity TQ detector with electrospray ionisation in a positive ionisation mode (2.5 kV), source temperature 120 °C, desolvation temperature 400 °C and desolvation gas flow 50 L/h. Cediranib was detected with a cone voltage of 36 V at multiple reaction monitoring (MRM) of *m/z* 451.4 > 111.9 and IS with a cone voltage of 40 V and MRM of *m/z* 316.1 > 300.1.

6.2.6 Immunohistochemistry

6.2.6.1 Immunohistochemistry

IHC was performed targeting the endothelial marker CD31 (AF3628, R&D Systems, Abingdon, UK), the hypoxia gold-standard marker pimonidazole HCl (Hypoxyprobe, Burlington, USA) and pericytes using α-smooth muscle actin (ab7817, Abcam, Cambridge, UK; Table 6.6.3). All secondary antibodies were purchased from Vector Laboratories Ltd (Burlingame, USA).

Table 6.6.3 Immunohistochemistry antibodies and concentrations.

IHC antigen	Blocking solution	Primary antibody concentration	Secondary antibody and concentration
CD31 Polyclonal goat IgG	Normal horse serum	1:200	Goat raised in horse; 1:200
Pimonidazole HCl Monoclonal mouse IgG	Normal horse serum	1:100	Mouse raised in horse; 1:200
αSMA Monoclonal mouse IgG	Normal horse serum	1:100	Mouse raised in horse; 1:200

Please refer to section 2.4.3 for the standard IHC protocol and to section 2.4.2 for the antigen-retrieval protocol used in αSMA, prior to standard IHC protocol.

6.2.6.2 Immunohistochemistry analysis

Analysis of stained sections was performed as described in section 2.4.4. Brain sections, every 200 μm across the brain metastasis region were selected for each antibody IHC. Mean brain metastasis foci positive staining was determined for each rat (15 ± 4 sections per rat, depending on brain section quality and tumour volume) and averaged for analysis and comparison between treatment groups at each time point. Baseline levels of staining were subtracted from both brain metastasis rim and core regions to correct for the variability in staining intensity and background staining observed at different days. No differences could be visually detected between the contralateral striata of metastasis-bearing rats of any treatment group compared to PBS-injected rats or naïve rats, used in previous chapters.

6.3 Results

6.3.1 Cediranib treatment inhibits brain metastasis growth over time

No significant differences were present between the estimated brain metastasis volumes measured on T_2-weighted images upon separation of the rats into cediranib and vehicle treatment groups following baseline imaging (day 0; Figure 6.2B). However, at later time points, the margins of the brain metastasis foci were more difficult to detect visually in the cediranib-treated rats on T_2-weighted anatomical MRI images than vehicle-treated brain metastases or than those at baseline. Therefore, for all rats, regardless of treatment group, histological brain sections from the end point were used to inform brain metastasis volume segmentations for MRI data analysis. Brain metastasis volume estimates from T_2-weighted images were significantly increased in all rats over time, independent of treatment group (Figure 6.2C). Of importance, vehicle-treated brain metastases were significantly larger after five days of treatment than either the cediranib-treated group ($p < 0.01$) or the cediranib + withdrawal group ($p < 0.05$; Figure 6.2C).

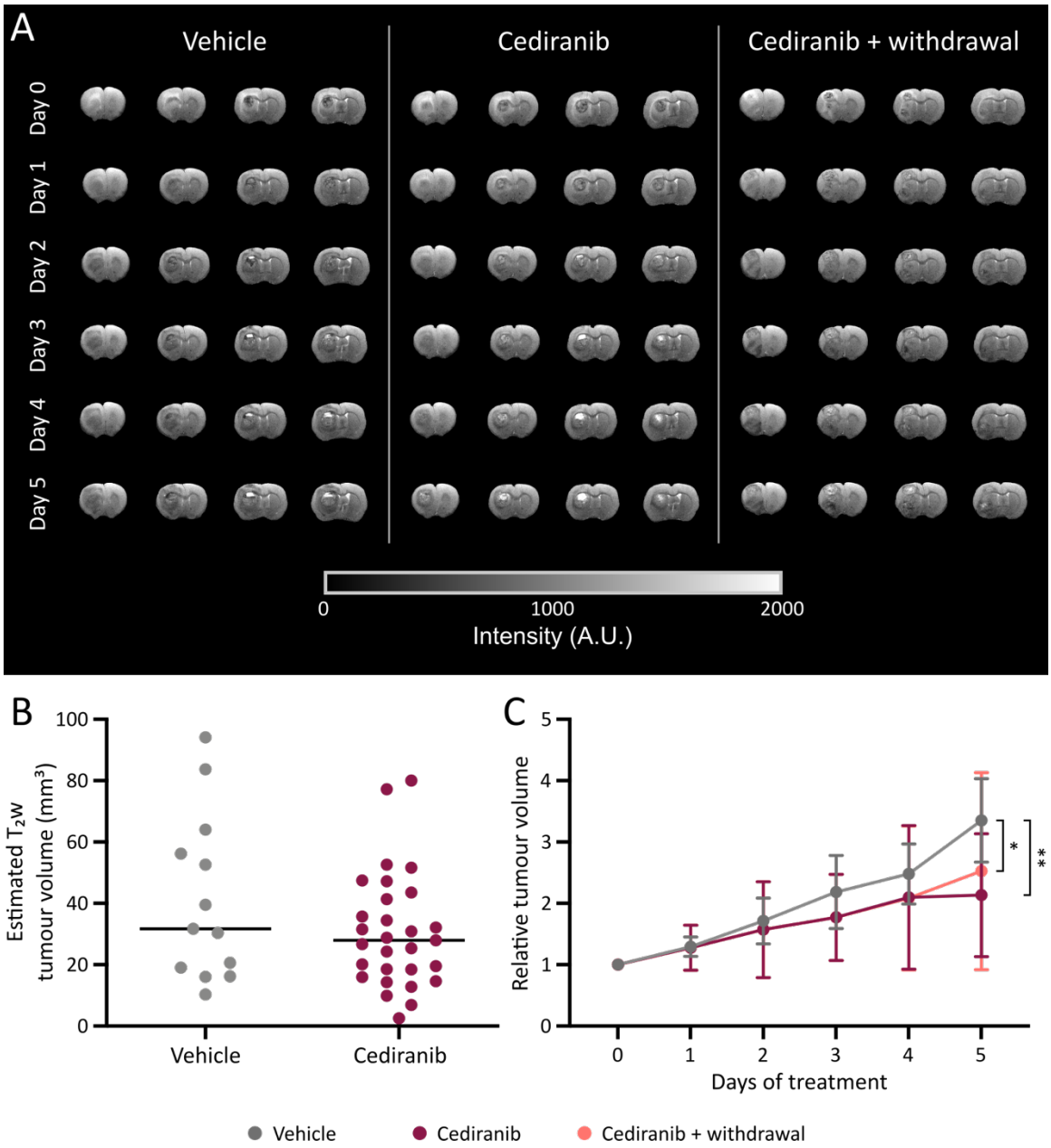

Figure 6.2 Anatomical changes in brain metastases treated with cediranib. **A** Representative T_2-weighted anatomical images from a vehicle control rat, cediranib-treated rat and cediranib + withdrawal rat (cediranib treatment during the first three days) before treatment (day 0) and daily for five days of treatment (4 mg/kg). Images were acquired on the same rat at each time point for each treatment group. **B** Graph showing detectable tumour volume on T_2-weighted MRI images prior to treatment. Each point representing one brain metastasis bearing rat (n = 13 for vehicle control; n = 29 for cediranib; n.s. on Student's unpaired t-test). **C** Graph of relative growth of brain metastases over time compared to starting volume measured on T_2-weighted images (* $p < 0.05$, ** $p < 0.01$; 2-way ANOVA with Tukey's multiple comparisons).

6.3.2 Dynamic contrast-enhanced MRI for detection of vascular normalisation with cediranib

K^{trans}, the permeability factor from DCE MRI, was measured daily in vehicle and cediranib-treated brain metastases to detect changes in tumour vasculature permeability. A significant decrease in K^{trans} was observed in cediranib-treated brain metastases as early as one day after treatment initiation when compared to baseline values ($p < 0.05$) and continued to decrease to day the 5 experimental end point ($p < 0.001$; Figure 6.3B, C). K^{trans} was significantly decreased in cediranib-treated brain metastases compared to vehicle-treated tumours from day 1 after cediranib treatment ($p < 0.001$). Moreover, upon withdrawal of cediranib, K^{trans} levels increased towards the values in the vehicle treatment group and were no longer significantly different from baseline at day 5, two days after the last cediranib dose. The decrease in K^{trans} during cediranib treatment suggests a strengthening of the BBB and decreased the leakiness of tumour associated vasculature. These changes appear to be rapidly reversed on withdrawal of cediranib treatment.

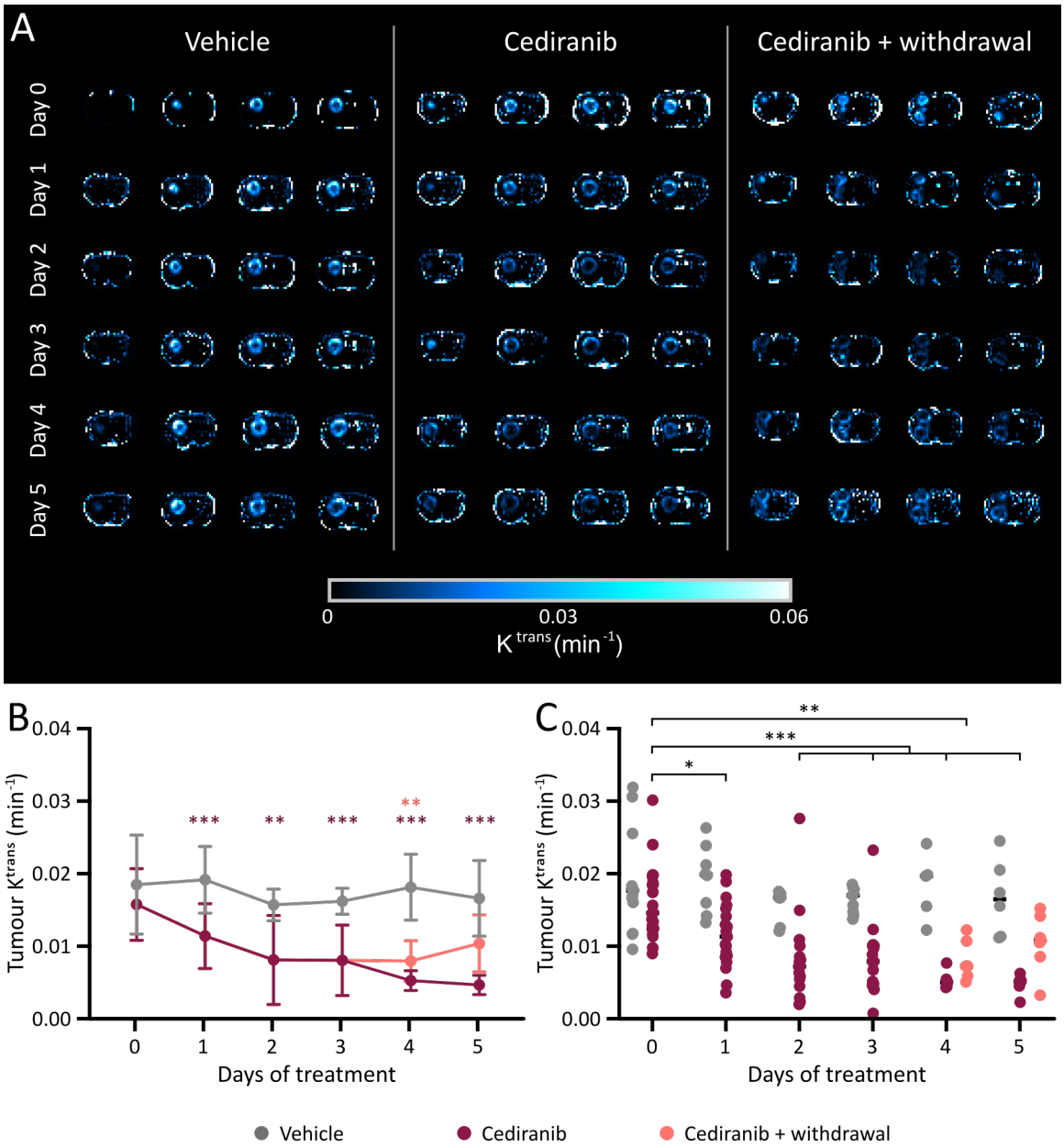

Figure 6.3 Brain metastasis permeability in cediranib-treated rats. **A** Representative K^{trans} maps calculated from DCE MRI in a vehicle control rat (left), cediranib-treated rat (middle) and cediranib + withdrawal rat (cediranib treatment during the first three days; right) before treatment (day 0) and daily for five days of treatment (4 mg/kg). K^{trans} maps shown were generated for the same rat at each time point in each treatment group. **B-C** Graphs showing K^{trans} measurements in vehicle, cediranib and cediranib + withdrawal (days 4 and 5 only) treated brain metastases over time given as the mean ± standard deviation (**B**) and for each individual metastasis-bearing rat (**C**; * $p < 0.05$, ** $p < 0.01$, *** $p < 0.001$; 2-way ANOVA with Tukey's multiple comparisons).

6.3.3 Changes detected by non-invasive MRI techniques during cediranib treatment of rat brain metastases

CBF measurements in rat brain metastases obtained from MP-pCASL MRI were significantly decreased five days after treatment initiation in vehicle-treated rats compared to baseline CBF levels ($p < 0.05$; Figure 6.4B, C). Furthermore, a significant decrease in brain metastasis CBF was detected following three days of vehicle treatment compared to the cediranib-treated group. Although the blood flow in cediranib-treated rat brain metastases also appeared to decrease over time, CBF measurements were not significantly changed in this treatment group across the five days of treatment compared to baseline CBF measurements, demonstrating the effect of cediranib on the maintenance of blood flow in the tumour region. Little difference could be detected in brain metastasis CBF measurements following cediranib withdrawal over two days, compared to CBF of brain metastasis still receiving cediranib treatment.

No significant changes could be detected between vehicle-treated and cediranib-treated brain metastases in APTR* (Figure 6.5), ADC (Figure 6.6) or in tumour T_1 relaxation values (Figure 6.7) at up to five days of treatment. Cediranib withdrawal did not affect the results in any of these three MRI techniques. However, a significant decrease in APTR* was measured in all treatment groups, over the course of the treatment. Similar results were observed in the brain metastasis T_1 relaxation values, where T_1 values were significantly decreased at all time points during treatment, except day three of treatment, compared to baseline tumour values ($p < 0.05$). After three days of cediranib or vehicle treatment, a few brain metastases showed signs an increase in the T_1 relaxation values of the tumour region, suggesting that cystic necrosis was occurring (Figure 6.7C).

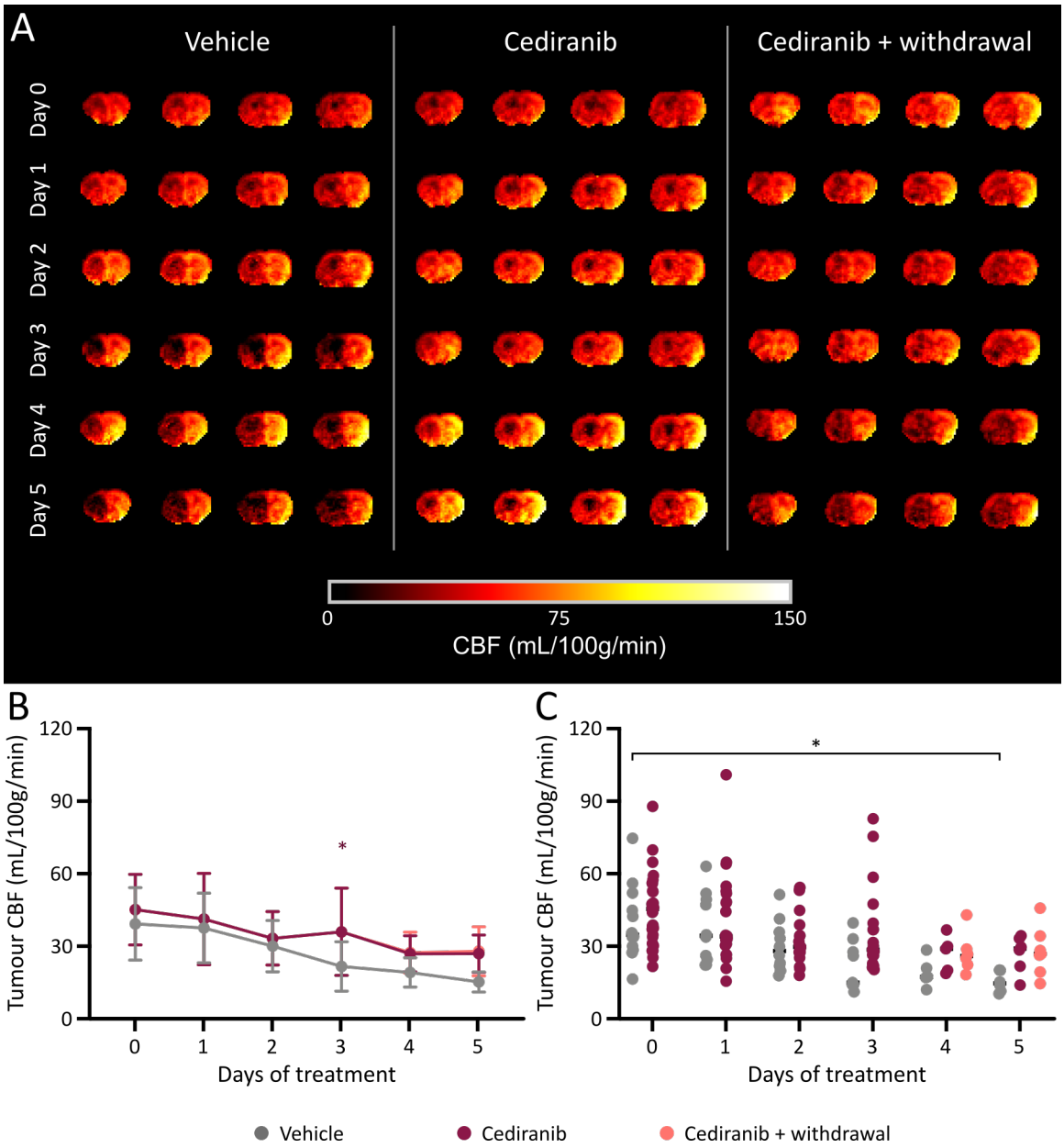

Figure 6.4 Effect of cediranib treatment on brain metastasis blood flow over time. **A** Representative apparent CBF maps from MP-pCASL MRI for a vehicle (left), cediranib (4 mg/kg; middle) and cediranib + withdrawal treated rat (cediranib treatment during the first three days; right) for five days of treatment. Apparent CBF maps shown were selected for the same rat at each time point in each treatment group. **B-C** Graphs showing blood flow measurements from brain metastases over time for vehicle, cediranib and cediranib + withdrawal (days 4 and 5 only) treatment groups given as mean ± standard deviation (**B**) and for each individual metastasis-bearing rat (**C**; * $p < 0.05$; 2-way ANOVA with Tukey's multiple comparisons).

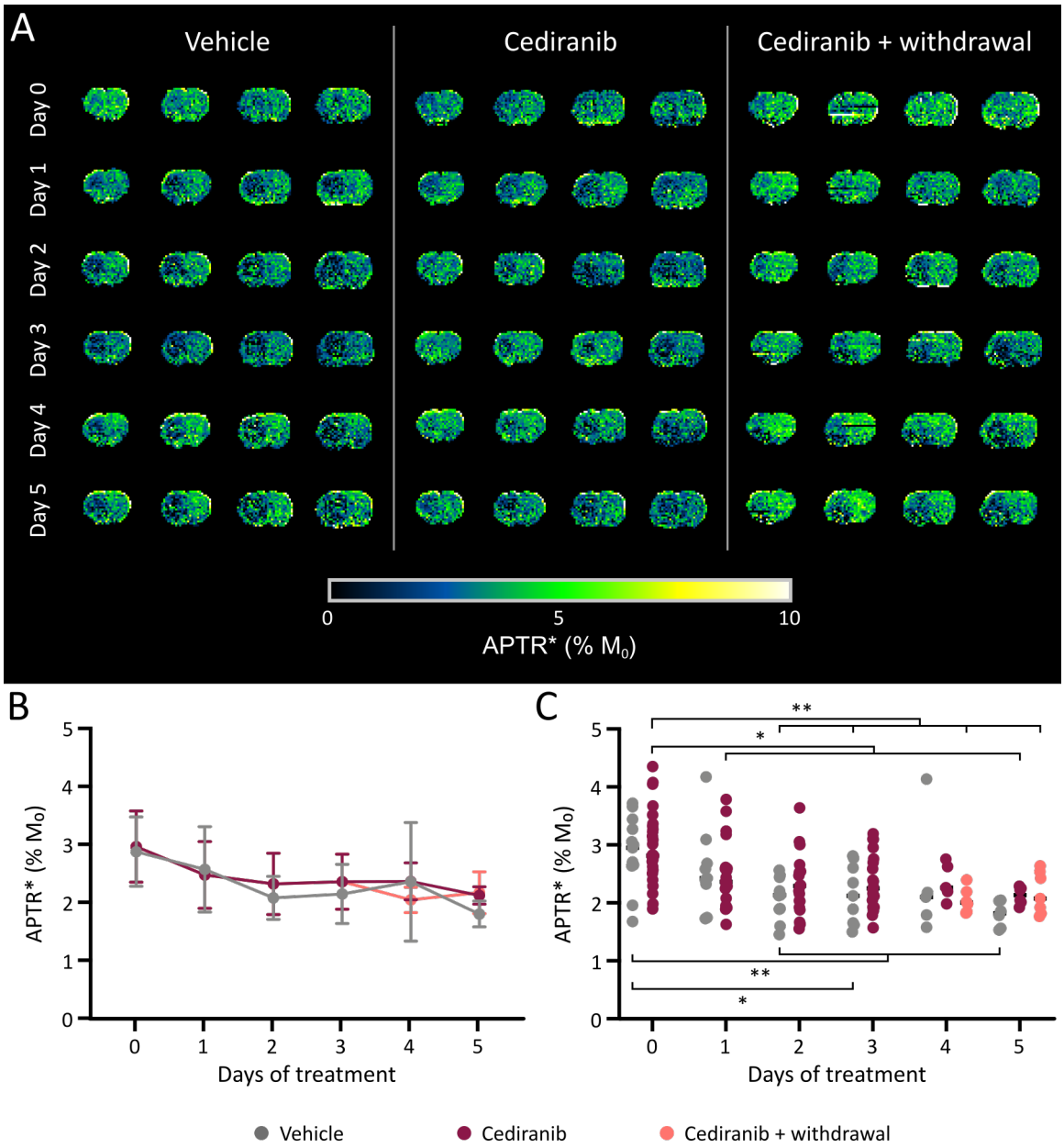

Figure 6.5 Changes in APTR in cediranib-treated brain metastases.* **A** Representative amine proton transfer ratio (APTR*) maps from CEST MRI for a vehicle (left), cediranib (4 mg/kg; middle) and cediranib + withdrawal treated rat (cediranib treatment during the first three days; right) for five days of treatment. APTR* maps shown were selected for the same rat at each time point in each treatment group. **B-C** Graphs showing APTR* measurements from brain metastases over time for vehicle, cediranib and cediranib + withdrawal (days 4 and 5 only) treatment groups given as mean ± standard deviation (**B**) and for each individual metastasis-bearing rat (**C**; * $p < 0.05$, ** $p < 0.01$; 2-way ANOVA with Tukey's multiple comparisons).

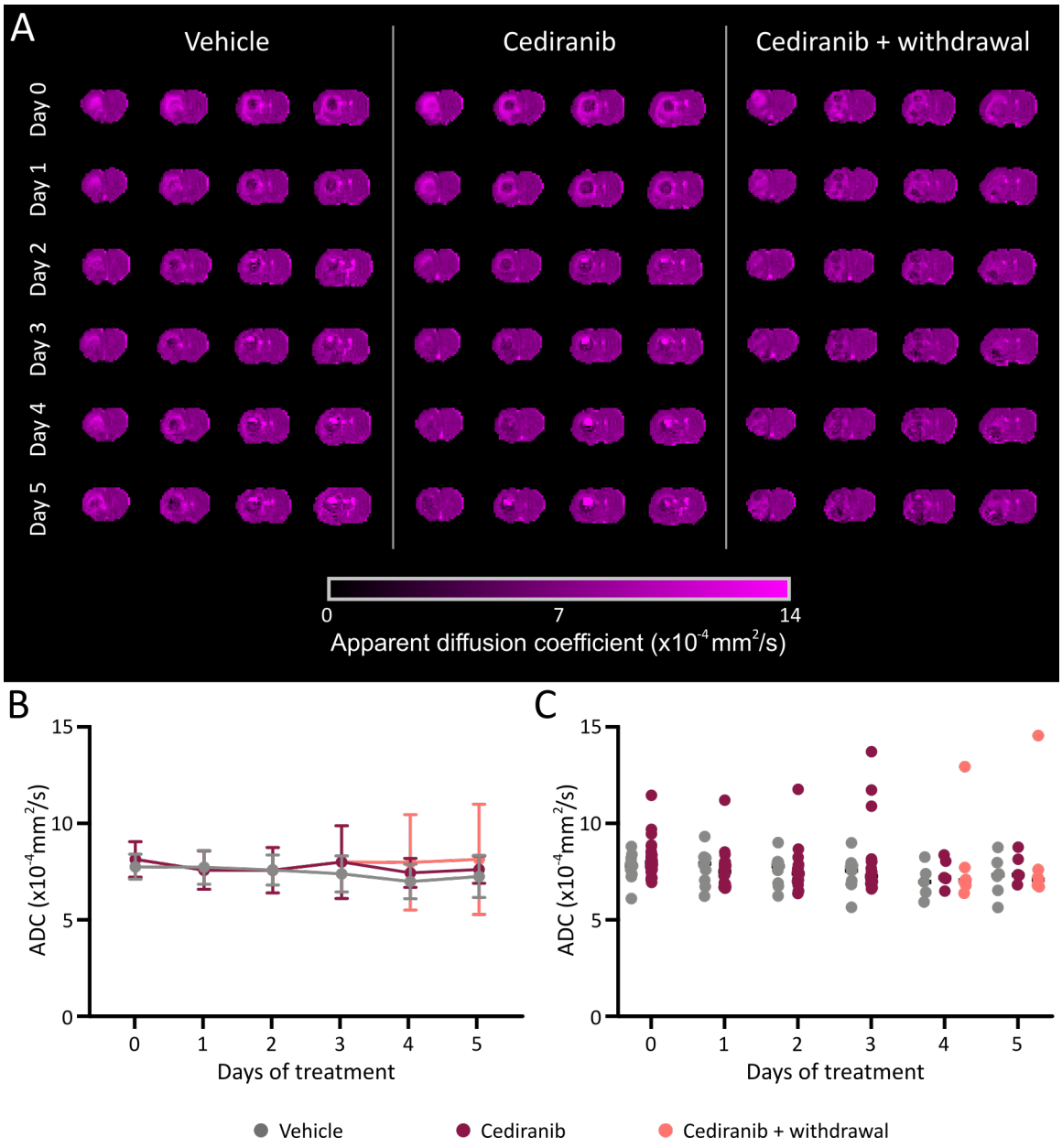

Figure 6.6 Apparent diffusion coefficients in cediranib-treated brain metastases. **A** Representative ADC maps generated from diffusion MRI acquisitions for a vehicle (left), cediranib (4 mg/kg; middle) and cediranib + withdrawal treated rat (cediranib treatment during the first three days; right) for five days of treatment. ADC maps were selected for the same rat at each time point in each treatment group. **B-C** Graphs showing ADC measurements from brain metastases over time for vehicle, cediranib and cediranib + withdrawal (days 4 and 5 only) treatment groups given as mean ± standard deviation (**B**) and for each individual metastasis-bearing rat (**C**; 2-way ANOVA with Tukey's multiple comparisons was not significant).

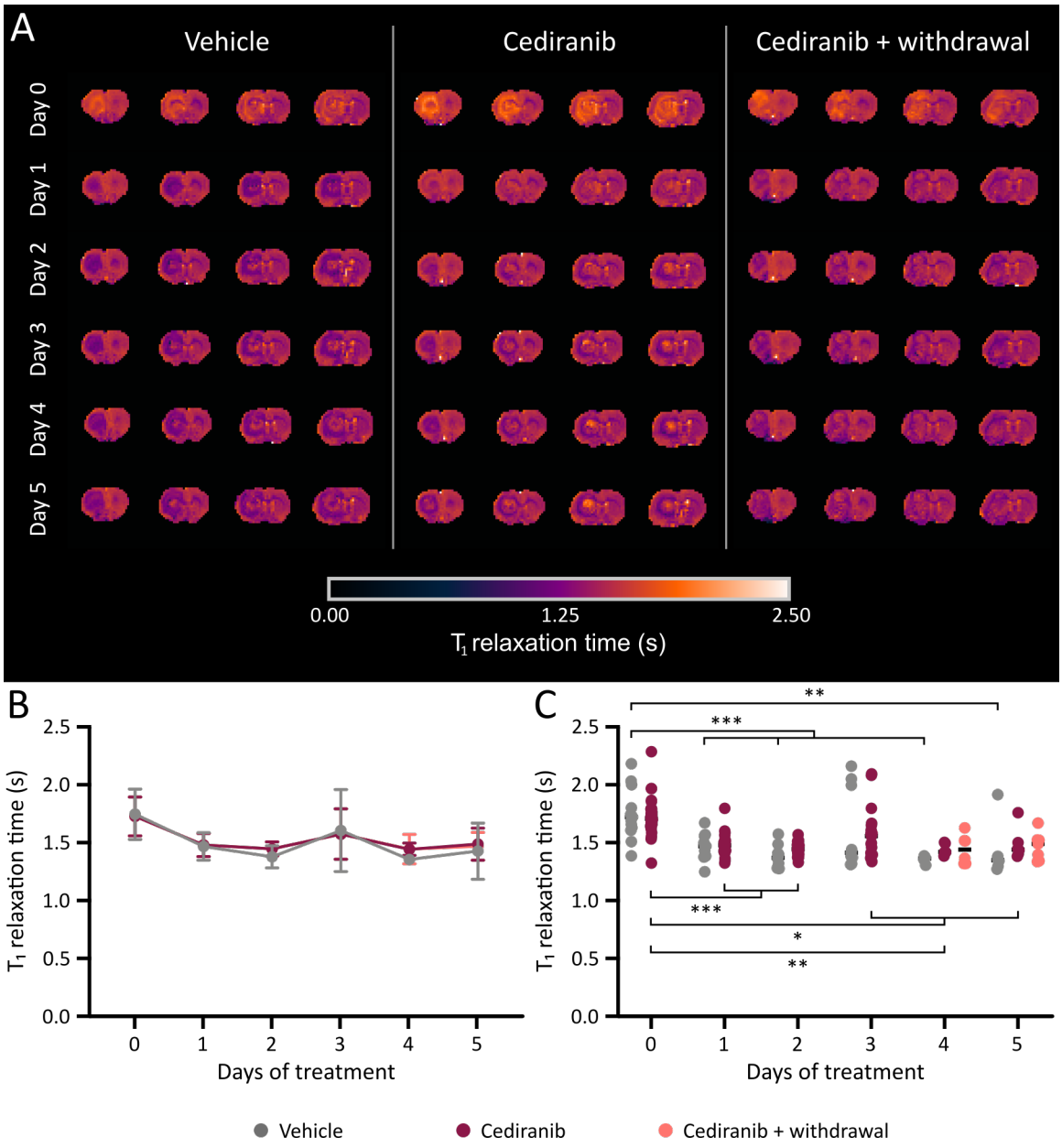

Figure 6.7 Effect of cediranib treatment on T_1 *relaxation of brain metastases.* **A** Representative T_1 relaxation maps of a vehicle control rat (left), cediranib-treated rat (middle) and cediranib + withdrawal rat (cediranib treatment during the first three days; right) before treatment (day 0) and daily for five days of treatment (4 mg/kg). T_1 maps shown were generated for the same rat at each time point in each treatment group. **B-C** Graphs showing T_1 relaxation values from vehicle, cediranib and cediranib + withdrawal (days 4 and 5 only) treated brain metastases over time given as the mean ± standard deviation (**B**) and for each individual metastasis-bearing rat (**C**; * $p < 0.05$, ** $p < 0.01$, *** $p < 0.001$; 2-way ANOVA with Tukey's multiple comparisons).

A summary of MRI changes over the course of cediranib and vehicle treatment are shown by a series of heatmaps in Figure 6.8 for the subset of brain metastasis-bearing rats that were followed during treatment for five days, relative to baseline imaging

results. Clear differences between the vehicle, cediranib and cediranib + withdrawal groups can be seen at early time points in K^{trans} results (Figure 6.8A) and in MP-pCASL MRI CBF measurements, especially after five days of treatment (Figure 6.8B). MRI results from APTR* and T_1 relaxation exhibit decreases relative to baseline imaging, independent of treatment group. ADC measurements displayed no evident trend in any treatment group and appeared the most consistent in brain metastases across the treatment duration. Mean treatment group results at day 5, relative to baseline imaging, highlight the group differences observed for K^{trans} and tumour blood flow in brain metastases (Figure 6.8F).

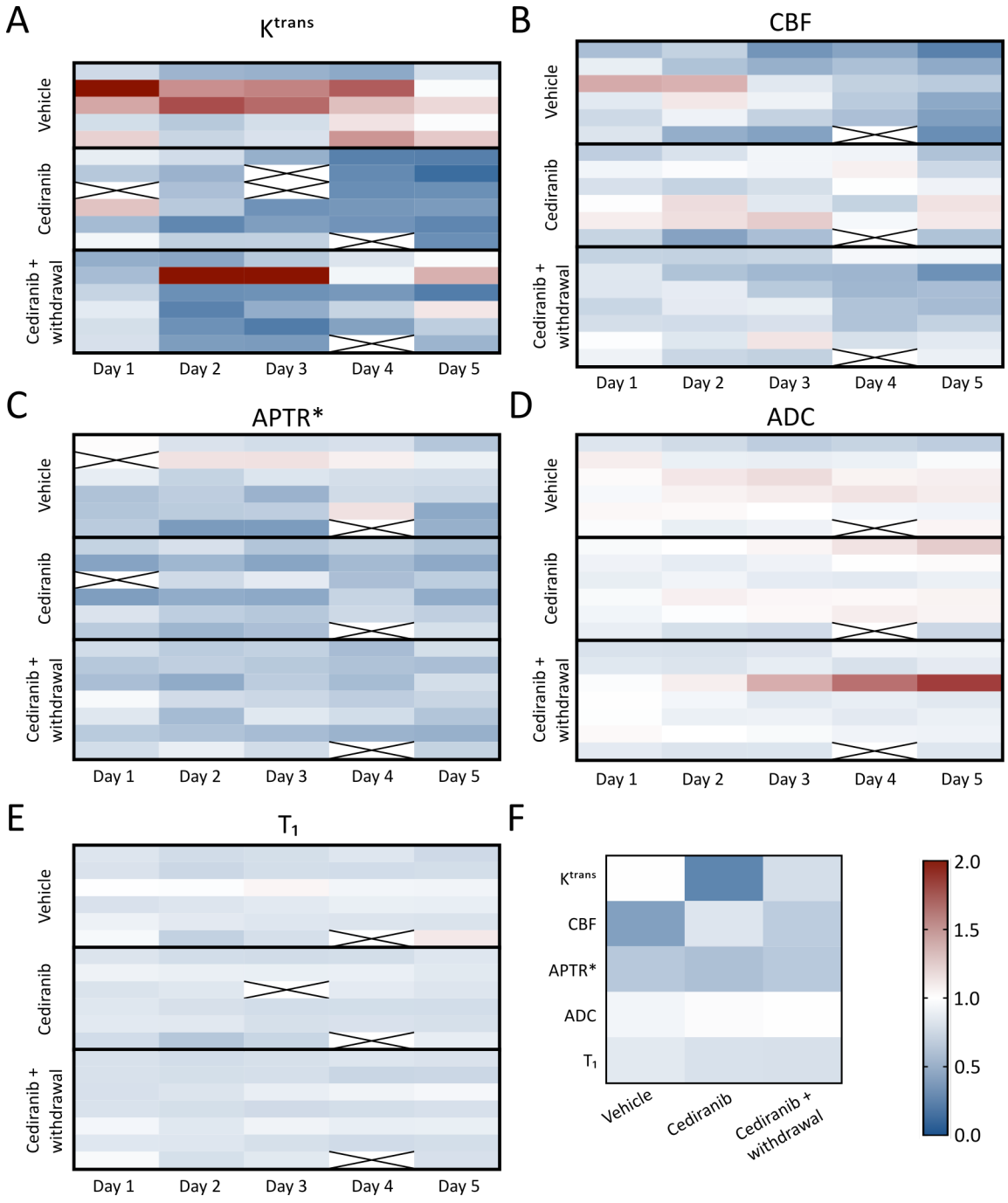

Figure 6.8 Summary of MRI findings of cediranib treatment and withdrawal in rat brain metastases. Heatmap of changes over time in K^{trans} (**A**), CBF (**B**), APTR* (**C**), ADC (**D**) and T_1 relaxation (**E**) in vehicle, cediranib and cediranib + withdrawal (cediranib treatment during the first three days) treated rat brain metastases. Increases are shown in red, decreases in blue and no change in white. Absence of result is represented by an X. **F** Summary of results from all MRI techniques after five days of treatment with vehicle or cediranib or two days of cediranib withdrawal (following three days of treatment) relative to baseline imaging.

6.3.4 Cediranib concentration in brain metastases

A previous study by Wang and colleagues demonstrated active efflux of cediranib by the BBB, limiting its effect in the brain (Wang, Agarwal and Elmquist, 2012). However, this quantitation took place in naïve rats with an intact BBB, which could limit the accumulation of cediranib in the tissue *per se*. Here, cediranib concentrations were significantly increased in brain metastases compared to the healthy striatum of the contralateral hemisphere ($p < 0.001$) and were similar to cediranib levels found in the blood plasma at the same time point (Figure 6.9A). Over time, there appeared to be a reduction in cediranib concentration in brain metastases relative to the healthy contralateral striatum (Figure 6.9B). However, this analysis was only performed in a small number of rats, particularly at day 1 and 2, and, therefore, is only a preliminary indication. Additionally, cediranib plasma concentration was calculated 2 hours after cediranib injection for five consecutive days and showed no significant changes over time (Figure 6.9C). The similar cediranib concentrations evident on different days suggests that previous doses of cediranib did not contribute to the concentrations measured daily in plasma each day and are no longer present in the bloodstream 24 hours after injection.

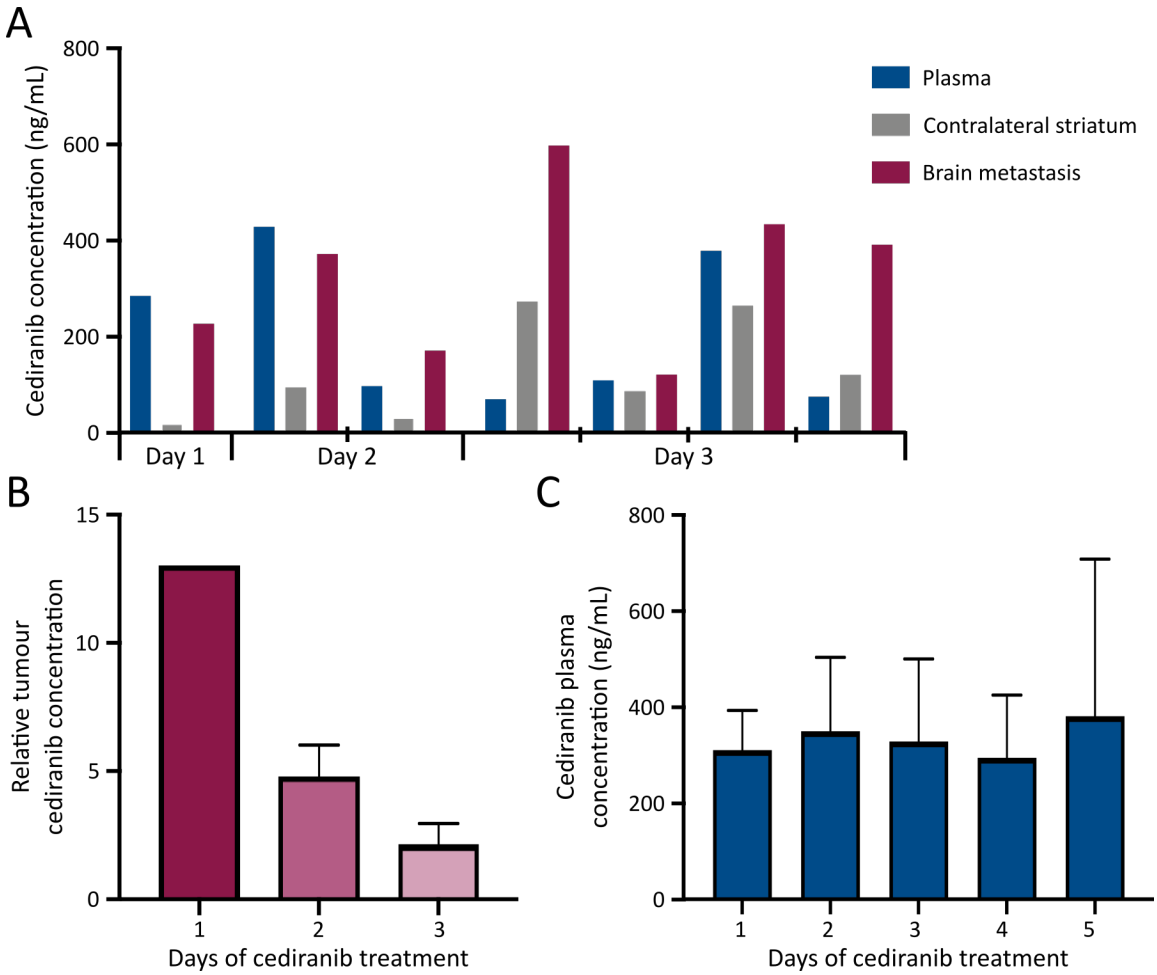

Figure 6.9 Cediranib concentration in brain metastases and rat plasma following treatment. **A** Cediranib concentration in plasma, healthy brain and brain metastasis foci following 1 (n = 1), 2 (n = 2) and 3 days (n = 4) of treatment (4 mg/kg i.v. daily). **B** Relative cediranib concentrations in brain metastases (metastasis concentration divided by contralateral tissue concentration), determined by HPLC-MS, after 1 (n = 1), 2 (n = 2) and 3 days (n = 4) of treatment. Brains were isolated approximately 3 hours following the last cediranib injection. **C** Blood plasma cediranib concentration over time. Plasma samples were extracted 2 hours post-cediranib injection and immediately preceded MRI session. End plasma concentration was obtained following the MRI session of approximately one hour, and immediately prior to saline perfusion. Data are shown as mean ± standard deviation (from left to right, n = 9, 12, 11, 4, 3, 9).

6.3.5 Histological assessment of rat brain metastases after cediranib treatment

As performed for the bevacizumab-treated brain metastases in Chapter 5, histological quantitation of microvessel density, presence of pericytes, VMI and levels of hypoxia in rat brain metastases were determined by immunohistochemistry for CD31 (Figure 6.10),

αSMA (Figure 6.11), the ratio between the two (Figure 6.12), and pimonidazole (Figure 6.13), respectively. Contrary to the MRI results, no significant differences were observed in any of the histological analyses using vascular normalisation markers between cediranib and vehicle-treated brain metastases following three and five days of treatment or in cediranib + withdrawal brain metastases. A significant increase in microvessel density and pericyte positive staining was consistently detected in the rim of brain metastatic foci, in all treatment groups and at all time points, compared to the core region or to the contralateral striatum. In contrast, the microvessel density and levels of pericyte staining were decreased in the core region of the brain metastases when compared to the contralateral striatum after three days of either treatment, and also after five days of treatment for the microvessel density. Although the levels of αSMA were increased at this later time point, this was only by about 1 % in all treatment groups. The majority of the core of brain metastasis foci was largely devoid of tumour nodules, which explained the reduction in vascular staining in this region. As in the previous chapter, the VMI of brain metastases was only calculated in the rim region of brain metastatic foci, since the core values for vascular staining were predominantly negative. No significant differences could be detected between treatment groups at either time point, yet a trend toward an increase in VMI over time can be observed. Finally, both the rim and the core of metastatic foci exhibited significantly greater levels of hypoxia than the healthy brain tissue of the contralateral striatum in cediranib and vehicle-treated rats. The same increase in brain metastasis hypoxia was observed in the cediranib + withdrawal group. Furthermore, levels of hypoxia were significantly increased between the tumour time points in both the rim and the core, for the cediranib-treated brain metastases, including the withdrawal group, but was only detected in the core of vehicle-treated rats. However,

a similar trend can be observed in the results from this treatment group compared to the cediranib group.

These histological results do not provide insights into the mechanism of action of cediranib for vascular normalisation of rat brain metastases, as would be suggested to occur through the decreased K^{trans} detected in DCE MRI over time and in the increased in brain metastasis blood flow related to vehicle-treated rats.

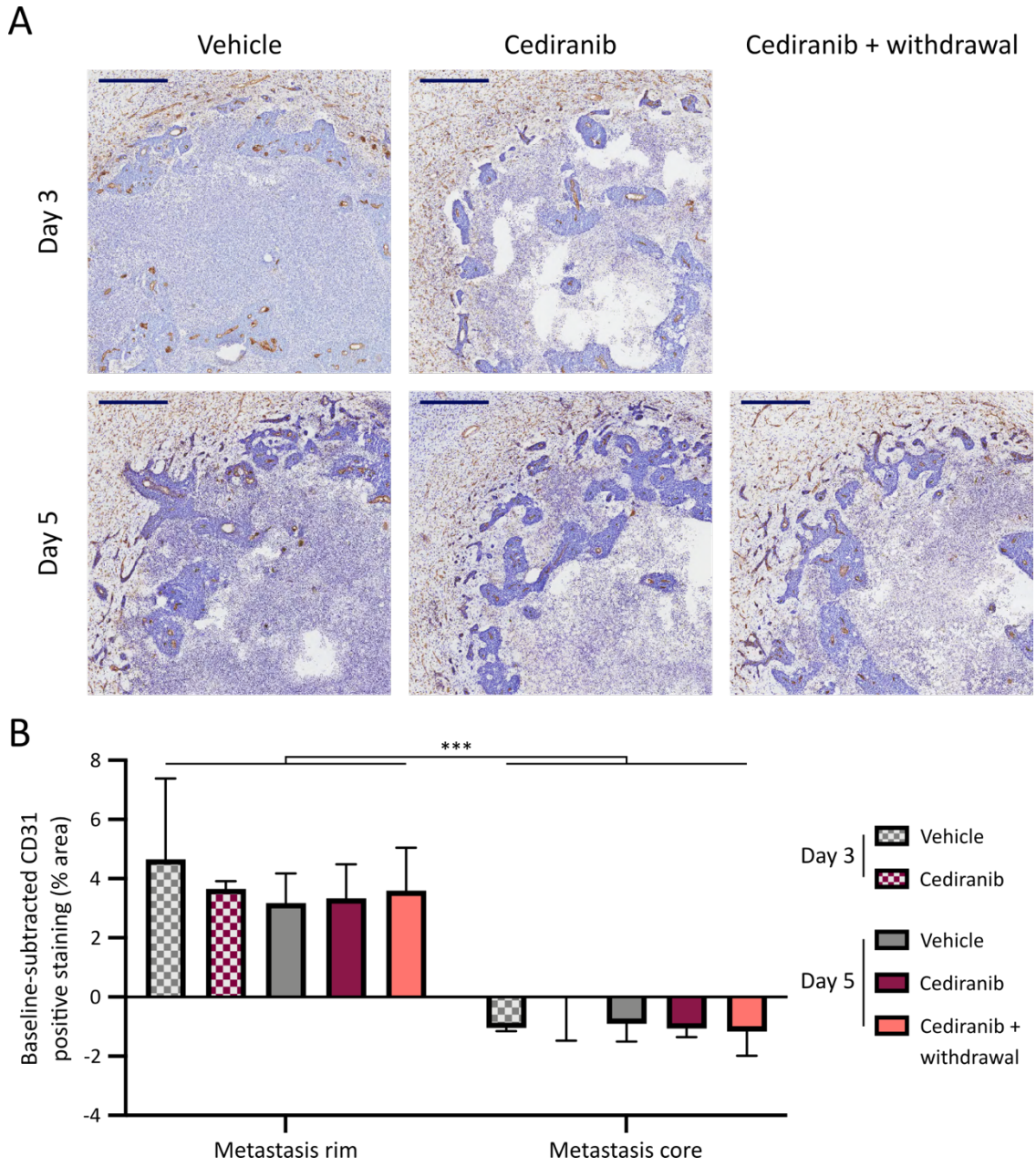

Figure 6.10 Microvessel density of brain metastases treated with cediranib. **A** Representative sections of CD31 IHC (brown stain), representing vasculature, in brain metastases treated with vehicle or cediranib (4 mg/kg) for three and five days, or with cediranib + withdrawal at day 5. **B** Percentage of baseline-subtracted (contralateral striatum) CD31 positive staining (brown) in brain metastasis foci of rats treated with vehicle (n = 2 rats; 32 sections) or cediranib (n = 3 rats; 45 sections) following three days of treatment and of rats treated with vehicle (n = 6 rats; 77 sections) and cediranib (n = 6 rats; 89 sections) following five days of treatment and in cediranib + withdrawal rats (cediranib, three days + withdrawal, two days; n = 7 rats; 111 sections. Data are represented as the mean staining percentage from rat brain metastases in each treatment group ± standard deviation (*** $p < 0.001$; 2-way ANOVA with Sidak's multiple comparisons).

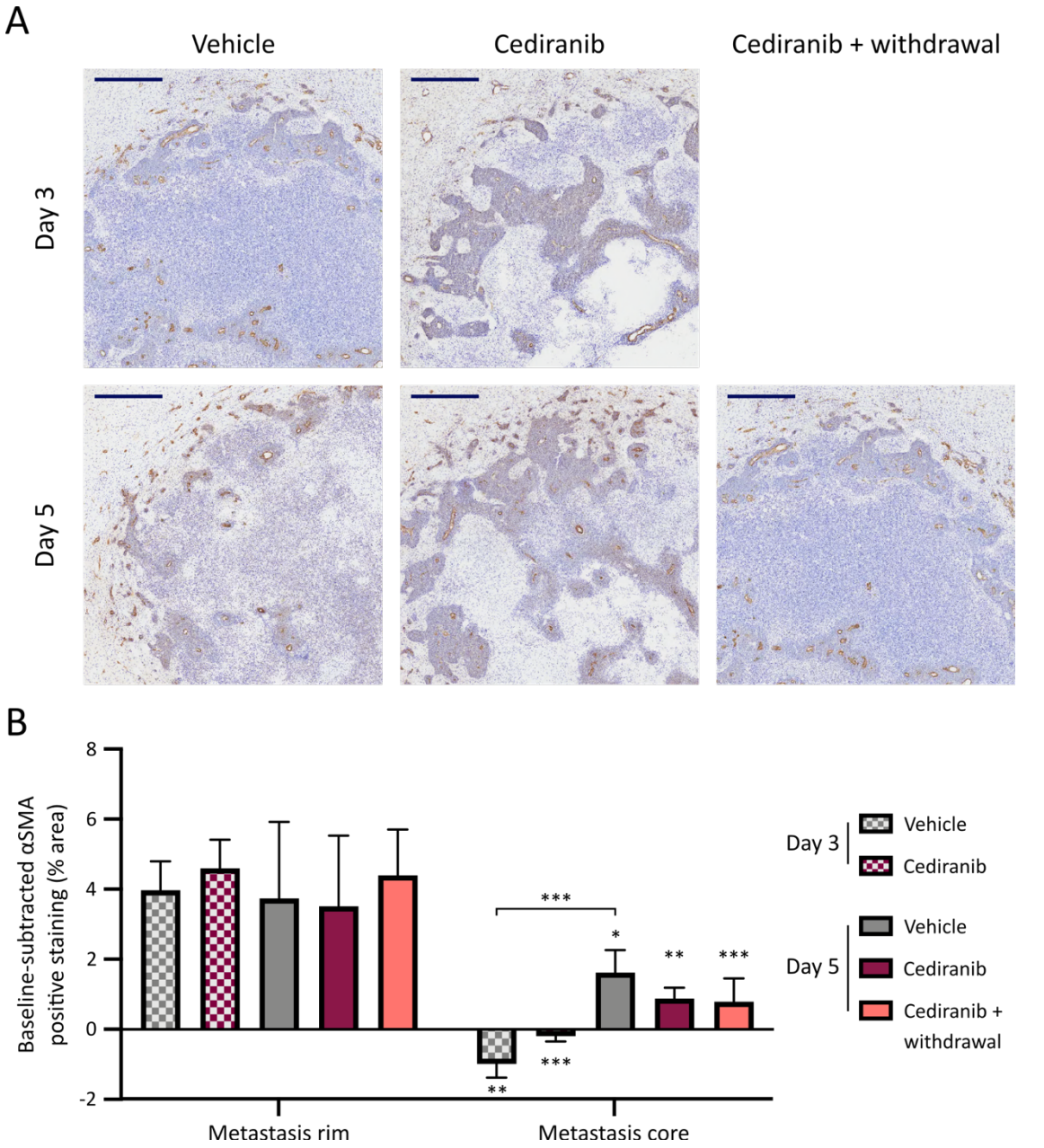

Figure 6.11 Pericyte positive staining in cediranib-treated brain metastases. **A** Representative sections of α-smooth muscle actin (αSMA) IHC (brown stain), representing pericytes, in brain metastases treated with vehicle or cediranib (4 mg/kg) for three and five days, or with cediranib + withdrawal at day 5. **B** Percentage of baseline-subtracted (contralateral striatum) αSMA positive staining (brown) in brain metastasis foci of rats treated with vehicle (*n* = 2 rats; 33 sections) or cediranib (*n* = 3 rats; 43 sections) following three days of treatment and of rats treated with vehicle (*n* = 6 rats; 84 sections) and cediranib (*n* = 6 rats; 93 sections) following five days of treatment and in cediranib + withdrawal rats (cediranib, three days + withdrawal, two days; *n* = 7 rats; 114 sections). Data are represented as the mean staining percentage from rat brain metastases in each treatment group ± standard deviation and * above bars in the core represent significant changes between the rim and core regions (* $p < 0.05$, ** $p < 0.01$, *** $p < 0.001$; 2-way ANOVA with Sidak's multiple comparisons).

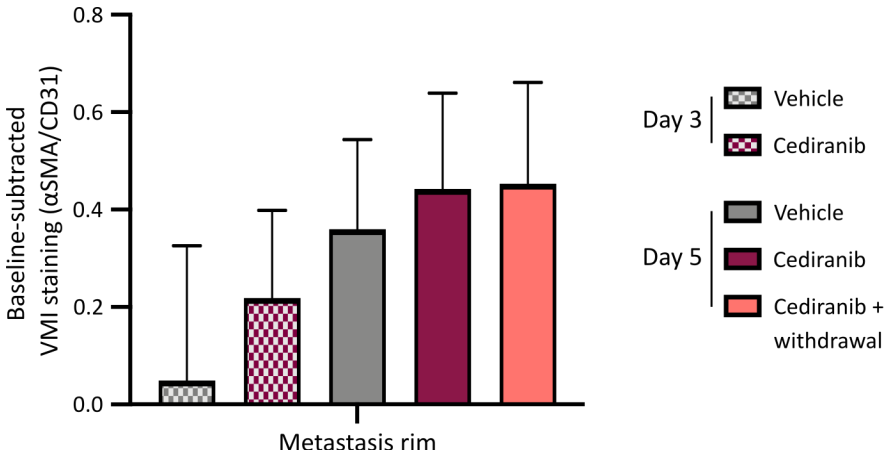

Figure 6.12 Vascular maturation index following cediranib treatment in brain metastases. Pericyte coverage of brain metastasis vasculature was determined by the ratio of baseline-corrected αSMA positive staining over baseline-corrected CD31 positive staining in consecutive brain sections. VMI of rats treated with vehicle (*n* = 2 rats) or cediranib (*n* = 3 rats) following three days of treatment (4 mg/kg) and of rats treated with vehicle (*n* = 6 rats) and cediranib (*n* = 6 rats) following five days of treatment and in cediranib + withdrawal rats (cediranib, three days + withdrawal, two days; *n* = 7 rats). Data are represented as mean rat brain metastasis VMI ± standard deviation (* $p < 0.05$; 2-way ANOVA with Sidak's multiple comparisons).

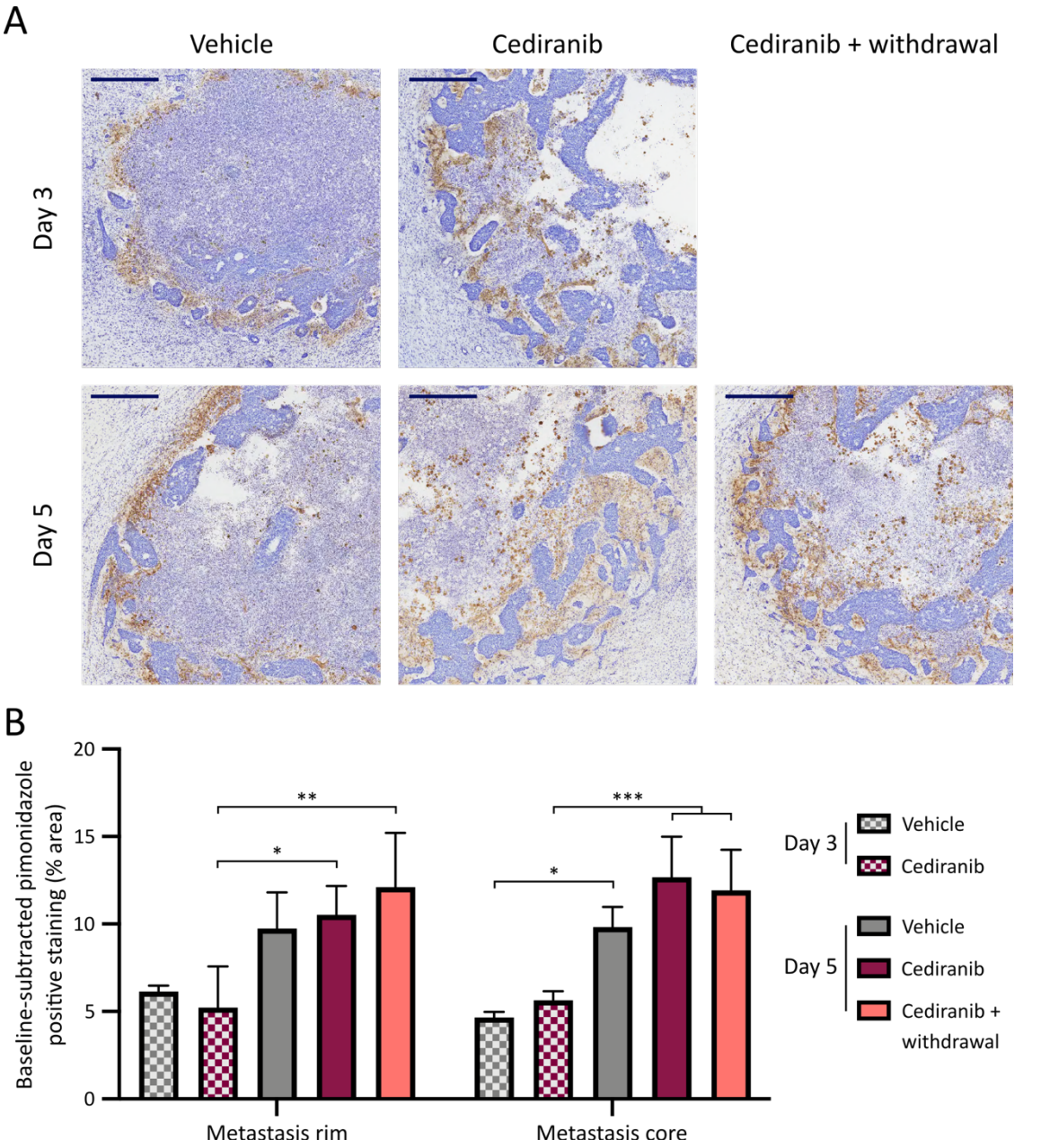

Figure 6.13 Effect of cediranib treatment on the hypoxic fraction of rat brain metastases. **A** Representative sections of pimonidazole IHC (brown stain), representing hypoxia, in brain metastases treated with vehicle or cediranib (4 mg/kg) for three and five days, or with cediranib + withdrawal at day 5. **B** Percentage of baseline-subtracted (contralateral striatum) pimonidazole positive staining (brown) in brain metastasis foci of rats treated with vehicle (n = 2 rats; 29 sections) or cediranib (n = 3 rats; 37 sections) following three days of treatment and of rats treated with vehicle (n = 6 rats; 83 sections) and cediranib (n = 6 rats; 83 sections) following five days of treatment and in cediranib + withdrawal rats (cediranib, three days + withdrawal, two days; n = 7 rats; 109 sections). Data are represented as mean staining percentage in rat brain metastases ± standard deviation (* $p < 0.05$, ** $p < 0.01$; 2-way ANOVA with Sidak's multiple comparisons).

6.4 Discussion

This study represents the first use of a vascular normalisation agent in a syngeneic rodent model of brain metastasis. Previous studies involving bevacizumab in brain metastasis xenograft nude mouse models have been performed (Bohn *et al.*, 2017), but are not all encompassing owing to the compromised immunological response in these tumour models and the diminished affinity of bevacizumab to rodent VEGF-A, secreted by mouse macrophages and fibroblasts, part of the tumour microenvironment (Galdiero *et al.*, 2013; Goel and Mercurio, 2013; Bridges and Harris, 2015; Elamin *et al.*, 2015; Xu *et al.*, 2018). Cediranib possesses an advantage over bevacizumab in that it can be used similarly in syngeneic and xenogeneic preclinical brain metastasis and primary tumour models, as well as in patients (European Medicines Agency, 2016).

6.4.1 Cediranib treatment of rat brain metastases yielded changes in MRI, supporting the vascular normalisation hypothesis

Since DCE MRI is the current detection method for vascular normalisation in clinical settings, it served here as a positive control for vascular normalisation and as a comparator for other MRI techniques, not requiring the injection of GBCAs, that could potentially replace DCE MRI for this purpose in the clinic. The observed decreases in K^{trans} over time in cediranib-treated brain metastases would imply that vascular normalisation occurred in this model. The decrease in K^{trans} suggested that a maturation of brain metastasis associated vessels was ongoing, but was dependent on daily administration of cediranib, as highlighted by increases in K^{trans} upon treatment withdrawal.

A significant decrease in apparent brain metastasis growth progression, as determined by tumour volume estimates from T_2-weighted images, was detected in cediranib-treated rats and cediranib + withdrawal rats compared to the vehicle group. This inhibition of tumour growth has been observed in previous preclinical studies and supports the vascular normalisation hypothesis for this rat model (Wedge *et al.*, 2005; Goodlad *et al.*, 2006; Miller *et al.*, 2006).

MP-pCASL MRI yielded CBF measurements that also displayed significant differences between cediranib and vehicle-treated brain metastases. The significant decrease in tumour associated blood flow present in vehicle-treated metastases was not seen in either the rats treated with cediranib for five days or in the cediranib + withdrawal group. This finding was in agreement with the hypothesis that CBF should not decrease upon vascular normalisation of brain metastases, as the maturation of tumour associated vessels will promote blood flow in this region. A small decrease in CBF was still observed in the cediranib-treated brain metastases and could be caused by starvation of the core region of the brain metastasis foci, resulting from this anti-angiogenic treatment. Withdrawal of cediranib treatment for a period of two days did not significantly impact the measured brain metastasis blood flow. Changes in tumour blood flow appear to occur at a slower pace than those detected by DCE MRI, but are also reporting different stages in the vascular normalisation process. One could argue that the existing tumour associated vessels, initially normalised through cediranib treatment, retain their perfusion capability for some time after the re-establishment of an impaired BBB in these vessels. Longer studies would have to be performed following withdrawal of cediranib to determine whether brain metastasis blood flow decreases would occur, as in the vehicle-treated group, in comparison to rats with daily administration of cediranib.

Evidence of vascular normalisation could be detected both by DCE MRI and MP-pCASL MRI, albeit at later time points in the latter. On the basis of these data, it appears that K^{trans} from DCE MRI remains the most sensitive and rapid detection method for vascular normalisation in rat brain metastases. However, CBF from MP-pCASL MRI could be used in combination with DCE MRI to further support the detection of vascular normalisation in brain metastases and could be especially valuable in patients where the use of GBCAs is contraindicated. Furthermore, MP-pCASL MRI can be performed more frequently than DCE MRI as it does not require administration of exogenous contrast agents and could, therefore, be used to detect non-responders of this therapeutic approach. Clinically, vascular normalisation is performed as part of combination therapies and MP-pCASL MRI could be used during combination therapy follow-up to detect changes in tumour blood flow and differentiate between relapse and pseudo-progression of the brain metastases, as previously shown in glioblastoma by Xu and colleagues (Xu *et al.*, 2017). To confirm this finding in brain metastases, combination therapies involving cediranib treatment should be performed in this rat model of breast cancer brain metastasis.

All other non-invasive MRI techniques performed in cediranib and vehicle-treated brain metastases did not yield significant differences between treatment groups. Perhaps changes would occur and be detected following a longer dosing regimen of cediranib. However, longer studies were not performed owing to the large size of brain metastases in the rats following five days of treatment. If longer treatment studies were to be performed, the brain metastasis tumour model would have to be replaced with a slower growing model.

6.4.2 Cediranib was efficiently delivered to sites of brain metastases

Cediranib has been shown to be rapidly distributed to most tissues in naïve rats, following administration, but with low concentrations found in the brain and spinal cord, suggesting that cediranib cannot cross the BBB (Wang, Agarwal and Elmquist, 2012; Tang *et al.*, 2017). Preliminary data acquired in this study indicated that cediranib concentrations in brain metastases were similar to plasma cediranib concentrations, demonstrating that tumour-associated BBB disruption allows distribution of cediranib to the relevant tumour tissue. Healthy brain tissue cediranib concentrations were significantly lower than those present in the tumour, suggesting a preferential distribution of cediranib in brain regions with a compromised BBB. The reduction in cediranib concentration in brain metastases over time agreed with previous findings indicating active efflux transport by P-gp (Wang, Agarwal and Elmquist, 2012), but also served to demonstrate the success of this therapy at the tumour site. In fact, this decrease in cediranib concentration in brain metastases over time elegantly demonstrated the selective accumulation of cediranib activity to brain regions that could benefit from vascular normalisation therapy in this model. However, it should be noted that the measurement of cediranib concentration in the brain was only performed in a small number of brain metastasis foci in this study and would need to be repeated at all time points assayed for firm conclusions to be reached.

The plasma concentrations of cediranib, two hours post i.v. injection, were similar following single or multiple treatments. The half-life of cediranib in rats is of approximately 12 hours (European Medicines Agency, 2016), in agreement with the results presented here, since no increase in cediranib concentration was observed as

dosing was repeated. As shown with DCE MRI results, daily dosing of cediranib was required to maintain its effects since clearance of cediranib in the blood was accomplished within 24 hours of dosing. Human data has demonstrated using radiolabelled cediranib, that cediranib is metabolised by flavin-containing monooxygenase 1 and 3 (FMO1, FMO3), and uridine 5'-diphospho-glucuronosyltransferase (UGT) and is mostly excreted through faeces (59 %) and urine (21 %), with < 1 % of intact drug being eliminated in urine (Reid *et al.*, 2007; Tang *et al.*, 2017).

In conclusion, cediranib distribution in brain metastases closely resembled blood plasma cediranib levels, but decreased over time, while vascular normalisation of tumour-associated vasculature appeared to continue.

6.4.3 Cediranib treatment of rat brain metastases could not be observed by histological analysis

Although K^{trans} and CBF changes were detected by MRI, no significant differences in microvessel density, amount of pericytes, vascular maturation index or hypoxia levels could be detected after three or five days of cediranib treatment. Most preclinical tumour studies involving cediranib have detected decreases in microvessel density as early as 52 hours after onset of cediranib treatment in lung, breast and thyroid cancer models (Wedge *et al.*, 2005; Miller *et al.*, 2006; Gomez-Rivera *et al.*, 2007). However, a study on intestinal cancer detected no such decrease in microvessel density even though a reduction in tumour size was observed (Goodlad *et al.*, 2006). Nevertheless, it is somewhat surprising that no reduction in microvessel density could be found at either the three day or five day treatment time points. It could be possible that in the brain

metastasis model used, endothelial cell death occurs at a slower rate and decreases in microvessel density would only occur over a longer dosing regimen. Additionally, an increase in pericytes should have been observed in cediranib-treated metastases to repair the BBB as well as a decrease in hypoxia levels in the rim of brain metastasis foci upon vascular normalisation.

It is possible that the sample size used was too small, preventing the detection of changes between groups, especially at the earlier time point of 3 days of treatment since only 2-3 rat brains were available for IHC. However, this seems unlikely as at the later time point, larger group numbers are present but the consistency in the IHC results is maintained.

The lack of differences between groups in all histological analyses performed could suggest that a systematic error in quantitation of histological results is occurring. The area of brain metastasis foci was selected as one large tumour for histological analysis. Perhaps individual brain metastasis foci comprising this overall metastasis region should be selected individually and the threshold analysis performed on these smaller regions. However, certain brain metastases are difficult to distinguish from the tumour microenvironment present in the core of the brain metastasis region. Furthermore, the surrounding rim of the brain metastasis region, contributing to the entire tumourigenic area, would be ignored. Also, it could be that the complex organisation of the metastases within the brain parenchyma is not significantly altered since it is not one solid tumour, but a combination of tens to hundreds of smaller tumour nodules and that the effects of vascular normalisation normally measured histologically do not present themselves in such tumour structures. Further analyses, e.g. looking at vessel diameter or tortuosity, should be performed on the existing histological sections, as well as other markers of anti-

angiogenic treatment, such as the angiogenesis marker Tie2 used in Chapter 4 or the phosphorylation of VEGFR2, which should both decrease following treatment with cediranib. Alternatively, histological analysis could altogether be dismissed and replaced by Western blotting or qPCR analysis of brain metastasis tissue to look at the expression levels of angiogenesis markers upon cediranib treatment.

Ultimately, anti-angiogenic or vascular normalising effects of cediranib in brain metastases could not be detected through histological analysis using the proposed markers for vascular normalisation.

6.5 Conclusion

The vascular normalisation effects of daily cediranib treatment could be detected by MRI and HPLC-MS in a model of rat breast cancer brain metastasis, but not through histological analysis. K^{trans} and tumour growth were significantly reduced in cediranib-treated brain metastases compared to vehicle-treated brain metastases. Moreover, a significant decrease in brain metastasis blood flow over time, compared to baseline brain metastasis blood flow, was detected in tumours that did not receive cediranib but not in those that did. HPLC-MS analysis of brain metastases relative to the healthy contralateral striatum tissue of the same rat displayed a decrease in cediranib distribution in the tumour over time, indicative of the BBB restoration occurring as a result of vascular normalisation. Finally, no histological differences in microvessel density, levels of pericytes, VMI or hypoxia levels were observed between cediranib and vehicle-treated brain metastases. This lack of differences between groups suggests either the presence of a systematic error in all histological analyses performed, the increased sensitivity of vascular normalisation detection of MRI compared to IHC, or that vascular normalisation effects cannot be detected histologically in brain metastases owing to the complex organisation of metastatic foci in the brain.

CHAPTER 7

Conclusions, critique and future work

7.1 Conclusions

The body of work presented in this thesis has focused on the optimisation of multiphase pseudo-continuous arterial spin labelling magnetic resonance imaging (MP-pCASL MRI) in rats and its application to a rat model of breast cancer brain metastasis to obtain quantitative measurements of cerebral and tumour blood flow. MP-pCASL MRI was also proposed as an alternative diagnostic imaging approach to dynamic contrast-enhanced (DCE) MRI for the detection of vascular normalisation in this preclinical tumour model.

Firstly, an optimisation of the MP-pCASL MRI sequence and analysis pipeline was developed in Chapter 3, using three strains of rats, to attempt a standardisation of ASL MRI for preclinical research. MP-pCASL MRI proved superior to its predecessor, pCASL MRI, since off-resonance effects and susceptibility artefacts present during blood labelling were accounted and corrected for by the addition of a multiphase component. Incorporation of supervoxel phase priors in four subregions of the brain during analysis

further improved data robustness and reproducibility. Resulting CBF measurements from MP-pCASL MRI were in agreement with gold-standard autoradiography CBF values in the same rats.

Once MP-pCASL MRI was optimised for rat CBF measurements, it was compared to clinically-relevant MRI techniques of brain tumour imaging, during growth and progression of a rat model of breast cancer brain metastasis, as a contrast agent-free technique in Chapter 4. MP-pCASL MRI was shown to provide brain metastasis blood flow measurements in accord with the decreased relative cerebral blood volume (rCBV) estimates, and it is proposed that MP-pCASL MRI could be used as the perfusion MRI technique of choice as a non-invasive imaging technique, replacing DSC and DCE MRI. Histological analysis of the brain metastasis model indicated the hypoxic and angiogenic features of this tumour model. Interestingly, an increased microvessel density was found in the brain metastasis foci, contradictory to the lower perfusion values in this region observed by MRI.

Finally, in Chapters 5 and 6, MP-pCASL MRI was proposed as a replacement to DCE MRI for the detection of vascular normalisation therapy in rat brain metastases. In Chapter 5 vascular normalisation was not achieved in brain metastases with bevacizumab, but was successful when using cediranib (Chapter 6), based on DCE MRI and MP-pCASL MRI results. A significant decrease in brain metastasis K^{trans}, the permeability factor obtained from DCE MRI, and a maintenance of baseline tumour blood flow were observed following treatment with cediranib, compared to vehicle-treated rats. However, histological differences between treatment groups were not observed when looking at microvessel density, pericytes, vascular maturation index or levels of hypoxia. This lack of histological evidence of vascular normalisation could potentially be attributed to the

multitude of small metastases comprising the tumour area, with the presence of large stromal components, leading to differences too small to detect in the large region analysed.

7.2 Critique and future work

7.2.1 Additional improvements to MP-pCASL MRI

In Chapter 3 of this thesis, a rather extensive optimisation of MP-pCASL MRI was performed in three strains of rats. This was the first instance where an angled labelling plane was used, improving the blood labelling through the neck and was also the first implementation of *multiphase* pCASL MRI in rats to address the off-resonance effects and susceptibility artefacts present in preclinical imaging. However, further optimisations could still be performed. For example, a 3D readout of MP-pCASL MRI was not attempted as it would require complex alterations to the pulse sequence and additional MRI physics development. Furthermore, the implementation of a 3D acquisition readout could limit the use of this technique to some scanners or centres only. On this basis, the 2D spin-echo EPI was retained in the current work. To fully standardise this technique, MP-pCASL MRI should be performed in rats on different MRI scanners and at different centres, thus validating the reliability of this technique. Of interest, development and validation of this MP-pCASL MRI method for mouse imaging on the same scanner was performed by another member of the group and also yielded CBF values in agreement with autoradiography results (Buck *et al.*, 2018)[1]. In this case, to translate from rat to mouse,

[1] I have contributed to this work.

the angle of the labelling plane and the post-label delay (PLD) were modified, and a respiration-gated acquisition profile was used to account for the more pronounced effect of respiration-induced artefacts in mouse brain.

Finally, validation of CBF measurements from MP-pCASL MRI was determined by [^{14}C]-iodoantipyrine autoradiography in naïve rats. However, such validation was not performed in the rat model of brain metastasis used in Chapters 4, 5 & 6. There is a possibility that dysregulated blood flow, such as is present in brain tumours, would impact the reliability of the CBF measurements, especially as a delayed arrival of labelled blood was detected in the brain metastasis region in Chapter 4. The later arrival of blood to this area, should it arrive after the increased PLD chosen for tumour imaging, could lead to an overestimation of tumour blood flow. Hence, autoradiography should be performed in rats with brain metastases to determine the potential effect of dysregulated flow on the accuracy of MP-pCASL MRI CBF measurements.

7.2.2 Consideration of brain metastasis heterogeneity in MRI analyses

In this thesis, brain regions containing metastatic foci were regarded as a single tumour mass when analysing MRI data. In doing so, the heterogeneity present in the tissue composition of brain metastases is ignored. The analysis of MRI data would perhaps benefit from the separation of the brain tumour mass through the use of supervoxels (as used for image phase prior map generation in the analysis pipeline for MP-pCASL MRI) or another clustering approach, based on combined voxel perfusion, permeability, relaxation values and diffusion changes compared to healthy tissue (e.g. low blood flow and high permeability as one cluster, *etc.*). However, the introduction of such a clustering

approach would inherently add complexity to the interpretation of MRI data since a number of clusters would have to be selected to accurately represent the heterogeneity present in the brain metastases. Furthermore, the output data for each of these subregions of the tumour could be presented individually or combined in such a way as to retain the complexity of the tumour region.

Alternatively, the area of metastatic foci could be divided into gadolinium-enhancing and non-enhancing regions. Yet, the direct translation of these segmentations from one MRI technique to another, e.g. T_1-weighted acquisition to spin-echo EPI, is rather complex owing to the resolution differences and to the distinct pattern of artefacts and image shifts present in image readout acquisitions (Erasmus *et al.*, 2004). By translating a segmentation from one imaging readout to another, the precision of the enhancing and non-enhancing regions of the brain metastases would diminish. Further complication arising from the division of the tumour into enhancing and non-enhancing tissue would present itself following treatment, as is the case in vascular normalisation where the voxels that were initially enhancing are normalised and lose their enhancement in response to therapy. Although the tumour heterogeneity in this region would still be present, it would not be accounted for in this scenario. Lastly, these arguments bring forth the question of whether the separation of the overall metastatic area to subregions for the MRI analysis would, in fact, be advantageous for tumour characterisation, treatment planning or assessment of treatment response since subregions present in the tumour could independently suggest opposing treatments. This heterogeneity between results from metastatic regions could lead to user bias or confusion. Additional research would need to be performed to confirm or deny the usefulness of this approach of brain metastasis MRI data interpretation.

7.2.3 Discrepancies between histological and MRI results

Often, in this thesis, the histological analysis when compared to MRI results yielded conflicting results. The only instances where histological results were in agreement with the MRI observations were in Chapter 4, where the lower CBF measurements in the brain metastases correlated with a decrease in microvessel density and an increase in the hypoxic fraction. Additionally, the angiogenic phenotype of the breast cancer brain metastases detected in Chapter 4 was predictive for the success of vascular normalisation therapy in the same tumour model in Chapter 6. However, the levels of CD31 vessel staining were increased compared to the contralateral baseline levels, which was not in agreement with MP-pCASL MRI CBF measurements, showing a reduction of blood flow in the brain metastasis region. As explained, these vessels may have been newly formed and not perfused or could have provided an increase in perfusion in the rim of the metastatic region too small to be detected by MRI spatial resolution. Moreover, in Chapter 6, another discrepancy between CD31 histological analysis and MRI occurred when a decrease in microvessel density was not present as would be expected with successful vascular normalisation. Perhaps the use of a different marker of vasculature, such as collagen type IV (marker of the basal lamina of vessels, instead of the endothelium), would serve better in both instances. Ideally, a marker of perfused vessels would be used, as was attempted through the injection of tomato lectin in the bloodstream prior to killing in Chapter 4, to only quantify presence of perfused vessels within the metastatic foci. Unfortunately, the leakage of lectins through the BBB increased background levels of staining, making quantitation of vessels in the brain metastasis region impossible.

In addition, brain metastasis levels of αSMA remained unchanged over time, irrespective of the treatment group. One possibility for this consistency in pericyte levels is the presence of co-opted vessels in brain metastases. These 'healthy' vessels co-opted by the tumour are already rich in pericytes. Furthermore, studies have shown that tumour rims, more likely to perform vessel co-option, are less affected by vascular normalisation therapy (Mehta *et al.*, 2011; Welti *et al.*, 2012), and that vessel co-option could be a source of anti-angiogenic treatment resistance by providing an answer to the nutrient demands of the tumour and ensuring its survival. Of particular interest, Leenders and colleagues have previously reported that bevacizumab treatment led in sustained tumour progression through vessel co-option, in a mouse model of lung cancer brain metastases (Leenders *et al.*, 2004). In the rat brain metastasis model used herein, a slower tumour progression could be observed in rats receiving cediranib treatment, which would suggest that, although vessel co-option was potentially occurring, angiogenesis was involved in the tumour progression.

In Chapters 5 and 6, additional histological analysis could be performed looking to assess levels of Tie2 expression, as performed in Chapter 4, as a positive control of anti-angiogenic treatment with either bevacizumab or cediranib. Tie2 levels would be expected to decrease in the metastatic foci if vascular normalisation treatment was effective. Similarly, in Chapter 6, levels of phosphorylated VEGFR2 in cediranib-treated rats would be expected to decrease since VEGFR2 activation is inhibited by cediranib. Finally, as an alternative to immunohistochemistry, immunofluorescence of CD31 and αSMA could be performed to better determine whether co-localisation of pericytes with vessels within brain metastases is affected by vascular normalisation treatment, serving as a modification of the vascular maturation index used here.

7.2.4 Clinical perspectives of MP-pCASL MRI and vascular normalisation of brain metastases

Addition of MP-pCASL MRI into routine clinical imaging could be very beneficial. Firstly, the multiphase component of MP-pCASL MRI will become more important as the presence of higher field strength scanners increases clinically. The increase in off-resonance effects occurring at 7 T compared to those at 1.5 T or 3 T will require a multiphase approach to pCASL MRI to produce high quality CBF maps. Additionally, MP-pCASL MRI is a completely non-invasive imaging approach since it does not require the injection of exogenous contrast agents and carries no risk of toxicity, contrary to currently used perfusion MRI techniques that require injection of GBCAs. Hence, MP-pCASL MRI can be performed at any time and repeated as often as necessary.

The work presented in Chapter 6, demonstrated the value of MP-pCASL MRI in the detection of vascular normalisation in brain metastases. Similar findings from Coquery and colleagues were previously shown, where an increase in CBF was detected in a rat brain glioma model by pCASL MRI following treatment with sorafenib, another vascular normalisation agent (Coquery *et al.*, 2018). These findings suggest that MP-pCASL MRI can be used for the preclinical detection of vascular normalisation in brain tumours and appears to be independent of the vascular normalising agent used. Moreover, cediranib has previously been used in glioblastoma patients for 112 days and an increase in CBF was reported for 23 % of patients, a stable CBF for 40 % of patients and a reduction in CBF occurred in 37 % of patients over time using a pulsed ASL MRI approach (Sorensen *et al.*, 2012). Altogether, the results presented in Chapter 6, together with the vascular normalisation studies mentioned, provide strong evidence supporting the addition of

MP-pCASL MRI in the current clinical imaging protocol for brain tumours and in vascular normalisation treatment.

However, it should be mentioned that, although MP-pCASL MRI could support current clinical MRI techniques, the reduction in Ktrans from DCE MRI remains a more sensitive and rapid approach at detecting vascular normalisation in brain metastases.

Lastly, treatment of brain metastasis with anti-angiogenic drugs promoting vascular normalisation could improve therapeutic response to radiotherapy by decreasing the hypoxic fraction present in these tumours (Jain, 2005; Senan and Smit, 2007; Goedegebuure *et al.*, 2019). Since radiotherapy is recommended in the presence of a single large brain metastasis (following surgical resection) and in cases of multiple smaller metastases, vascular normalisation could be used to improve the treatment in these cases. It is of interest to note that radiotherapy has been shown to reduce P-glycoprotein activity in rats (Bart *et al.*, 2007) and, thus, this effect could further enhance bioavailability of agents, such as cediranib and potentiate vascular normalisation.

7.3 Concluding remarks

In this thesis, ASL MRI is optimised in naïve rats to MP-pCASL MRI and applied to a rat breast cancer brain metastasis model with and without vascular normalisation therapy. MP-pCASL MRI was used to follow tumour progression and to detect CBF changes occurring during vascular normalisation in these brain metastases. On the basis of these studies, MP-pCASL MRI is recommended to be implemented in preclinical cancer research to obtain accurate and reliable measurements of CBF in naïve rats and tumour blood flow in a rat brain metastasis model. Further, MP-pCASL MRI could readily be incorporated

into routine clinical practice, as it does not require hardware specific alterations to current imaging systems or the approval of a novel injectable agent. The work presented here suggests that MP-pCASL MRI would be of particular use in the imaging, differentiation and in treatment planning for brain tumours, including brain metastases, following their detection using conventional imaging techniques. The main advantage of MP-pCASL MRI is its completely non-invasive nature by using blood as an endogenous contrast agent; therefore, it could replace GBCA-dependent perfusion MRI techniques, such as DCE MRI and dynamic susceptibility contrast MRI. Finally, MP-pCASL MRI could be used for the detection of vascular normalisation therapy in brain metastases and provide a more robust treatment follow-up.

REFERENCES

Abdel Razek, A. A. K. and Nada, N. (2018) 'Arterial spin labeling perfusion-weighted MR imaging: correlation of tumor blood flow with pathological degree of tumor differentiation, clinical stage and nodal metastasis of head and neck squamous cell carcinoma', *European Archives of Oto-Rhino-Laryngology*. Springer Berlin Heidelberg, 275(5), pp. 1301–1307. doi: 10.1007/s00405-018-4950-3.

Acosta, A., Aslanidi, G., Voutetakis, A., Bruce, J., Zolotukhin, S., Toivonen, R., Mayranpaa, M. and Savontaus, M. (2008) '145. Ultrasound and Micro-Bubbles Coated with Anti-VCAM-1 Antibody for Selective Gene Delivery to Unstable Atherosclerotic Plaques in Mouse Aorta Post Angioplasty', *Molecular Therapy*, 16, pp. S55–S56. doi: 10.1016/s1525-0016(16)39548-x.

Ahmad, S. A., Liu, W., Jung, Y. D., Fan, F., Wilson, M., Reinmuth, N., Shaheen, R. M., Bucana, C. D. and Ellis, L. M. (2001) 'The effects of angiopoietin-1 and -2 on tumor growth and angiogenesis in human colon cancer', *Cancer Research*, 61(4), pp. 1255–1259.

Ahn, M.-J., Kim, D.-W., Kim, T. M., Lin, C.-C., Ratnayake, J., Carlie, D. J., Yin, X., Yang, Z., Jiang, H. and Yang, J. C.-H. (2016) 'Phase I study of AZD3759, a CNS penetrable EGFR inhibitor, for the treatment of non-small-cell lung cancer (NSCLC) with brain metastasis (BM) and leptomeningeal metastasis (LM).', *Journal of Clinical Oncology*. American Society of Clinical Oncology, 34(15_suppl), p. 9003. doi: 10.1200/JCO.2016.34.15_suppl.9003.

Alegria, F. C. (2009) 'Bias of amplitude estimation using three-parameter sine fitting in the presence of additive noise', *Measurement: Journal of the International Measurement Confederation*. Elsevier Ltd, 42(5), pp. 748–756. doi: 10.1016/j.measurement.2008.12.006.

Alsop, D. C., Detre, J. a., Golay, X., Günther, M., Hendrikse, J., Hernandez-Garcia, L., Lu, H., Macintosh, B. J., Parkes, L. M., Smits, M., van Osch, M. J. P., Wang, D. J. J., Wong, E. C. and Zaharchuk, G. (2014) 'Recommended implementation of arterial spin-labeled perfusion MRI for clinical applications: A consensus of the ISMRM perfusion study group and the european consortium for ASL in dementia', *Magn Reson Med*, 116(October 2013), pp. 102–116. doi: 10.1002/mrm.25197.

Alsop, D. C. and Detre, J. A. (1996) 'Reduced transit-time sensitivity in noninvasive magnetic resonance imaging of human cerebral blood flow.', *Journal of Cerebral Blood Flow and Metabolism*, pp. 1236–49. doi: 10.1097/00004647-199611000-00019.

Anderson, R. L., Balasas, T., Callaghan, J., Coombes, R. C., Evans, J., Hall, J. A., Kinrade, S., Jones, D., Jones, P. S., Jones, R., Marshall, J. F., Panico, M. B., Shaw, J. A., Steeg, P. S., Sullivan, M., Tong, W., Westwell, A. D. and Ritchie, J. W. A. (2019) 'A framework for the development of effective anti-metastatic agents', *Nature Reviews Clinical Oncology*. Springer US, 16(3), pp. 185–204. doi: 10.1038/s41571-018-0134-8.

Asao, C., Korogi, Y., Kitajima, M., Hirai, T., Baba, Y., Makino, K., Kochi, M., Morishita, S. and

Yamashita, Y. (2005) 'Diffusion-weighted imaging of radiation-induced brain injury for differentiation from tumor recurrence', *American Journal of Neuroradiology*, 26(6), pp. 1455–1460.

Ballard, P., Yates, J. W. T., Yang, Z., Kim, D. W., Yang, J. C. H., Cantarini, M., Pickup, K., Jordan, A., Hickey, M., Grist, M., Box, M., Johnström, P., Varnäs, K., Malmquist, J., Thress, K. S., Jänne, P. A. and Cross, D. (2016) 'Preclinical comparison of osimertinib with other EGFR-TKIs in EGFR-mutant NSCLC brain metastases models, and early evidence of clinical brain metastases activity', *Clinical Cancer Research*, 22(20), pp. 5130–5140. doi: 10.1158/1078-0432.CCR-16-0399.

Baluk, P., Morikawa, S., Haskell, A., Mancuso, M. and McDonald, D. M. (2003) 'Abnormalities of Basement Membrane on Blood Vessels and Endothelial Sprouts in Tumors', *American Journal of Pathology*, 163(5), pp. 1801–1815. doi: 10.1016/S0002-9440(10)63540-7.

Barnholtz-Sloan, J. S., Sloan, A. E., Davis, F. G., Vigneau, F. D., Lai, P. and Sawaya, R. E. (2004) 'Incidence proportions of brain metastases in patients diagnosed (1973 to 2001) in the Metropolitan Detroit Cancer Surveillance System', *Journal of Clinical Oncology*, 22(14), pp. 2865–2872. doi: 10.1200/JCO.2004.12.149.

Bart, J., Nagengast, W. B., Coppes, R. P., Wegman, T. D., Van Der Graaf, W. T. A., Groen, H. J. M., Vaalburg, W., De Vries, E. G. E. and Hendrikse, N. H. (2007) 'Irradiation of rat brain reduces P-glycoprotein expression and function', *British Journal of Cancer*, 97(3), pp. 322–326. doi: 10.1038/sj.bjc.6603864.

Basser, P. J. and Jones, D. K. (2002) 'Diffusion-tensor MRI: Theory, experimental design and data analysis - A technical review', *NMR in Biomedicine*, 15(7–8), pp. 456–467. doi: 10.1002/nbm.783.

Batchelor, T. T., Duda, D. G., Di Tomaso, E., Ancukiewicz, M., Plotkin, S. R., Gerstner, E., Eichler, A. F., Drappatz, J., Hochberg, F. H., Benner, T., Louis, D. N., Cohen, K. S., Chea, H., Exarhopoulos, A., Loeffler, J. S., Moses, M. A., Ivy, P., Sorensen, A. G., Wen, P. Y., *et al.* (2010) 'Phase II study of cediranib, an oral pan-vascular endothelial growth factor receptor tyrosine kinase inhibitor, in patients with recurrent glioblastoma', *Journal of Clinical Oncology*, 28(17), pp. 2817–2823. doi: 10.1200/JCO.2009.26.3988.

Batchelor, T. T., Mulholland, P., Neyns, B., Nabors, L. B., Campone, M., Wick, A., Mason, W., Mikkelsen, T., Phuphanich, S., Ashby, L. S., DeGroot, J., Gattamaneni, R., Cher, L., Rosenthal, M., Payer, F., Jürgensmeier, J. M., Jain, R. K., Sorensen, A. G., Xu, J., *et al.* (2013) 'Phase III randomized trial comparing the efficacy of cediranib as monotherapy, and in combination with lomustine, versus lomustine alone in patients with recurrent glioblastoma', *Journal of Clinical Oncology*, 31(26), pp. 3212–3218. doi: 10.1200/JCO.2012.47.2464.

Baum, O., Suter, F., Gerber, B., Tschanz, S. A., Buergy, R., Blank, F., Hlushchuk, R. and Djonov, V. (2010) 'VEGF-A promotes intussusceptive angiogenesis in the developing chicken chorioallantoic membrane', *Microcirculation*, 17(6), pp. 447–457. doi: 10.1111/j.1549-8719.2010.00043.x.

Benjamin, L. E., Golijanin, D., Itin, A., Pode, D. and Keshet, E. (1999) 'Selective ablation of immature blood vessels in established human tumors follows vascular endothelial growth factor withdrawal', *Journal of Clinical Investigation*, 103(2), pp. 159–165. doi: 10.1172/JCI5028.

Bergers, G. and Benjamin, L. E. (2003) 'Tumorigenesis and the angiogenic switch', *Nature Reviews Cancer*, 3(6), pp. 401–410. doi: 10.1038/nrc1093.

Bloch, F. (1946) 'Nuclear induction', *Physica*, 70(7–8), pp. 460–474. doi: 10.1016/0031-8914(51)90068-7.

Bohn, K. A., Adkins, C. E., Nounou, M. I. and Lockman, P. R. (2017) 'Inhibition of VEGF and angiopoietin-2 to reduce brain metastases of breast cancer burden', *Frontiers in Pharmacology*, 8(APR), pp. 1–10. doi: 10.3389/fphar.2017.00193.

Bosnian, F. T., Havenith, M. and Cleutjens, J. P. M. (1985) 'Basement membranes in cancer', *Ultrastructural Pathology*, 8(4), pp. 291–304. doi: 10.3109/01913128509141519.

Bridges, E. and Harris, A. L. (2015) 'Vascular-Promoting therapy reduced tumor growth and progression by improving chemotherapy efficacy', *Cancer Cell*. Elsevier Inc., 27(1), pp. 7–9. doi: 10.1016/j.ccell.2014.12.009.

Buck, J., Larkin, J. R., Simard, M. A., Khrapitchev, A. A., Chappell, M. A. and Sibson, N. R. (2018) 'Sensitivity of multiphase pseudocontinuous arterial spin labelling (MP pCASL) magnetic resonance imaging for measuring brain and tumour blood flow in mice', *Contrast Media and Molecular Imaging*, 2018. doi: 10.1155/2018/4580919.

Bulakbasi, N., Kocaoglu, M., Örs, F., Tayfun, C. and Ügöz, T. (2003) 'Combination of single-voxel proton MR spectroscopy and apparent diffusion coefficient calculation in the evaluation of common brain tumors', *American Journal of Neuroradiology*, 24(2), pp. 225–233.

Buxton, R. B., Frank, L. R., Wong, E. C., Siewert, B., Warach, S. and Edelman, R. R. (1998) 'A general kinetic model for quantitative perfusion imaging with arterial spin labeling.', *Magnetic resonance in medicine : official journal of the Society of Magnetic Resonance in Medicine / Society of Magnetic Resonance in Medicine*, 40(3), pp. 383–396. doi: 10.1002/mrm.1910400308.

Candolfi, M., Curtin, J. F., Nichols, W. S., Muhammad, A. K. M. G., King, G. D., Pluhar, G. E., McNiel, E. A., Ohlfest, J. R., Freese, A. B., Moore, P. F., Lerner, J., Lowenstein, P. R. and Castro, M. G. (2007) 'Intracranial glioblastoma models in preclinical neuro-oncology: Neuropathological characterization and tumor progression', *Journal of Neuro-Oncology*, 85(2), pp. 133–148. doi: 10.1007/s11060-007-9400-9.

Carmeliet, P. and Jain, R. K. (2000) 'Angiogenesis in cancer and other diseases', *Nature*, 407(6801), pp. 249–257. Available at: www.nature.com.

Carmeliet, P. and Jain, R. K. (2011) 'Principles and mechanisms of vessel normalization for cancer and other angiogenic diseases.', *Nature reviews. Drug discovery*. Nature Publishing Group, 10(6), pp. 417–27. doi: 10.1038/nrd3455.

Carugo, D., Owen, J., Crake, C., Lee, J. Y. and Stride, E. (2015) 'Biologicallyand acoustically compatible chamber for studying ultrasound-mediated delivery of therapeutic compounds', *Ultrasound in Medicine and Biology*, 41(7), pp. 1927–1937. doi: 10.1016/j.ultrasmedbio.2015.03.020.

Cascone, T. and Heymach, J. V. (2012) 'Targeting the angiopoietin/Tie2 pathway: Cutting tumor vessels with a double-edged sword?', *Journal of Clinical Oncology*, 30(4), pp. 441–444. doi: 10.1200/JCO.2011.38.7621.

Chappell, M. A., Groves, A. R., Whitcher, B. and Woolrich, M. W. (2009) 'Variational Bayesian Inference for a Nonlinear Forward Model', *IEEE Transactions on Signal Processing*, 57(1), pp. 223–236. doi: 10.1109/TSP.2008.2005752.

Chappell, M. A., Donahue, M. J., Tee, Y. K., Khrapitchev, A. A., Sibson, N. R., Jezzard, P. and Payne, S. J. (2013) 'Quantitative Bayesian model-based analysis of amide proton transfer MRI', *Magnetic Resonance in Medicine*, 70(2), pp. 556–567. doi: 10.1002/mrm.24474.

Chappell, M. A., Craig, M., Irving, B. and Croal, P. (2017) *Quantiphyse*. Available at: www.quantiphyse.org (Accessed: 13 July 2018).

Chen, L., Liu, M., Bao, J., Xia, Y., Zhang, J., Zhang, L., Huang, X. and Wang, J. (2013) 'The correlation between apparent diffusion coefficient and tumor cellularity in patients: A meta-analysis', *PLoS ONE*, 8(11). doi: 10.1371/journal.pone.0079008.

Cheng, V. W. T., Soto, M. S., Khrapitchev, A. A., Perez-Balderas, F., Zakaria, R., Jenkinson, M. D., Middleton, M. R. and Sibson, N. R. (2019) 'VCAM-1–targeted MRI Enables Detection of Brain Micrometastases from Different Primary Tumors', *Clinical Cancer Research*, 25(2), pp. 533–543. doi: 10.1158/1078-0432.CCR-18-1889.

Chernov, M. F., Hayashi, M., Izawa, M., Ono, Y. and Hori, T. (2006) 'Proton magnetic resonance spectroscopy (MRS) of metastatic brain tumors: Variations of metabolic profile', *International Journal of Clinical Oncology*, 11(5), pp. 375–384. doi: 10.1007/s10147-006-0589-y.

Choong, E. S., Lo, S., Drummond, M., Fogarty, G. B., Menzies, A. M., Guminski, A., Shivalingam, B., Clarke, K., Long, G. V. and Hong, A. M. (2017) 'Survival of patients with melanoma brain metastasis treated with stereotactic radiosurgery and active systemic drug therapies', *European Journal of Cancer*. Elsevier Ltd, 75, pp. 169–178. doi: 10.1016/j.ejca.2017.01.007.

Clavreul, A., Pourbaghi-Masouleh, M., Roger, E. and Menei, P. (2019) 'Nanocarriers and nonviral methods for delivering antiangiogenic factors for glioblastoma therapy: the story so far', *International Journal of Nanomedicine*. Dove Press, Volume 14, pp. 2497–2513. doi: 10.2147/IJN.S194858.

Connell, J. J., Chatain, G., Cornelissen, B., Vallis, K. A., Hamilton, A., Seymour, L., Anthony, D. C. and Sibson, N. R. (2013) 'Selective permeabilization of the blood-brain barrier at sites of metastasis', *Journal of the National Cancer Institute*, 105(21), pp. 1634–1643. doi: 10.1093/jnci/djt276.

Coquery, N., Serduc, R., Rémy, C., Barbier, E. L. and Lemasson, B. (2018) 'Cluster versus ROI analysis to assess combined antiangiogenic therapy and radiotherapy in the F98 rat-glioma model', *NMR in Biomedicine*, 31(8), pp. 1–9. doi: 10.1002/nbm.3933.

Dai, W., Garcia, D., De Bazelaire, C. and Alsop, D. C. (2008) 'Continuous flow-driven inversion for arterial spin labeling using pulsed radio frequency and gradient fields', *Magnetic Resonance in Medicine*, 60(6), pp. 1488–1497. doi: 10.1002/mrm.21790.

Daphu, I., Sundstrøm, T., Horn, S., Huszthy, P. C., Niclou, S. P., Sakariassen, P., Immervoll, H., Miletic, H., Bjerkvig, R. and Thorsen, F. (2013) 'In vivo animal models for studying brain metastasis: Value and limitations', *Clinical and Experimental Metastasis*, 30(5), pp. 695–710. doi: 10.1007/s10585-013-9566-9.

Debacker, C. S., Daoust, A., Köhler, S., Voiron, J., Warnking, J. M. and Barbier, E. L. (2017) 'Impact of tissue T1 on perfusion measurement with arterial spin labeling', *Magnetic Resonance in Medicine*, 77(4), pp. 1656–1664. doi: 10.1002/mrm.26255.

Detre, J. A., Leigh, J. S., Williams, D. S. and Koretsky, A. P. (1992) 'Perfusion imaging.', *Magnetic Resonance in Medicine*, 23(1), pp. 37–45. doi: 10.1002/mrm.1910230106.

Dickson, P. V., Hamner, J. B., Sims, T. L., Fraga, C. H., Ng, C. Y. C., Rajasekeran, S., Hagedorn, N. L., McCarville, M. B., Stewart, C. F. and Davidoff, A. M. (2007) 'Bevacizumab-induced transient remodeling of the vasculature in neuroblastoma xenografts results in improved delivery and efficacy of systemically administered chemotherapy', *Clinical Cancer Research*, 13(13), pp. 3942–3950. doi: 10.1158/1078-0432.CCR-07-0278.

Dietrich, J., Wang, D. and Batchelor, T. T. (2009) 'Cediranib: profile of a novel anti-angiogenic agent in patients with glioblastoma', *Expert Opinion on Investigational Drugs*. Taylor & Francis, 18(10), pp. 1549–1557. doi: 10.1517/13543780903183528.

Dings, R. P. M., Loren, M., Heun, H., McNiel, E., Griffioen, A. W., Mayo, K. H. and Griffin, R. J. (2007) 'Scheduling of radiation with angiogenesis inhibitors anginex and avastin improves therapeutic outcome via vessel normalization', *Clinical Cancer Research*, 13(11), pp. 3395–3402. doi: 10.1158/1078-0432.CCR-06-2441.

Donnem, T., Hu, J., Ferguson, M., Adighibe, O., Snell, C., Harris, A. L., Gatter, K. C. and Pezzella, F. (2013) 'Vessel co-option in primary human tumors and metastases: An obstacle to effective anti-angiogenic treatment?', *Cancer Medicine*, 2(4), pp. 427–436. doi: 10.1002/cam4.105.

E. Konofagou, E., Tunga, Y.-S., Choia, J., Deffieuxa, T., Baseria, B. and Vlachosa, F. (2012) 'Ultrasound-Induced Blood-Brain Barrier Opening', *Current Pharmaceutical Biotechnology*, 13(7), pp. 1332–1345. doi: 10.2174/138920112800624364.

Edelman, R. R., Darby, G. and Nobre, A. C. (1994) 'Qualitative Mapping ofCerebral Blood Flow', *Neuroradiology*, 192, pp. 513–520. Available at: papers2://publication/uuid/C0A69208-121F-489B-A274-022F4C5778B3.

Eis, S. and Kramer, J. (2019) *Anesthesia Inhalation Agents Cardiovascular Effects*, *StatPearls*. StatPearls Publishing. Available at: http://www.ncbi.nlm.nih.gov/pubmed/31082134 (Accessed: 21 December 2019).

Elamin, Y. Y., Rafee, S., Toomey, S. and Hennessy, B. T. (2015) 'Immune Effects of Bevacizumab: Killing Two Birds with One Stone', *Cancer Microenvironment*, 8(1), pp. 15–21. doi: 10.1007/s12307-014-0160-8.

Erasmus, L. J., Hurter, D., Naudé, M., Kritzinger, H. G. and Acho, S. (2004) 'A short overview of MRI artefacts', *SA Journal of Radiology*, 8(2), pp. 13–17.

European Medicines Agency (2005) 'Avastin - information', pp. 1–61. doi: 10.1051/vetres.

European Medicines Agency (2016) 'Zemfirza - Assessment Report', (September), pp. 1–112.

Ewing, J. (1928) *Neoplastic Diseases: A Treatise on Tumors*. 3rd edn. Philadelphia: WB Saunders.

Ewing, J. R., Wei, L., Knight, R. A., Pawa, S., Nagaraja, T. N., Brusca, T., Divine, G. W. and Fenstermacher, J. D. (2003) 'Direct Comparison of Local Cerebral Blood Flow Rates Measured by MRI Arterial Spin-Tagging and Quantitative Autoradiography in a Rat Model of Experimental Cerebral Ischemia', *Journal of cerebral blood flow and metabolism : official journal of the International Society of Cerebral Blood Flow and Metabolism*, 23, pp. 198–209. doi: 10.1097/01.WCB.0000046147.31247.E8.

Fakhrejahani, E. and Toi, M. (2012) 'Tumor angiogenesis: Pericytes and maturation are not to be ignored', *Journal of Oncology*, 2012. doi: 10.1155/2012/261750.

Ferrara, N., Hillan, K. J., Gerber, H. P. and Novotny, W. (2004) 'Discovery and development of bevacizumab, an anti-VEGF antibody for treating cancer', *Nature Reviews Drug Discovery*, 3(5), pp. 391–400. doi: 10.1038/nrd1381.

Ferré, J. C., Bannier, E., Raoult, H., Mineur, G., Carsin-Nicol, B. and Gauvrit, J. Y. (2013) 'Arterial spin labeling (ASL) perfusion: Techniques and clinical use', *Diagnostic and Interventional Imaging*. Elsevier Masson SAS, 94(12), pp. 1211–1223. doi: 10.1016/j.diii.2013.06.010.

Fidler, I. J. and Kripke, M. L. (1977) 'Metastasis results from preexisting variant cells within a malignant tumor', *Science*, 197(4306), pp. 893–895. doi: 10.1126/science.887927.

Fink, K. and Fink, J. (2013) 'Imaging of brain metastases', *Surgical Neurology International*, 4(SUPPL4), pp. 209–219. doi: 10.4103/2152-7806.111298.

Fischer, C., Jonckx, B., Mazzone, M., Zacchigna, S., Loges, S., Pattarini, L., Chorianopoulos, E., Liesenborghs, L., Koch, M., De Mol, M., Autiero, M., Wyns, S., Plaisance, S., Moons, L., van Rooijen, N., Giacca, M., Stassen, J. M., Dewerchin, M., Collen, D., *et al.* (2007) 'Anti-PlGF Inhibits Growth of VEGF(R)-Inhibitor-Resistant Tumors without Affecting Healthy Vessels', *Cell*, 131(3), pp. 463–475. doi: 10.1016/j.cell.2007.08.038.

Folkman, J. (1995) 'Angiogenesis in cancer, vascular, rheumatoid and other disease', 1(1), pp. 27–31.

Frumovitz, M., Munsell, M. F., Burzawa, J. K., Byers, L. A., Ramalingam, P., Brown, J. and Coleman, R. L. (2017) 'Combination therapy with topotecan, paclitaxel, and bevacizumab improves progression-free survival in recurrent small cell neuroendocrine carcinoma of the cervix', *Gynecologic Oncology*, 144(1), pp. 46–50. doi: 10.1016/j.ygyno.2016.10.040.

Fukumura, D., Duda, D. G., Munn, L. L. and Jain, R. K. (2010) 'Tumor microvasculature and microenvironment: Novel insights through intravital imaging in pre-clinical models', *Microcirculation*, 17(3), pp. 206–225. doi: 10.1111/j.1549-8719.2010.00029.x.

Galdiero, M. R., Bonavita, E., Barajon, I., Garlanda, C., Mantovani, A. and Jaillon, S. (2013) 'Tumor associated macrophages and neutrophils in cancer', *Immunobiology*. Elsevier GmbH., 218(11), pp. 1402–1410. doi: 10.1016/j.imbio.2013.06.003.

Garcia, C., Dubois, G. G., Xavier, L. L., Geraldo, H. H., da Fonseca, C. C. C., Correia, H. H., Meirelles, F., Ventura, G., Romão, L., Canedo, S. H. S., de Souza, M. M., de Menezes, L. R. L., Moura-Neto, V., Tovar-Moll, F. and Lima, S. R. S. (2014) 'The orthotopic xenotransplant of human glioblastoma successfully recapitulates glioblastoma-microenvironment interactions in a non-immunosuppressed mouse model', *BMC Cancer*, 14(1), pp. 1–11. doi: 10.1186/1471-2407-14-923.

Garcia, D. M., de Bazelaire, C. and Alsop, D. C. (2005) '"Pseudo-continuous flow driven adiabatic inversion for arterial spin labeling,"' *Proceedings of the 13th Meeting in International Society of Magnetic Resonance in Medicine*, 62(1986), p. 2005.

Gavrilovic, I. T. and Posner, J. B. (2005) 'Brain metastases: Epidemiology and pathophysiology', *Journal of Neuro-Oncology*, 75(1), pp. 5–14. doi: 10.1007/s11060-004-8093-6.

Gianni-Barrera, R., Trani, M., Reginato, S. and Banfi, A. (2011) 'To sprout or to split? VEGF, Notch and vascular morphogenesis', *Biochemical Society Transactions*, 39(6), pp. 1644–1648. doi: 10.1042/BST20110650.

Goedegebuure, R. S. A., De Klerk, L. K., Bass, A. J., Derks, S. and Thijssen, V. L. J. L. (2019) 'Combining radiotherapy with anti-angiogenic therapy and immunotherapy; A therapeutic triad for cancer?', *Frontiers in Immunology*, 10(JAN), pp. 1–15. doi: 10.3389/fimmu.2018.03107.

Goel, H. L. and Mercurio, A. M. (2013) 'VEGF targets the tumour cell', *Nature Reviews Cancer*. Nature Publishing Group, 13(12), pp. 871–882. doi: 10.1038/nrc3627.

Goel, S., Duda, D. G., Xu, L., Munn, L. L., Boucher, Y., Fukumura, D. and Jain, R. K. (2011) 'Normalization of the vasculature for treatment of cancer and other diseases.', *Physiological reviews*, 91(3), pp. 1071–121. doi: 10.1152/physrev.00038.2010.

Gomez-Rivera, F., Santillan-Gomez, A. A., Younes, M. N., Kim, S., Fooshee, D., Zhao, M., Jasser, S. A. and Myers, J. N. (2007) 'The tyrosine kinase inhibitor, AZD2171, inhibits vascular endothelial growth factor receptor signaling and growth of anaplastic thyroid

cancer in an orthotopic nude mouse model', *Clinical Cancer Research*, 13(15), pp. 4519–4527. doi: 10.1158/1078-0432.CCR-06-2636.

Goodlad, R. A., Ryan, A. J., Wedge, S. R., Pyrah, I. T., Alferez, D., Poulsom, R., Smith, N. R., Mandir, N., Watkins, A. J. and Wilkinson, R. W. (2006) 'Inhibiting vascular endothelial growth factor receptor-2 signaling reduces tumor burden in the ApcMin/+ mouse model of early intestinal cancer', *Carcinogenesis*, 27(10), pp. 2133–2139. doi: 10.1093/carcin/bgl113.

De Graaf, R. A., Brown, P. B., McIntyre, S., Nixon, T. W., Behar, K. L. and Rothman, D. L. (2006) 'High magnetic field water and metabolite proton T1 and T 2 relaxation in rat brain in vivo', *Magnetic Resonance in Medicine*, 56(2), pp. 386–394. doi: 10.1002/mrm.20946.

Groves, A. R., Chappell, M. A. and Woolrich, M. W. (2009) 'Combined spatial and non-spatial prior for inference on MRI time-series', *NeuroImage*. Elsevier Inc., 45(3), pp. 795–809. doi: 10.1016/j.neuroimage.2008.12.027.

Gu, S., Xue, J., Xi, Y., Tang, R., Jin, W., Chen, J. J., Zhang, X., Shao, Z. M. and Wu, J. (2019) 'Evaluating the effect of Avastin on breast cancer angiogenesis using synchrotron radiation', *Quantitative Imaging in Medicine and Surgery*, 9(3), pp. 418–426. doi: 10.21037/qims.2019.03.09.

Gudbjartsson, H. and Patz, S. (2018) 'Vernetztes Kompetenzmanagement. Gestaltung von Lernprozessen in organisationsübergreifenden Strukturen', *Journal of Experimental Psychology: General*, pp. 910–914. doi: 10.1007/978-3-662-54954-4.

Guo, B. J., Yang, Z. L. and Zhang, L. J. (2018) 'Gadolinium Deposition in Brain: Current Scientific Evidence and Future Perspectives', *Frontiers in Molecular Neuroscience*, 11(September), pp. 1–12. doi: 10.3389/fnmol.2018.00335.

Gupta, G. P. and Massagué, J. (2006) 'Cancer Metastasis: Building a Framework', *Cell*, 127(4), pp. 679–695. doi: 10.1016/j.cell.2006.11.001.

Hal, D. G. and Stoica, G. (1994) 'Evaluation of Potential Oncogene Alterations in the ENU1564 Rat Mammary Tumor Model', *Anticancer Research*, 14, pp. 481–488.

Hall, D. G. and Stoica, G. (1994) 'Characterization of brain and bone-metastasizing clones selected from an ethylnitrosourea-induced rat mammary carcinoma', *Clinical & Experimental Metastasis*, 12(4), pp. 283–295. doi: 10.1007/BF01753835.

Hanahan, D. and Folkman, J. (1996) 'Patterns and emerging mechanisms of the angiogenic switch during tumorigenesis', *Cell*, 86(3), pp. 353–364. doi: 10.1016/S0092-8674(00)80108-7.

Hanahan, D. and Weinberg, R. A. (2000) 'The Hallmarks of Cancer', *Cell*, 100(1), pp. 57–70. doi: 10.1007/s00262-010-0968-0.

Hanahan, D. and Weinberg, R. A. (2011) 'Hallmarks of cancer: The next generation', *Cell*. Elsevier Inc., 144(5), pp. 646–674. doi: 10.1016/j.cell.2011.02.013.

Hart, I. R. and Fidler, I. J. (1980) 'Role of organ selectivity in the determination of metastatic patterns of b16 melanoma', *Cancer Research*, 40(7), pp. 2281–2287.

Hashizume, H., Baluk, P., Morikawa, S., McLean, J. W., Thurston, G., Roberge, S., Jain, R. K. and McDonald, D. M. (2000) 'Openings between defective endothelial cells explain tumor vessel leakiness', *American Journal of Pathology*. American Society for Investigative Pathology, 156(4), pp. 1363–1380. doi: 10.1016/S0002-9440(10)65006-7.

Heckman, C. A., Holopainen, T., Wirzenius, M., Keskitalo, S., Jeltsch, M., Ylä-Herttuala, S., Wedge, S. R., Jürgensmeier, J. M. and Alitalo, K. (2008) 'The tyrosine kinase inhibitor cediranib blocks ligand-induced vascular endothelial growth factor receptor-3 activity

and lymphangiogenesis', *Cancer Research*, 68(12), pp. 4754–4762. doi: 10.1158/0008-5472.CAN-07-5809.

Helfrich, I., Edler, L., Sucker, A., Thomas, M., Christian, S., Schadendorf, D. and Augustin, H. G. (2009) 'Angiopoietin-2 levels are associated with disease progression in metastatic malignant melanoma', *Clinical Cancer Research*, 15(4), pp. 1384–1392. doi: 10.1158/1078-0432.CCR-08-1615.

Helmlinger, G., Yuan, F., Dellian, M. and Jain, R. K. (1997) 'Interstitial pH and pO2 gradients in solid tumors in vivo: High-resolution measurements reveal a lack of correlation', *Nature Medicine*, 3(2), pp. 177–182.

Hendrich, K. S., Kochanek, P. M., Melick, J. A., Schiding, J. K., Statler, K. D., Williams, D. S., Marion, D. W. and Ho, C. (2001) 'Cerebral perfusion during anesthesia with fentanyl, isoflurane, or pentobarbital in normal rats studied by arterial spin-labeled MRI', *Magnetic Resonance in Medicine*, 46(1), pp. 202–206. doi: 10.1002/mrm.1178.

Herscovitch, P. and Raichle, M. E. (1985) 'What is the correct value for the brain-blood partition coefficient for water?', *Journal of Cerebral Blood Flow and Metabolism*, 5(1), pp. 65–69. doi: 10.1038/jcbfm.1985.9.

Hirschler, L., Debacker, C. S., Voiron, J., Köhler, S., Warnking, J. M. and Barbier, E. L. (2017) 'Interpulse phase corrections for unbalanced pseudo-continuous arterial spin labeling at high magnetic field', *Magnetic Resonance in Medicine*, 00, pp. 1–11. doi: 10.1002/mrm.26767.

Holash, J., Maisonpierre, P. C., Compton, D., Boland, P., Alexander, C. R., Zagzag, D., Yancopoulos, G. D. and Wiegand, S. J. (1999) 'Vessel cooption, regression, and growth in tumors mediated by angiopoietins and VEGF', *Science*, 284(5422), pp. 1994–1998. doi: 10.1126/science.284.5422.1994.

Hollingworth, W., Medina, L. S., Lenkinski, R. E., Shibata, D. K., Bernal, B., Zurakowski, D., Comstock, B. and Jarvik, J. G. (2006) 'A systematic literature review of magnetic resonance spectroscopy for the characterization of brain tumors', *American Journal of Neuroradiology*, 27(7), pp. 1404–1411.

Huang, Y., Stylianopoulos, T., Duda, D. G., Fukumura, D. and Jain, R. K. (2013) 'Benefits of vascular normalization are dose and time dependent - Letter', *Cancer Research*, 73(23), pp. 7144–7146. doi: 10.1158/0008-5472.CAN-13-1989.

Hurwitz, H., Fehrenbacher, L., Novotny, W., Cartwright, T., Hainsworth, J., Heim, W., Berlin, J., Baron, A., Griffing, S., Holmgren, E., Ferrara, N., Fyfe, G., Rogers, B., Ross, R. and Kabbinavar, F. (2004) 'Bevacizumab plus Irinotecan, Fluorouracil, and Leucovorin for Metastatic Colorectal Cancer', *The New England journal of medicine*, 350(23), pp. 2335–2342.

Iida, H., Ohata, H., Iida, M., Watanabe, T. and Dohi, S. (1998) 'Isoflurane and Sevoflurane Induce Vasocilation of Cerebral Vessels via ATP-sensitive K+ Channel Activation', *Anesthesiology*, 89(4), pp. 954–960.

Imanishi, Y., Hu, B., Jarzynka, M. J., Guo, P., Elishaev, E., Bar-Joseph, I. and Cheng, S. Y. (2007) 'Angiopoietin-2 stimulates breast cancer metastasis through the α5β1 integrin-mediated pathway', *Cancer Research*, 67(9), pp. 4254–4263. doi: 10.1158/0008-5472.CAN-06-4100.

Inai, T., Mancuso, M., Hashizume, H., Baffert, F., Haskell, A., Baluk, P., Hu-Lowe, D. D., Shalinsky, D. R., Thurston, G., Yancopoulos, G. D. and McDonald, D. M. (2004) 'Inhibition of vascular endothelial growth factor (VEGF) signaling in cancer causes loss of endothelial fenestrations, regression of tumor vessels, and appearance of basement

membrane ghosts', *American Journal of Pathology*. American Society for Investigative Pathology, 165(1), pp. 35–52. doi: 10.1016/S0002-9440(10)63273-7.

Irving, B., Popescu, I. A., Bates, R., Allen, P. D., Gomes, A. L., Kannan, P., Kinchesh, P., Gilchrist, S., Kersemans, V., Smart, S., Schnabel, J. A., Brady, S. J. M. and Chappell, M. A. (2016) 'maskSLIC: Regional Superpixel Generation with Application to Local Pathology Characterisation in Medical Images', *CoRR*, pp. 1–7. Available at: http://arxiv.org/abs/1606.09518.

Iuchi, T., Shingyoji, M., Sakaida, T., Hatano, K., Nagano, O., Itakura, M., Kageyama, H., Yokoi, S., Hasegawa, Y., Kawasaki, K. and Iizasa, T. (2013) 'Phase II trial of gefitinib alone without radiation therapy for Japanese patients with brain metastases from EGFR-mutant lung adenocarcinoma', *Lung Cancer*. Elsevier Ireland Ltd, 82(2), pp. 282–287. doi: 10.1016/j.lungcan.2013.08.016.

Iwamoto, F. M. and Fine, H. A. (2010) 'Bevacizumab for malignant gliomas', *Archives of Neurology*, 67(3), pp. 285–288. doi: 10.1001/archneurol.2010.11.

Jackson, A., O'Connor, J. P. B., Parker, G. J. M. and Jayson, G. C. (2007) 'Imaging tumor vascular heterogeneity and angiogenesis using dynamic contrast-enhanced magnetic resonance imaging', *Clinical Cancer Research*, 13(12), pp. 3449–3459. doi: 10.1158/1078-0432.CCR-07-0238.

Jahanian, H., Noll, D. C. and Hernandez-Garcia, L. (2011) 'B 0 field inhomogeneity considerations in pseudo-continuous arterial spin labeling (pCASL): Effects on tagging efficiency and correction strategy', *NMR in Biomedicine*, 24(10), pp. 1202–1209. doi: 10.1002/nbm.1675.

Jain, R. K. (2001) 'Normalizing tumor vasculature with anti-angiogenic therapy : A new paradigm for combination therapy', *Nature Medicine*, 7(9), pp. 987–989.

Jain, R. K. (2005) 'Normalization of Tumor Vasculature: An Emerging Concept in Antiangiogenic Therapy', *Sience*, 307(5706), pp. 58–62. doi: 10.1126/science.1104819.

Jain, R. K., Duda, D. G., Clark, J. W. and Loeffler, J. S. (2006) 'Lessons from phase III clinical trials on anti-VEGF therapy for cancer', *Nature Clinical Practice Oncology*, 3(1), pp. 24–40. doi: 10.1038/ncponc0403.

Jung, Y., Wong, E. C. and Liu, T. T. (2010) 'Multiphase pseudocontinuous arterial spin labeling (MP-PCASL) for robust quantification of cerebral blood flow', *Magnetic Resonance in Medicine*, 64(3), pp. 799–810. doi: 10.1002/mrm.22465.

Kaelin, W. G. and Ratcliffe, P. J. (2008) 'Oxygen Sensing by Metazoans: The Central Role of the HIF Hydroxylase Pathway', *Molecular Cell*, 30(4), pp. 393–402. doi: 10.1016/j.molcel.2008.04.009.

Kamp, M. A., Grosser, P., Felsberg, J., Slotty, P. J., Steiger, H. J., Reifenberger, G. and Sabel, M. (2012) '5-Aminolevulinic acid (5-ALA)-induced fluorescence in intracerebral metastases: A retrospective study', *Acta Neurochirurgica*, 154(2), pp. 223–228. doi: 10.1007/s00701-011-1200-5.

Katakami, N., Inaba, Y., Sugata, S., Tsurusaki, M., Itoh, T., Machida, T., Tanaka, H., Nakayama, T., Morikawa, T., Breuer, J. and Aitoku, Y. (2011) 'Magnetic Resonance Evaluation of Brain Metastases From Systemic Malignances With Two Doses of Gadobutrol 1.0 M Compared With Gadoteridol', *Investigative Radiology*, 46(7), pp. 411–418. doi: 10.1097/rli.0b013e3182145a6c.

Kato, T., Muro, K., Yamaguchi, K., Bando, H., Hazama, S., Amagai, K., Baba, H., Denda, T., Shi, X., Fukase, K., Sakamoto, J. and Mishima, H. (2012) 'Cediranib in combination with mFOLFOX6 in Japanese patients with metastatic colorectal cancer: Results from the

randomised phase II part of a phase I/II study', *Annals of Oncology*, 23(4), pp. 933–941. doi: 10.1093/annonc/mdr359.

Kendrew, J., Odedra, R., Logié, A., Taylor, P. J., Pearsall, S., Ogilvie, D. J., Wedge, S. R. and Jürgensmeier, J. M. (2013) 'Anti-tumour and anti-vascular effects of cediranib (AZD2171) alone and in combination with other anti-tumour therapies', *Cancer Chemotherapy and Pharmacology*, 71(4), pp. 1021–1032. doi: 10.1007/s00280-013-2097-x.

Kienast, Y., Von Baumgarten, L., Fuhrmann, M., Klinkert, W. E. F., Goldbrunner, R., Herms, J. and Winkler, F. (2010) 'Real-time imaging reveals the single steps of brain metastasis formation', *Nature Medicine*. Nature Publishing Group, 16(1), pp. 116–122. doi: 10.1038/nm.2072.

Kilkenny, C., Browne, W. J., Cuthill, I. C., Emerson, M. and Altman, D. G. (2013) 'Improving bioscience research reporting: The arrive guidelines for reporting animal research', *Animals*, 4(1), pp. 35–44. doi: 10.3390/ani4010035.

Kim, D.-W., Yang, J. C.-H., Chen, K., Cheng, Z., Yin, L., Martin, P. D., Yang, Z., Jiang, H. and Ahn, M.-J. (2015) 'AZD3759, an EGFR inhibitor with blood brain barrier (BBB) penetration for the treatment of non-small cell lung cancer (NSCLC) with brain metastasis (BM): Preclinical evidence and clinical cases.', *Journal of Clinical Oncology*. American Society of Clinical Oncology, 33(15_suppl), p. 8016. doi: 10.1200/jco.2015.33.15_suppl.8016.

Kim, K. J., Li, B., Winer, J., Armanini, M., Gillett, N., Phillips, H. S. and Ferrara, N. (1993) 'Growth Factor-Induced Tumour Growth in Vivo', 362(April), pp. 841–844.

Kim, L. S., Huang, S., Lu, W., Chelouche Lev, D. and Price, J. E. (2004) 'Vascular endothelial growth factor expression promotes the growth of breast cancer brain metastases in nude mice', *Clinical and Experimental Metastasis*, 21(2), pp. 107–118. doi: 10.1023/B:CLIN.0000024761.00373.55.

Kim, S.-G., Harel, N., Jin, T., Kim, T., Lee, P. and Zhao, F. (2013) 'Cerebral blood volume MRI with intravascular superparamagnetic iron oxide nanoparticles.', *NMR in biomedicine*, 26(8), pp. 949–62. doi: 10.1002/nbm.2885.

Kim, S. G. and Tsekos, N. V. (1997) 'Perfusion imaging by a flow-sensitive alternating inversion recovery (fair) technique: Application to functional brain imaging', *Magnetic Resonance in Medicine*, 37(3), pp. 425–435. doi: 10.1002/mrm.1910370321.

Kim, T. and Kim, S. G. (2005) 'Quantification of cerebral arterial blood volume and cerebral blood flow using MRI with modulation of tissue and vessel (MOTIVE) signals', *Magnetic Resonance in Medicine*, 54(2), pp. 333–342. doi: 10.1002/mrm.20550.

Kohen, M. C., Tatlipinar, S., Cumbu, A. and Uslu, Ü. (2018) 'The effects of bevacizumab treatment in a rat model of retinal ischemia and perfusion injury', *Molecular Vision*, 24(October 2014), pp. 239–251.

Küsters, B., Leenders, W. P. J., Wesseling, P., Smits, D., Verrijp, K., Ruiter, D. J., Peters, J. P. W., Van der Kogel, A. J. and De Waal, R. M. W. (2002) 'Vascular endothelial growth factor-A165 induces progression of melanoma brain metastases without induction of sprouting angiogenesis', *Cancer Research*, 62(2), pp. 341–345.

Larkin, J. R., Simard, M. A., Khrapitchev, A. A., Meakin, J. A., Okell, T. W., Craig, M., Ray, K. J., Jezzard, P., Chappell, M. A. and Sibson, N. R. (2018) 'Quantitative blood flow measurement in rat brain with multiphase arterial spin labelling magnetic resonance imaging', *Journal of Cerebral Blood Flow & Metabolism*, p. 0271678X1875621. doi: 10.1177/0271678X18756218.

Ledermann, J. A., Embleton, A. C., Raja, F., Perren, T. J., Jayson, G. C., Rustin, G. J. S., Kaye,

S. B., Hirte, H., Eisenhauer, E., Vaughan, M., Friedlander, M., González-Martín, A., Stark, D., Clark, E., Farrelly, L., Swart, A. M., Cook, A., Kaplan, R. S. and Parmar, M. K. B. (2016) 'Cediranib in patients with relapsed platinum-sensitive ovarian cancer (ICON6): A randomised, double-blind, placebo-controlled phase 3 trial', *The Lancet*. Ledermann et al. Open Access article distributed under the terms of CC BY, 387(10023), pp. 1066–1074. doi: 10.1016/S0140-6736(15)01167-8.

Lee, H. B. and Blaufox, M. D. (1985) '（1985大鼠的血容量）Blood Volume in the Rat The estimation of blood volume is important in studies', *J Nucl Med*, 25, pp. 72–76.

Leenders, W. P. J., Küsters, B., Verrijp, K., Maass, C., Wesseling, P., Heerschap, A., Ruiter, D., Ryan, A. and De Waal, R. (2004) 'Antiangiogenic therapy of cerebral melanoma metastases results in sustained tumor progression via vessel co-option', *Clinical Cancer Research*, 10(18 I), pp. 6222–6230. doi: 10.1158/1078-0432.CCR-04-0823.

Leithner, C., Muller, S., Fuchtemeier, M., Lindauer, U., Dirnagl, U. and Royl, G. (2010) 'Determination of the brain-blood partition coefficient for water in mice using MRI', *Journal of Cerebral Blood Flow and Metabolism*, 30(11), pp. 1821–1824. doi: jcbfm2010160 [pii]\r10.1038/jcbfm.2010.160.

Less, J. R., Skalak, T. C., Sevick, E. M. and Jain, R. K. (1991) 'Microvascular Architecture in a Mammary Carcinoma: Branching Patterns and Vessel Dimensions', *Cancer Research*, 51(1), pp. 265–273.

Less, J. R., Posner, M. C., Skalak, T. C., Wolmark, N. and Jain, R. K. (1997) 'Geometric resistance and microvascular network architecture of human colorectal carcinoma', *Microcirculation*, 4(1), pp. 25–33. doi: 10.3109/10739689709148315.

Lin, Y. S., Nguyen, C., Mendoza, J. L., Escandon, E., Fei, D., Meng, Y. G. and Modi, N. B. (1999) 'Preclinical pharmacokinetics, interspecies scaling, and tissue distribution of a humanized monoclonal antibody against vascular endothelial growth factor', *Journal of Pharmacology and Experimental Therapeutics*, 288(1), pp. 371–378.

Lindner, T., Ahmeti, H., Juhasz, J., Helle, M., Jansen, O., Synowitz, M. and Ulmer, S. (2018) 'A comparison of arterial spin labeling and dynamic susceptibility perfusion imaging for resection control in glioblastoma surgery', *Oncotarget*, 9(26), pp. 18570–18577. doi: 10.18632/oncotarget.24970.

Liu, J., Li, C., Chen, Y., Lv, X., Lv, Y., Zhou, J., Xi, S., Dou, W., Qian, L., Zheng, H., Wu, Y. and Chen, Z. (2019) 'Diagnostic performance of multiparametric MRI in the evaluation of treatment response in glioma patients at 3T', *Journal of Magnetic Resonance Imaging*, p. jmri.26900. doi: 10.1002/jmri.26900.

Liu, T. B., Perlin, D. S. and Xue, C. (2012) 'Molecular mechanisms of cryptococcal meningitis', *Virulence*, 3(2), pp. 173–181. doi: 10.4161/viru.18685.

Lu, G., Rao, M., Zhu, P., Liang, B., El-Nazer, R. T., Fonkem, E., Bhattacharjee, M. B. and Zhu, J. J. (2019) 'Triple-drug Therapy with Bevacizumab, Irinotecan, and Temozolomide plus Tumor Treating Fields for Recurrent Glioblastoma: A retrospective study', *Frontiers in Neurology*, 10(JAN), pp. 1–10. doi: 10.3389/fneur.2019.00042.

Lu, Y., Luan, S., Liu, L., Xiong, J., Wen, J., Qu, J., Geng, D. and Yin, B. (2017) 'Evaluation of the applicability of territorial arterial spin labeling in meningiomas for presurgical assessments compared with 3-dimensional time-of-flight magnetic resonance angiography', *European Radiology*. European Radiology, 27(10), pp. 4072–4081. doi: 10.1007/s00330-017-4760-9.

Maeda, K., Mies, G., Oláh, L. and Hossmann, K. a (2000) 'Quantitative measurement of local cerebral blood flow in the anesthetized mouse using intraperitoneal

[14C]iodoantipyrine injection and final arterial heart blood sampling.', *Journal of cerebral blood flow and metabolism : official journal of the International Society of Cerebral Blood Flow and Metabolism*, 20(1), pp. 10–4. doi: 10.1097/00004647-200001000-00003.

Malayeri, A. A., Brooks, K. M., Bryant, L. H., Evers, R., Kumar, P., Reich, D. S. and Bluemke, D. A. (2016) 'National Institutes of Health Perspective on Reports of Gadolinium Deposition in the Brain', *Journal of the American College of Radiology*. Elsevier Inc, 13(3), pp. 237–241. doi: 10.1016/j.jacr.2015.11.009.

Marckmann, P., Skov, L., Rossen, K., Dupont, A., Damholt, M. B., Heaf, J. G. and Thomsen, H. S. (2006) 'Nephrogenic systemic fibrosis: Suspected causative role of gadodiamide used for contrast-enhanced magnetic resonance imaging', *Journal of the American Society of Nephrology*, 17(9), pp. 2359–2362. doi: 10.1681/ASN.2006060601.

Mazzone, M., Dettori, D., Leite de Oliveira, R., Loges, S., Schmidt, T., Jonckx, B., Tian, Y. M., Lanahan, A. A., Pollard, P., Ruiz de Almodovar, C., De Smet, F., Vinckier, S., Aragon??s, J., Debackere, K., Luttun, A., Wyns, S., Jordan, B., Pisacane, A., Gallez, B., *et al.* (2009) 'Heterozygous Deficiency of PHD2 Restores Tumor Oxygenation and Inhibits Metastasis via Endothelial Normalization', *Cell*, 136(5), pp. 839–851. doi: 10.1016/j.cell.2009.01.020.

McGee, M. C., Hamner, J. B., Williams, R. F., Rosati, S. F., Sims, T. L., Ng, C. Y., Gaber, M. W., Calabrese, C., Wu, J., Nathwani, A. C., Duntsch, C., Merchant, T. E. and Davidoff, A. M. (2010) 'Improved Intratumoral Oxygenation Through Vascular Normalization Increases Glioma Sensitivity to Ionizing Radiation', *International Journal of Radiation Oncology Biology Physics*, 76(5), pp. 1537–1545. doi: 10.1016/j.ijrobp.2009.12.010.

Meakin, J. A. (2014) *Velocity selective preparations in Magnetic Resonance Imaging*. University of Oxford.

Medinger, M., Esser, N., Zirrgiebel, U., Ryan, A., Jürgensmeier, J. M. and Drevs, J. (2009) 'Antitumor and antiangiogenic activity of cediranib in a preclinical model of renal cell carcinoma', *Anticancer Research*, 29(12), pp. 5065–5076.

Mehta, S., Hughes, N. P., Buffa, F. M., Li, S. P., Adams, R. F., Adwani, A., Taylor, N. J., Levitt, N. C., Padhani, A. R., Makris, A. and Harris, A. L. (2011) 'Assessing early therapeutic response to bevacizumab in primary breast cancer using magnetic resonance imaging and gene expression profiles', *Journal of the National Cancer Institute - Monographs*, (43), pp. 71–74. doi: 10.1093/jncimonographs/lgr027.

Millauer, B., Wizigmann-Voos, S., Schnürch, H., Martinez, R., Møller, N. P. H., Risau, W. and Ullrich, A. (1993) 'High affinity VEGF binding and developmental expression suggest Flk-1 as a major regulator of vasculogenesis and angiogenesis', *Cell*, 72(6), pp. 835–846. doi: 10.1016/0092-8674(93)90573-9.

Miller, K. D., Miller, M., Mehrotra, S., Agarwal, B., Mock, B. H., Zheng, Q. H., Badve, S., Hutchins, G. D. and Sledge, G. W. (2006) 'A physiologic imaging pilot study of breast cancer treated with AZD2171', *Clinical Cancer Research*, 12(1), pp. 281–288. doi: 10.1158/1078-0432.CCR-05-0219.

Mori, S. and Van Zijl, P. C. M. (2002) 'Fiber tracking: Principles and strategies - A technical review', *NMR in Biomedicine*, 15(7–8), pp. 468–480. doi: 10.1002/nbm.781.

Morikawa, A., Peereboom, D. M., Thorsheim, H. R., Samala, R., Balyan, R., Murphy, C. G., Lockman, P. R., Simmons, A., Weil, R. J., Tabar, V., Steeg, P. S., Smith, Q. R. and Seidman, A. D. (2015) 'Capecitabine and lapatinib uptake in surgically resected brain metastases from metastatic breast cancer patients: A prospective study', *Neuro-Oncology*, 17(2), pp.

289–295. doi: 10.1093/neuonc/nou141.

Morikawa, S., Baluk, P., Kaidoh, T., Haskell, A., Jain, R. K. and McDonald, D. M. (2002) 'Abnormalities in pericytes on blood vessels and endothelial sprouts in tumors', *American Journal of Pathology*. American Society for Investigative Pathology, 160(3), pp. 985–1000. doi: 10.1016/S0002-9440(10)64920-6.

Morton, R., Ko, A. l. and Silbergeld, D. L. (2018) 'Principles of Neurological Surgery, Chapter 40 - Brain Metastasis', in Ellenbogen, R. G. et al. (eds). Philadelphia, pp. 586-592.e1. doi: https://doi.org/10.1016/B978-0-323-43140-8.00040-8.

Msayib, Y., Craig, M., Simard, M. A., Larkin, J. R., Shin, D. D., Liu, T. T., Sibson, N. R., Okell, T. W. and Chappell, M. A. (2019) 'Robust estimation of quantitative perfusion from multi-phase pseudo-continuous arterial spin labelling', *Magnetic Resonance in Medicine*, (May), p. 308. doi: 10.1002/mrm.27965.

Muller, Y. A., Chen, Y., Christinger, H. W., Li, B., Cunningham, B. C., Lowman, H. B. and De Vos, A. M. (1998) 'VEGF and the Fab fragment of a humanized neutralizing antibody: Crystal structure of the complex at 2.4 Å resolution and mutational analysis of the interface', *Structure*, 6(9), pp. 1153–1167. doi: 10.1016/S0969-2126(98)00116-6.

Nagy, J. A., Vasile, E., Feng, D., Sundberg, C., Brown, L. F., Detmar, M. J., Lawitts, J. A., Benjamin, L., Tan, X., Manseau, E. J., Dvorak, A. M. and Dvorak, H. F. (2002) 'Vascular permeability factor/vascular endothelial growth factor induces lymphangiogenesis as well as angiogenesis', *Journal of Experimental Medicine*, 196(11), pp. 1497–1506. doi: 10.1084/jem.20021244.

Naresh, K. N., Nerurkar, A. Y. and Borges, A. M. (2001) 'Angiogenesis is redundant for tumour growth in lymph node metastases', *Histopathology*, 38(5), pp. 466–470. doi: 10.1046/j.1365-2559.2001.01061.x.

Nayak, L., Lee, E. Q. and Wen, P. Y. (2012) 'Epidemiology of brain metastases', *Current Oncology Reports*, 14(1), pp. 48–54. doi: 10.1007/s11912-011-0203-y.

Noguchi, T., Yoshiura, T., Hiwatashi, a., Togao, O., Yamashita, K., Nagao, E., Shono, T., Mizoguchi, M., Nagata, S., Sasaki, T., Suzuki, S. O., Iwaki, T., Kobayashi, K., Mihara, F. and Honda, H. (2008) 'Perfusion imaging of brain tumors using arterial spin-labeling: Correlation with histopathologic vascular density', *American Journal of Neuroradiology*, 29(4), pp. 688–693. doi: 10.3174/ajnr.A0903.

Okada, Y., Akisue, T., Hara, H., Kishimoto, K., Kawamoto, T., Imabori, M., Kishimoto, S. I., Fukase, N., Onishi, Y. and Kurosaka, M. (2010) 'The effect of bevacizumab on tumour growth of malignant fibrous histiocytoma in an animal model', *Anticancer Research*, 30(9), pp. 3391–3395.

Okell, T. W. (2011) *Assessment of Collateral Blood Flow in the Brain using Magnetic Resonance Imaging*. University of Oxford.

Orzi, F., Capone, F. T. and Mangiardi, M. (2006) 'Models for quantitative neuroimaging', *Proceedings of Science*, 39, pp. 1–4. doi: 10.22323/1.039.0013.

Østergaard, L. (2005) 'Principles of cerebral perfusion imaging by bolus tracking', *Journal of Magnetic Resonance Imaging*, 22(6), pp. 710–717. doi: 10.1002/jmri.20460.

Ota, M., Ishikawa, M., Sato, N., Okazaki, M., Maikusa, N., Hori, H., Hattori, K., Teraishi, T., Ito, K. and Kunugi, H. (2014) 'Pseudo-continuous arterial spin labeling MRI study of schizophrenic patients', *Schizophrenia Research*. Elsevier B.V., 154(1–3), pp. 113–118. doi: 10.1016/j.schres.2014.01.035.

Oxford, U. of (2019) *University Policy on the Use of Animals in Scientific Research*, *University of Oxford*. Available at: http://www.ox.ac.uk/news-and-events/animal-

research/university-policy-on-the-use-of-animals-in-scientific-research.
Paget, S. (1889) 'The distribution of secondary growths in cancer of the breast', *The Lancet*, 1, pp. 571–573.
Park, J. E., Kim, H. S., Park, K. J., Choi, C. G. and Kim, S. J. (2015) 'Histogram analysis of amide proton transfer imaging to identify contrast-enhancing low-grade brain tumor that mimics high-grade tumor: Increased accuracy of MR perfusion[1]', *Radiology*, 277(1), pp. 151–161. doi: 10.1148/radiol.2015142347.
Parkes, L. M. and Tofts, P. S. (2002) 'Improved accuracy of human cerebral blood perfusion measurements using arterial spin labeling: Accounting for capillary water permeability', *Magnetic Resonance in Medicine*, 48(1), pp. 27–41. doi: 10.1002/mrm.10180.
Passalidou, E., Stewart, M., Trivella, M., Steers, G., Pillai, G., Dogan, A., Leigh, I., Hatton, C., Harris, A., Gatter, K. and Pezzella, F. (2003) 'Vascular patterns in reactive lymphoid tissue and in non-Hodgkin's lymphoma', *British Journal of Cancer*, 88(4), pp. 553–559. doi: 10.1038/sj.bjc.6600742.
Patan, S., Munn, L. L. and Jain, R. K. (1996) 'Intussusceptive microvascular growth in a human colon adenocarcinoma xenograft: A novel mechanism of tumor angiogenesis', *Microvascular Research*, 51(2), pp. 260–272. doi: 10.1006/mvre.1996.0025.
Paulis, Y. W. J., Soetekouw, P. M. M. B., Verheul, H. M. W., Tjan-Heijnen, V. C. G. and Griffioen, A. W. (2010) 'Signalling pathways in vasculogenic mimicry', *Biochimica et Biophysica Acta - Reviews on Cancer*, 1806(1), pp. 18–28. doi: 10.1016/j.bbcan.2010.01.001.
Pease, N. J., Edwards, A. and Moss, L. J. (2005) 'Effectiveness of whole brain radiotherapy in the treatment of brain metastases: A systematic review', *Palliative Medicine*, 19(4), pp. 288–299. doi: 10.1191/0269216305pm1017oa.
Pekar, J., Jezzard, P., Roberts, D. A., Leigh, J. S., Frank, J. A. and McLaughlin, A. G. (1996) 'Perfusion imaging with compensation for asymmetric magnetization transfer effects', *Magnetic Resonance in Medicine*, 35(1), pp. 70–79. doi: 10.1002/mrm.1910350110.
Pendse, N., Wissmeyer, M., Altrichter, S., Vargas, M., Delavelle, J., Viallon, M., Federspiel, A., Seeck, M., Schaller, K. and Lövblad, K. O. (2010) 'Interictal arterial spin-labeling MRI perfusion in intractable epilepsy', *Journal of Neuroradiology*, 37(1), pp. 60–63. doi: 10.1016/j.neurad.2009.05.006.
Perles-Barbacaru, T. A., Procissi, D., Demyanenko, A. V. and Jacobs, R. E. (2012) 'Quantitative pharmacologic MRI in mice', *NMR in Biomedicine*, 25(4), pp. 498–505. doi: 10.1002/nbm.1760.
Pezzella, F., Di Bacco, A. D., Andreola, S., Nicholson, A. G., Pastorino, U. and Harris, A. L. (1996) 'Angiogenesis in primary lung cancer and lung secondaries', *European Journal of Cancer Part A*, 32(14), pp. 2494–2500. doi: 10.1016/S0959-8049(96)00377-2.
Pezzella, F., Pastorino, U., Tagliabue, E., Andreola, S., Sozzi, G., Gasparini, G., Menard, S., Gatter, K. C., Harris, A. L., Fox, S., Buyse, M., Pilotti, S., Pierotti, M. and Rilke, F. (1997) 'Non-small-cell lung carcinoma tumor growth without morphological evidence of neo-angiogenesis', *American Journal of Pathology*, 151(5), pp. 1417–1423.
Pishko, G. L., Muldoon, L. L., Pagel, M. A., Schwartz, D. L. and Neuwelt, E. A. (2015) 'Vascular endothelial growth factor blockade alters magnetic resonance imaging biomarkers of vascular function and decreases barrier permeability in a rat model of lung cancer brain metastasis', *Fluids and Barriers of the CNS*, 12(1), pp. 1–10. doi: 10.1186/2045-8118-12-5.
Pollock, J. M., Tan, H., Kraft, R. a, Whitlow, C. T., Burdette, J. H. and Maldjian, J. a (2009)

Arterial Spin Labeled MRI Perfusion Imaging: Clinical Applications, *Magn Reson Imaging Clin N Am*. doi: 10.1016/j.mric.2009.01.008.Arterial.

Porta, R., Sánchez-Torres, J. M., Paz-Ares, L., Massutí, B., Reguart, N., Mayo, C., Lianes, P., Queralt, C., Guillem, V., Salinas, P., Catot, S., Isla, D., Pradas, A., Gúrpide, A., De Castro, J., Polo, E., Puig, T., Tarón, M., Colomer, R., *et al.* (2011) 'Brain metastases from lung cancer responding to erlotinib: The importance of EGFR mutation', *European Respiratory Journal*, 37(3), pp. 624–631. doi: 10.1183/09031936.00195609.

Poussaint, T. Y., Vajapeyam, S., Ricci, K. I., Panigrahy, A., Kocak, M., Kun, L. E., Boyett, J. M., Pollack, I. F. and Fouladi, M. (2016) 'Apparent diffusion coefficient histogram metrics correlate with survival in diffuse intrinsic pontine glioma: A report from the Pediatric Brain Tumor Consortium', *Neuro-Oncology*, 18(5), pp. 725–734. doi: 10.1093/neuonc/nov256.

Presta, L. G., Chen, H., O'Connor, S. J., Chisholm, V., Meng, Y. G., Krummen, L., Winkler, M. and Ferrara, N. (1997) 'Humanization of an anti-vascular endothelial growth factor monoclonal antibody for the therapy of solid tumors and other disorders', *Cancer Research*, 57(20), pp. 4593–4599.

Preusser, M., Capper, D., Ilhan-Mutlu, A., Berghoff, A. S., Birner, P., Bartsch, R., Marosi, C., Zielinski, C., Mehta, M. P., Winkler, F., Wick, W. and Von Deimling, A. (2012) 'Brain metastases: Pathobiology and emerging targeted therapies', *Acta Neuropathologica*, 123(2), pp. 205–222. doi: 10.1007/s00401-011-0933-9.

Pries, A. R., Cornelissen, A. J. M., Sloot, A. A., Hinkeldey, M., Dreher, M. R., Höpfner, M., Dewhirst, M. W. and Secomb, T. W. (2009) 'Structural adaptation and heterogeneity of normal and tumor microvascular networks', *PLoS Computational Biology*, 5(5). doi: 10.1371/journal.pcbi.1000394.

Pries, A. R., Höpfner, M., le Noble, F., Dewhirst, M. W. and Secomb, T. W. (2010) 'The shunt problem: control of functional shunting in normal and tumour vasculature', *Nature Reviews Cancer*, 10(8), pp. 587–593. doi: 10.1038/nrc2895.The.

Probst, R. J., Lim, J. M., Bird, D. N., Pole, G. L., Sato, A. K. and Claybaugh, J. R. (2006) 'Gender differences in the blood volume of conscious Sprague-Dawley rats.', *Journal of the American Association for Laboratory Animal Science : JAALAS*, 45(2), pp. 49–52. doi: 10.1016/j.drugalcdep.2008.02.002.A.

Qiao, X. J., Ellingson, B. M., Kim, H. J., Wang, D. J. J., Salamon, N., Linetsky, M., Sepahdari, A. R., Jiang, B., Tian, J. J., Esswein, S. R., Cloughesy, T. F., Lai, A., Nghiemphu, L. and Pope, W. B. (2015) 'Arterial spin-labeling perfusion MRI stratifies progression-free survival and correlates with epidermal growth factor receptor status in glioblastoma', *American Journal of Neuroradiology*, 36(4), pp. 672–677. doi: 10.3174/ajnr.A4196.

Raica, M. and Cimpean, A. M. (2010) 'Platelet-derived growth factor (PDGF)/PDGF receptors (PDGFR) axis as target for antitumor and antiangiogenic therapy', *Pharmaceuticals*, 3(3), pp. 572–599. doi: 10.3390/ph3030572.

Ramalingam, S. S., Belani, C. P., MacK, P. C., Vokes, E. E., Longmate, J., Govindan, R., Koczywas, M., Ivy, S. P. and Gandara, D. R. (2010) 'Phase II study of cediranib (AZD 2171), an inhibitor of the vascular endothelial growth factor receptor, for second-line therapy of small cell lung cancer (National Cancer Institute #7097)', *Journal of Thoracic Oncology*. International Association for the Study of Lung Cancer, 5(8), pp. 1279–1284. doi: 10.1097/JTO.0b013e3181e2fcb0.

Ray, K. J. (2017) *Measurement of pH using Chemical Exchange Saturation Transfer Magnetic Resonance Imaging*. University of Oxford.

Ray, K. J., Simard, M. A., Larkin, J. R., Coates, J., Kinchesh, P., Smart, S. C., Higgins, G. S., Chappell, M. A. and Sibson, N. R. (2019) 'Tumor pH and protein concentration contribute to the signal of amide proton transfer magnetic resonance imaging', *Cancer Research*, 79(7), pp. 1343–1352. doi: 10.1158/0008-5472.CAN-18-2168.

Reck, M., Von Pawel, J., Zatloukal, P., Ramlau, R., Gorbounova, V., Hirsh, V., Leighl, N., Mezger, J., Archer, V., Moore, N. and Manegold, C. (2009) 'Phase III trial of cisplatin plus gemcitabine with either placebo or bevacizumab as first-line therapy for nonsquamous non-small-cell lung cancer: AVAiL', *Journal of Clinical Oncology*, 27(8), pp. 1227–1234. doi: 10.1200/JCO.2007.14.5466.

Régina, A., Demeule, M., Laplante, A., Jodoin, J., Dagenais, C., Berthelet, F., Moghrabi, A. and Béliveau, R. (2001) 'Multidrug resistance in brain tumors: Roles of the blood-brain barrier', *Cancer and Metastasis Reviews*, 20(1–2), pp. 13–25. doi: 10.1023/A:1013104423154.

Reid, A., Tang, A., Spicer, J., Gallerani, E., Mears, D., Shaw, H., Karavasilis, V., Settatree, S., Yap, T., Marriot, C., Puchalski, T., Harrison, M., Naish, J., Mann, H. and De-Bono, J. (2007) 'An exploration of the ability of DCE-CT scans to evaluate blood flow in an open, pharmacokinetic (PK) and mass balance study of ¹⁴[C]-cediranib', *Molecular Cancer Therapeutics*, 6(11 Supplement), p. B259 LP-B259. Available at: http://mct.aacrjournals.org/content/6/11_Supplement/B259.abstract.

Reivich, M., Jehle, J., Sokoloff, L. and Kety, S. S. (1969) 'Measurement of regional cerebral blood flow with antipyrine-14C in awake cats.', *Journal of Applied Physiology*, 27(2), pp. 296–300. Available at: http://jap.physiology.org/content/27/2/296.short.

Rempp, K. A., Brix, G., Wenz, F., Becker, C. R., Gückel, F. and Lorenz, W. J. (1994) 'Quantification of Regional Cerebral Blood Flow and Volume with Dynamic Susceptibility Contrast-enhanced MR Imaging', *Radiology*, 193, pp. 637–641.

Ribatti, D., Vacca, A., Nico, B., Roncali, L. and Dammacco, F. (2001) 'Postnatal vasculogenesis', *Mechanisms of Development*, 100(2), pp. 157–163. doi: 10.1016/S0925-4773(00)00522-0.

Ritchie, H. and Roser, M. (2019) 'Causes of Death', *Our World in Data*.

Robertson, R. T., Levine, S. T., Haynes, S. M., Gutierrez, P., Baratta, J. L., Tan, Z. and Longmuir, K. J. (2014) 'Use of labeled tomato lectin for imaging vasculature structures', *Histochemistry and Cell Biology*, 143(2), pp. 225–234. doi: 10.1007/s00418-014-1301-3.

Rohatgi, A. (2010) *WebPlotDigitizer*. Available at: https://automeris.io/WebPlotDigitizer.

Rubenstein, J. L., Kim, J., Ozawa, T., Zhang, M., Westphal, M., Deen, D. F. and Shuman, M. A. (2000) 'Anti-VEGF antibody treatment of glioblastoma prolongs survival but results in increased vascular cooption', *Neoplasia*, 2(4), pp. 306–314.

Sakurada, O., Kennedy, C., Jehle, J., Brown, J., Carbin, G. and Sokoloff, L. (1978) 'Measurement of local cerebral blood flow with iodo [14C] antipyrine.', *American journal of physiology*, 234(5), pp. H59-66.

Saltz, L. B., Clarke, S., Díaz-Rubio, E., Scheithauer, W., Figer, A., Wong, R., Koski, S., Lichinitser, M., Yang, T. S., Rivera, F., Couture, F., Sirzén, F. and Cassidy, J. (2008) 'Bevacizumab in combination with oxaliplatin-based chemotherapy as first-line therapy in metastatic colorectal cancer: A randomized phase III study', *Journal of Clinical Oncology*, 26(12), pp. 2013–2019. doi: 10.1200/JCO.2007.14.9930.

Sandler, A., Gray, R., Perry, M. C., Brahmer, J., Schiller, J. H., Dowlati, A., Lilenbaum, R. and Johnson, D. H. (2006) 'Paclitaxel-carboplatin alone or with bevacizumab for non-small-cell lung cancer', *New England Journal of Medicine*, 355(24), pp. 2542–2550. doi:

10.1056/NEJMoa061884.

Sardari Nia, P., Hendriks, J., Friedel, G., Van Schil, P. and Van Marck, E. (2007) 'Distinct angiogenic and non-angiogenic growth patterns of lung metastases from renal cell carcinoma', *Histopathology*, 51(3), pp. 354–361. doi: 10.1111/j.1365-2559.2007.02800.x.

Satuito, M. and Tom, J. (2016) 'Potent inhalational anesthetics for dentistry', *Anesthesia Progress*, 63(1), pp. 42–49. doi: 10.2344/0003-3006-63.1.42.

Schindelin, J., Arganda-Carreras, I., Frise, E., Kaynig, V., Longair, M., Pietzsch, T., Preibisch, S., Rueden, C., Saalfeld, S., Schmid, B., Tinevez, J. Y., White, D. J., Hartenstein, V., Eliceiri, K., Tomancak, P. and Cardona, A. (2012) 'Fiji: An open-source platform for biological-image analysis', *Nature Methods*, 9(7), pp. 676–682. doi: 10.1038/nmeth.2019.

Schinkel, A. H. (1999) 'P-Glycoprotein, a gatekeeper in the blood-brain barrier', *Advanced Drug Delivery*, 36, pp. 179–194.

Schouten, L. J., Rutten, J., Huveneers, H. A. M. and Twijnstra, A. (2002) 'Incidence of brain metastases in a cohort of patients with carcinoma of the breast, colon, kidney, and lung and melanoma', *Cancer*, 94(10), pp. 2698–2705. doi: 10.1002/cncr.10541.

Schuff, N., Matsumoto, S., Kmiecik, J., Studholme, C., Du, A., Ezekiel, F., Miller, B. L., Kramer, J. H., Jagust, W. J., Chui, H. C. and Weiner, M. W. (2009) 'Cerebral blood flow in ischemic vascular dementia and Alzheimer's disease, measured by arterial spin-labeling magnetic resonance imaging', *Alzheimer's and Dementia*. Elsevier Ltd, 5(6), pp. 454–462. doi: 10.1016/j.jalz.2009.04.1233.

Schuff, N., Zhang, Y., Zhan, W., Lenoci, M., Ching, C., Boreta, L., Mueller, S. G., Wang, Z., Marmar, C. R., Weiner, M. W. and Neylan, T. C. (2011) 'Patterns of altered cortical perfusion and diminished subcortical integrity in posttraumatic stress disorder: An MRI study', *NeuroImage*. Elsevier Inc., 54(SUPPL. 1), pp. S62–S68. doi: 10.1016/j.neuroimage.2010.05.024.

Semenza, G. L. and Wang, G. L. (1992) 'A nuclear factor induced by hypoxia via de novo protein synthesis binds to the human erythropoietin gene enhancer at a site required for transcriptional activation.', *Molecular and Cellular Biology*, 12(12), pp. 5447–5454. doi: 10.1128/mcb.12.12.5447.

Senan, S. and Smit, E. F. (2007) 'Design of Clinical Trials of Radiation Combined with Antiangiogenic Therapy', *The Oncologist*, 12(4), pp. 465–477. doi: 10.1634/theoncologist.12-4-465.

Serres, S., Soto, M. S., Hamilton, A., McAteer, M. A., Carbonell, W. S., Robson, M. D., Ansorge, O., Khrapitchev, A., Bristow, C., Balathasan, L., Weissensteiner, T., Anthony, D. C., Choudhury, R. P., Muschel, R. J. and Sibson, N. R. (2012) 'Molecular MRI enables early and sensitive detection of brain metastases', *Proceedings of the National Academy of Sciences of the United States of America*, 109(17), pp. 6674–6679. doi: 10.1073/pnas.1117412109.

Serres, S., Martin, C. J., Sarmiento Soto, M., Bristow, C., O'Brien, E. R., Connell, J. J., Khrapitchev, A. A. and Sibson, N. R. (2014) 'Structural and functional effects of metastases in rat brain determined by multimodal MRI', *International Journal of Cancer*, 134(4), pp. 885–896. doi: 10.1002/ijc.28406.

Sfiligoi, C., De Luca, A., Cascone, I., Sorbello, V., Fuso, L., Ponzone, R., Biglia, N., Audero, E., Arisio, R., Bussolino, F., Sismonde, P. and De Bortoli, M. (2003) 'Angiopoietin-2 expression in breast cancer correlates with lymph node invasion and short survival', *International Journal of Cancer*, 103(4), pp. 466–474. doi: 10.1002/ijc.10851.

Shen, Q. and Duong, T. (2016) 'Magnetic resonance imaging of cerebral blood flow in animal stroke models', *Brain Circulation*, 2(1), p. 20. doi: 10.4103/2394-8108.178544.

Shen, X. (2008) *Vasodilation Effect of Inhalational Anesthetics - ClinicalTrials.gov*. Available at: https://clinicaltrials.gov/ct2/show/NCT00815269 (Accessed: 21 December 2019).

Shen, Z., Lei, J., Li, X., Wang, Z., Bao, X. and Wang, R. (2018) 'Multifaceted assessment of the APP/PS1 mouse model for Alzheimer's disease: Applying MRS, DTI, and ASL', *Brain Research*. Elsevier B.V., 1698(June), pp. 114–120. doi: 10.1016/j.brainres.2018.08.001.

Sherwood, L. M. and Parris, E. E. (1971) 'Tumor angiogenesis: Therapeutic implications', *The New England journal of medicine*, 285, pp. 1182–1186.

Siemann, D. W., Brazelle, W. D. and Jürgensmeier, J. M. (2009) 'The Vascular Endothelial Growth Factor Receptor-2 Tyrosine Kinase Inhibitor Cediranib (Recentin; AZD2171) Inhibits Endothelial Cell Function and Growth of Human Renal Tumor Xenografts', *International Journal of Radiation Oncology Biology Physics*, 73(3), pp. 897–903. doi: 10.1016/j.ijrobp.2008.10.031.

Siewert, B., Schlaug, G., Edelman, R. R. and Warach, S. (1997) 'Comparison of EPISTAR and T2*-weighted gadolinium-enhanced perfusion imaging in patients with acute cerebral ischemia', *Neurology*, 48(3), pp. 673–680.

Simonsen, C. Z., Østergaard, L., Vestergaard-Poulsen, P., Røhl, L., Bjørnerud, A. and Gyldensted, C. (1999) 'CBF and CBV measurements by USPIO bolus tracking: Reproducibility and comparison with Gd-based values', *Journal of Magnetic Resonance Imaging*, 9(2), pp. 342–347. doi: 10.1002/(SICI)1522-2586(199902)9:2<342::AID-JMRI29>3.0.CO;2-B.

Smedby, K. E., Brandt, L., Bäcklund, M. L. and Blomqvist, P. (2009) 'Brain metastases admissions in Sweden between 1987 and 2006', *British Journal of Cancer*, 101(11), pp. 1919–1924. doi: 10.1038/sj.bjc.6605373.

Soni, N., Dhanota, D. P., Kumar, S., Jaiswal, A. and Srivastava, A. (2017) 'Perfusion MR imaging of enhancing brain tumors: Comparison of arterial spin labeling technique with dynamic susceptibility contrast technique YR - 2017/9/1', *Neurology India*, 65(5), pp. 1046–1052. doi: 10.4103/neuroindia.NI_871_16.

Sorensen, A. G., Emblem, K. E., Polaskova, P., Jennings, D., Kim, H., Ancukiewicz, M., Wang, M., Wen, P. Y., Ivy, P., Batchelor, T. T. and Jain, R. K. (2012) 'Increased survival of glioblastoma patients who respond to antiangiogenic therapy with elevated blood perfusion', *Cancer Research*, 72(2), pp. 402–407. doi: 10.1158/0008-5472.CAN-11-2464.

Soto, M. S., Serres, S., Anthony, D. C. and Sibson, N. R. (2014) 'Functional role of endothelial adhesion molecules in the early stages of brain metastasis', *Neuro-Oncology*, 16(4), pp. 540–551. doi: 10.1093/neuonc/not222.

Steeg, P. S. (2006) 'Tumor metastasis: Mechanistic insights and clinical challenges', *Nature Medicine*, 12(8), pp. 895–904. doi: 10.1038/nm1469.

Stelzer, K. (2013) 'Epidemiology and prognosis of brain metastases', *Surgical Neurology International*, 4(SUPPL4). doi: 10.4103/2152-7806.111296.

Stessels, F., Van Den Eynden, G., Van Der Auwera, I., Salgado, R., Van Den Heuvel, E., Harris, A. L., Jackson, D. G., Colpaert, C. G., Van Marck, E. A., Dirix, L. Y. and Vermeulen, P. B. (2004) 'Breast adenocarcinoma liver metastases, in contrast to colorectal cancer liver metastases, display a non-angiogenic growth pattern that preserves the stroma and lacks hypoxia', *British Journal of Cancer*, 90(7), pp. 1429–1436. doi: 10.1038/sj.bjc.6601727.

Suh, C. H., Kim, H. S., Jung, S. C. and Kim, S. J. (2018) 'Diffusion-weighted imaging and

diffusion tensor imaging for differentiating high-grade glioma from solitary brain metastasis: A systematic review and meta-analysis', *American Journal of Neuroradiology*, 39(7), pp. 1208–1214. doi: 10.3174/ajnr.A5650.

Sun, B., Huang, Z., Wu, S., Ding, L., Shen, G., Cha, L., Wang, J. and Song, S. (2016) 'Cystic brain metastasis is associated with poor prognosis in patients with advanced breast cancer', *Oncotarget*, 7(45), pp. 74006–74014. doi: 10.18632/oncotarget.12176.

Sunwoo, L., Yun, T. J., You, S.-H., Yoo, R.-E., Kang, K. M., Choi, S. H., Kim, J., Sohn, C.-H., Park, S.-W., Jung, C. and Park, C.-K. (2016) 'Differentiation of Glioblastoma from Brain Metastasis: Qualitative and Quantitative Analysis Using Arterial Spin Labeling MR Imaging', *Plos One*, 11(11), p. e0166662. doi: 10.1371/journal.pone.0166662.

Swartz, J. E., Driessen, J. P., van Kempen, P. M. W., de Bree, R., Janssen, L. M., Pameijer, F. A., Terhaard, C. H. J., Philippens, M. E. P. and Willems, S. (2018) 'Influence of tumor and microenvironment characteristics on diffusion-weighted imaging in oropharyngeal carcinoma: A pilot study', *Oral Oncology*, 77(September 2017), pp. 9–15. doi: 10.1016/j.oraloncology.2017.12.001.

Tabouret, E., Chinot, O., Metellus, P., Tallet, A., Viens, P. and Gonçalves, A. (2012) 'Global Incidence and Prevalence of BM', 4662, pp. 4655–4662.

Tang, W., McCormick, A., Li, J. and Masson, E. (2017) 'Clinical Pharmacokinetics and Pharmacodynamics of Cediranib', *Clinical Pharmacokinetics*. Springer International Publishing, 56(5), pp. 689–702. doi: DOI 10.1007/s40262-016-0488-y.

Tebbutt, N. C., Wilson, K., Gebski, V. J., Cummins, M. M., Zannino, D., Van Hazel, G. A., Robinson, B., Broad, A., Ganju, V., Ackland, S. P., Forgeson, G., Cunningham, D., Saunders, M. P., Stockler, M. R., Chua, Y., Zalcberg, J. R., Simes, R. J., Price, T. J., Price, T., *et al.* (2010) 'Capecitabine, bevacizumab, and mitomycin in first-line treatment of metastatic colorectal cancer: Results of the Australasian Gastrointestinal Trials Group randomized phase III MAX study', *Journal of Clinical Oncology*, 28(19), pp. 3191–3198. doi: 10.1200/JCO.2009.27.7723.

Tempfer, H., Kaser-Eichberger, A., Lehner, C., Gehwolf, R., Korntner, S., Kunkel, N., Wagner, A., Gruetz, M., Heindl, L. M., Schroedl, F. and Traweger, A. (2018) 'Bevacizumab Improves Achilles Tendon Repair in a Rat Model', *Cellular Physiology and Biochemistry*, 46(3), pp. 1148–1158. doi: 10.1159/000489057.

Terman, B. I., Dougher-Vermazen, M., Carrion, M. E., Dimitrov, D., Armellino, D. C., Gospodarowicz, D. and Böhlen, P. (1992) 'Identification of the KDR tyrosine kinase as a receptor for vascular endothelial cell growth factor', *Biochemical and Biophysical Research Communications*, 187(3), pp. 1579–1586. doi: 10.1016/0006-291X(92)90483-2.

Thomas, D. L., Lythgoe, M. F., van der Weerd, L., Ordidge, R. J. and Gadian, D. G. (2006) 'Regional variation of cerebral blood flow and arterial transit time in the normal and hypoperfused rat brain measured using continuous arterial spin labeling MRI.', *Journal of cerebral blood flow and metabolism : official journal of the International Society of Cerebral Blood Flow and Metabolism*, 26(2), pp. 274–282. doi: 10.1038/sj.jcbfm.9600185.

Thomlinson, R. H. (1977) 'Hypoxia and tumours', *Journal of Clinical Pathology*, (S3-11), pp. 105–113. doi: 10.1136/jcp.s3-11.1.105.

Tofts, P. S. (2010) 'T1-weighted DCE Imaging Concepts: Modelling, Acquisition and Analysis', *Magnetom Flash*, (3), pp. 30–39.

Togao, O., Yoshiura, T., Keupp, J., Hiwatashi, A., Yamashita, K., Kikuchi, K., Suzuki, Y., Suzuki, S. O., Iwaki, T., Hata, N., Mizoguchi, M., Yoshimoto, K., Sagiyama, K., Takahashi,

M. and Honda, H. (2014) 'Amide proton transfer imaging of adult diffuse gliomas: Correlation with histopathological grades', *Neuro-Oncology*, 16(3), pp. 441–448. doi: 10.1093/neuonc/not158.

Tong, R. T., Boucher, Y., Kozin, S. V., Winkler, F., Hicklin, D. J. and Jain, R. K. (2004) 'Vascular normalization by vascular endothelial growth factor receptor 2 blockade induces a pressure gradient across the vasculature and improves drug penetration in tumors', *Cancer Research*, 64(11), pp. 3731–3736. doi: 10.1158/0008-5472.CAN-04-0074.

Vajkoczy, P., Farhadi, M., Gaumann, A., Heidenreich, R., Erber, R., Wunder, A., Tonn, J. C., Mengerand, M. D. and Breier, G. (2002) 'Microtumor growth initiates angiogenic sprouting with simultaneous expression of VEGF, VEGF receptor-2, and angiopoietin-2', *Journal of Clinical Investigation*, 109(6), pp. 777–785. doi: 10.1172/JCI0214105.

Vermeulen, P. B., Colpaert, C., Salgado, R., Royers, R., Hellemans, H., Van Den Heuvel, E., Goovaerts, G., Dirix, L. Y. and Van Marck, E. (2001) 'Liver metastases from colorectal adenocarcinomas grow in three patterns with different angiogenesis and desmoplasia', *Journal of Pathology*, 195(3), pp. 336–342. doi: 10.1002/path.966.

Walker, A. E., Robins, M. and Weinfeld, F. D. (1985) 'Epidemiology of brain tumors: The national survey of intracranial neoplasms', *Neurology*, 35(2), pp. 219–226.

Wang, G. L. and Semenza, G. L. (1995) 'Purification and characterization of hypoxia-inducible factor', *Journal of Biological Chemistry*, pp. 1230–1237. doi: 10.1074/jbc.270.3.1230.

Wang, J., Alsop, D. C., Li, L., Listerud, J., Gonzalez-At, J. B., Schnall, M. D. and Detre, J. A. (2002) 'Comparison of quantitative perfusion imaging using arterial spin labeling at 1.5 and 4.0 Tesla', *Magnetic Resonance in Medicine*, 48(2), pp. 242–254. doi: 10.1002/mrm.10211.

Wang, T., Agarwal, S. and Elmquist, W. F. (2012) 'Brain Distribution of Cediranib Is Limited by Active Efflux at the Blood-Brain Barrier', *Journal of Pharmacology and Experimental Therapeutics*, 341(2), pp. 386–395. doi: 10.1124/jpet.111.190488.

Wang, T., Oberoi, R. K. and Elmquist, W. F. (2011) 'Determination of cediranib in mouse plasma and brain tissue using high-performance liquid chromatography-mass spectrometry', *Journal of Chromatography B: Analytical Technologies in the Biomedical and Life Sciences*. Elsevier B.V., 879(32), pp. 3812–3817. doi: 10.1016/j.jchromb.2011.10.025.

Weber, M.-A., Thilmann, C., Lichy, M. P., Günther, M., Delorme, S., Zuna, I., Bongers, A., Schad, L. R., Debus, J., Kauczor, H.-U., Essig, M. and Schlemmer, H.-P. (2004) 'Assessment of irradiated brain metastases by means of arterial spin-labeling and dynamic susceptibility-weighted contrast-enhanced perfusion MRI: initial results.', *Investigative radiology*, 39(5), pp. 277–287. doi: 10.1097/01.rli.0000119195.50515.04.

Weber, M. A., Zoubaa, S., Schlieter, M., Jüttler, E., Huttner, H. B., Geletneky, K., Ittrich, C., Lichy, M. P., Kroll, A., Debus, J., Giesel, F. L., Hartmann, M. and Essig, M. (2006) 'Diagnostic performance of spectroscopic and perfusion MRI for distinction of brain tumors', *Neurology*, 66(12), pp. 1899–1906. doi: 10.1212/01.wnl.0000219767.49705.9c.

Wedge, S. R., Kendrew, J., Hennequin, L. F., Valentine, P. J., Barry, S. T., Brave, S. R., Smith, N. R., James, N. H., Dukes, M., Curwen, J. O., Chester, R., Jackson, J. A., Boffey, S. J., Kilburn, L. L., Barnett, S., Richmond, G. H. P., Wadsworth, P. F., Walker, M., Bigley, A. L., *et al.* (2005) 'AZD2171: A highly potent, orally bioavailable, vascular endothelial growth factor receptor-2 tyrosine kinase inhibitor for the treatment of cancer', *Cancer*

Research, 65(10), pp. 4389–4400. doi: 10.1158/0008-5472.CAN-04-4409.

Wells, J. A., Thomas, D. L., King, M. D., Connelly, A., Lythgoe, M. F. and Calamante, F. (2010) 'Reduction of errors in ASL cerebral perfusion and arterial transit time maps using image de-noising', *Magnetic Resonance in Medicine*, 64(3), pp. 715–724. doi: 10.1002/mrm.22319.

Welti, J. C., Powles, T., Foo, S., Gourlaouen, M., Preece, N., Foster, J., Frentzas, S., Bird, D., Sharpe, K., Weverwijk, A. Van, Robertson, D., Soffe, J., Erler, J. T., Pili, R., Springer, C. J., Mather, S. J. and Reynolds, A. R. (2012) 'Contrasting effects of sunitinib within in vivo models of metastasis', *Angiogenesis*, 15(4), pp. 623–641. doi: 10.1007/s10456-012-9291-z.

Wen, P. Y. and Loeffler, J. S. (2000) 'Brain Metastases', *Current Treatment Options in Oncology*, 1, pp. 447–458. doi: 10.1016/j.ncl.2018.04.010.

Wesseling, P., van der Laak, J. A. W. M., de Leeuw, H., Ruiter, D. J. and Burger, P. C. (2009) 'Quantitative immunohistological analysis of the microvasculature in untreated human glioblastoma multiforme', *Journal of Neurosurgery*, 81(6), pp. 902–909. doi: 10.3171/jns.1994.81.6.0902.

Wheeler, C., Stephens, T., Byth, K., Green, T., Wedge, S., Blakey, D. and Hughes, A. (2003) 'Novel approaches in oncology at AstraZeneca', *European Journal of Cancer, Supplement*, 1(8 SPEC. ISS.), pp. 3–8. doi: 10.1016/S1359-6349(03)80014-9.

Williams, D. S., Detre, J. A., Leigh, J. S. and Koretsky, A. P. (1992a) 'Magnetic resonance imaging of perfusion using spin inversion of arterial water.', *Proceedings of the National Academy of Sciences of the United States of America*, 89(1), pp. 212–216. doi: 10.1073/pnas.89.9.4220e.

Williams, D. S., Detre, J. A., Leigh, J. S. and Koretsky, A. P. (1992b) 'Magnetic resonance imaging of perfusion using spin inversion of arterial water.', *Proceedings of the National Academy of Sciences of the United States of America*, 89(1), pp. 212–6. doi: 10.1073/pnas.89.9.4220e.

Wong, E. C., Buxton, R. B. and Frank, L. R. (1997) 'Implementation of quantitative perfusion imaging techniques for functional brain mapping using pulsed arterial spin labeling.', *NMR in biomedicine*, 10(4–5), pp. 237–249. Available at: http://eutils.ncbi.nlm.nih.gov/entrez/eutils/elink.fcgi?dbfrom=pubmed&id=9430354&retmode=ref&cmd=prlinks.

Wu, B., Warnock, G., Zaiss, M., Lin, C., Chen, M., Zhou, Z., Mu, L., Nanz, D., Tuura, R. and Delso, G. (2016) 'An overview of CEST MRI for non-MR physicists', *EJNMMI Physics*, 3(1). doi: 10.1186/s40658-016-0155-2.

Xu, Q., Liu, Q., Ge, H., Ge, X., Wu, J., Qu, J. and Xu, K. (2017) 'Tumor recurrence versus treatment effects in glioma', 50(November).

Xu, Q., Gu, J., Lv, Y., Yuan, J., Yang, N., Chen, J., Wang, C., Hou, X., Jia, X., Feng, L. and Yin, G. (2018) 'Angiogenesis for tumor vascular normalization of endostar on hepatoma 22 tumor-bearing mice is involved in the immune response', *Oncology Letters*, 15(3), pp. 3437–3446. doi: 10.3892/ol.2018.7734.

Yancopoulos, G. D., Davis, S., Gale, N. W., Rudge, J. S., Wiegand, S. J. and Holash, J. (2000) 'Vascular-specific growth factors and blood vessel formation', *Nature*, 407(6801), pp. 242–248. doi: 10.1038/35025215.

Yang, J., Liao, C., Liu, Y., Yang, G., Ke, T. and Ding, Y. (2018) 'MR imaging biomarkers evaluating vascular normalization window after anti-vessel treatment', 9(15), pp. 11964–11976.

Yano, S., Shinohara, H., Herbst, R. S., Kuniyasu, H., Bucana, C. D., Ellis, L. M., Davis, D. W., McConkey, D. J. and Fidler, I. J. (2000) 'Expression of vascular endothelial growth factor is necessary but not sufficient for production and growth of brain metastasis', *Cancer Research*, 60(17), pp. 4959–4967.

Yoneda, T., Williams, P. J., Hiraga, T., Niewolna, M. and Nishimura, R. (2001) 'A Bone-Seeking Clone Exhibits Different Biological Properties from the MDA-MB-231 Parental Human Breast Cancer Cells and a Brain-Seeking Clone In Vivo and In Vitro', *Journal of Bone and Mineral Research*, 16(8), pp. 1486–1495. doi: 10.3892/or.2011.1572.

Yoshida, H., Yoshimura, H., Matsuda, S., Ryoke, T., Kiyoshima, T., Kobayashi, M. and Sano, K. (2018) 'Effects of peritumoral bevacizumab injection against oral squamous cell carcinoma in a nude mouse xenograft model: A preliminary study', *Oncology Letters*, 15(6), pp. 8627–8634. doi: 10.3892/ol.2018.8399.

Yuan, F., Chen, Y., Dellian, M., Safabakhsh, N., Ferrara, N. and Jain, R. K. (1996) 'Time-dependent vascular regression and permeability changes in established human tumor xenografts induced by an anti-vascular endothelial growth factor/vascular permeability factor antibody', *Proceedings of the National Academy of Sciences of the United States of America*, 93(25), pp. 14765–14770. doi: 10.1073/pnas.93.25.14765.

Yushkevich, P. A., Piven, J., Hazlett, H. C., Smith, R. G., Ho, S., Gee, J. C. and Gerig, G. (2006) 'User-guided 3D active contour segmentation of anatomical structures: Significantly improved efficiency and reliability', *NeuroImage*, 31(3), pp. 1116–1128. doi: 10.1016/j.neuroimage.2006.01.015.

Zhao, X., Wen, Z., Zhang, G., Huang, F., Lu, S., Wang, X., Hu, S., Chen, M. and Zhou, J. (2013) 'Three-dimensional turbo-spin-echo amide proton transfer MR imaging at 3-tesla and its application to high-grade human brain tumors', *Molecular Imaging and Biology*, 15(1), pp. 114–122. doi: 10.1007/s11307-012-0563-1.

Zhou, J., Lal, B., Wilson, D. A., Laterra, J. and Van Zijl, P. C. M. (2003) 'Amide Proton Transfer (APT) Contrast for Imaging of Brain Tumors', *Magnetic Resonance in Medicine*, 50(6), pp. 1120–1126. doi: 10.1002/mrm.10651.

Zhou, J., Tryggestad, E., Wen, Z., Lal, B., Zhou, T., Grossman, R., Wang, S., Yan, K., Fu, D., Ford, E., Tyler, B., Laterra, J. and Zijl, P. C. M. Van (2011) 'Differentiation between glioma and radiation necrosis', *Nature medicine*, 17(1), pp. 130–134. doi: 10.1038/nm.2268.Differentiation.

Van Zijl, P. C. M. and Yadav, N. N. (2011) 'Chemical exchange saturation transfer (CEST): What is in a name and what isn't?', *Magnetic Resonance in Medicine*, 65(4), pp. 927–948. doi: 10.1002/mrm.22761.

APPENDIX I

Peer-reviewed article

In 2018, Dr. James Larkin and I published the following peer-reviewed article as co-first authors in the Journal of Cerebral Blood Flow and metabolism. It demonstrates the main findings from Chapter 3 of this thesis.

Original Article

JCBFM

Journal of Cerebral Blood Flow & Metabolism
0(00) 1–13
© Author(s) 2018
Reprints and permissions:
sagepub.co.uk/journalsPermissions.nav
DOI: 10.1177/0271678X18756218
journals.sagepub.com/home/jcbfm
SAGE

Quantitative blood flow measurement in rat brain with multiphase arterial spin labelling magnetic resonance imaging

James R Larkin[1], Manon A Simard[1], Alexandre A Khrapitchev[1], James A Meakin[2], Thomas W Okell[2], Martin Craig[3], Kevin J Ray[1], Peter Jezzard[2], Michael A Chappell[3] and Nicola R Sibson[1]

Abstract

Cerebral blood flow is an important parameter in many diseases and functional studies that can be accurately measured in humans using arterial spin labelling (ASL) MRI. However, although rat models are frequently used for preclinical studies of both human disease and brain function, rat CBF measurements show poor consistency between studies. This lack of reproducibility is due, partly, to the smaller size and differing head geometry of rats compared to humans, as well as the differing analysis methodologies employed and higher field strengths used for preclinical MRI. To address these issues, we have implemented, optimised and validated a multiphase pseudo-continuous ASL technique, which overcomes many of the limitations of rat CBF measurement. Three rat strains (Wistar, Sprague Dawley and Berlin Druckrey IX) were used, and CBF values validated against gold-standard autoradiography measurements. Label positioning was found to be optimal at 45°, while post-label delay was optimised to 0.55 s. Whole brain CBF measures were 109 ± 22, 111 ± 18 and 100 ± 15 mL/100 g/min by multiphase pCASL, and 108 ± 12, 116 ± 14 and 122 ± 16 mL/100 g/min by autoradiography in Wistar, SD and BDIX cohorts, respectively. Tumour model analysis shows that the developed methods also apply in disease states. Thus, optimised multiphase pCASL provides robust, reproducible and non-invasive measurement of CBF in rats.

Keywords

Arterial spin labelling, autoradiography, cerebral blood flow, multiphase, rats

Received 21 July 2017; Revised 1 December 2017; Accepted 22 December 2017

Introduction

Arterial spin labelling (ASL) is increasingly gaining popularity in the clinic for its functional MRI (fMRI) capabilities, as well as for perfusion analysis in the brain in diseases such as stroke[1,2] and cancer.[3,4] Despite its apparent simplicity, the many variations of ASL have complicated its implementation in routine clinical practice. To this end, the ASL 'white paper' was published in 2015 and gave recommended clinical guidelines for the purpose of standardising ASL across multiple scanners and centres.[5] The final recommendations of the white paper include using a pseudo-continuous ASL (pCASL) labelling approach combined with a single post-label delay (PLD), varying slightly depending on the subject's age and health status.

Simple transposition of the recommended clinical methods to pre-clinical systems, however, is not sufficient to achieve high quality CBF measurements.

[1]Department of Oncology, Cancer Research UK & Medical Research Council Oxford Institute for Radiation Oncology, University of Oxford, Oxford, UK
[2]Wellcome Centre for Integrative Neuroimaging, FMRIB Division, University of Oxford, John Radcliffe Hospital, Headington, Oxford, UK
[3]Institute of Biomedical Engineering, University of Oxford, Oxford, UK

The first two authors contributed equally to this work.

Corresponding author:
Nicola R Sibson, Department of Oncology, CRUK and MRC Oxford Institute for Radiation Oncology, University of Oxford, Old Road Campus Research Building, Oxford OX3 7LJ, UK.
Email: nicola.sibson@oncology.ox.ac.uk

Interspecies differences mean that a direct transposition of acquisition parameters yields spurious and error-prone data. These issues pose a significant problem as pre-clinical models of disease are of critical importance in many fields and accurate, non-invasive and quantitative measurement of blood flow is a crucial parameter in many studies. The problems with pre-clinical ASL stem mostly from issues associated with the high field strengths that are used pre-clinically, as well as rodent-specific head and neck geometry. High quality ASL images are dependent upon a uniform magnetic field, not only in the imaging plane, but also in the labelling plane. Off-resonance effects arising from poor magnetic field homogeneity and neck geometry lead to differing labelling efficiency in each vessel in the labelling plane. These differences in labelling efficiencies lead to errors in the calculated CBF, that cannot be corrected from the matched pairs of label and control images acquired during a pCASL MRI experiment. This problem is exacerbated in pre-clinical imaging studies for two reasons: (1) the air spaces in the rodent head (throat, oesophagus, mouth, and nasal cavities) are very close to the labelling and imaging planes, causing large magnetic susceptibility artefacts and off-resonance effects; and (2) the higher field strengths used (typically $\geq$7 T) make it more difficult to create a homogenous magnetic field. As a result of the above issues, a wide range of CBF measurements in rodents have been reported, often spanning ranges that are neither physiologically realistic (e.g. $>300\,\text{mL}/100\,\text{g}/\text{min}$[6–10]), nor in agreement with gold-standard autoradiography measures of perfusion.[11] Thus, there is a need to improve the application of ASL MRI in rodents and to achieve a similar standardization to that now implemented clinically.

Multiphase pCASL (MP pCASL) is a variant of ASL where instead of acquiring the traditional label and control images, images are acquired following labelling with radio-frequency (RF) pulses at multiple phase increments.[12] These increments span 360° allowing fitting of the data to an expected function, rather than simply subtracting label from control. These extra phase increments make the acquisition of MP pCASL more time consuming than a simple label-control experiment. However, in a rodent, where the exact magnetic environment in the labelling plane is unknown and likely to be inhomogeneous, the MP pCASL acquisition has the potential to enable post hoc correction for the off-resonance effects in the neck and return true values for CBF. Thus, MP pCASL offers a way to trade increased scan time for a markedly increased confidence in CBF values in rodents. An alternative to MP pCASL, proposed recently by Hirschler et al.,[13] attempts to solve the off-resonance problem through the use of dedicated pre-scans. The proposed approach uses large voxels across each hemisphere, with a high SNR, and then rapidly iterates through a substantial number of phase offsets. These pre-scans are used to determine optimal acquisition parameters for the following ASL acquisition. The drawback with this approach is that where adjacent arteries have different phase offsets, a single value must be chosen for both if using a pre-scan approach, whereas the optimal value may be used for each artery with a post hoc approach. Additionally, the pre-scans must be processed while the rat is still anaesthetised, instead of a complete post hoc processing that is possible with a full MP pCASL acquisition.

The primary aim of this study, therefore, was to implement, optimise and validate an MP variant of pCASL in rats, in order to improve the accuracy and reliability of rodent CBF measurements via post hoc correction for optimal phase. This study was performed in three different strains of rat (Wistar, Sprague Dawley (SD) and Berlin Druckrey IX (BDIX)) to enable robust assessment of the reliability and applicability of the MP pCASL method. CBF measurements are compared to those obtained by ^{14}C-iodoantipyrine autoradiography, the pre-clinical gold-standard technique for quantitative CBF determination.[11,14]

Materials and methods

Animals

Female Wistar, SD and BDIX rats weighing 180–400 g were used throughout. All animal experiments were approved by the UK Home Office (Animals [Scientific Procedures] Act 1986) and conducted in accordance with the University of Oxford Policy on the Use of Animals in Scientific Research and the ARRIVE guidelines.[15] Animals were housed in individually ventilated cages under a 12-h light/12-h dark cycle with food and water ad libitum. All animals were housed in cages of three or four animals, depending on body mass.

Carotid blood flow measurement

Rats ($n=3$ per strain) were anaesthetised with isoflurane and laid supine on an ultrasound stage. Body temperature was maintained at *ca.* 37°C using a homeothermic pad under the animal. Each animal's carotid arteries were observed by ultrasound for 30 s at 10–12 respiration rates at 39–65 breaths per minute. B-mode ultrasound videos were acquired and used to determine the time-averaged mean and peak blood velocities at each respiration rate (Figure SI1 and Supplementary Methods for full details).

Simulations of ASL

Numerical simulations using the Bloch equations were conducted using previously developed code[16] in Matlab (Mathworks, Natick, MA) to determine theoretical blood inversion during the ASL pulse sequence (i.e. M(z), expressible as labelling efficiency – the percentage of maximum inversion possible). A pCASL sequence was simulated with a pulse train of 600 μs Hanning-shaped pulses, each separated by 600 μs. Simulated T_1 and T_2 of blood was 2.1 s and 33 ms, respectively, measured from oxygenated rat blood at 37°C. The ratio G_{max}/G_{av} during labelling was fixed at 20. Blood velocity was simulated from 1 to 100 cm/s, labelling gradient strengths were varied to correspond to a labelling plane thickness from 2 to 10 mm and labelling pulse flip angle varied from 2 to 90°. The relationship between G_{max} and labelling plane thickness (Thk_{lab}) is given by $Thk_{lab} = BW_{trans}/(\gamma_0 \cdot G_{max})$, where BW_{trans} is the transmitted RF bandwidth (4.3 kHz) and γ_0 is the gyromagnetic ratio (42.58 MHz/T).

Magnetic resonance imaging

Rats were anaesthetised with isoflurane and imaged using a 9.4 T MRI spectrometer (Agilent) with a 72 mm volume transmit coil and a 4-channel surface receive array (Rapid Biomedical; $n = 7$ per strain). Respiration rate was maintained between 40 and 60 breaths per minute by adjusting isoflurane concentration.

A multiphase pCASL sequence[12] was implemented by varying the phase increments of pulses in the labelling train from 0° to 315° in eight steps of 45°. The labelling plane (6.2 mm thick) was placed in the neck of the rat, either perpendicular to, or at 45° to, the animal's rostro-caudal axis. The location of the labelling plane was set through the use of a midline sagittal fast spin echo image (FOV = 50 × 50 mm, matrix = 256 × 256, thickness = 2 mm, TR = 1 s; TE_{eff} = 40 ms, T_{exp} = 34 s, single scan). For the MP pCASL, a multi-slice single-shot spin-echo echo planar imaging (EPI) sequence was used for the imaging readout (FOV = 32 × 32 mm, matrix = 64 × 64, thickness = 1 mm, 10 slices, TE = 28.7 ms). Slices were acquired in an anterior-posterior direction. Blood labelling (tagging) was achieved with a pulse train comprising Hanning-shaped pulses of 600 μs duration and 40° flip angle, each separated by 600 μs (50% duty cycle). A schematic of the pulse sequence is shown in Figure 1. Proton-density calibration images for absolute CBF quantitation were acquired for all animals, using both the surface receive array and the volume transmit coil, by omitting labelling pulses. For all animals, T_1 maps were obtained using an inversion recovery method (inversion time varied in nine logarithmic steps from 0.013 to 8 s, TR = 10 s) and T_2 maps were obtained using a multi-echo approach (echo time varied in nine logarithmic steps from 30 to 160 ms, TR = 10 s). Readouts were spin-echo EPI acquisitions as for the ASL acquisitions.

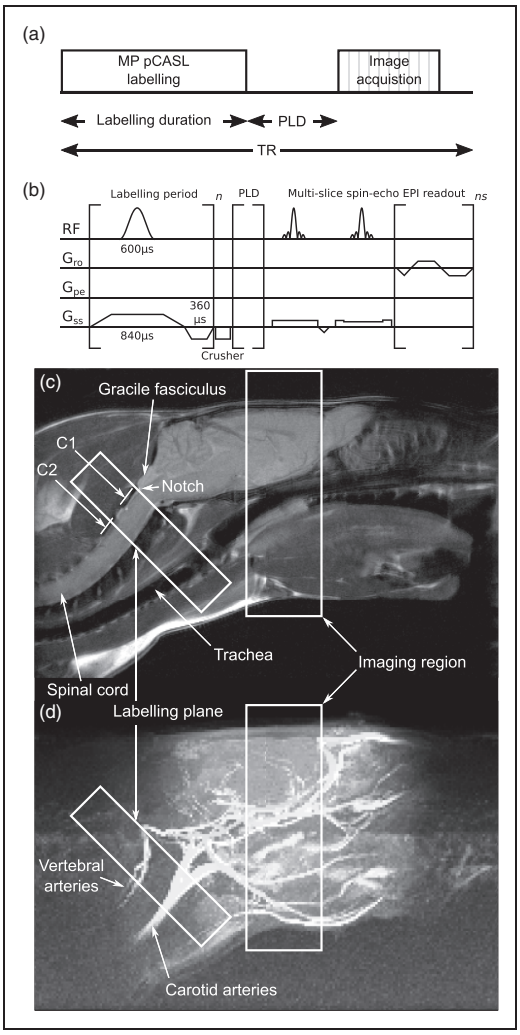

Figure 1. (a) Schematic of the multiphase pCASL sequence. (b) Pulse timing diagram of the sequence. (c and d) Location of the labelling and imaging regions shown in relation to the brain and the major vessels of the neck, superimposed over (c) an anatomical, fast spin-echo sagittal midline image of an SD rat head, and (d) a maximum intensity projection of time-of-flight angiography with the same field of view. Positions of C1 and C2 vertebra are visible and the notch immediately caudal to the gracile fasciculus is easily identified.

Arterial transit time (ATT) was measured by acquiring data with 12 PLDs (10, 15, 20, 25, 30, 50, 100, 200, 300, 500, 750 and 1000 ms; PLD), each with the same

eight phase angles (acquisition time = 14 min 41 s for all 12 PLDs combined). The spacing of PLDs was chosen to obtain good fits for typical BATs observed in pilot data. Multi-PLD images were acquired with only two slices – in naïve animals, the first immediately posterior to the olfactory sulcus (i.e. most anterior slice of the full imaging region) and the second 10 mm posterior to the first (i.e. most posterior slice of the imaging region); in tumour-bearing animals, the slices were positioned across the tumour. This reduction in imaging slices was necessary as each slice took 50 ms to acquire and obtaining 10 slices would lead to an unacceptable minimum delay before acquiring the last slice.

In a subset of animals also used for autoradiography ($n = 3$ per strain), more extensive optimisations were carried out. Label duration was varied as follows: 0.4 s, 0.9 s, 1.4 s (TR = 4 s, T_{exp} = 1 min 29 s), 2.4 s (TR = 5 s, T_{exp} = 1 min 39 s), 3.7 s (TR = 6.3 s, T_{exp} = 2 min 4 s), 5.0 s (TR = 7.6 s, T_{exp} = 2 min 30 s), all with PLD = 550 ms. Label location was varied serially along the neck vasculature in 2 mm increments. To confirm labelling plane location with respect to the brain and brain vasculature, time of flight (TOF) angiography was used to visualise vessels and brain-midline sagittal anatomical MRI was used to show the labelling plane location with respect to the vessels. TOF angiography: T_1-weighted 3D gradient echo readout (FOV = 40 × 40 × 60 mm, matrix = 128 × 128 × 192, TR = 30 ms, FA = 30°, axial excitation slab, T_{exp} = 12 min 17 s). Anatomical MRI: T_2-weighted fast spin-echo readout (FOV = 40 × 60 mm, matrix = 128 × 192, TR = 1 s, TE_{eff} = 10 ms, single 2 mm slice at brain midline, T_{exp} = 2 min 8 s).

T_1 and T_2 times of re-oxygenated post-mortem blood were determined at 37°C, using a heated water jacket sample holder to maintain the temperature. Oxygenation was confirmed as complete using an i-STAT blood-gas analyser (Abbot, UK).

Data fitting and analysis

ASL data analysis and perfusion quantitation were performed using a custom version of BASIL,[17] which is available as part of the FMRIB Software Library (www.fmrib.ox.ac.uk/fsl/basil). The multiphase acquisition data are expected to fit a modified Fermi function of the form

$$f(phase) = Mag\left(-2\left[\frac{1}{1+e^{(|phase|-\alpha)/\beta}}\right]\right) + Off$$

where α and β were 70 and 19, respectively; chosen by minimisation of root-mean-square error on data fitting of 12 rats from three strains (data not shown), *phase* is the phase angle in degrees, *Mag* is the magnitude (amplitude) and *Off* is the offset from 0.[12] The Fermi function was fitted to the multiphase data to obtain the magnitude of the multiphase ASL signal. Fitting was performed using the Variational Bayesian algorithm within the FSL tool fabber, which incorporates normally distributed priors on all the parameters.[17] Since 3-parameter models such as this are prone to over-estimation of amplitude in the presence of additive noise,[18] a multi-step analysis process was used to minimise bias. Firstly, the raw multiphase data were fitted with unconstrained priors, producing voxel-wise estimates of phase, magnitude and offset. The phase maps were clustered using a supervoxel approach[19] with four supervoxels per phase map, a smoothing (σ) of 0.8 and a compactness of 0.1. This was used to define ROIs from the data that represent individual flow territories as indicated by their phase value arising from the phase offset present in the feeding artery. For each supervoxel region, the original multiphase data were averaged for all voxels across each phase, yielding a new higher SNR multiphase dataset. This dataset was fitted to the Fermi function, estimating a single phase value for each supervoxel ROI. These final phase values were used as a high precision prior for the final fitting of the original raw multiphase data, yielding a voxel-wise map of magnitude and offset. Figure 2 shows a flow chart of this methodology, including example images derived by the process. Datasets from this manuscript are available upon request.

The resultant maps of the magnitude of the fitted function, representing the presence of labelled water in each voxel and equivalent to the subtracted label-control images from traditional pCASL, were processed with oxford_asl (part of the FMRIB software library[17,20]) in the same way as would be done with conventional label-control difference data and according to the one-compartment kinetic model of Buxton et al.[21] to produce relative CBF maps. In the subset of animals used for autoradiography ($n = 3$ per strain), comparisons to the one-compartment model were made by also fitting the data according to the two-compartment kinetic model of Parkes and Tofts.[22] This two-compartment model includes an extravascular water pool in addition to the blood compartment water pool and has two described solutions, one 'slow' and one 'fast'. The slow solution assumes that labelled water never leaves the tissue voxel, while the fast solution assumes that venous blood has the same magnetisation as blood in the voxel. Maps were corrected for coil sensitivity inhomogeneity, using the ratio of proton density images acquired with the surface receive array and the volume coil. Final calibration to absolute CBF units was performed using a reference region M0 value method. The striatum was chosen as a reference region since the use of CSF, as used in

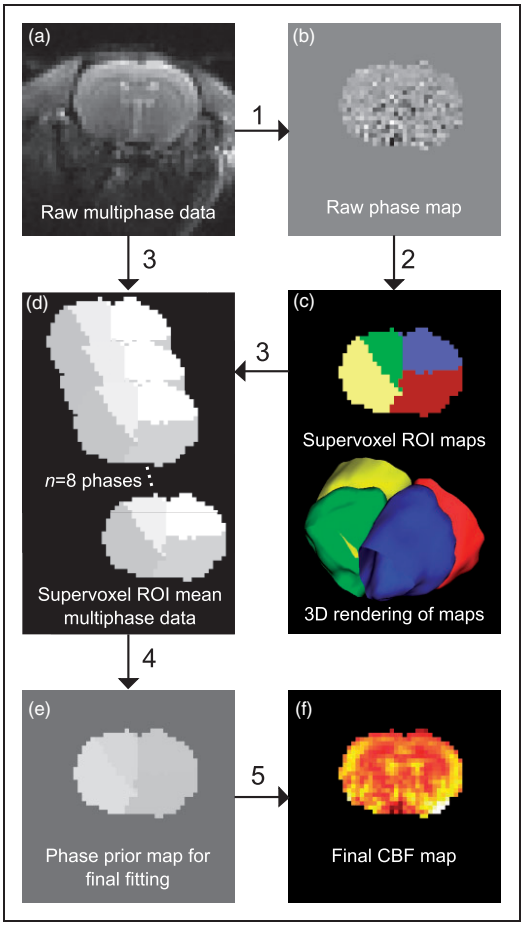

Figure 2. Schematic showing the use of supervoxels in preparing high precision phase map priors. The raw multiphase data (a) are initially fitted to the Fermi function with low precision priors (1) to yield a raw phase map (b). This raw phase map contains good spatial information but the phase values themselves are overestimated. The data are smoothed and clustered using supervoxels (2) to yield ROIs for each supervoxel phase cluster present (c). The raw multiphase data are then combined with the supervoxel ROIs (3) to yield high SNR supervoxel-ROI means of the multiphase data (d). This high SNR multiphase dataset is then fitted again (4) yielding a high precision phase map (e) which can be used to generate the final CBF maps (f), in combination with the raw data (5).

humans, was not practical in rats owing to its small volume and consequent partial volume effects that prevent selection of voxels containing CSF alone. The rat striatum is large enough to provide sufficient voxels for analysis, is clearly identifiable, and is easy to use for in vivo T_1 and T_2 time quantitation. A striatum-specific tissue:blood partition coefficient for water of 0.97[23] and a single inversion efficiency, 82%, calculated as a mean for the three strains from simulations of each strain-specific carotid blood velocity (see results) was used. Relaxation parameters for quantitation were: blood, $T_1 = 2.09 \pm 0.02$ s, $T_2 = 33.2 \pm 0.3$ ms; reference tissue (striatum), $T_1 = 1.5 \pm 0.2$ s; $T_2 = 40 \pm 8$ ms; whole brain, $T_1 = 1.6 \pm 0.3$ s.

For conventional label-control analysis, 0° and 180° images from the multiphase acquisition were used as label and control, respectively. CBF quantitation was carried out using the voxel-wise calculation recommended in the White Paper[5]

$$CBF = \frac{6000 \cdot \lambda \cdot (SI_{control} - SI_{label}) \cdot e^{\frac{PLD}{T_{1,blood}}}}{2 \cdot \alpha \cdot T_{1,blood} \cdot SI_{PD,Str} \cdot \left(1 - e^{-\frac{\tau}{T_{1,blood}}}\right)}$$

where λ is the brain/blood partition coefficient of water (0.9 mL/g), $SI_{control}$ and SI_{label} are the signal intensities of the control and label images, PLD is the post label delay (0.55 s), $T_{1,blood}$ is the longitudinal relaxation time of rat arterial blood at 37°C (2.1 s), α is the labelling efficiency for pCASL (0.85), $SI_{PD,Str}$ is the mean signal intensity for an ROI drawn across the striatum of the proton-density-weighted reference image with no labelling pulses, corrected for short TR by multiplying by $(1/(1\text{-}e^{-TR/T1,tissue}))$ where $T_{1,tissue}$ is the measured longitudinal relaxation time for rat brain (1.6 s), and τ is the label duration (1.4 s).

Autoradiography

CBF was determined using gold standard autoradiography[11,14] in all three strains ($n = 3$ per strain). Briefly, rats were anaesthetised and 4[N-methyl-^{14}C] iodoantipyrine was infused into the femoral vein over 1 min (50 µCi in 0.5 mL saline). The rat was killed by pentobarbitone infusion, immediately decapitated, and the head frozen. Brain slices (20 µm thickness) were exposed to X-ray film with calibrated images being converted to CBF values. CBF maps were aligned with respective to MRI CBF maps. Whole brain, striatum and cortex ROIs were drawn on the MRI maps and the same ROIs were transferred to the autoradiography images for comparison. Full methodological details are given in the Supplementary Methods.

Intracerebral model of brain metastasis

Female BDIX rats ($n = 3$) were anaesthetised with isoflurane (1.5–3% in 70:30 N_2O:O_2) and placed in a stereotactic frame. An incision was made on the scalp and a burr hole drilled 1 mm anterior and 3 mm lateral to bregma; 1000 ENU1564 cells in 1 µL PBS were injected using a drawn glass capillary (<100 µm diameter) to a depth of 3.5 mm in the left striatum. The scalp

was sutured and animals were allowed to recover. Tumour-bearing BDIX rats were subjected to MRI three weeks after tumour induction. Group size was chosen from a power calculation assuming a 30% decrease in blood flow in tumours, with standard deviation equal in both groups to that observed in naïve animals and $1-\beta = 0.9$.

Statistical analysis

All results are presented as mean ± S.D, unless otherwise specified. Differences between groups were determined using one-way ANOVA followed, where required, by Tukey's multiple comparison post hoc tests.

Results

Angiography and labelling plane orientation

Time-of-flight angiography showed orientation and location of major vessels with respect to head, neck and brain anatomy visible on high-resolution structural images (Figure 1(c) and (d)). No discernible differences in relative geometry were evident between strains of rat or between smaller and larger rats (range from 180 to 340 g). Carotid and vertebral arteries ran at angles of $42 \pm 7^\circ$ and $44 \pm 8^\circ$, respectively, with respect to the longitudinal axis of the rat and in no strain was there a significant difference in angle between the carotid and vertebral arteries. The bend in the vertebral arteries immediately rostral to the C1 vertebra, and just prior to the entrance into the skull, marks the limit of the region where the vessels are straight and parallel. This point can be seen as the notch immediately caudal to the gracile fasciculus and is easily visible on sagittal midline anatomical images (Figure 1(c)).

The orientation of the labelling plane across the neck impacted both absolute CBF quantitation and error in quantitation of the CBF maps. Flow-driven adiabatic inversion is most efficient when the flow of blood is perpendicular to the labelling plane. A labelling plane at 45° with respect to the longitudinal axis of the animal crosses the arteries close to perpendicularly. The CBF maps obtained at the optimal 45° labelling angle exhibited lower variance in voxel-wise CBF values ($p < 0.01$; F test) and yielded more physiologically realistic absolute CBF values than images acquired with a labelling plane at 0° ($p < 0.001$; *t*-test; Figure SI2(a)). Example of CBF maps is shown in Figure SI2(b).

Blood velocity measurements

Carotid artery blood flow velocities were measured by Doppler ultrasound in Wistar, SD and BDIX rats ($n = 3$ for each strain). Typical acquisition traces and images, from which mean and peak (systolic) flow velocities were determined, are shown in Figure SI1. Mean carotid artery flow velocity was significantly higher in SD rats compared to either BDIX or Wistar rats (47 ± 6 cm/s for SD vs. 30 ± 10 cm/s for BDIX, $p < 0.001$; and 35 ± 7 cm/s for Wistar, $p < 0.01$; Figure 3(a)). Peak carotid artery flow velocity was lowest in BDIX rats (100 ± 30 cm/s), higher in Wistar rats (130 ± 20 cm/s; $p < 0.01$) and higher again in SD rats (170 ± 20 cm/s; $p < 0.01$). No significant difference was evident in either peak or mean flow velocity as a function of respiration rate within any strain (Figure 3(b)).

Simulation results

Numerical simulations showed that inversion efficiencies diminished dramatically with low flip angles (<30°), especially with narrow labelling planes and/or high blood velocities. However, there exists a plateau of high and relatively uniform inversion efficiency at greater labelling region thicknesses and flip angles (Figure 3(c)). A labelling region thickness of 6.2 mm and a flip angle of 40° was selected for in vivo experiments to achieve maximum inversion efficiency across a range of physiologically relevant blood velocities (25–50 cm/s; Figure SI3). No significant difference in inversion efficiencies was evident between strains, despite the higher mean blood velocity in the SD rats, which is a result of the non-linear relationship between velocity and inversion efficiency (Figure SI3). Mean inversion efficiency for the three strains of rats was 82%.

Relaxometry

Whole, 100% oxygenated rat blood relaxation times at 37°C and 9.4 T were: $T_1 = 2.09 \pm 0.02$ s; $T_2 = 33.2 \pm 0.3$ ms. Striatal relaxation times *in* vivo were: $T_1 = 1.5 \pm 0.2$ s; $T_2 = 40 \pm 8$ ms. Whole brain in vivo T_1 relaxation time was 1.6 ± 0.3 s ($n = 21$ rats across 3 strains). These values were used to calibrate quantitation procedures as described in the 'Methods'.

PLD and arrival time

Images acquired with varying PLDs, between 10 and 1000 ms, were used to construct blood bolus arrival time maps (Figure 4(a)). Evaluation of arrival time in two slices, one at the front and one at the back of the imaging region within the brain, allowed the range of possible arrival times to be determined. Example of multi-PLD data for whole animals and example of single voxels are shown in Figure SI4. As expected, blood arrived at the anterior slice later than it arrived at the posterior slice in all strains ($p < 0.001$, Kolmogorov–Smirnov test; Figure 4(b)), but a large

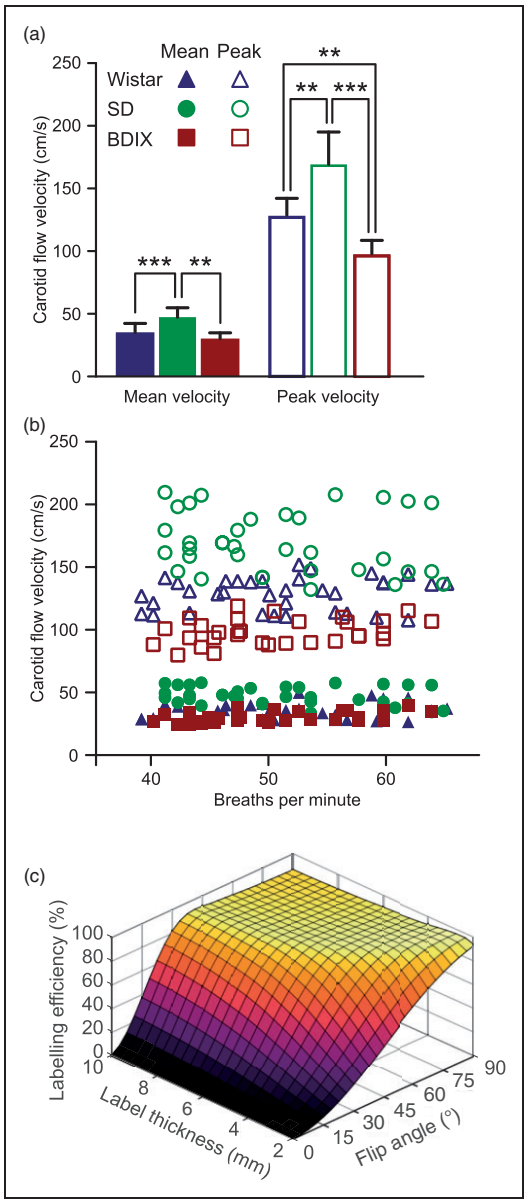

Figure 3. (a) Mean and peak carotid artery flow velocities in three strains of rats; Wistar, SD and BDIX. (b) Mean and peak carotid artery flow velocities as a function of anaesthetic depth, as indicated by breathing rate. (c) Bloch simulation results showing labelling efficiency (inversion achieved as a percentage of theoretical inversion possible), for blood as it passes through labelling planes of 2–10 mm thickness with flip angles in the labelling pulse train between 2° and 90° at 37 cm/s (mean carotid velocity for all rats studied).

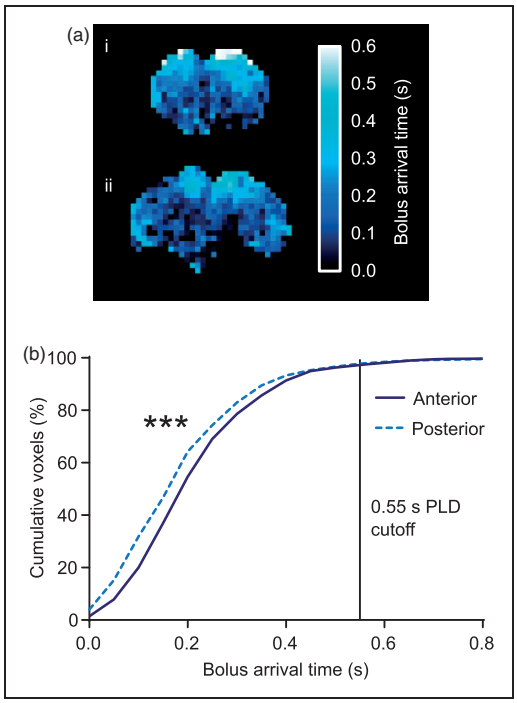

Figure 4. (a) Bolus arrival time maps from (i) anterior slice (immediately caudal to the olfactory sulcus), and (ii) posterior slice (10 mm caudal to the anterior slice) from an example BDIX rat brain. (b) Cumulative frequency distributions of voxel arrival time in the anterior and posterior slices from all rat strains ($n = 18$; $^{***}p < 0.001$). The PLD cut-off represents the point at which arterial transit (cumulative voxels) had occurred in 97% of voxels imaged.

overlap was evident between the range of arrival times at the front and back of the brain. A PLD of 550 ms was chosen for subsequent imaging as 97% of voxels in both slices had an arrival time shorter than this. For tumour-bearing BDIX rats, mean arrival time for voxels within the tumour was slower for those voxels in a comparable contralateral ROI (Figure SI5, $p < 0.001$). CBF was heterogeneous across the tumour area and where CBF in the tumour was greater than the minimum CBF of the contralateral ROI (i.e. excluding voxels in core hypoxic regions of the tumour), >87% of tumour voxels had an arrival time of ≤650 ms. We therefore used a PLD of 650 ms for tumour-bearing animals. Voxels in the core of the tumour where CBF was very low had longer arrival times (up to 1600 ms).

Labelling plane location and labelling duration

The position of the labelling plane was moved along the axis of the vessels in the neck over a range of 12 mm. The extent of this range was ultimately limited by

interference with the imaging plane at the rostral end and by efficiency of the labelling coil (volume transmit RF coil) at the caudal end. However, before reaching the rostral limit, the labelling plane moves across regions where the feeding arteries have entered the brain and no longer run perpendicular to the labelling plane; for example, as the vertebral arteries enter the skull, blood flows parallel to the labelling plane (Figure 1(d)). These imperfections affect labelling efficiency and lead to artificially decreased CBF values (Figure 5(a)). As the labelling plane was moved caudally from this point, through the region where the feeding vessels are straight and parallel, no significant effect on calculated CBF values was found.

No significant differences were found between CBF values obtained at any label duration from 0.9 s to 3.7 s. However, a significantly lower CBF was obtained with the longest label duration of 5 s compared to the shortest duration of 0.4 s (113 ± 15 vs. 92 ± 11 mL/100 g/min, $p < 0.05$; Figure 5(b)). SNR efficiency (expressed as $accumulated\ signal/\sqrt{T_{exp}}$) exhibits a sharp increase up to a label duration of 1.4 s, then remains broadly similar with label durations between 1.4 s and 5 s, albeit with a peak at around 2.4 s (Figure SI6). For all subsequent acquisitions, a label duration of 1.4 s was used to reduce scan time.

Observed phase offsets within and between animals

Optimal phase offsets varied both between and within animals, with greater variation between animals. Within animals, the range of optimal phases between supervoxel regions varied from 6 to 107° (median 21°, first and third quartiles: 11° and 31°). Between animals, the absolute phase offset was distributed widely across the complete 360° (a graphical plot of all phase offsets for all supervoxels is shown in Figure SI7). No correlation was evident between mean phase offset for an

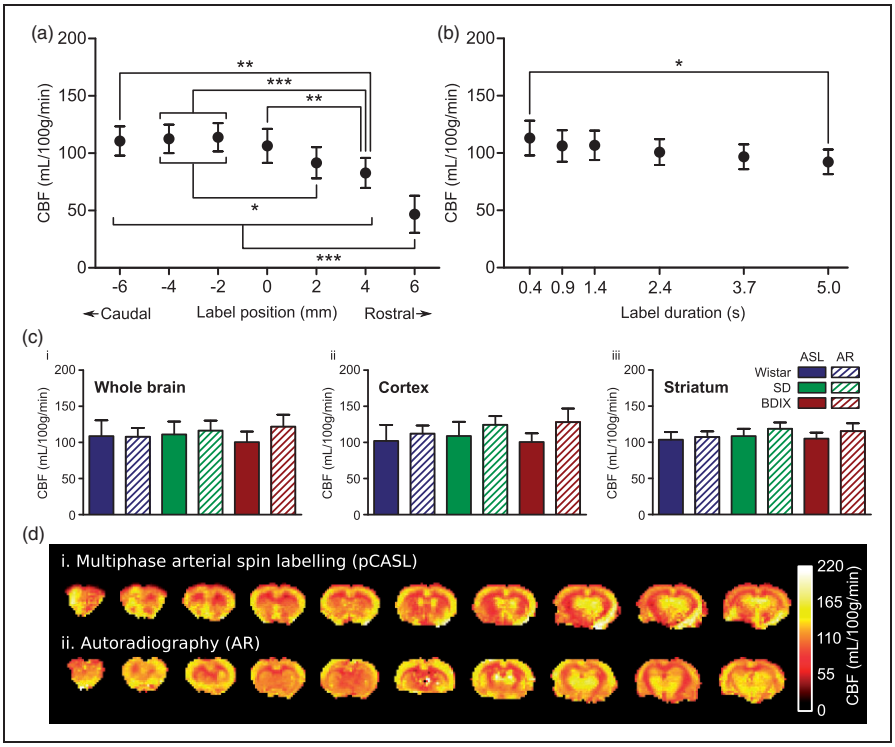

Figure 5. (a) Effect of labelling plane location on CBF measurements. Negative label positions are located towards the tail of the animals, positive positions towards the nose; 0 mm is the position of the labelling plane shown in Figure 1, at which the labelling plane is entirely spanning straight and parallel vessels, each passing close to perpendicular through the labelling plane. ***$p < 0.001$, **$p < 0.01$, *$p < 0.05$; $n = 9$ across three strains. (b) Effect of label duration on CBF measurements: *$p < 0.05$; $n = 9$ across three strains. (c) Comparison between autoradiography (AR) and pCASL (1.4 s label duration) derived CBF values from ROIs covering (i) the whole brain, (ii) the cortex, or (iii) the striatum. (d) Example CBF maps obtained using (i) multiphase pCASL MRI and (ii) autoradiography in a Wistar rat.

individual animal and the dispersion of phase angles is observed between supervoxel territories for that animal. Moving the labelling plane within the neck of an animal was sufficient to elicit significant changes in optimal phase angles observed in some, but not all, cases, likely reflecting the unique magnetic environment in each animal's neck.

Model fitting comparison and correlation between pCASL and autoradiography CBF values

No significant differences were found in any region (cortex, striatum or whole brain) or strain between CBF values obtained by autoradiography and multiphase pCASL MRI when fitted with the one-compartment model.[21] Representative pCASL MRI data acquired with a label duration of 1.4 s are shown in Figure 5(c), but no differences between pCASL MRI and autoradiography CBF measures were found at any label duration from 0.9 s to 3.7 s. Autoradiography values for whole brain perfusion were 108 ± 12, 116 ± 14 and 122 ± 16 mL/100 g/min in Wistar, SD and BDIX rats, respectively, compared to multiphase pCASL CBF values in the same animals of 109 ± 22, 111 ± 18 and 100 ± 15 mL/100 g/min, respectively, with the one-compartment model. Mean CBF values across all animals ($n = 9$) obtained using autoradiography (115 ± 14 mL/100 g/min) and multiphase pCASL analysed using the one-compartment model (107 ± 13 mL/100 g/min) were not significantly different. In contrast, the CBF values from the two implementations of the two-compartment model were both significantly different to the autoradiography CBF measures (95 ± 11 mL/100 g/min for the slow implementation, $p < 0.05$; and 157 ± 19 mL/100 g/min for the fast implementation, $p < 0.001$; one-way ANOVA with Dunnett's test). CBF values obtained using the one-compartment and slow two-compartment models were not significantly different.

Multiphase analysis vs. label-control analysis

A comparison between multiphase analysis and the White Paper-recommended label-control analysis was made for each animal. Label-control images (effectively two phases) can be acquired in one-quarter the time of the eight-phase multiphase acquisitions, and therefore, four averages were used for the label-control acquisitions for legitimate comparison. Label-control subtractions gave images with lower CBF values ($p < 0.01$) and higher standard deviations (F-test, $p < 0.01$). Additionally, some regions appeared hypoperfused in the label-control images, but multiphase images showed that they were in fact normally perfused (Figure 6).

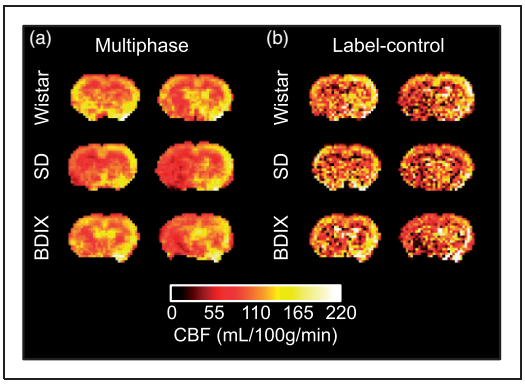

Figure 6. Comparison of CBF maps from single-average multiphase pCASL acquisitions and four-average label-control acquisitions in the same animal; total imaging time 89 s in each case. Note the lower CBF values, areas of greater heterogeneity and the regions with decreased apparent perfusion in the label-control maps.

Strain-specific CBF measurements and brain metastasis model

Having validated the optimised multiphase pCASL parameters through comparison of CBF values with gold standard autoradiography, a larger cohort of each strain ($n = 7$ per group, including the three autoradiography animals) were subsequently used to assess reproducibility of the multiphase pCASL measurements. Example of strain-specific maps of multiphase pCASL CBF values is shown in Figure 7. Wistar rats had a significantly higher CBF than the other two strains ($p < 0.001$). However, within each strain, no significant differences in CBF were found between ROIs studied. Whole brain CBF varied very little between strains, being 106 ± 17, 96 ± 22 and 95 ± 10 mL/100 g/min in Wistar, SD and BDIX rats, respectively. These values show good correspondence with those obtained in the autoradiography experiment. In tumour-bearing rats ($n = 3$), blood flow was decreased to 60 ± 5 mL/100 g/min in an ROI covering the tumour area from 93 ± 3 mL/100 g/min in a comparable contralateral ROI ($p < 0.001$, Figure SI5).

Discussion

In this work, a multiphase pCASL MRI technique was optimised for pre-clinical studies in rats. We have identified imaging parameters that address the issues associated with high magnetic field strength imaging in rodents. The single largest factor in improving image quality was the implementation and use of the multiphase pCASL technique instead of a simple label-control sequence. Choice of imaging parameters was

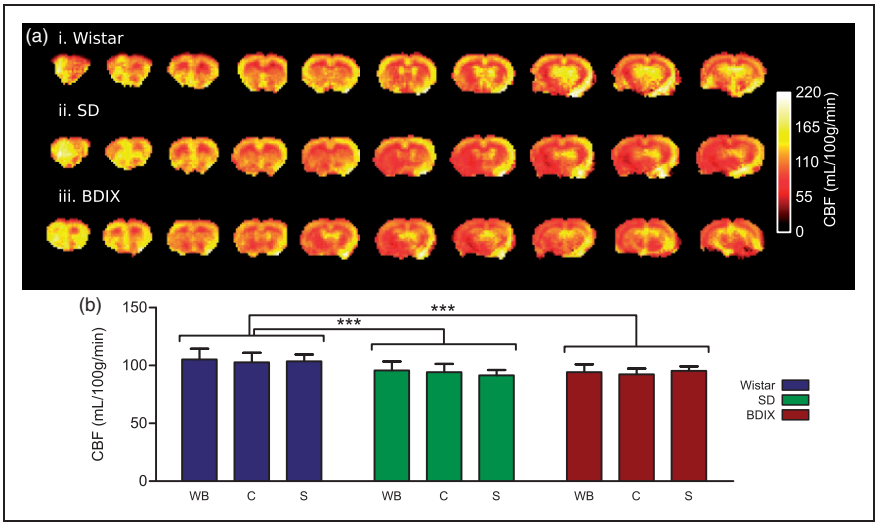

Figure 7. (a) Example cerebral blood flow maps acquired using the optimised multiphase pCASL sequence for three strains of rat; Wistar, SD and BDIX. Eight averages were acquired per image, total imaging time = 11 min 52 s. (b) CBF mean of whole brain (WB), cortex (c), and striatum (S) in three strains of rats. $n = 7$ rats/strain; $^{*}p < 0.05$.

validated by comparison of rat CBF values obtained by multiphase pCASL to gold-standard autoradiography in the same animals. Reproducible and robust CBF measurements were demonstrated using these optimised parameters and methodology.

Multiphase pCASL vs. label-control ASL

In this work, we used a pCASL implementation for MRI CBF data acquisition, which is the clinically recommended method since it does not require continuous RF transmitting hardware and reduces magnetization transfer effects inherently present in the earlier implemented CASL approach. Moreover, pCASL retains the well-defined bolus duration present in CASL, essential for accurate CBF quantification, while maintaining a higher SNR than PASL.[5,24] Finally, as with CASL, blood labelling occurs in a narrower plane by flow-driven adiabatic inversion. We also implemented a multiphase approach, rather than the traditionally used single label-control sequence, and this yielded the greatest increase in signal-to-noise and image quality. While the multiphase pCASL acquisitions take up to four times longer than traditional label-control pairs to acquire, the total imaging time of 89 s for an eight phase acquisition is not excessive and yields images that show a considerable qualitative and quantitative improvement over acquiring four averages of label-control subtraction in the same time frame. Note, also, that some regions in the label-control analysis have artificially reduced CBF values that affect entire vascular territories. This result is a consequence of off-resonance effects such that one or more vessels running through the labelling plane are affected differently to the other vessels, and this cannot be corrected without the multiphase data.

Labelling plane parameters

The ideal labelling plane should be positioned at a point where the traversing arteries are both straight, and angled to be approximately perpendicular to the direction of flow in the vessels. If both criteria are met, the exact distance of the labelling plane from the imaging region is less important. However, for consistency, one location should be chosen for all animals. This point could be determined on an animal-by-animal basis through the use of angiography, but this scan can be avoided through the use of an anatomical reference, as suggested by Alsop et al.[5] Thus, in rodents, our data suggest that optimal positioning can be achieved by placing the labelling plane immediately caudal to the marked bends in the vertebral arteries, just behind the gracile fasciculus and to the rear of the top of the atlas vertebra (as shown in Figure 1). This anatomical marker is readily identifiable on quick sagittal midline scans and does not vary between rat strains, making it an ideal location.

Corollaries to the position of the labelling plane are its orientation and the label duration. The selection of a 45° labelling plane, instead of a 0° plane, decreases error associated with CBF measurements and, importantly, brings the magnitude of the values closely into alignment with the autoradiography data. With regard

to the duration of the labelling period, ASL signal increases as label duration increases, albeit with a plateau at longer labelling times ($signal \propto 1\text{-}(e^{-(\text{label duration}/T1)})$). The efficiency of accumulated signal is unacceptably low with label durations <1.4 s but broadly similar with label durations from 1.4 s to 5 s, giving investigators the option to vary label duration (and thus experimental acquisition time), to best align with their experimental goals. The shorter acquisition for the 1.4 s label duration offers the better compromise in our current application (Figure SI6).

One important aspect of the analysis pipeline is the selection of the correct phase priors for model fitting. It is a mathematical problem that three component models, with a phase, amplitude and offset (such as the Fermi function used herein), are prone to overestimation of the amplitude when noise is increased.[18] Noise in the multiphase pCASL signal is increased with short label durations as there is less labelled blood in the imaging plane, meaning that changes in image intensity are closer to acquisition and biological noise floors. A consequence of this effect is that, without steps to choose the correct phase for data, the magnitude (and hence CBF) is overestimated (data not shown). By using the supervoxels to cluster phase maps (predominantly within vascular territories in the brain), then averaging the voxels in the original multiphase pCASL data within each ROI, the SNR of the raw data was increased at the expense of spatial resolution. This approach can be justified since phase estimates are not expected to vary on a voxel-wise basis within whole vascular territories. By using the supervoxel approach, higher precision fitting was possible, yielding more accurate phase values and improved magnitude fitting results. Consequently, the relationship between label duration and CBF is broadly flat using this approach, without overestimation of CBF at the shorter label durations. Despite these corrections, however, a slight trend for increased measured CBF is still seen at the shortest label durations, probably an artefact of the very poor ASL data achieved with such short label durations. In contrast, a trend towards decreased CBF at the longest label durations is evident, which may be either a consequence of inaccurate T_1 estimates or a consequence of not considering outflow of labelled blood from the tissue during the labelling period. In humans, this outflow is considered negligible, but in rats may confer a moderate contribution at long labelling times.

Arrival time and PLD selection

A short PLD is advantageous for maximising the ASL signal as it minimises T_1 recovery of the ASL signal from the labelled water in the imaging region. However, if the PLD is too short, the transit of labelled blood through the arteries and into the tissue will be incomplete: this can lead to signal from arterial blood artificially increasing the measured CBF values near arteries and underestimation of tissue CBF elsewhere. In this study, the BAT in naïve rats was <550 ms in 97% of voxels, independent of strain. Consequently, a PLD of 550 ms was chosen as the best compromise for maximum signal without arterial contamination. However, in the case of pre-clinical models of brain pathology, particularly where vascular changes are expected to occur, such as stroke or cancer, assessment of BATs in representative animals would be necessary to determine an appropriate PLD for imaging, or multi-PLD protocols could be considered. For example, in our tumour-bearing BDIX rats, we chose a longer PLD to compensate for the later arrival exhibited by tortuous tumour vessels. In all cases, this choice will be a compromise between increasing PLD to accommodate voxels with a later arrival time and decreasing PLD to prevent too much signal decay by T_1 relaxation.

Validation with gold standard measurements and model comparisons

Autoradiography measurements represent the gold standard in brain perfusion quantitation and have a long literature validation behind them.[11,14,25] However, autoradiography is an invasive and terminal procedure, as well as being complex and time consuming to perform and quantify. These factors render autoradiography unsuitable for large numbers of studies, but it remains an excellent calibration point for non-invasive measurements such as pCASL MRI. Here, we compared the autoradiography CBF measurements with CBF values produced by one- and two-compartment kinetic models. The range of the CBF values produced from the three models likely represents an outside limit to the true CBF value, which the autoradiography measurements suggest falls at the lower end of the range. The fast model may be over-estimating CBF because it does not incorporate a complete venous outflow term, which is likely to be more important as flow rates increase. The one-compartment model and the slow implementation of the two-compartment model are in closer agreement and have both been used pre-clinically previously.[8] Our results demonstrate that the one-compartment model was the closest match to the autoradiography data and, combined with the optimised imaging parameters, produced consistent CBF values from both naïve and diseased rats.

Strain comparison

Three pre-clinically relevant strains of rats were used throughout this work to assess the reliability of the method across different strains and to determine

whether strain specific differences could be observed. Comparing between strains, Wistar rats had significantly higher CBF than SD and BDIX rats, while SD rats exhibited a higher mean carotid blood velocity than the other two strains. Despite this difference in velocity, no significant difference in inversion efficiency was observed between the strains. Thus, we used a single inversion efficiency of 82% for all rat strains, which eliminates the need to determine strain-specific carotid artery velocities for accurate quantitation. We did not observe any differences in blood arrival time to the brain between strains, meaning that a single PLD is suitable for all strains of naïve rat.

Conclusions

This paper proposes optimised parameters for ASL in rats with the aim of improving and standardising quantitative ASL in high magnetic field pre-clinical settings. A multiphase pCASL approach was employed, in which images are acquired at multiple phase angles instead of the traditional label-control (0°–180°) technique, allowing correction for inevitable off-resonance effects and enhancing image quality in both naïve animals and in a brain tumour model system. The optimal labelling plane position and label parameters for efficient blood inversion, the optimal labelling duration for maximum efficiency of data accumulation, and optimal PLD for minimisation of contamination from arterial signal in CBF maps have been determined. Using gold-standard autoradiography, it was confirmed that the optimised multiphase pCASL method yields accurate CBF values and, thus, provides a rapid and reproducible method for non-invasively measuring CBF in rats.

Funding

The author(s) disclosed receipt of the following financial support for the research, authorship, and/or publication of this article: This work was supported by the Cancer Research UK (grant number C5255/A15935 to NRS), the CRUK/EPSRC Cancer Imaging Centre (grant number C5255/A16466) in Oxford and the EPSRC (grant number EP/P012361/1). The Wellcome Centre for Integrative Neuroimaging is supported by the core funding from the Wellcome Trust (203139/Z/16/Z).

Acknowledgements

The authors would like to thank James Thompson and Luke Bird for assistance with the quantitative densitometry, Sean Smart and Paul Kinchesh for assistance with the MRI, Karla Watson, Jade Harris and Jessica Law for assistance with animal husbandry, and Axel de Bernardi for additional data handling.

Declaration of conflicting interests

The author(s) declared no potential conflicts of interest with respect to the research, authorship, and/or publication of this article.

Authors' contributions

JRL, MAS, AAK, JAM, TWO, MC and KJR performed experiments and collected data, NRS, MAC, PJ, JRL and MAS designed the study, JRL and MAS wrote the manuscript, and all authors critically reviewed the manuscript and approved the final version to be published.

Supplementary material

Supplementary material for this paper can be found at the journal website: http://journals.sagepub.com/home/jcb

ORCID iD

James R Larkin http://orcid.org/0000-0002-4169-8447.
Manon A Simard http://orcid.org/0000-0001-5363-1699.

References

1. Miyaji Y, Yokoyama M, Kawabata Y, et al. Arterial spin-labeling magnetic resonance imaging for diagnosis of late seizure after stroke. *J Neurol Sci* 2014; 339: 87–90.
2. Zhang S, Yao Y, Zhang S, et al. Comparative study of DSC-PWI and 3D-ASL in ischemic stroke patients. *J Huazhong Univ Sci Technolog Med Sci* 2015; 35: 923–927.
3. Silva AC, Kim SG and Garwood M. Imaging blood flow in brain tumors using arterial spin labeling. *Magn Reson Med* 2000; 44: 169–173.
4. Qiao XJ, Ellingson BM, Kim HJ, et al. Arterial spin-labeling perfusion MRI stratifies progression-free survival and correlates with epidermal growth factor receptor status in glioblastoma. *Am J Neuroradiol* 2015; 36: 672–677.
5. Alsop DC, Detre JA, Golay X, et al. Recommended implementation of arterial spin-labeled perfusion MRI for clinical applications: a consensus of the ISMRM perfusion study group and the European consortium for ASL in dementia. *Magn Reson Med* 2015; 73: 102–116.
6. Kim T and Kim S-G. Quantification of cerebral arterial blood volume and cerebral blood flow using MRI with modulation of tissue and vessel (MOTIVE) signals. *Magn Reson Med* 2005; 54: 333–342.
7. Thomas DL, Lythgoe MF, Weerd L van der, et al. Regional variation of cerebral blood flow and arterial transit time in the normal and hypoperfused rat brain measured using continuous arterial spin labeling MRI. *J Cereb Blood Flow Metab* 2006; 26: 274–282.
8. Debacker CS, Daoust A, Köhler S, et al. Impact of tissue T1 on perfusion measurement with arterial spin labeling. *Magn Reson Med* 2017; 77: 1656–1664.

9. Hendrich KS, Kochanek PM, Melick JA, et al. Cerebral perfusion during anesthesia with fentanyl, isoflurane, or pentobarbital in normal rats studied by arterial spin-labeled MRI. *Magn Reson Med* 2001; 46: 202–206.
10. Wells JA, Lythgoe MF, Gadian DG, et al. In vivo Hadamard encoded continuous arterial spin labeling (H-CASL). *Magn Reson Med* 2010; 63: 1111–1118.
11. Sakurada O, Kennedy C, Jehle J, et al. Measurement of local cerebral blood flow with iodo [14C] antipyrine. *Am J Physiol* 1978; 234: H59–H66.
12. Jung Y, Wong EC and Liu TT. Multiphase pseudocontinuous arterial spin labeling (MP-PCASL) for robust quantification of cerebral blood flow. *Magn Reson Med* 2010; 64: 799–810.
13. Hirschler L, Debacker CS, Voiron J, et al. Interpulse phase corrections for unbalanced pseudo-continuous arterial spin labeling at high magnetic field. *Magn Reson Med* 2017; 79: 1314–1324.
14. Reivich M, Jehle J, Sokoloff L, et al. Measurement of regional cerebral blood flow with antipyrine-14C in awake cats. *J Appl Physiol* 1969; 27: 296–300.
15. Kilkenny C, Browne WJ, Cuthill IC, et al. Improving bioscience research reporting: the ARRIVE guidelines for reporting animal research. *PLoS Biol* 2010; 8: e1000412.
16. Okell TW, Chappell MA, Woolrich MW, et al. Vessel-encoded dynamic magnetic resonance angiography using arterial spin labeling. *Magn Reson Med* 2010; 64: 698–706.
17. Chappell MA, Groves AR, Whitcher B, et al. Variational Bayesian Inference for a Nonlinear Forward Model. *IEEE Trans Signal Process* 2009; 57: 223–236.
18. Alegria FC. Bias of amplitude estimation using three-parameter sine fitting in the presence of additive noise. *Measurement* 2009; 42: 748–756.
19. Irving B, Popescu IA, Bates R, et al. maskSLIC: regional superpixel generation with application to local pathology characterisation in medical images. CoRR, https://arxiv.org/pdf/1606.09518.pdf (2016, accessed 16 January 2018).
20. Groves AR, Chappell MA and Woolrich MW. Combined spatial and non-spatial prior for inference on MRI time-series. *Neuroimage* 2009; 45: 795–809.
21. Buxton RB, Frank LR, Wong EC, et al. A general kinetic model for quantitative perfusion imaging with arterial spin labeling. *Magn Reson Med* 1998; 40: 383–396.
22. Parkes LM and Tofts PS. Improved accuracy of human cerebral blood perfusion measurements using arterial spin labeling: accounting for capillary water permeability. *Magn Reson Med* 2002; 48: 27–41.
23. Leithner C, Müller S, Füchtemeier M, et al. Determination of the brain-blood partition coefficient for water in mice using MRI. *J Cereb Blood Flow Metab* 2010; 30: 1821–1824.
24. Pollock JM, Tan H, Kraft RA, et al. Arterial spin-labeled MR perfusion imaging: clinical applications. *Magn Reson Imaging Clin N Am* 2009; 17: 315–338.
25. Ewing JR, Wei L, Knight RA, et al. Direct comparison of local cerebral blood flow rates measured by MRI arterial spin-tagging and quantitative autoradiography in a rat model of experimental cerebral ischemia. *J Cereb Blood Flow Metab* 2003; 23: 198–209.

APPENDIX II

Detection of perfused vessels in rat brain metastases

Aim

To visualise perfused vessels in a rat model of breast cancer brain metastasis using fluorescence-conjugated tomato lectin (from *Lycopersicon esculentum*), as opposed to all vessels regardless of function, as performed Chapter 4.

Method

As previously shown by Robertson and colleagues, tomato lectin binds to endothelial cells of rodent vasculature and can be seen as quickly as 1 minute after their intravenous injection (Robertson *et al.*, 2014).

BDIX rats were injected intracerebrally with ENU cells (as described in section 2.2.1) and tumours were grown for three weeks. Prior to killing and perfusion-fixation, rats were

injected with 90 µL of tomato lectin (1 mg/mL; DL-1174, Vector Laboratories Ltd, Burlingame, USA), and 1 minute later, were overdosed with pentobarbitone. Subsequently, rats were perfusion fixed, the brains isolated and processed for sectioning at a thickness of 20 µm on a cryostat, as described in sections 2.2.2 and 2.4.1, respectively.

Slides with rat brain sections were mounted with coverslips using DPX mountant (Sigma-Aldrich, UK) and, subsequently scanned using the Aperio Scanscope FL (Leica Biosystems, Germany).

Result and discussion

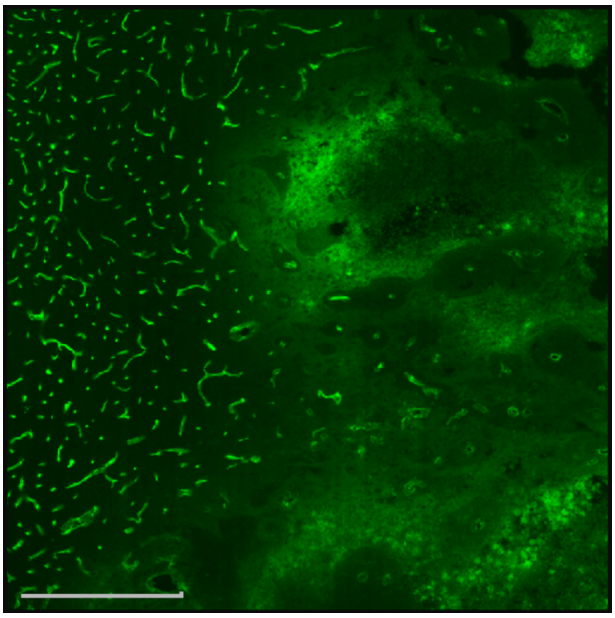

*Figure II.1 Tomato lectin in brain metastases.*Representative image of tomato lectin staining observed in brain metastases (scale bar = 0.4 mm).

As demonstrated in Figure II.1, injection of tomato lectin intravenously led to the visualisation of perfused vessels in the healthy brain but proved inconclusive in the brain metastasis region. This could potentially be attributed to an accumulation of tomato

lectin in the tumour through passage of the lectins across the blood-brain barrier, resulting in high levels of background fluorescence in this region. Owing to this complication, the application of this technique to the model of brain metastasis using in this thesis was not pursued.